Investigation of the Bubble Detector Response to High LET Space Radiation

by

Alexander L. Miller

A thesis submitted to the
School of Graduate and Postdoctoral Studies in partial
fulfillment of the requirements for the degree of

Doctor of Philosophy in Nuclear Engineering

Faculty of Energy Systems and Nuclear Science

University of Ontario Institute of Technology

Oshawa, Ontario, Canada

August 2018

THESIS EXAMINATION INFORMATION

Submitted by: **Alexander L. Miller**

Doctor of Philosophy in Nuclear Engineering

Thesis title: **Investigation of the Bubble Detector Response to High LET Space Radiation**

An oral defense of this thesis took place on July 31, 2018 in front of the following examining committee:

Examining Committee:

Chair of Examining Committee	Eleodor Nichita
Research Supervisor	Rachid Machrafi
Examining Committee Member	Anthony Waker
Examining Committee Member	Igor Pioro
University Examiner	Glenn Harvel
External Examiner	Emily Corcoran, Royal Military College

The above committee determined that the thesis is acceptable in form and content and that a satisfactory knowledge of the field covered by the thesis was demonstrated by the candidate during an oral examination. A signed copy of the Certificate of Approval is available from the School of Graduate and Postdoctoral Studies.

ABSTRACT

The radiation environment aboard spacecraft is a complex mixture of neutrons, photons, protons, heavy ions and other particles. A special type of superheated droplet detectors referred to as space bubble detectors (SBD) have been used to evaluate the equivalent dose due to neutrons in various space missions aboard the International Space Station. Protons and other heavy charged particles are a significant component of the high LET radiation field and also contribute to the SBD measurements. The calibration of the bubble detectors is established using a known Americium Beryllium(AmBe) neutron field. However, the space neutron field is considerably different from the AmBe field. Current models assume that bubbles are formed as a result of radiation interactions above a certain minimum LET threshold and experiments have shown that the LET threshold may be different for different ions.In order to interpret the bubble detector measurements in space radiation fields, a systematic investigation of the response of bubble detectors to high LET radiation encountered inspace has been performed. A series of experiments have been conducted with different high LET radiation including protons and energetic heavy ions using different facilities at the National Institute of Radiological Science in Chiba, Japan, and the ProCure Proton Therapy Center in Oklahoma, USA. High energy neutron experiments were conducted at the Los Alamos Neutron Science Center. A correction factor of 1.8 ± 0.2 has been determined to correlate the AmBe calibrated sensitivity to neutron equivalent dose measurements aboard the ISS. The LET threshold required to form a bubble in SBD was found to depend on the charge Z of the ion. An analytical model to evaluate the SBD response to high LET radiation aboard the ISS has been developed and compared to measurements.

Keywords: Space Bubble Detectors, Space Radiation, High LET Radiation, International Space Station

AUTHOR'S DECLARATION

I hereby declare that this thesis consists of original work of which I have authored. This is a true copy of the thesis, including any required final revisions, as accepted by my examiners.

I authorize the University of Ontario Institute of Technology to lend this thesis to other institutions or individuals for the purpose of scholarly research. I further authorize University of Ontario Institute of Technology to reproduce this thesis by photocopying or by other means, in total or in part, at the request of other institutions or individuals for the purpose of scholarly research. I understand that my thesis will be made electronically available to the public.

Alex Miller

STATEMENT OF CONTRIBUTIONS

The experimental work and measurements with charged particles in this thesis were performed at the ProCure Proton Therapy Center in Oklahoma, USA and at the National Institute of Radiological Science (NIRS)in Chiba, Japan. The high energy neutron measurement was performed at the Los Alamos National Laboratory in New Mexico, USA.

I significantly contributed to the design of the experiments and executed a series of experimental measurements at the NIRS facilities with charged particles. I also was responsible for the analysis of the experimental data collected in different experiments. I solely designed and programmed all MATLAB programs and performed the analysis and calculations presented in Chapter 4. I developed all models related to LET threshold for bubble formation in the bubble detector presented in Chapter 4, sections 4.3 and 4.4.

Part of the work described in this thesis, section 4.1 has been published/submitted as:

- A. Miller, R. Machrafi, E. Benton, H. Kitamura, S. Kodaira "Comparison of the Space Bubble Detector Response to Space-Like Neutron Spectra and High Energy Protons", Acta Astronautica,151(2018) 1-6.
- R. Machrafi, A. Miller, E. Benton, H. Kitamura, S. Kodaira "Study of the Response of the Space Bubble Detector to heavy Charged Particles" (submitted to Radiation Measurement Journal and it is under review).

I performed the analysis of the experimental data including determining the response functions, calculating the equivalent dose for neutron experiments, determining the calibration factor, and writing of the manuscript.

Some results in this thesis have been presented at different international scientific conferences as follows:

• A. Miller, R. Machrafi, E. Benton, H. Kitamura, S. Kodaira. (2017).Characterization of Bubble Detectors Used in Space Radiation Dosimetry: Charged Particle. 68th International Astronautical Congress, 2017-09-27. Adelaide, Australia.

•R. Machrafi, A. Miller, E. Benton, L. Tomi, B. Gersey, R. Wilkins. (2015). Ground Testing of Bubble Detectors used in Space Radiation Dosimetry: Response to High Energy Neutrons. 20thWorkshops on Radiation Monitoring for the International Space Station, 2015-09-08. Cologne, Germany

I hereby certify that I am the sole author of this thesis. I have used standard referencing practices to acknowledge ideas, research techniques, or other materials that belong to others. Furthermore, I hereby certify that I am the sole source of the creative works and/or inventive knowledge described in this thesis.

Acknowledgments

I am eternally grateful to my supervisor, Dr. Rachid Machrafi who has inspired and cultivated my abilities so much. I appreciate his support throughout all of my graduate research work. I thank my supervisory committee; Dr. Anthony Waker, who taught me everything I know about dosimetry, and Dr. Igor Pioro, for their guidance.

I would also like to thank Dr. Eric Benton for sharing his expertise and for his excellent advice. His insight on radiation in space and the use of experimental facilities have been invaluable. I would also like to share my personal gratitude for Dr. Satoshi Kodaira and Hisashi Kitamura as well as all of the NIRS staff for their hard work and assistance during the experiments at HIMAC.

I thank the Canadian Space Agency for their funding to support this research. I also thank the Natural Sciences and Engineering Research Council for their funding. I am personally grateful for the Ontario Graduate Scholarship funding for my graduate research.

Last, I thank my family who nurtured me, guided me and supported me the whole time.

TABLE OF CONTENTS

LIST OF FIGURES

LIST OF TABLES

LIST OF NOMENCLATURE

Acronyms

AmBe: Americium Beryllium (neutron source)

BBND: Bonner Ball Neutron Detector (Bonner Sphere)

BDRIII: Bubble Detector Reader

BDS: Bubble Detector Spectrometer

BF: Binary Filter (acrylic heavy charged particle beam blockers)

BION: Biocosmos, Russian Satellite

BTI: Bubble Technology Industries

CERN: European Council for Nuclear Research

CREME96: Cosmic Ray Effects on Micro-Electronics (1996 Revision) GCR: Galactic Cosmic Rays

HIMAC: Heavy Ion Medical Accelerator in Chiba

ICE House: Irradiation of Chips and Electronics House

ICRP: International Committee on Radiological Protection

ISO: International Organization for Standardization

ISS: International Space Station

JEM: Japanese Experimental Module

JPM: Japanese Pressurized Module

LANSCE: Los Alamos Neutron Science Centre

LEO: Low Earth Orbit

LET: Linear Energy Transfer

MATLAB: Matrix Laboratory (Mathematics software)

MRM1: Mini-Research Module-1

NCRP: National Council on Radiation Protection

NIRS: National Institute of Radiological Sciences

OLTARIS: On-Line Tool for the Assessment of Radiation In Space

PHITS: Particle and Heavy Ion Transport code System

PMMA: Poly-Methyl MethAcrylate (Acrylic)

PND: Personal Neutron Dosimeter

RBE: Relative Biological Effectiveness

SAA: South Atlantic Anomaly

SBD: Space Bubble Detector

SBDS: Space Bubble Detector Spectrometer

SPE: Solar Particle Events

SPND: Space Personal Neutron Dosimeter

SRIM: Stopping and Ranges of Ions in Matter

STS: Space Transport System (Space shuttle)

TEPC: Tissue Equivalent Proportional Counter

TIFF: Tagged Image File Format

UOIT: University of Ontario Institute of Technology

Symbols and Units

amu: atomic mass unit

atm: atmosphere

Ar: argon

C: carbon

c: speed of light, [m/s]

Cf: californium

Cl: chlorine

cm: centimeter

D: absorbed dose, [J/kg]

D_{min}: minimum energy density

$D_{threshold}$: threshold energy density

e: electron charge

E: energy, [MeV]

eV: electron Volt

Fe: iron

GeV: gigaelectron Volt (10^9 eV)

Gy: Grey, absorbed dose,[J/kg]

H: hydrogen

$H^*(10)$: ambiend dose equivalent, [Sv]

H: equivalent dose, [Sv]

He: helium

h_{fg}: latent heat of vaporization

J: Joule, [kg m^2/s^2]

K: Kelvin (absolute temperature)

keV: kilo Electron Volt (1,00010^3 eV)

kg: kilo gram

Kr: krypton

LET_∞: unrestricted LET, [keV/μm]

LETr: restricted LET, confined to distance , r [keV/μm]

m: meter

MeV: mega electron Volt (10^6 eV)

m_o : rest mass, [amu]

n: neutron

N: atom density [atoms/cm^3]

N: nitrogen

N_b: number of bubbles

Ne: neon

nm: nano-meter

O: oxygen

p: proton

P_s: saturated vapor pressure [atm]

P': external vapor pressure [atm]

Q: quality factor

R_i : bubble detector response for particle i(bubbles/(particle/cm^2))

r: radius [μm]

R_c : vaporembryo critical radius [μm]

r_c: ion track core radius [μm]

r_{max}: ion track radius

S: reduced super heat

S: sulfur

S_{AmBe}: bubble detector sensitivity to AmBe neutron spectra,[bubbles/μSv]

Si: silicon

Sv: Sievert, unit of equivalent dose

T: ambient temperature, [K]

T_b: liquid boiling temperature, [K]

T_c: critical temperature, [K]

v: particle velocity

v': specific volume of liquid, [cm^3/g]

v'': specific volume of vapour, [cm^3/g]

Xe: xenon

Z^*: effective ion charge

Z: ion Charge

β: ratio of velocity to speed of light (v/c)

γ: surface tension, [J/m^2]

$\rho_{m:}$ density, [g/cm^3]

σ: uncertainty in value

$\boldsymbol{\Phi}$: fluence, [particles/cm^2]

$\frac{dE}{dx}$: LET, [keV/μm]

$\bar{\varepsilon}$: mean imparted energy, [J]

μm: micro-meter (micron)

INTRODUCTION

The radiation environment aboard spacecraft is a complex mixture of neutrons, photons, protons, heavy ions and other charged particles [1]. The radiation exposure to astronauts during manned space missions could pose adverse health effects [2][3]. Thus, it is necessary to monitor radiation exposure carefully and to be able to predict radiation exposure during mission planning [4]. The complexity of the radiation environment within spacecraft makes both accurate measurements and reliable prediction of radiation dose on specific missions very difficult to achieve [5]. Heavy ions, neutrons, and protons are present in large energy ranges [6]. Furthermore, the response of most radiation detectors and dosimeters is limited and not able to accurately measure the dose from all particles and all energies simultaneously [7]. The radiation field experienced by an astronaut aboard a spacecraft may vary significantly over time based on orbit parameters, altitude, solar conditions or even specific location in the spacecraft due to different shielding[8]. A significant portion of the radiation dose received by astronauts comes from protons and neutrons because the flux of these particles is comparatively large and both include particles from low energy to high energy particles [9]. The highly localized linear energy transfer (LET) of these particles makes them of particular concern for the equivalent dose received by astronauts during manned space flight missions [10]. Furthermore, neutrons are particularly hard to measure accurately because they are uncharged particles that interact with matter in many complicated ways and the probability of their interaction varies significantly with the incident energy and target nuclei structure [11].

A substantial amount of work has been done to calculate and measure the radiation dose that astronauts receive during specific manned space missions and to determine any health

effects that may be induced by these radiation exposures [12][13]. The Matroshka-R and the Radi-N programs are two examples that have been implemented to determine the radiation dose to astronauts aboard the International Space Station (ISS) [9][14]. Neutron radiation exposure is believed to be responsible for ~30 % to 50 % of the total equivalent dose astronauts receive [15]. These programs have put significant effort into measuring neutron dose accurately. Both of these programs have employed bubble detectors as neutron detectors and there have been a large number of measurements on the ISS as well as on satellite missions and on other spacecraft. Bubble detectors are a class of radiation detectors that generate visible bubbles within a medium when exposed to radiation. Bubble Technology Industries (BTI) is a company based in Chalk River, Canada, which manufactures unique bubble detectors that are designed to perform measurements aboard spacecraft. Both the Matroshka-R and the Radi-N experiments have used BTI bubble detectors in various experiments. The two kinds of space bubble detectors manufactured by BTI are the space bubble detector (SBD) and the space bubble detector spectrometer (SBDS). See Appendix A for a list of SPND and SBDS experiments performed aboard the ISS.

The SBD is a bubble detector that produces observable bubbles when a high LET particle interacts with the detector sensitive media [16]. A digital reader is used to image the detector and counts the number of expanded bubbles after a radiation exposure. The number of visible bubbles after a given exposure is directly proportional to the fluence of high LET particles [17]. The calibration of these devices is performed by counting the bubbles after an exposure to a known AmBe neutron field. However, when the detector is used in the space environment, protons and other heavy charged particles also have high LET and contribute to the number of visible bubbles in the detector [18]. Hence, the number of bubbles observed after a radiation

exposure is a result of interactions with neutrons, protons, and heavy charged particles[19]. In order to determine the neutron dose using bubble detectors, it is necessary to evaluate the contribution of each radiation type. The mechanisms of bubble formation are not known on the microscopic scale and no model has ever been developed to accurately describe whether a particular radiation type of a given energy and LET will form a bubble or not. It is simply known that high LET radiation can form bubbles and low LET radiation cannot. Another significant challenge in determining the neutron dose using bubble detectors on spacecraft is the substantial difference of the neutron energy spectrum on spacecraft compared to the AmBe spectra traditionally used for the bubble detector calibration. AmBe neutrons have energies from thermal to ~11 MeV with most neutrons in the fast range of the spectrum. Spacecraft have a large energy span extending from thermal energies to neutrons above 1,000 MeV. The vast difference of the dose to fluence conversion factor over the spacecraft spectrum means that bubbles formed by these neutrons could have a significantly different equivalent dose than the AmBe neutrons used to calibrate the detector [18].

The space bubble detector spectrometer (SBDS) is another device used in different space missions to evaluate the neutron spectra. The system is a set of six bubble detectors and it is used to measure a course neutron spectrum based on the response of each individual detector in the set. Each of the six detectors has a different energy threshold for neutron induced bubble formation. After exposure, a response matrix is used to determine the neutron spectrum [20]. However, these bubble detectors are also sensitive to protons and heavy ions.

Motivation of Thesis

Currently, bubble detector measurements aboard the ISS and in other space missions are carried out simply by counting the number of bubbles, assuming that the observed bubbles are a result of neutron interaction only. The response of the bubble detector to the heavy charged particles is unknown and consequently, their contribution to the reading in the detectors remains unknown. The AmBe calibration is multiplied by a scaling factor of 1.62 to compensate for the difference in neutron spectrum [21]. The proton and heavy ion contributions have been considered negligible. There is no physical model that explains the mechanism of bubble formation that can be used to interpret the measurements and the readings of the bubble detector in terms of the contribution of neutrons, protons, and heavy ions. Calculations based on empirical data from a limited number of experiments have been used to estimate bubble detector measurements on different ISS missions [18]. These estimates have consistently under-predicted the number of bubbles by a factor of two, indicating that the formation of bubbles is not well represented in this method. In addition, the LET threshold model of bubble formation does not explain the differences in bubble formation observed when the bubble detector is exposed to known proton, and heavy ion beams [22].

Objective of Thesis

The objectives of this thesis are to investigate the response of bubble detectors to high LET radiation encountered in the space environment. In particular, to develop an effective physical model of the mechanism of bubble formation in these detectors based on their physical properties and ion track structures. More specifically to systematically investigate:

1. The response of bubble detectors to high LET radiation encountered in the space environment.

2. Determine the minimum LET required for bubble formation in a space bubble detector and investigate its dependence on the charge Z of the incident charged particle.

3. Establish an effective model of the mechanism of bubble formation in these detectors based on their physical properties and the ion track structure.

4. Evaluate the readings of the space bubble detector in a complex space radiation field.

Novelty and Contribution

Bubble detectors are widely used in the field of neutron dosimetry and have been successful in terrestrial applications. However, the response of these detectors onboard spacecraft to neutrons, protons and high energy heavy charged particles is not well understood. The work presented in this thesis has the following features:

- Experimental study of the bubble detectors response to a neutron spectrum similar to the neutron spectrum expected aboard spacecraft.
- For the first time, experimental investigation of the bubble detector response to high energy protons (above 60 MeV).
- Systematical investigation of the bubble detector response to a large number of heavy charged particles including He, C, O, Ne, Si and Fe and determination of the LET threshold required for bubble formation for each ion.
- For the first time, the Z-dependence of the LET threshold required for bubble formation has been studied within the framework of ion track structure models.

- For the first time, a predictive model for bubble formation in space missions has been developed and compared to measurements.

The work performed in this thesis is directly applicable to the analysis and interpretation of SBD and SBDS measurements aboard the ISS and other spacecraft. The response of SBD and SBDS to neutrons, protons and heavy ions analyzed in this thesis will improve our understanding of bubble detector measurements in space and will aid in radiation protection dosimetry, and radiation measurements in complex space environments. Some results have already been published [23]. The analysis of LET, range, ion track structure and bubble formation in bubble detectors for energetic protons and heavy ions in this thesis will also have impact on the bubble detector use in high energy particle facilities. Bubble detectors are currently used for neutron dosimetry in radiation therapy facilities (for example, secondary neutron dose in photon therapy beams [24][25][26]). Results presented in this thesis may be useful for bubble detector measurements in proton or carbon therapy facilities and help in beam characterization or treatment analysis.

Approach

This thesis includes an extensive and systematical campaign of ground-based experimental investigations of the bubble detector response to neutrons, high energy protons and heavy charged particles using different neutron and heavy charged particle facilities. In addition, simulations using the stopping and range of ions in matter (SRIM) code, particle and heavy ion transport code system (PHITS) and the Online-Tool for the Assessment of Radiation in Space (OLTARIS) have been used along with the experimental investigations to evaluate the response

of space bubble detectors in complex radiation fields. A series of experimental investigations of the space bubble detector response to high energy protons and heavy charged particles including He, C, O, Ne, Si and Fe with known LET have been performed as well as experiments with spallation neutrons.

Outline of the Thesis

This thesis consists of an introduction that gives a description of the scope of the work, a brief description of the bubble detectors and their current use in space environment. Chapter 1 provides an overview of dosimetric quantities, radiation interaction, radiation detection principles and a brief description of the bubble detectors along with an introduction to space radiation. Chapter 2 provides a detailed literature survey on experiments and modeling of superheated droplet detectors as well as bubble detector measurements in spacecraft. Chapter 3focuses on the methodology used in both experimental investigation and modeling. Chapter 4 presents the results of the investigation carried out with different heavy charged particles, high-energy neutrons as well as a discussion of the experimental results and modeling. Chapter 4 ends with an evaluation of the bubble detector readings in complex space radiation fields and a comparison of analytical models and experimental measurements aboard the ISS. The thesis ends with a conclusion, future work and a list of references and appendices.

CHAPTER 1: BACKGROUND AND THEORY

1.1 Radiation Dosimetry

One property of all ionizing radiation is that damage can occur in DNA or cell structures in living organisms and can result in undesirable effects such as cell death, mutations, and cancer [27]. Human exposure to ionizing radiation is known to cause these effects. Avoiding, preventing and limiting human exposure to radiation is a standard practice. However, background radiation is always present and eliminating exposure to radiation is impossible. It is also evident that the level of risk from radiation exposure is proportional to the amount of the exposure such that low exposures may be acceptable and high exposures may pose a risk [28]. Unfortunately, the specific mechanisms that lead to the harmful effects of radiation exposure in humans are extremely complicated. Quantifying radiation levels and directly correlating those levels to specific harmful effects such as different types of cancer is difficult and in many cases impossible [27]. In practice, only some specific quantities can be measured with practical radiation detectors and estimates of risk are correlated to those quantities based on biological studies [29].

1.1.1 Absorbed Dose

In principle, the simplest radiation quantity that can describe the amount of radiation experienced by a body in a radiation field is the absorbed dose. This is the total amount of energy absorbed by the body divided by the mass usually given in units of J/kg or Gy. This is a conceptually simple macroscopic quantity for large bodies absorbing energy from ionizing radiation. The concept of absorbed dose at a point or within microscopic volumes comparable to

cells or microscopic bubbles in a bubble detector is less clear since the spatial distribution of energy deposition by ionizing radiation may be comparatively large and nonhomogenous [30]. Absorbed dose, *D,* is defined as the stochastic quantity of mean energy imparted by ionizing energy $d\bar{\varepsilon}$ in an infinitesimal volume with mass dm [29].

$$D = \frac{d\bar{\varepsilon}}{dm} \tag{1.1}$$

1.1.2 Equivalent Dose

The microscopic structure of ionizing radiation damage in living cells is not fully described by the stochastic quantity absorbed dose [30]. The drastic difference of energy deposition between x-ray, gamma, electron, neutron and heavy ion radiation in living organisms means that DNA damage and visible biological effects may be noticeably different from one radiation type to another, even for the same absorbed dose quantity [31]. Another quantity has been developed called the equivalent dose and it attempts to relate the level of biological damage to the absorbed dose by comparing the sensitivity of cells to different types of radiation exposures. The absorbed dose is multiplied by a quality factor, Q which is meant to express the effectiveness of the specific radiation type at adverse biological effects. This is based on extensive biological studies of radiation exposure and included in the Relative Biological Effectiveness (RBE) [27]. The simplest form is the whole body equivalent dose for an external radiation field where the equivalent dose, H is given as the product of the absorbed dose and the radiation quality factor [32].

$$H = D \cdot Q \tag{1.2}$$

The unit of the equivalent dose is Sievert (Sv). By convention, the quality factor is given relative to photon radiation such that the equivalent dose of 1 Gy of photons is 1 Sv. For neutrons and heavy ions, the level of biological damage is related to the energy of the particle so that the quality factor is actually a function of the particle energy $Q = Q(E)$ [27]. Further studies have been used to define the effective dose which describes the entire whole body effect of radiation exposure to humans with consideration for individual organs and tissues with different sensitivity to radiation [33].

Effective dose is not a practical quantity to directly measure in external radiation fields since radiation exposure to specific organs may not be well known. For radiation protection purposes another dosimetric quantity called the ambient dose equivalent, $H^*(10)$ is used to estimate the whole body effective dose for an external radiation field. This is defined as the total equivalent dose as calculated with radiation quality factors $Q(E)$ for the radiation field (including secondary radiation) after penetrating 10 mm into a 30 cm diameter sphere made of tissue equivalent plastic [34]. This quantity is meant to give an estimate of radiation damage to sensitive internal organs without requiring a sophisticated model of a whole human body and detailed knowledge radiation penetration into each tissue and organ.

1.1.3 Fluence-to-Dose Conversion Factors

The complex radiation fields encountered in spacecraft have many different particles with a large distribution of energies. For an individual particle type, the quality factor may be very different for particles with different energies. Fluence-to-equivalent dose conversion factors have been developed by radiation protection institutions such as International Commission on Radiological Protection (ICRP) and National Council on Radiation Protection (NCRP) to

calculate the total equivalent dose from the whole range of particles in a known field. The conversions are given as the equivalent dose per unit fluence of external radiation exposure. The fluence and the quality factors are typically both functions of the particle energy so the equivalent dose is integrated over all energies.

$$H = \int_0^\infty \Phi(E) \cdot CF(E)\, dE \tag{1.3}$$

Where H is the equivalent dose, $CF(E)$is the fluence to equivalent dose conversion factor at energy E and Φ is the particle fluence at energy E [35]. Dose conversion factors are also often given for ambient dose equivalent. Figure 1 shows the dose conversion factors for neutrons with energies from 10^{-8} to 10^{2} MeV from NCRP report no.38 for equivalent dose and ICRP 74 for ambient dose equivalent.

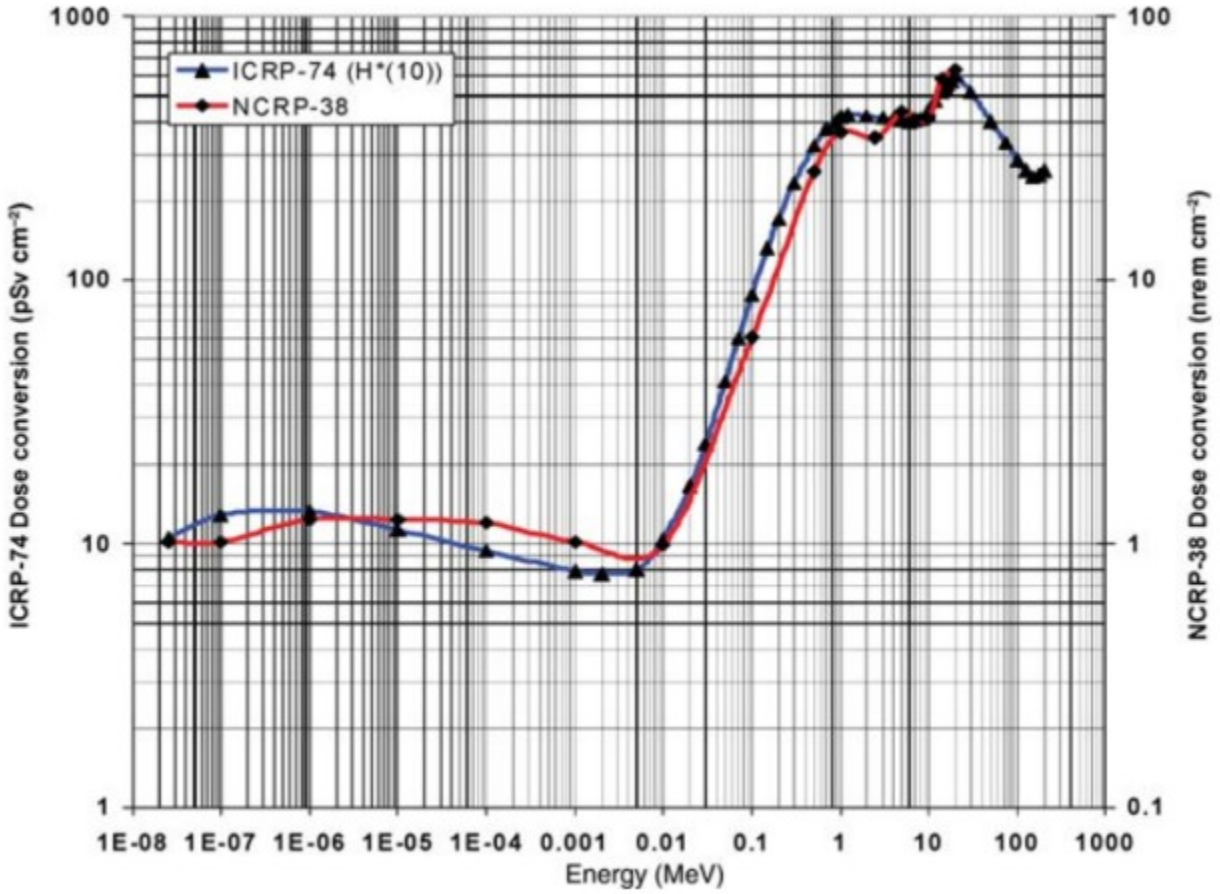

Figure 1: ICRP-74 and NCRP-38 dose conversion factors for neutrons [18]

1.2 Radiation Interaction with Matter

The detection and measurement of radiation fields are fundamentally determined by how particles interact with the atoms and molecules that make up the detector. Consideration of the interactions of radiation with matter is important in understanding the capability of detectors to measure and quantify a complex radiation field such as those experienced in space.

1.2.1 Photon Interactions with Matter

High energy photons such as x-rays and gamma rays are abundant in the space environment [36]. Photons primarily interact with electrons in the detector material through the photoelectric effect, Compton scattering or *via* pair production if the photon energy is above the minimum threshold energy. Radiation detectors use the resulting high energy free electrons to measure the photon as an interaction event and may count the number of events (as a Geiger counter) or measure the photon energy based on the kinetic energy of the electron in the detector (as with proportional counters or scintillation spectrometers) [37].

1.2.2 Electron Interactions with Matter

High energy free electrons slow down and stop in matter since they interact very strongly with the large number of bound electrons *via* Coulomb forces. As free electrons traverse through matter the energy is transferred to the material. This energy results in various effects which may be exploited by radiation detectors as measurement mechanisms. For example, recoil high energy electrons are multiplied to a measurable current in gaseous detectors and resulting electron-hole pairs are used in scintillation detectors, thermo-luminescent detectors, and semiconductor detectors [37].

1.2.3 Heavy Charged Particle Interactions with Matter

Protons, alpha particles and high energy atomic nuclei (heavy ions) are considered to be heavy charged particles and they interact strongly with the electrons when traveling through materials. The mass of protons and all other heavier charged particles is much greater than the mass of a single electron, so energetic heavy charged particles tend to interact with a large number of electrons and transfer energy to the electrons as they pass by. The heavy charged particle will slow down and stop in the material as a result and the electrons may be left in an excited state or be ionized and travel through the material as free electrons. The energy imparted to each electron depends on the proximity to the heavy charged particle and the charge and mass of the heavy charged particle. The net result is a large number of ionized free electrons and excitations along the heavy charged particle path while the charged particle will slow down continuously and stop in the material [37]. The incremental energy transferred from the heavy charged particle, *dE* to the stopping medium as it traverses an incremental distance, *dx* through the material defines the linear energy transfer (LET) and is described by the Bethe formula;

$$\frac{dE}{dx} = \frac{4\pi e^4 z^2}{m_0 v^2} NZ \left[ln\left(\frac{2m_0 v^2}{I}\right) - ln\left(1 - \frac{v^2}{c^2}\right) - \frac{v^2}{c^2}\right] \quad (1.4)$$

Where *e* is the electron charge, m_0 is the electron rest mass, *z* is the charge of the heavy charged particle, *v* is the velocity of the heavy charged particle, *N* and *Z* are the number density and atomic number of the absorber atoms, and *c* is the speed of light in a vacuum[7]. LET is often given as keV deposited per μm traveled by the heavy charged particle. As energetic heavy charged particles slow down, the LET increases. As seen in the Bethe formula, while the particle slows down and the velocity approaches zero, the LET may become large. At the very end of the

heavy charged particle track, electrons from the stopping material are captured by the heavy charged particle and subsequently the charge, velocity and stopping power will become zero. At this point, the heavy charged particle stops and this is called the end of the range of the ion. The short region of significantly increased LET near the end of the heavy charged particle range is called the Bragg peak[7]. Figure 2 shows the Bragg peak of an alpha particle penetrating into a material. The LET of a single alpha particle is compared to the mean LET for a parallel beam of many alpha particles entering the material with the same initial energy. There are a large number of charged particle-electron interactions along the alpha particle paths so the net result is a stochastic effect where the alpha particles slow down continuously with a range that varies from particle to particle. This phenomenon acts to spread out the Bragg peak and is called particle straggling [38].

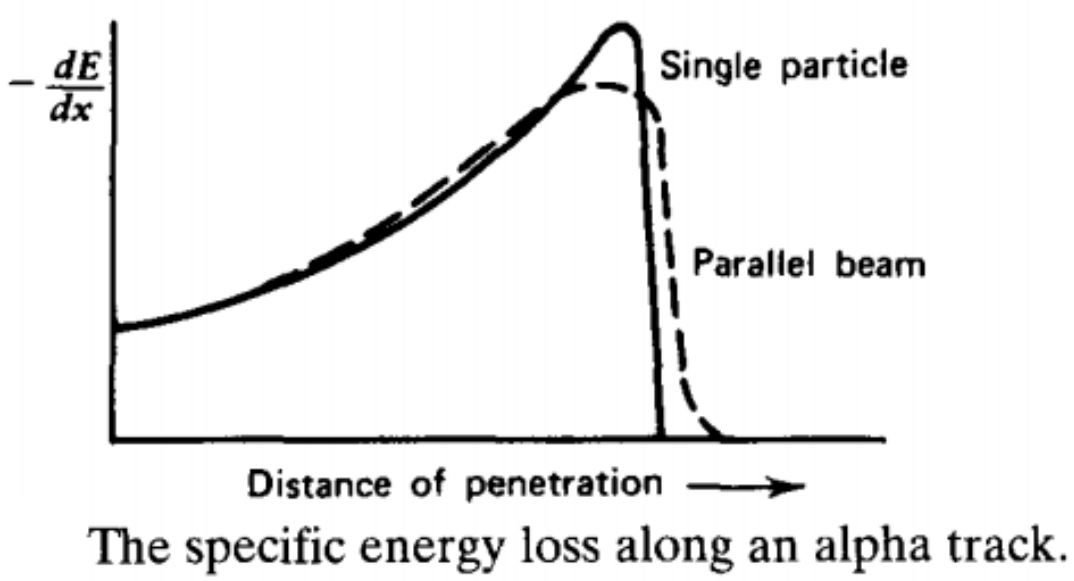

Figure 2: Bragg peak of alpha particle [7]

*(*Figure reproduced with permission *from John Wiley and Sons)*

1.2.4 Neutron Interactions

Neutrons are uncharged heavy particles and thus do not interact with material *via* Coulomb forces unlike electrons and heavy charged particles. In fact, neutrons may pass directly through several centimeters of a detector material without interacting at all making them difficult to detect and measure [37]. Neutrons have essentially no interaction with electrons in materials and only interact in the event of a direct collision with a nucleus. The neutron is either absorbed by the nucleus or else it scatters and imparts some of its energy to the nucleus and continues in an altered trajectory with decreased kinetic energy. There are a large number of possible neutron interactions with a nucleus and many interactions are unique to the specific isotope of the nucleus. Furthermore, the probability of each possible interaction varies significantly with neutron energy where some interactions are much more likely with lower energy neutrons, some interactions require minimum threshold energy to occur, and some interactions become more likely at higher neutron energies or in specific resonant energies [39]. Due to all possibilities of neutron interaction in a detector material, it is very difficult to construct an accurate and efficient neutron detector that can measure and quantify all neutrons in a widely varying field such as the neutron field present aboard spacecraft. A brief description of the small number of possible neutron interactions that are particularly relevant to bubble detectors follows. The single most important neutron interaction in the context of bubble detector measurements is elastic and inelastic scattering events. This is where a neutron scatters off a nucleus which recoils with kinetic energy imparted from the neutron where the neutron is deflected by some angle and continues to travel through the material. The kinetic energy of the recoil nucleus depends on the mass of the nucleus, the initial energy of the neutron and the angle of the deflected neutron.

Similarly, inelastic scattering results in a scattered neutron and recoil nucleus; however, some of the energy is absorbed by the nucleus leaving it in an excited state a gamma ray is emitted as the nucleus de-excites down to its ground state. Transmutation interactions occur when the neutron upsets the nucleus upon collision and changes the number and configuration of bound nucleons. Two important examples are the neutron-proton and the neutron-alpha interactions where the neutron is absorbed by the nucleus and a proton or alpha particle is ejected. This reaction mechanism is important in bubble detectors since it produces high LET protons, alphas, and recoil nuclei directly from single events with fast neutrons [39]. For example, the reaction $^{1}n + {}^{35}Cl \rightarrow {}^{1}H + {}^{35}S$ has a large cross-section for neutrons in the range 1 to 10 MeV and contributes to the bubble detector sensitivity to neutrons in this energy range [40].

1.2.5 Heavy Ion Track Structure

The large number of secondary energetic electrons produced along the path of a heavy charged particle assume a specific structure. The heavy charged particle path is typically a straight vector with electrons ejected outward from the center point of the path and stopping in a short distance as energy is dissipated into the medium [41]. Occasionally some electrons may be imparted with a large amount of energy and be ejected very far away from the heavy charged particle path. In general the distance of the secondary electrons depend on kinetic energy, charge and mass of the heavy charged particle where a high energy heavy charged particle will eject many electrons very far away from the ion path while a lower energy heavy charged particle will have much shorter ranged secondary electrons and excitations very close to the centre of the ion path. In all cases, the energy density at the center of the path is large and decreases significantly

radially outwards as the secondary electrons diverge [42]. Figure 3 illustrates the ion track structure of an iron ion stopping in a nuclear emulsion measured during the Apollo XVII lunar mission [43]. The scale of the photomicrograph in Figure 3 is 10 microns per division. The figure is divided into three sections for clarity with labels at points C, B and A indicating where the picture should be joined as a single straight image if the whole track was to be shown continuously.

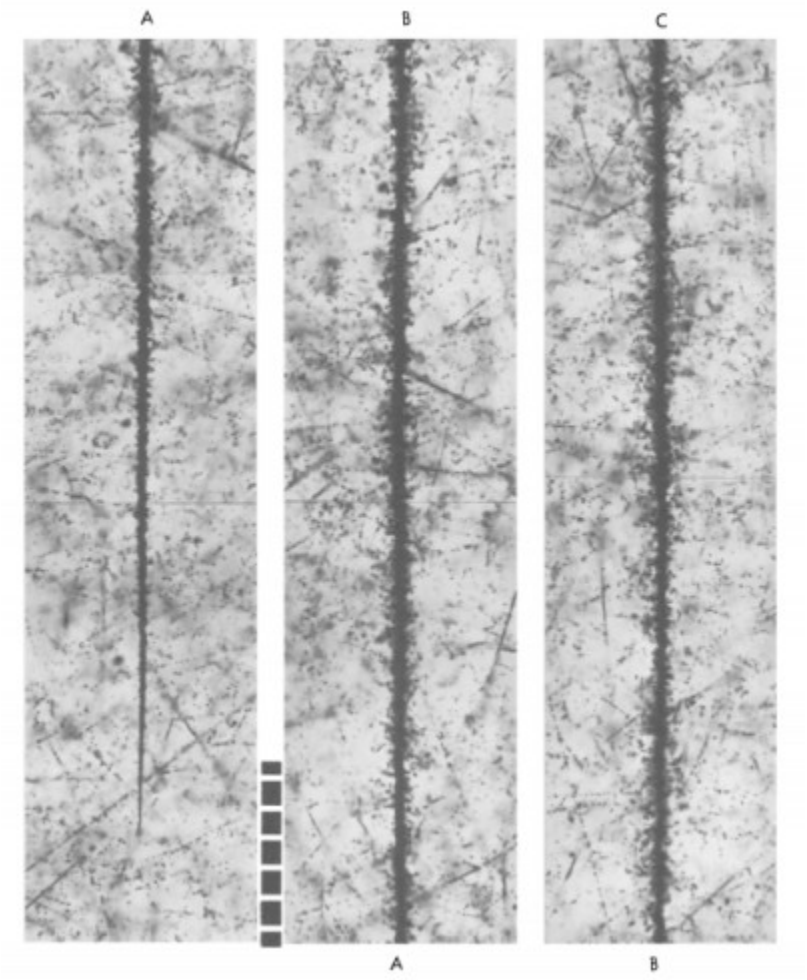

Figure 3: Nuclear emulsion of iron ion track [43]

(Figure reproduced with permission from Springer Nature)

The iron ion in Figure 3 enters from the top right of the figure (point C) and travels thru point B then point A where it finally comes to rest near the bottom left of the figure. There is an apparent effective radius of the track where most of the electrons appear to stop around the same distance from the track center. This appears to narrow and become very small near the end of the track where most of the energy is concentrated in the middle of the ion track. The end of the ion range is also very apparent where the track suddenly stops. Some of the electrons along the high energy portion of the track (between point C and A) travel much further away from the ion path and these are often called delta rays (high energy secondary electrons that travel far away from heavy ion tracks). Considering the Bragg peak it is evident that the LET is increasing as the ion stops and the density of the secondary electrons along the track is becoming large at the end of the track.

LET is the parameter most commonly associated with heavy ion energy deposition since it describes the amount of energy deposited per unit distance traveled by the ion. However, the parameter does fully describe the secondary electron distribution and the location of energy deposition from the secondary electrons is unspecified. In principle, a very highly energetic heavy ion with a large charge and large mass could produce extremely energetic secondary electrons which could deposit the energy very far away from the ion track. When considering radiobiological effects, DNA damage and microscopic geometries, the energy deposited by secondary electrons at distances greater than tens, hundreds or thousands of microns away from the ion path may not be relevant[31]. Thus, the parameter LET has been further defined to include a parameter that indicates the range of the secondary electrons. When the total energy deposited per unit distance traveled is considered for all secondary electrons regardless of their range, the parameter is called LET_{∞} and is simply the familiar parameter described in Equation

(1.4). This is the usual form of LET and if no subscript is specified LET_{∞} is assumed. However, if one is considering only the energy deposition locally to the ion track then a distance can be specified in the subscript such that only energy deposited by secondary electrons with a range less than that distance is considered. For example, $LET_{5\mu m}$ is the total energy deposited within a 5 μm radius per unit distance traveled by the heavy ion. This is called the restricted LET since it restricts the effects to a region around the ion track [44]. Restricted LET is also equivalently specified by the maximum secondary electron energy which is also directly related to the secondary electron range. For example, LET_{50eV} is the total energy deposited by secondary electrons with initial energy less than 50 eV per unit distance traveled by the heavy ion.

Different ions of different energies may have the same LET, but differences in the charge Z means that the ions will undergo a different frequency of collisions with electrons. In addition, differences in mass mean that the velocity, momentum and kinetic energy are different, the energy imparted to electrons is different and the range of the secondary electrons is different. Thus, different ions have a different distribution of energy around the ion track based on the ions kinetic energy, LET, properties of the material and the charge and mass of the ion [45]. Three prominent analytical models have been developed to calculate the dose distribution around ions (track structure models). Namely, the Katz model, the Chatterjee model, and the Kiefer model [43][46][47]. All three of these models can be used to calculate the radial dose distribution of an ion stopping in a material based on the ions kinetic energy and the properties of the material (often just the density). All three models include an effective radius called r_{max} or the edge of the 'penumbra' which is effectively the maximum distance of secondary electrons. In each model there is a high concentration of dose near the center of the ion track and a significantly reduced dose further away that vanishes towards r_{max} [48]. The Chatterjee model includes two separate

regions. The 'core' where half of the LET energy is deposited uniformly in a very small region near the ion track and the penumbra where the dose falls off and vanishes at r_{max}. All three models have been shown to fit well with data measured from ion track structures over a wide range of ions, energies, and materials [49]. However, none of the three models perfectly describes all experimentally measured values [50][51]. For example, Figure 4 depicts the radial dose distribution around a 73.2 MeV He ion in water [48]. The Chatterjee, Katz and Keifer models have been plotted together with experimental data [50]. All three models fit the data well in the 20 nm to 2µm range. However, r_{max} appears to be overestimated by all three models with the Chatterjee model having the best-estimated end of the range of the secondary electrons and the Katz model having the largest overestimation. The radial dose is slightly underestimated below 20 nm by all three models.

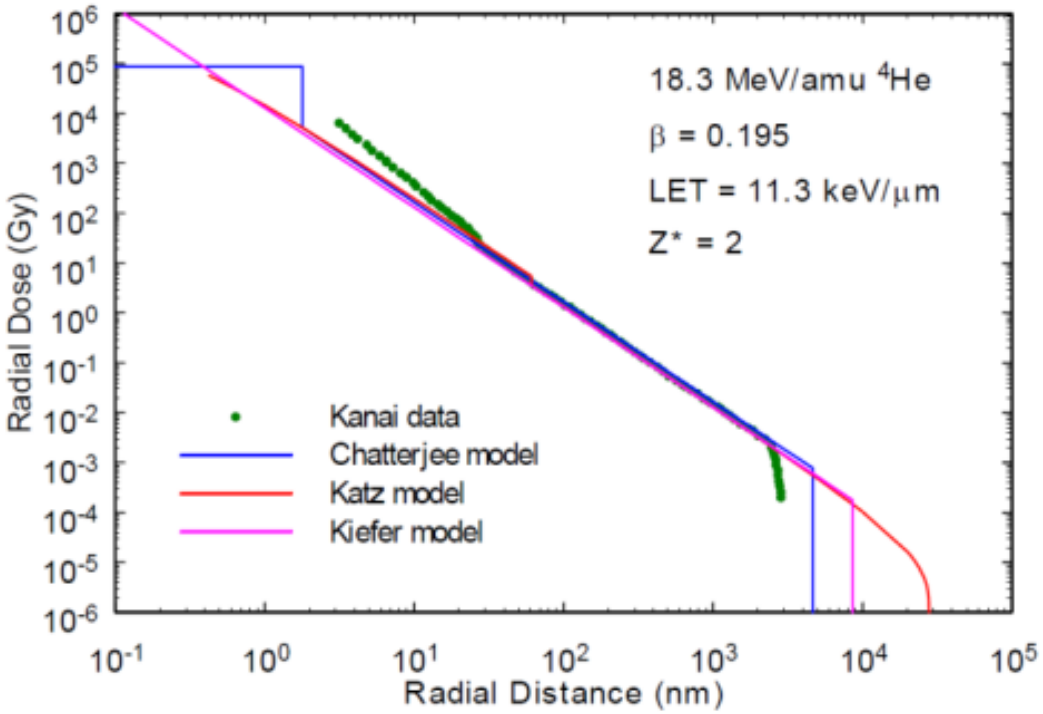

Figure 4: Ion track structure for 18.3 MeV/n He in water [48]

(Figure reproduced with permission from author)

The Chatterjee track structure model defines the ion "core radius" r_c and the penumbra r_{max} where half of the energy deposited along the track remains in the ion core and the other half diverges outward. The ion core is considered to be a small region near the ion track with a constant high energy density where approximately half of the energy is deposited from excitations. The size of the core radius is effectively defined by the region of electron excitation around the ion track and calculated using the plasma oscillation frequency. The critical radius can be calculated with the following equation from [48]:

$$r_c = \frac{5.314\times10^{12}}{\sqrt{N}} \times \beta \text{ (nm)} \tag{1.5}$$

Where r_c is the ion track core radius and β is *v/c* and N is the electron density of the material (3.34×10^{23}electrons/cm^3 for STP liquid water).

The ion track "penumbra" radius (r_{max}) is defined by the maximum range of the secondary electrons and has been determined empirically from electron range data. The maxim radius can be calculated with the following equation from [48]:

$$r_{max} = \frac{3.85\times10^{5}}{\rho_M} \beta^{2.7} \text{ (nm)} \tag{1.6}$$

Where ρ_M is the material density (the density is 1.29 g/cm^3 for bubble detectors)

The Katz track structure model does not include a "core" region and defines the ion penumbra r_{max} using empirical data with range-energy relations of electrons. r_{max} for the Katz model is given by the following equation from [48]:

$$r_{max} = \frac{6.24\times10^{6}}{\rho_M} \frac{\beta^2}{(1-\beta^2)} \text{(nm)} \tag{1.7}$$

The Keifer model is based on classical collision dynamics and also defines the ion penumbra, r_{max} by the following equation from [48]:

$$r_{max} = \frac{61.6\, E^{1.7}}{\rho_M} \text{(nm)} \tag{1.8}$$

Where E is the ion energy in MeV/amu.

The restricted stopping power can be calculated using r_{max} and the ion core radius r_c as defined by the Chatterjee model. The stopping power restricted to a distance r is given by the following equation from [43]:

$$LET_r = \frac{LET_\infty}{2}\left[1 + \frac{1+2\ln(r/r_c)}{1+2\ln(r_{max}/r_c)}\right] \tag{1.9}$$

Where r is the limit of the secondary radiation range, LET_∞ is the unrestricted stopping power, r_{max} is the penumbra radius and r_c is the "core" radius. The Chatterjee restricted stopping power equation assumes that half of the energy deposited per unit distance remains within the core due to excitations. The rest of the energy is deposited between r_c and r_{max} by secondary electrons that diverge from the ion track with a density relation of $1/r^2$ [52].

1.3 Properties of Bubble Detectors

1.3.1 Physical Properties of Bubble Detector

There are many different superheated drop detectors and bubble detectors that can be made of different materials using different manufacturing processes [53]. However, the research in this thesis will focus on the bubble detector® produced by BTI since these are the specific type

of bubble detectors used in spacecraft radiation monitoring programs. Bubble detectors are passive radiation dosimeters that produce visible bubbles when exposed to specific forms of radiation. This is achieved by storing mechanical energy in metastable superheated droplets that are held in a liquid state while suspended in a firm transparent polyacrylamide emulsion gel. When radiation deposits energy into the superheated liquid drop, the drop may expand into a visible bubble, provided the energy deposited locally is sufficient [54]. Bubble detectors have a 10 ml active volume of gel with ~10^4 evenly dispersed superheated droplets. The gel is held in a 1.6 cm (diameter) by 7 cm (length) plastic tube with a rounded end and a metal piston affixed to the other end. The plastic walls of the bubble detector are 1 mm thick and the rounded end has a radius of 8 mm. The piston holds the bubble detector gel under pressure in order to compress the dispersed droplets into a superheated state [55]. In this configuration, no bubbles will form even if high LET radiation is present. When a measurement is desired, the piston can be released so that the bubble detector gel is held at a lower pressure, but still enough to hold the droplets in a superheated liquid state. The superheated liquid droplets are invisible to the naked eye with a diameter of approximately 20μm (called microdroplets). When high LET radiation deposits energy into the superheated microdroplets, they may expand into a visible bubble with a diameter of 0.1 – 0.6 mm [56]. After a radiation exposure, these bubbles may be counted visually by eye or the detector may be entered into the BDR-III™ bubble reader device [57]. This device takes two separate intersecting images of the bubble detector and uses imaging processing software to identify bubbles and count them automatically. Bubbles may also be counted using a pressure sensor or acoustic pulses produced during bubble formation [54][58]. A diagram of the bubble detector and the bubble detector reader is shown in Figure 5. When the measurement is complete, the bubble detector piston may be compressed into the original state and all visible

bubbles will be re-compressed into invisible superheated microdroplets. Thus, the bubble detector may be used repeatedly in a large number of experiments without being damaged or losing sensitivity. Unfortunately, the bubble detector gel does harden over time and will become too firm for bubble formation after an extended period whether it is used or not. Also, micro droplets may migrate and coalesce over time giving large permanent volumes of superheated liquid. Thus, calibrated bubble detectors are given an expiration date after which measurements are no longer expected to be accurate (approximately 8 months after manufacture) [59]. The bubble detector spectrometer (BDS) is a set of six bubble detectors called BDS10, BDS100, BDS600, BDS1000, BDS2500, and BDS10000. Each of the BDS detectors has a different minimum energy threshold for bubble formation from neutron radiation [20]. In a neutron spectrum measurement, all six bubble detectors are exposed to the same radiation field simultaneously. After irradiation, the number of bubbles in each of the six detectors is counted in the bubble reader. The number of bubbles is related to the fluence of neutrons above the minimum energy threshold for each detector [60]. A response matrix is used to unfold the matrix and give a course 6 bin neutron spectrum [61].

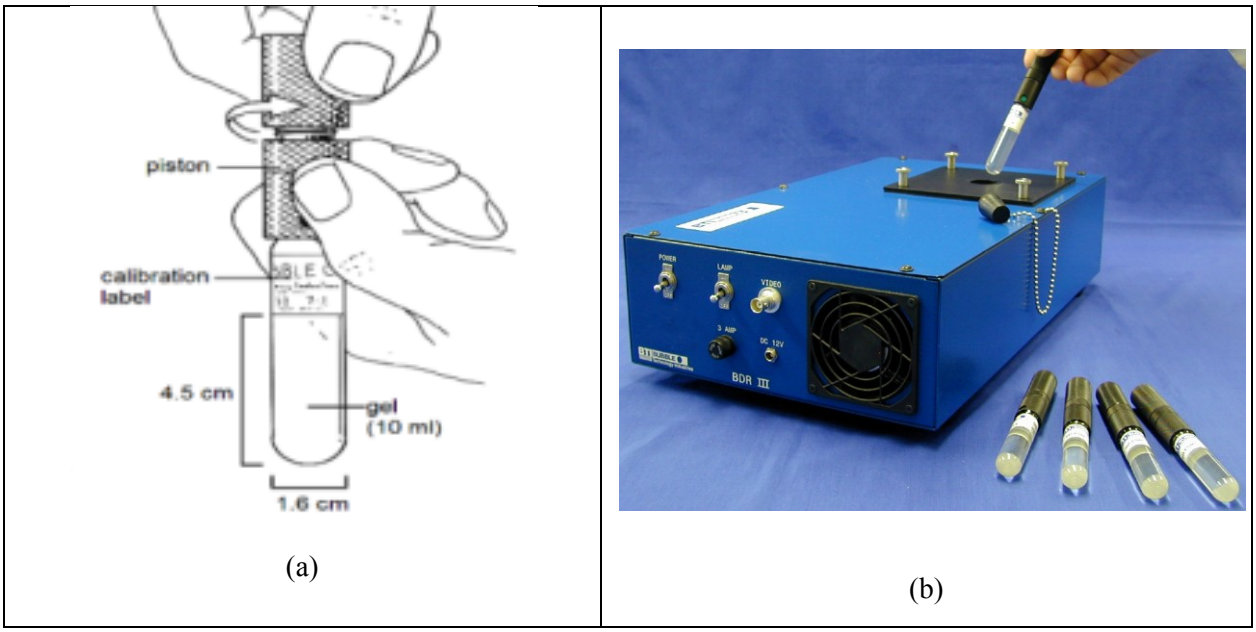

(a) (b)

Figure 5: (a) Space bubble detector and (b) BDR-III bubble reader [57]

Another parameter that is used to characterize superheated drop detectors and bubble detectors is the "reduced superheat", *S* and is defined as in [62],

$$S = \frac{T - T_b}{T_c - T_b} \tag{1.10}$$

Where T is the detector temperature, T_b is the liquid boiling point (a function of gel pressure) and T_c is the critical temperature of the detector medium. S is a dimensionless quantity that typically assumes values from 0.1 – 0.5 for most kinds of bubble detectors. The minimum neutron energy required for bubble formation is directly proportional to S for various types of bubble detectors at different temperature and pressures [62]. For BTI space bubble detectors, the reduced super heat is given as $S \approx 0.3$ and the minimum effective neutron energy required for bubble formation is given as 100 keV [55]. The formation of bubbles is affected by the ambient temperature. This is an undesirable property because variations in temperature are expected in typical bubble detector measurements where the detector may be worn on a person or be placed around different

locations. Temperature compensated bubble detectors and SBD have been developed so that the response does not change in the range 14º to 47ºC [63].

For the space bubble detector spectrometer (SBDS), the pressure is varied for each of the six detectors in the set giving a different *S* for each detector and thus a different minimum neutron energy for bubble formation of 10 keV, 100 keV, 600 keV, 1000 keV, 2500 keV and 10000 keV respectively [61].

1.3.2 Terrestrial Measurements with Bubble Detectors

Bubble detectors are generally used as personal neutron dosimeters (PND). They are effective as neutron dosimeters for terrestrial applications because they only produce bubbles in response to high LET radiation [56]. The radiation fields common in terrestrial applications such as in nuclear power plants, radiotherapy, and medical imaging usually only include low LET photons or beta radiation. Deeply penetrating high LET radiation is only present from a limited number of well-known neutron sources. In addition, background radiation on earth is also lacking in neutrons and deeply penetrating high LET radiation [64]. High LET alpha particles and heavy ions are only present from radioactive alpha decay or nuclear fission and in these cases the energy of the particles is insufficient to penetrate the bubble detectors 1 mm plastic wall. Therefore, the only bubbles formed inside bubble detectors for typical terrestrial applications are from nuclear fission such as in nuclear power reactors or from laboratory neutron sources such as AmBe, ^{252}Cf spontaneous fission sources or secondary radiation produced in particle accelerators. The neutron fission spectrum includes neutrons with energies from 0 to ~10 MeV with most neutrons between 0 and 2 MeV. As the neutrons enter the bubble

detector, they may scatter or interact in a transmutation interaction and produce secondary protons, alphas or heavy ions with high LET that will stop in the detector and form visible bubbles. The number of bubbles present in the detector after an irradiation is linearly proportional to the total fluence of neutrons [56].

1.3.3 Bubble Detector Equivalent dose Calibration

Bubble detectors are calibrated using an AmBe field where a number of measurements are made with different fluences. Since the AmBe spectrum is well known, the equivalent dose can be calculated using fluence to dose conversion factors. The number of bubbles present after an irradiation is linearly proportional to the fluence and the equivalent dose is extracted directly from the fluence so that the number of bubbles is linearly proportional to the equivalent dose. BTI bubble detectors are calibrated using the NCRP report 38 and given as bubbles produced per unit equivalent dose in bubbles/mRem or bubbles/μSv [72]. The AmBe neutron spectrum is shown in Figure 6 a) along with the fission neutron spectrum in Figure 6 b).

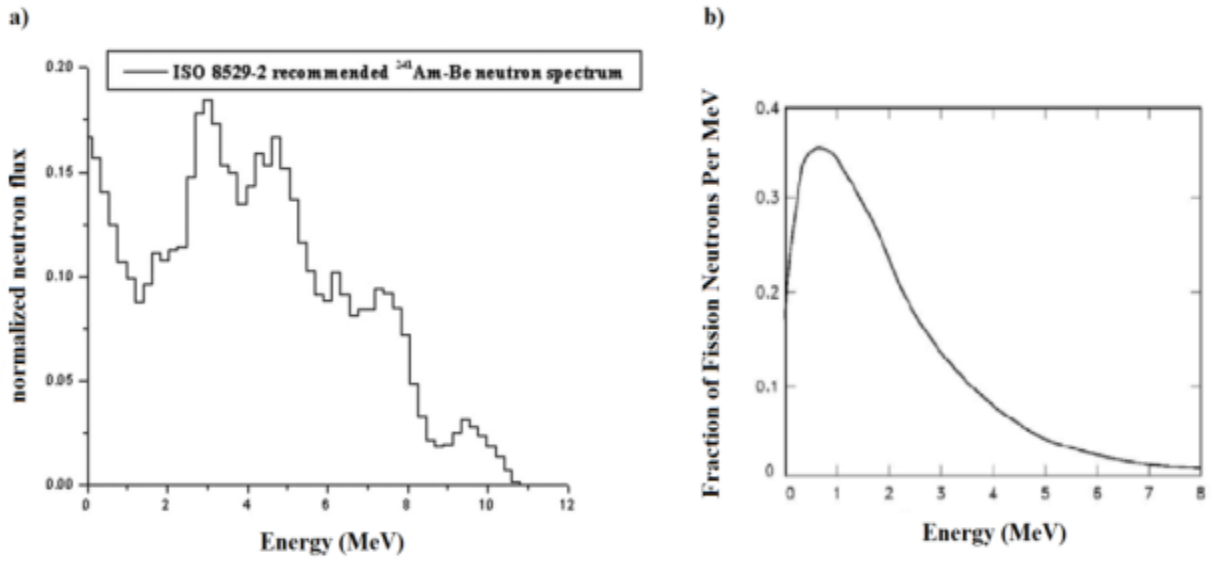

Figure 6:(a) ISO AmBe spectrum and (b) fission neutron spectrum[65]

(Figure reproduced with permission from Oxford University Press)

The equivalent dose calibration with AmBe neutrons is applicable to measurements of fission neutrons because the spectra are sufficiently similar and the bubble detector sensitivity to neutrons from 100 keV to 10 MeV is relatively constant [19].

1.4 Radiation Environment in Space

The ionizing radiation environment encountered in spacecraft includes photons, neutrons, protons, alpha particles and heavy charged particles. Photons, electrons and heavy charged particles come from solar particle events (SPE), galactic cosmic rays (GCR) and trapped radiation in the earth's magnetic field. Secondary neutrons are created when radiation interacts with the spacecraft material or the earth's upper atmosphere in nuclear spallation or transmutation reactions. All of these radiation fields vary over time and are affected by the

regular periodic cycles of the sun known as the solar cycle. The sunspot number (also known as the WOLF number) is a quantity defined by the number of sunspots on the surface of the sun at a given time and it is a commonly used to identify the phases of the solar cycle. Sunspots are darkened regions of reduced surface temperature that are visible on the surface of the sun. Individual sunspots last from a few days to a few months and they occur more frequently in periods of increased solar activity as well as increased magnetic activity, coronal mass ejections and solar flares [66].

1.4.1 Galactic Cosmic Rays

The radiation environment aboard spacecraft varies greatly based on many variable conditions and can fluctuate rapidly or change considerably over long periods of time [9]. This work shall focus on spacecraft in low earth orbit (LEO) and particularly the ISS since most bubble detector measurements have been made on the ISS and it accounts for a large portion of the total manned space missions. The radiation environment aboard the ISS includes many different particle types and each particle type has a wide-ranging energy spectrum. One of the main sources of radiation in space is galactic cosmic rays (GCR). These are energetic protons, alpha particles and heavy ions that originate outside of our solar system. The relative abundance of each ion in is shown in Figure 7 a) along with particle energy spectra for a few of the most common ions (Figure 7 b).

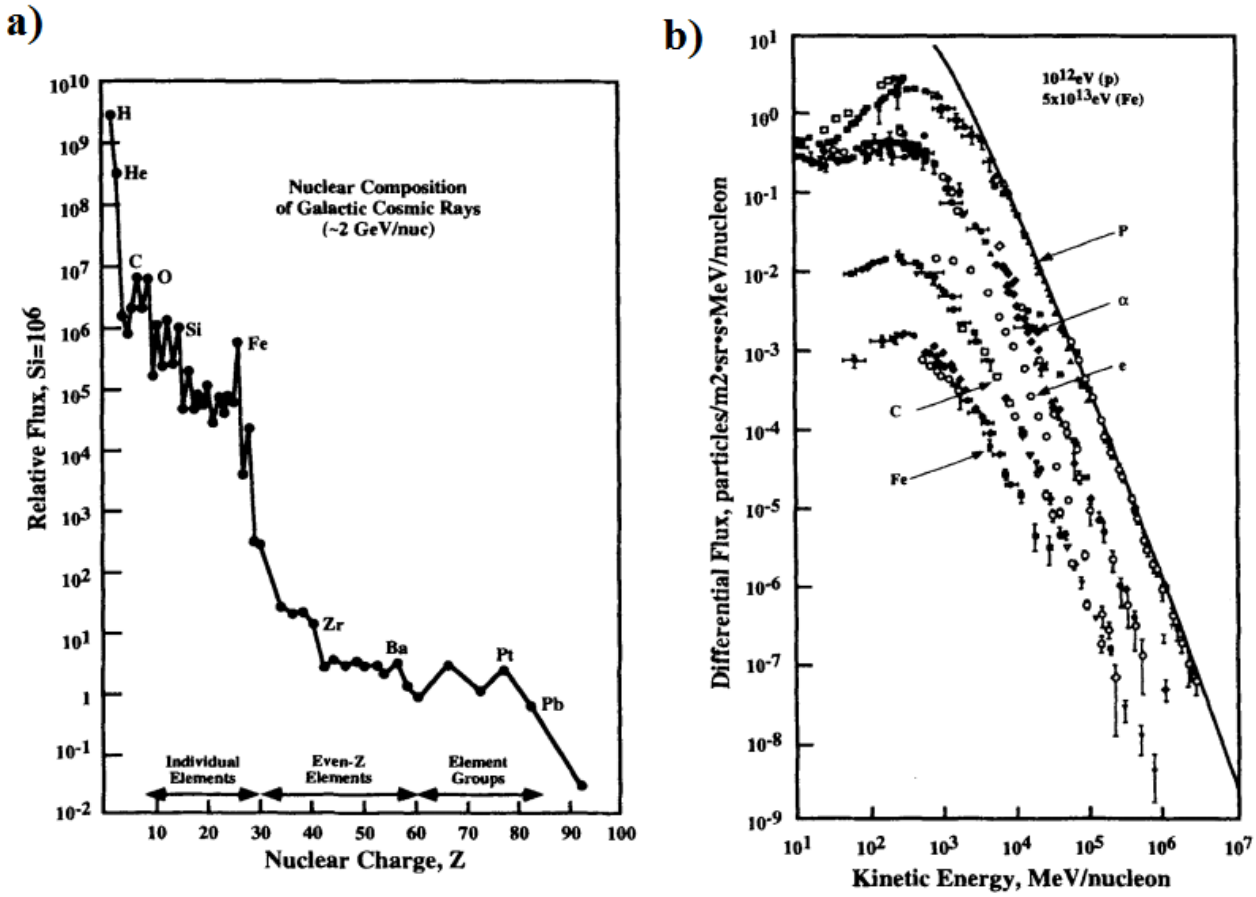

Figure 7:(a) Relative abundance of GCR ions and (b) GCR energy spectra[13]

(Figure reproduced with permission from American Institute of Aeronautics and Astronautics, Inc.)

Although the GCR spectra for all ions remains relatively constant in time, the amount of GCR present in LEO actually varies based on solar activity. Solar cycles cause changes in the interplanetary magnetic field which attenuates and deflect GCR away from earth. Lower energy particles are more significantly affected by solar activity than higher energy particles. Increased solar activity causes decreased GCR fluxes and particle fluxes with energies less than 100 MeV/nucleon may vary by as much as a factor of 10 where particles with energies greater than 10 GeV/nucleon may only vary by less than 20% from solar activity [13].

1.4.2 Trapped Radiation

The earth's magnetic field deflects a large amount of solar and galactic radiation away from the earth. However, some particles can be trapped in radiation belts (called the Van Allen Belts) where they gyrate along magnetic field lines and revolve around the earth confined by the Lorentz Force. Figure 8 shows the trajectory of a particle trapped in a radiation belt around the earth.

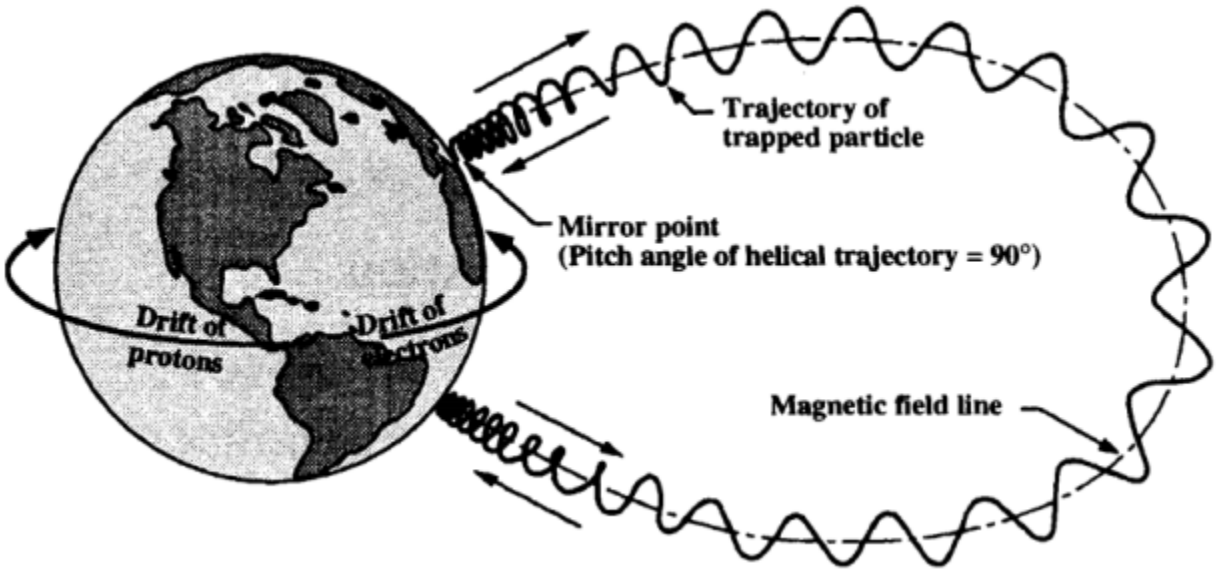

Figure 8: Trajectory of trapped radiation particle [13]

(Figure reproduced with permission from American Institute of Aeronautics and Astronautics, Inc.)

Trapped radiation belts include electrons, protons, alphas and heavy charged particles each of which moves along particular lines based on the particle energy, charge, mass, and location. The net effect is two distinct quasi-torrid shaped radiation belts enveloping the earth called the inner radiation belt and the outer radiation belt. The density of ionizing radiation in the

radiation belts is very large at the point of closest approach to the earth. The earth's magnetic dipole is also not aligned with the earth's axis of rotation so the trapped radiation belts are also tilted and skewed relative to the earth's rotational axis. As a result, the belts are closest to the earth over the South Atlantic Ocean near Brazil in a location called the South Atlantic Anomaly (SAA). For astronauts in LEO, the SAA is actually the largest source of ionizing radiation exposure [13][67]. The trapped radiation belts are also dynamic and particle fluxes change with solar conditions as the earth's magnetic field is altered by the solar cycle and solar particle events [68]. In addition, the earth's upper atmosphere heats up and expands near the solar maximum and the attenuation of trapped particles increases [66].

1.4.3 Ionizing Radiation aboard the ISS

Ionizing radiation aboard the ISS includes photons, electrons, neutrons and heavy charged particles from GCR, trapped radiation, and secondary radiation. Of particular interest in ISS are the neutron and proton particle fluxes and their energy spectra. This is because neutrons and protons have a large flux that is a few orders of magnitude larger than other particles [9]. In addition neutrons and protons are high LET particles and contribute a much larger equivalent dose to astronauts than all of the photons and electrons. The energy spectra of neutrons and protons vary significantly depending on conditions such as the solar cycle, solar emissions, current location of the ISS, geomagnetic cutoff rigidity, passage through the South Atlantic Anomaly, shielding and position within the ISS [69]. The geomagnetic cutoff rigidity is a parameter that describes the flux of radiation particles in earth orbit based on orbit parameters [2]. However, for SPND and SBDS experiments on board the ISS, a single time averaged

neutron and proton spectrum are considered to be representative of the average net particle fluxes overextended measurement periods of (5-7 days) behind typical shielding within the ISS [70].

The neutron energy spectrum on the ISS has been measured using a Bonner Ball Neutron Detector (BBND) by Koshiishi*et al.* from March 23 to November 14, 2001, and the data seems to fit well with predictive models as shown in Figure 9 [71]. The neutron spectra in Figure 9 were measured successively in 2 different locations of the US Laboratory module with different shielding. These locations are labeled as "before relocation" (LAB 1D3 deck) and "after relocation" (LAB 1P1 Port) and illustrate how the neutron flux may vary depending on the position within in the ISS due to different amounts of shielding. Please see Appendix B for a diagram of the ISS including locations and modules. Spallation neutrons are mostly highly energetic with energies from a few keV to hundreds of MeV. The large contribution of neutrons with energies below 1 eV comes from albedo from the earth's upper atmosphere.

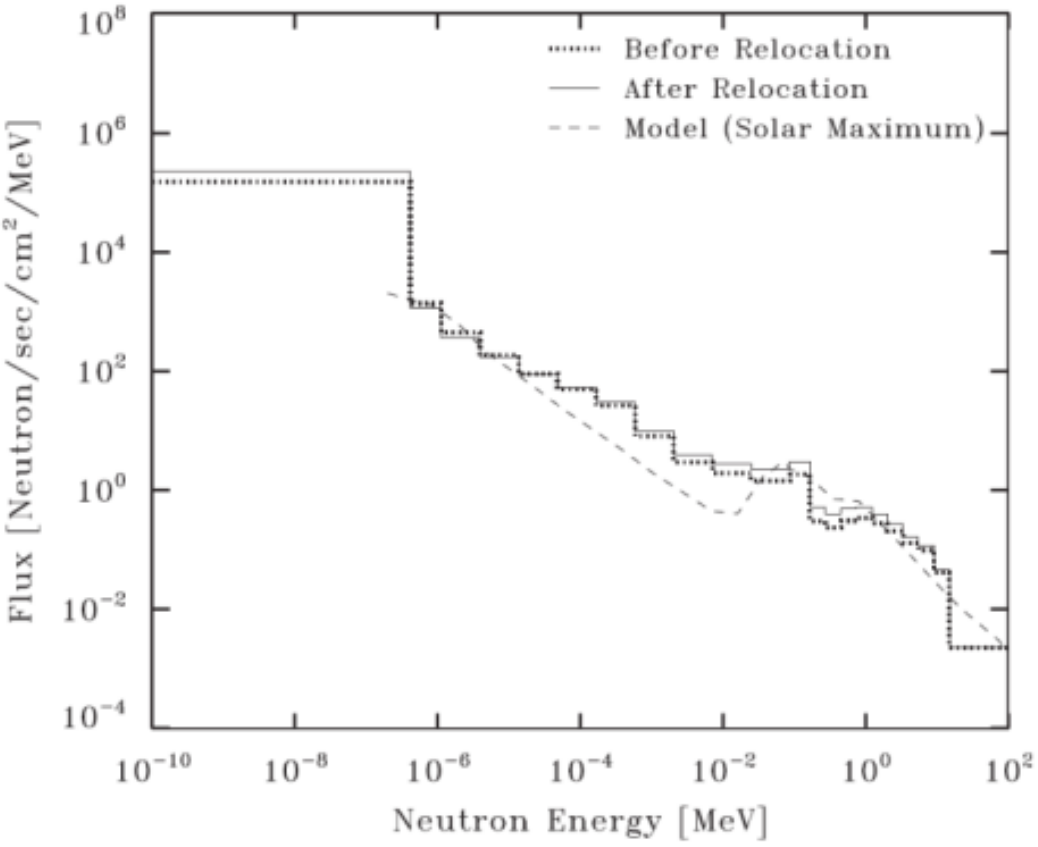

Figure 9:BBND measured neutron spectrum on the ISS with model prediction [71]

(Figure reproduced with permission from Elsevier)

The ISS has a typical average altitude of approximately 400 km but has varied from ~320 km to ~450 km and it fluctuates frequently from apogee to perigee in a single orbit. In addition to shielding effects, the neutron spectrum varies with altitude as well as with latitude, position, and solar activity. A map of the neutron equivalent dose rate measured in the ISS shows this regional variation where the dose rates are shown to increase almost two orders of magnitude in the region of the SAA (see Figure 10). However, bubble detector measurements typically occur over a large number of orbits (~50 to over 100) so an effective time-averaged spectrum over a long measurement period (as shown in Figure 9) is applicable.

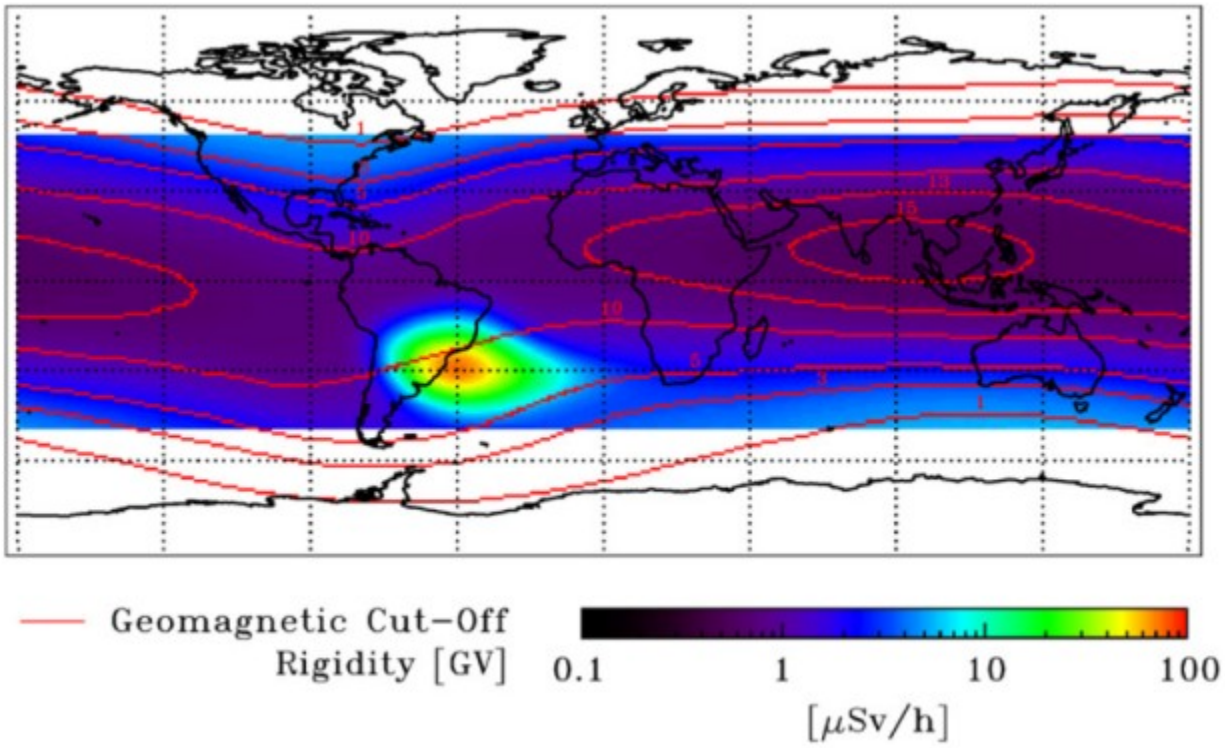

Figure 10: Neutron equivalent dose rate measured in ISS and geomagnetic cut-off rigidity at average ISS altitude [71]

(Figure reproduced with permission from Elsevier)

The average proton flux in the ISS has been modeled and shows a peak around 100 MeV. Protons are more abundant than neutrons in the region 100 to 1,000 MeV [69]. High-energy heavy ions with charge $Z \geq 2$ are also present on the ISS, but the relative abundance of these ions is orders of magnitude below neutrons and protons. Figure 11 shows the flux of neutrons and protons aboard the ISS from GCR and trapped radiation.

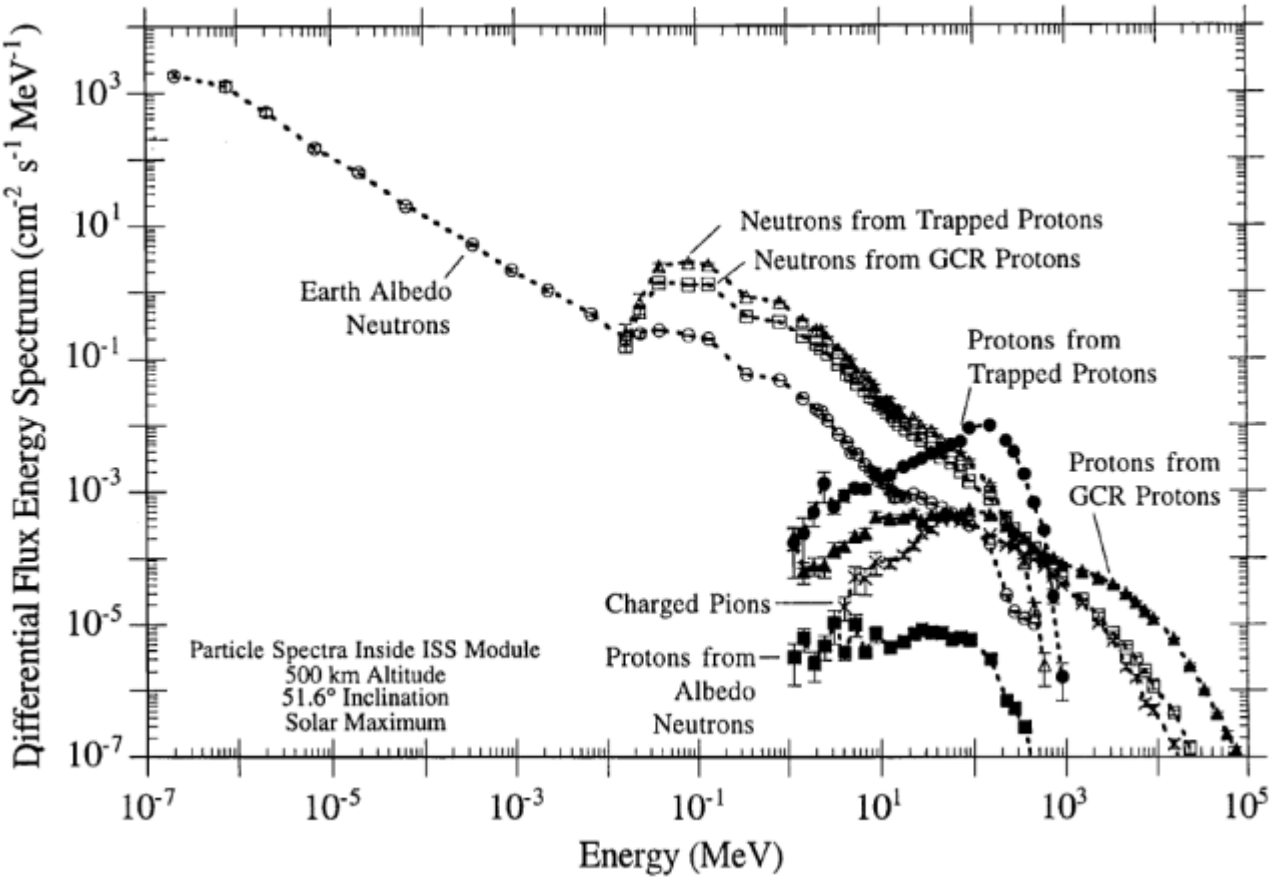

Figure 11: Calculated neutron and proton spectrum on the ISS [69]

(Figure reproduced with permission from Elsevier)

CHAPTER 2: LITERATURE REVIEW

An extensive literature survey has been performed and a collection of relevant papers has been reviewed. The literature used to develop this thesis has been divided into six main categories and the significance of the findings in each category is presented in this chapter. The main categories are as follows:

1) Bubble detector theory and physics of bubble formation
2) Experiments with neutron irradiation of bubble detectors
3) Experiments with proton irradiation of bubble detectors
4) Experiments with heavy ion irradiation of bubble detectors
5) Radiation Environment in spacecraft (ISS)
6) Bubble detector measurements in spacecraft (ISS)
7) Heavy ion track structure

2.1 Bubble Detector Theory and Physics of Bubble Formation

Bubble detectors are considered to be effective neutron dosimeters. However, the visible bubbles counted in bubble detector measurements are not formed directly by neutrons. Visible bubbles are formed by high LET charged particles when they deposit energy into the liquid microdroplets. Neutrons produce these high LET charged particles by elastic scattering, inelastic scattering and nuclear interactions within the bubble detector. The microscopic (~20 μm) superheated liquid droplets (liquid microdroplets) are held in a steady-state superheated condition above the boiling point *via* pressure exerted on the liquid by the bubble detector gel

[72]. As a charged ion passes through a liquid microdroplet, energy is deposited *via* ionization along the ion track. Electrons of the constituent atoms of the bubble detector material are ionized and travel outward stopping in the detector. This energy disperses into the liquid as kinetic energy, which serves to raise the temperature in a localized region called a 'thermal spike' along the heavy ion track. Microscopic vapour cavities (<100 nm) are generated along the heavy ion track with volumes that are proportional to the amount of locally deposited energy. If the vapour cavities reach a critical size, the expansion of the vapour becomes irreversible and the whole liquid microdroplet evaporates and expands into a large visible bubble (0.1-0.6 mm) [73]. The amount of energy required and the critical size of the vapour cavity depend on the composition of the liquid micro droplet, the composition of the gel, the pressure and temperature of the system [74][75][76]. From thermodynamics, the size of the critical radius of a vapour embryo required for evaporation into a visible bubble can be calculated. The expansion of a visible bubble is a result of a phase change and stable growth of a vapor embryo called nucleation. Nucleation is defined by the surface energy and Gibbs free energy of the system [77]. For bubble detectors the critical radius is given by the following equation from [78]:

$$R_c = \frac{2\gamma}{(P_s - P')(1 - \frac{v'}{v''})} \tag{2.1}$$

Where R_c is the critical radius of the vapour embryo, γ is the surface tension of the superheated liquid, P_s is the saturated vapour pressure of the liquid, P' is the external pressure on the liquid, v' is the specific volume of the liquid and v'' is the specific volume of the vapour [78].

The minimum energy, E_{min} required for visible energy formation can also be calculated as [79],

$$E_{min} = \frac{16\pi}{3} \frac{\gamma^3}{(P_s - P')^2} \left[1 + \frac{\rho_V \, h_{fg}}{(P_s - P')}\right] \tag{2.2}$$

Where ρ_V is the vapour density and h_{fg} is the latent heat of vaporization.

The value of R_C for bubble detectors has been calculated as 13.3 nm and 32.1 nm for different bubble detectors and was calculated to be between 28-56 nm for BTI bubble detectors [79][80]. The minimum energy for visible bubble formation in bubble detectors has been calculated as 8.99 keV at 25^{o} C and as between 7.80 keV - 82.94 keV for BTI bubble detectors [79][80].

A significant amount of work has been done in order to determine exactly how visible bubbles are formed in bubble detectors. The main principles of radiation-induced thermal spikes and evaporation of liquid droplets into visible bubbles are understood [74]. However, the details of this phenomenon on the nm and μm scale are not well known and thus the response of bubble detectors to some forms of radiation may not be well modeled or predicted based on current theories.

Bubble detectors are considered to be high LET threshold detectors where bubbles are formed from high LET radiation when the energy deposition into a region within the liquid microdroplet is sufficient to cause vaporization [81]. The minimum energy required for bubble formation (E_{min}) has been determined based on thermodynamics and the critical radius (R_c) of the microscopic vapour cavity has also been calculated [79]. However, the structure of energy deposition of high LET radiation on the nm scale is not well known. Moreover, the transfer of energy from high LET ionization to thermal energy in the microdroplets is complicated and the dynamic distribution of thermal energy on the nm scale during the time of bubble formation is not known. Therefore a simplistic approach has generally been adopted to explain bubble formation. LET has been designated as the parameter of radiation that explains visible bubble formation since it describes the energy deposited in the local region during a short time period

(enough time for a bubble to form without the energy dispersing). So a minimum threshold of LET is considered to be sufficient to determine whether bubbles will form or not [79][81]. The LET threshold for bubble formation has been calculated as the minimum energy required for bubble formation divided by the length of the ion track over which that energy must be deposited as the ion passes through a microdroplet. A simplistic estimate of the length required is the diameter of the critical bubble ($2\ R_c$). However, the energy deposited from an ion does transfer away from the point of deposition (*i.e.* delta rays move and deposit energy as they collide). Energy deposited *via* ionization outside the critical radius of the vapour embryo may migrate into the critical radius and conversely, energy deposited as ionization inside the critical radius may migrate out far away. In an attempt to solve this problem, a correction factor has been applied in order to make an effective length over which energy must be deposited. Thus, the LET threshold for bubble formation has been calculated in [79]

$$\frac{dE}{dx}_{min} = \frac{E_{min}}{k \cdot R_c} \tag{2.3}$$

Where $\frac{dE}{dx}_{min}$ is the minimum LET threshold required for visible bubble formation. E_{min} is the energy required for bubble formation and R_c is the critical radius of a vapour embryo. The length along the ion track over which E_{min} must be deposited for bubble formation is called the "effective length" $k \cdot R_c$. k is the correction factor for effective length and it has been estimated as between 2 and 13 [79]. There has never been any specific calculation to determine a true value for k based on ion track structure or thermodynamics in bubble detectors. The LET threshold for bubble formation in bubble detectors has been calculated as a value between 23.21 and 493.7 keV/µm by [79].

The LET threshold of bubble formation calculated above does not account for differences in different types of radiation or different ion charges. All radiation with LET_∞ above the minimum LET threshold is assumed to produce visible bubbles and all radiation below the minimum LET threshold is assumed to produce no bubbles [81]. However, experiments have experimentally determined that nitrogen ions require less LET for bubble formation than argon ions in superheated drop detectors. Green *et al.* also found the same result in BTI bubble detectors, with a minimum LET threshold of 116 ± 40 keV/μm for N ions and 230 ± 20 keV/μm for Ar ions [55]. Andrews *et al.* have suggested that ion track structure may explain why the minimum LET threshold for bubble formation is different for different ions, but no calculations or specific models have been developed [62].

2.2 Experiments with Bubble Detectors

Many experiments have been carried out with irradiation of various superheated droplet detectors and bubble detectors in different radiation fields. Some of the areas of interest included testing the sensitivity of the bubble detector in terms of the number of bubbles produced per unit fluence of irradiation or determining the energy or LET thresholds for bubble formation. A review of experiments relevant to radiation fields expected aboard spacecraft is presented in this section.

2.2.1 Neutron Experiments

A very large number of experiments measuring the response to neutrons were completed during the development of bubble detectors. Many of the experiments involved measuring the

number of bubbles produced after exposure to a known fluence of mono-energetic neutrons. BTI bubble detectors have been determined to have a relatively flat response to neutron radiation for energies between 300 keV to 2 MeV [72]. The response to neutrons decreases below 300 keV where the sensitivity almost vanishes below 100 keV and the sensitivity above 20 MeV also decreases [55]. However, few early experiments were performed for neutrons above 20 MeV since the focus of bubble detectors was for conventional terrestrial neutron dosimetry where most neutrons are less than 10 MeV.

Further experiments were performed to test the bubble detector response to neutrons in the range of 10-100 MeV since there was a desire to use them for aircraft and spacecraft neutron dosimetry [73][82]. Measurements with mono-energetic neutrons showed a low sensitivity to neutrons below 100 keV, a flat response to neutrons from 300 keV to 20 MeV and a slightly reduced response to neutrons around 100 MeV as shown from various experiments in Figure 12[55]. Experiments with neutrons from 0-1,000 MeV at CERN (European Commission high energy Reference field Facility) were performed to calibrate bubble detectors for aircraft dosimetry. It was concluded that multiplying the AmBe calibration sensitivity by a factor of 1.62 would give an equivalent calibration for aircraft neutron dosimetry and this has been applied to space bubble detectors as well [7]. The scaling factor is necessary because the equivalent dose for the high energy neutrons increases significantly with energy (see Figure 1) but the SBD sensitivity decreases for neutrons above 10 MeV. Therefore, the number of bubbles produced in an SBD after irradiation with high energy neutrons underestimates the equivalent dose using the AmBe calibration (bubbles/μSv). Multiplying the result by the scaling factor (1.62) compensates for the lower sensitivity and larger dose equivalent of the high energy neutrons [7].

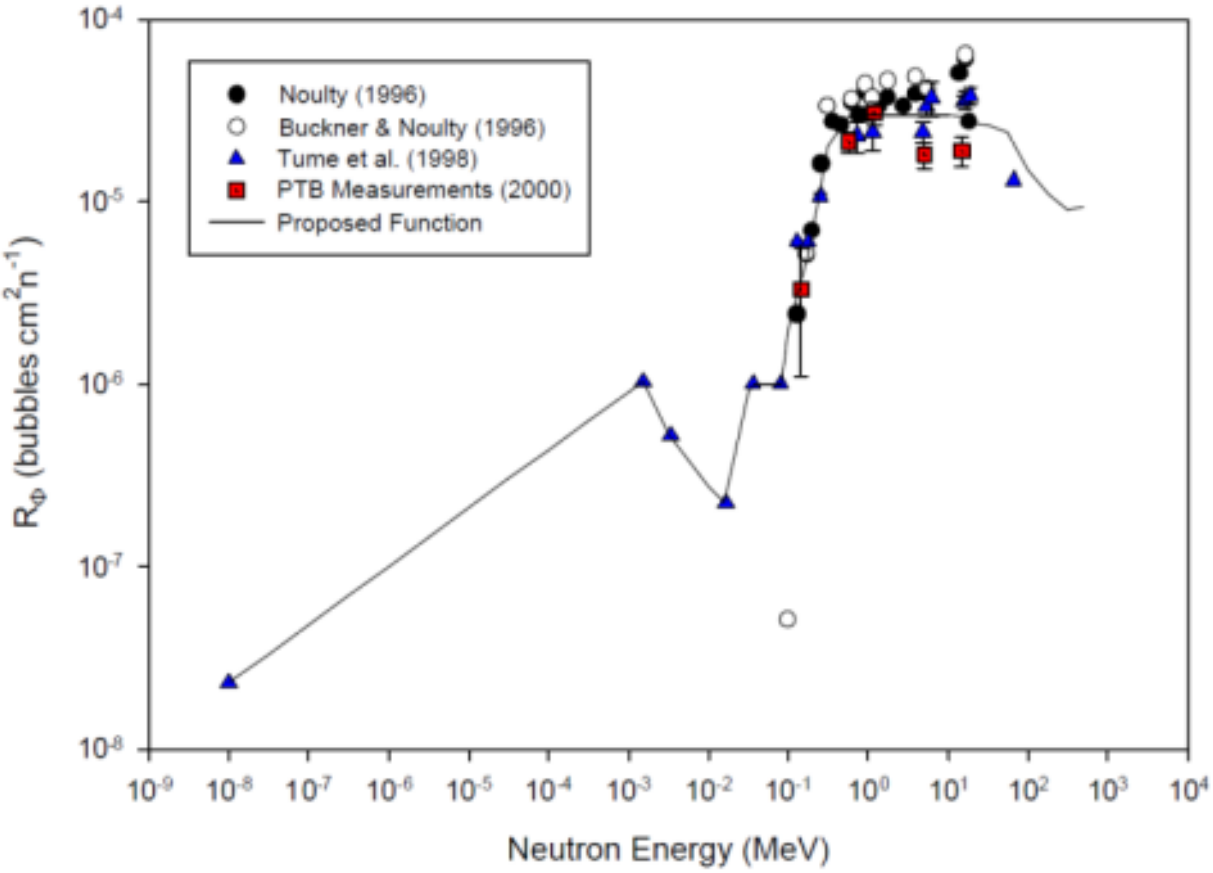

Figure 12: Bubble detector response to neutrons (for a detector with unit sensitivity 0.1 bubbles/μSv) [55]

A model has been developed using the Geant4 Monte-Carlo software toolkit to evaluate the bubble detector response to neutrons of various energies. The model has been analyzed using a single LET_∞ minimum threshold for bubble formation due to secondary heavy ions of 130 keV/μm and is plotted in Figure 13 along with experimental data of monoenergetic neutron measurements [55]. This agrees well with the measured data and proposed function from Figure 12. Unfortunately, few experiments have been done for neutrons above 15 MeV, while half of the total neutron equivalent dose on spacecraft is believed to come from neutrons above 15 MeV [55]. The response of the bubble detector spectrometer set (BDS) to neutrons has also been

measured and is shown in Figure 14 [61]. The response to neutrons increases after a minimum threshold neutron energy for each of the six detectors and remains relatively flat until 10 MeV, above which there is a decrease in sensitivity.

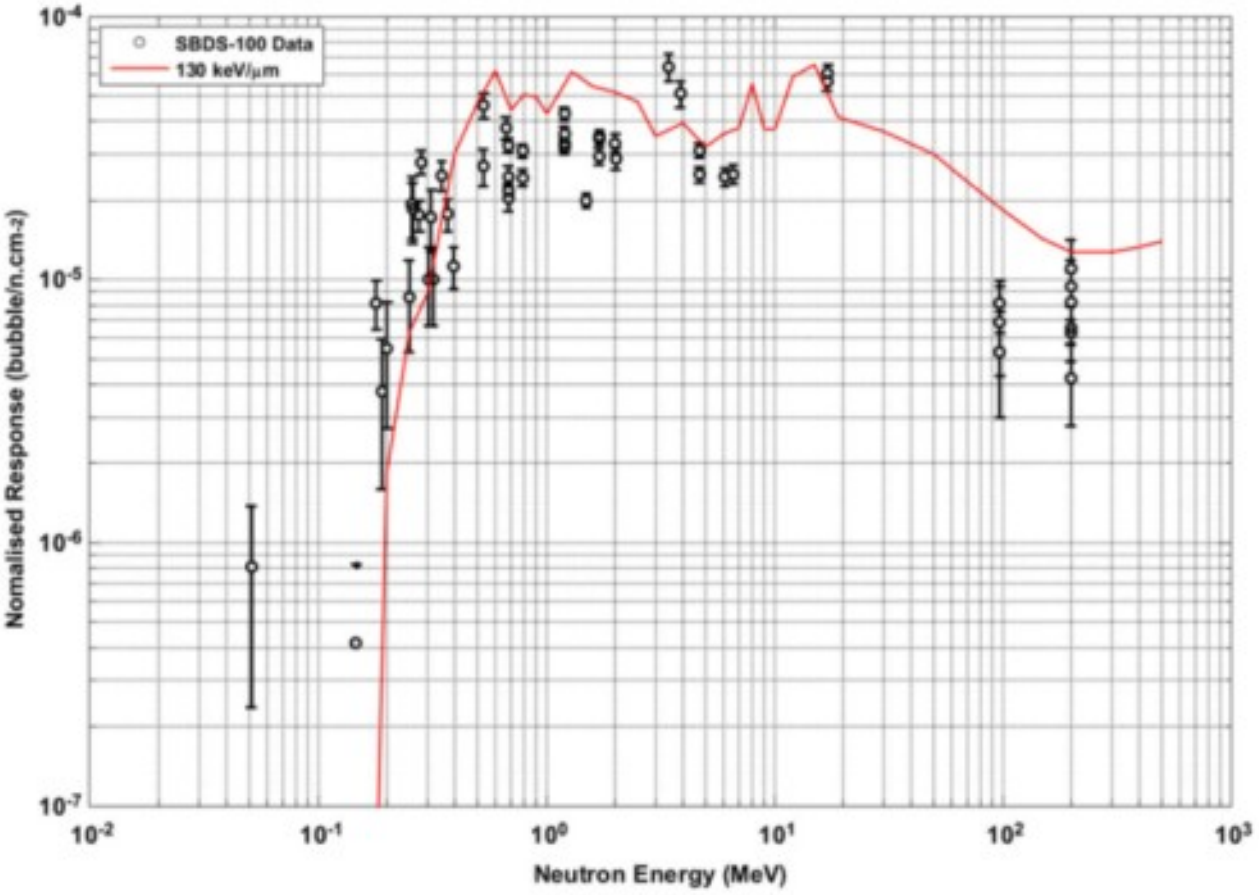

Figure 13: Geant4 Monte-Carlo model of bubble detector response to neutrons of various energies and experimental data [83]

(Figure reproduced with permission from Oxford University Press)

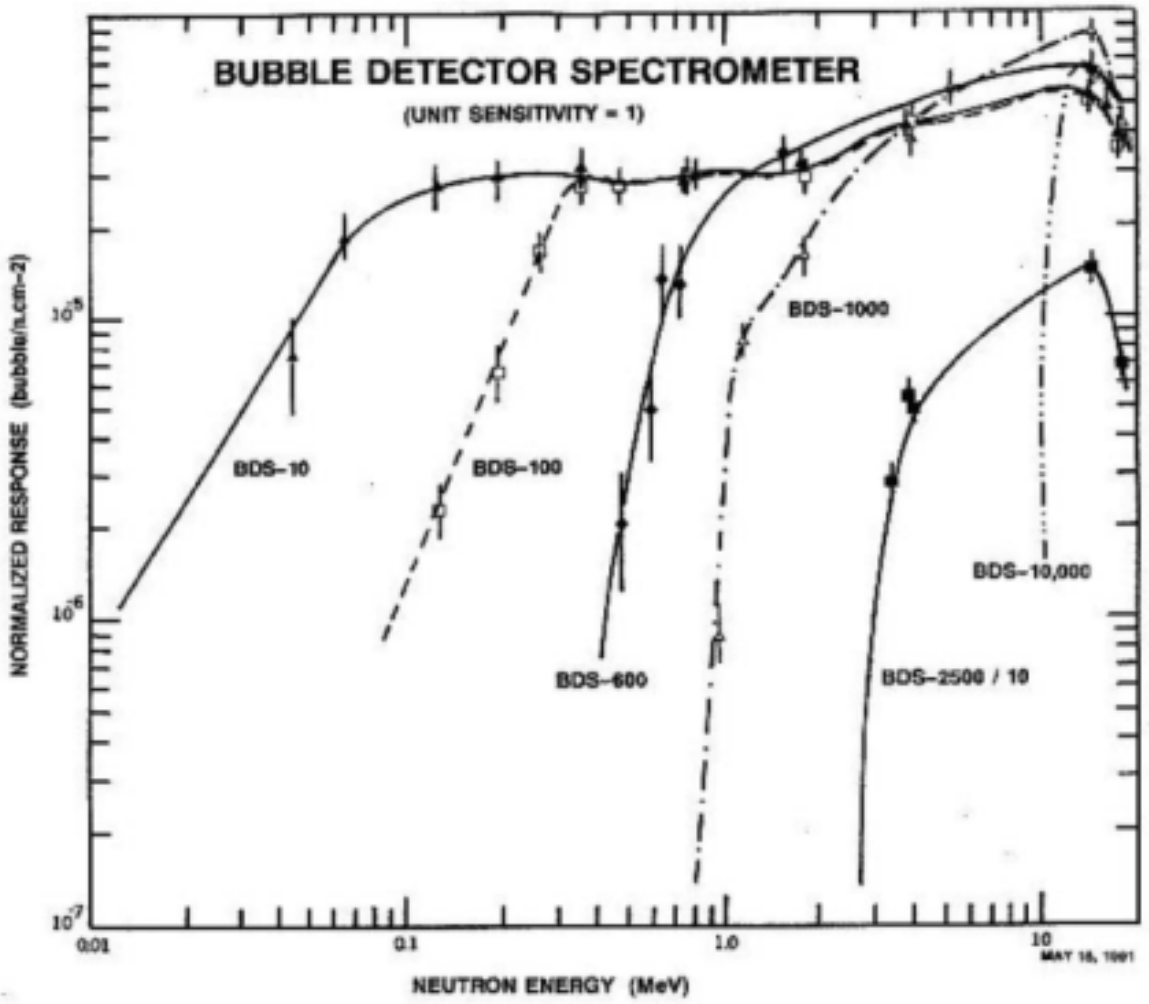

Figure 14: Bubble detector spectrometer response to neutrons [61]

(Figure reproduced with permission from Oxford University Press)

2.2.2 Proton Experiments

Protons are abundant in the radiation field of aircraft and in spacecraft. Thus, many experiments have been done to measure the sensitivity of bubble detectors to proton radiation [18][79]. In these experiments, bubble detectors have been exposed to a given fluence of monoenergetic protons. The number of bubbles produced is counted and the sensitivity of the

bubble detector is given as a number of bubbles per unit fluence of protons. This is further normalized by dividing the result by the detectors AmBe sensitivity (bubbles per μSv) relative to a standard 0.1 bubbles per μSv since the number of bubbles produced per unit dose is different for each individual detector as determined by the total number of microdroplets present in the detector. This is measured for various proton energies to produce a complete response function for protons with units of bubbles per unit fluence divided by the relative AmBe sensitivity as shown in Figure 15. Unfortunately, no experiments have been reported for the sensitivity of protons from 70 – 200 MeV which is the range of highest fluence on the ISS.

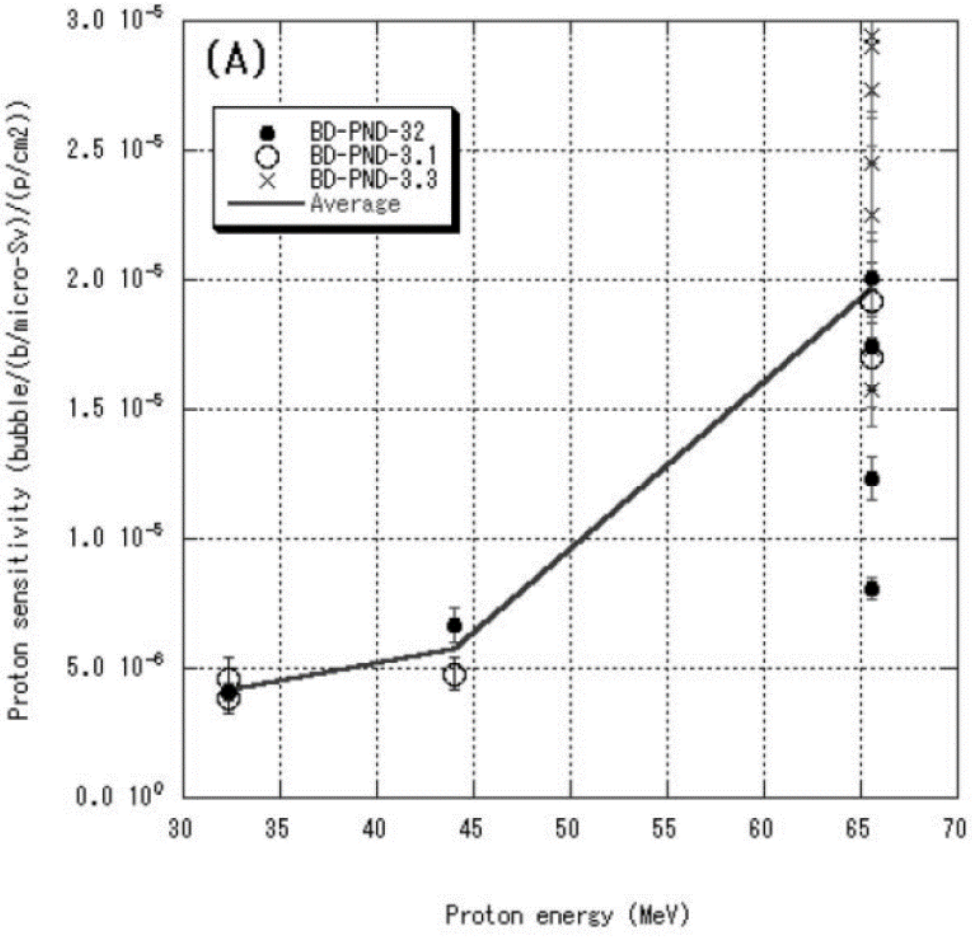

Figure 15: Bubble detector proton sensitivity[79]

(Figure reproduced with permission from Oxford University Press)

Experiments have been done where the proton beam has been incident along the bubble detectors central axis. In this case, bubbles appear uniformly along the proton track through the detector until the end of the range. Models using the Stopping and Range of Ions in Matter (SRIM) computer code have been used to compare the theoretical range of ions in bubble detectors with the distribution of bubbles after proton irradiation [18].The LET of protons in these experiments may be as low as 1 keV/μm at the beginning of the track, which is below the LET threshold calculated by Takada *et al.* It is believed that bubbles in this region may be produced by recoil heavy nuclei with a much higher LET. There does not appear to be an increase in the number of bubbles formed near the Bragg peak as shown in Figure 17.

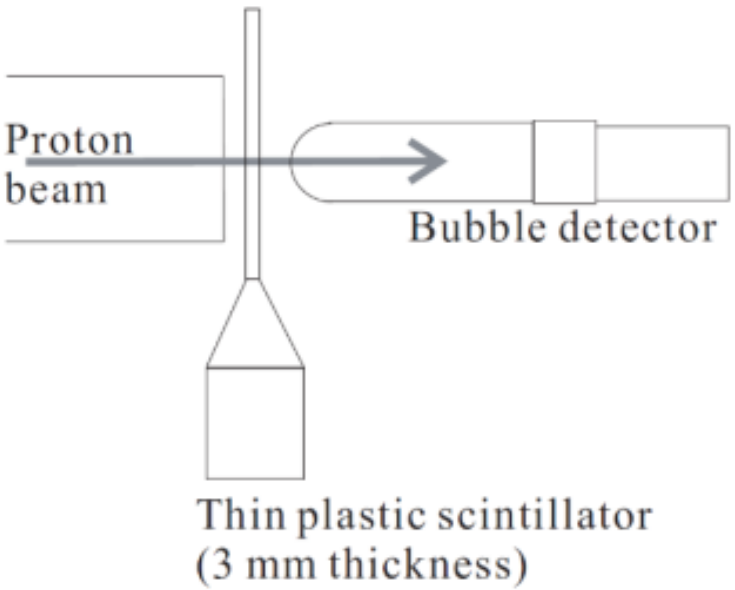

Figure 16 Proton irradiation experiments [79]

(Figure reproduced with permission from Oxford University Press)

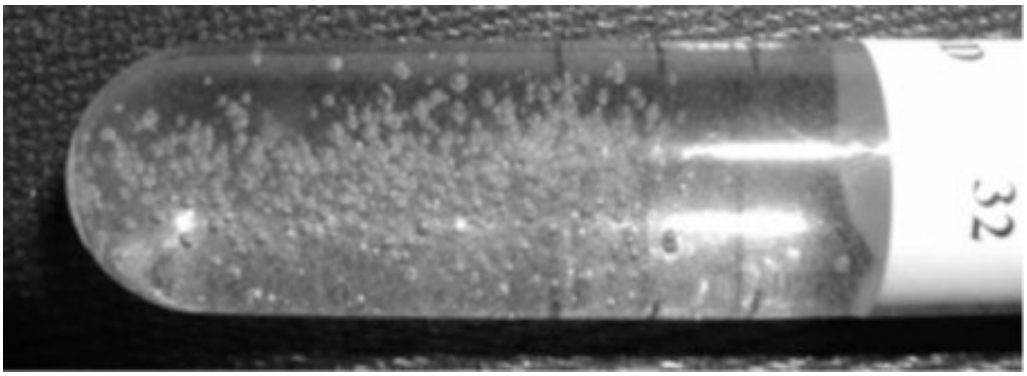

Figure 17: Bubble detector irradiated with 9×10^5 protons/cm^2 at 70 MeV [79]

(Figure reproduced with permission from Oxford University Press)

2.2.3 Heavy Charged Particle Experiments

Bubble detectors have also been tested with He, C, Si, Ar, Fe, Kr and Xe ions in various bubble detectors [18][78][81][84][85]. Also, experiments have been carried out with N, Ar and Kr ions in various bubble detectors and BTI space bubble detectors [55][62].Unlike the experiments with protons, all heavy ion experiments showed an increase in the number of bubbles near the Bragg peak at the end of the ion range. Figure 18 shows an experiment with Ar ions incident along the detector axis for three different bubble detectors with different temperatures [55]. In each detector, there are few bubbles as the Ar ions enter the detector (from the right in the image). As the Ar ions slow down toward the end of the range, the LET of the Ar ions increases. At some point in each of the detectors, there is a sudden increase in the number of bubbles. This is called the 'bubble front' by the authors and it is different for each of the detectors based on the temperature and pressure of the gel (*i.e.* reduced superheat, *S*) [55]. The LET of the ions at the beginning of the bubble front as calculated by SRIM has been called the minimum LET threshold of bubble formation. These experiments found that the minimum LET threshold for bubble formation of N ions was less than the LET threshold for Ar ions. Similar

experiments performed by Guo *et al.* with He and Fe ions found a minimum LET threshold for bubble formation in various kinds of bubble detectors[18][84][78]. However, Guo *et al.*have assumed the minimum LET threshold is a constant value for all ions regardless of mass or charge in all calculations and has not reported any difference in LET threshold based on ion charge [81]. In other similar experiments, Andrews *et al.*have reported a larger minimum LET threshold required for bubble formation for Ar ions than for N ions [62]. No experiments have been done to determine if there is a trend of minimum LET threshold for bubble formation for different ions.

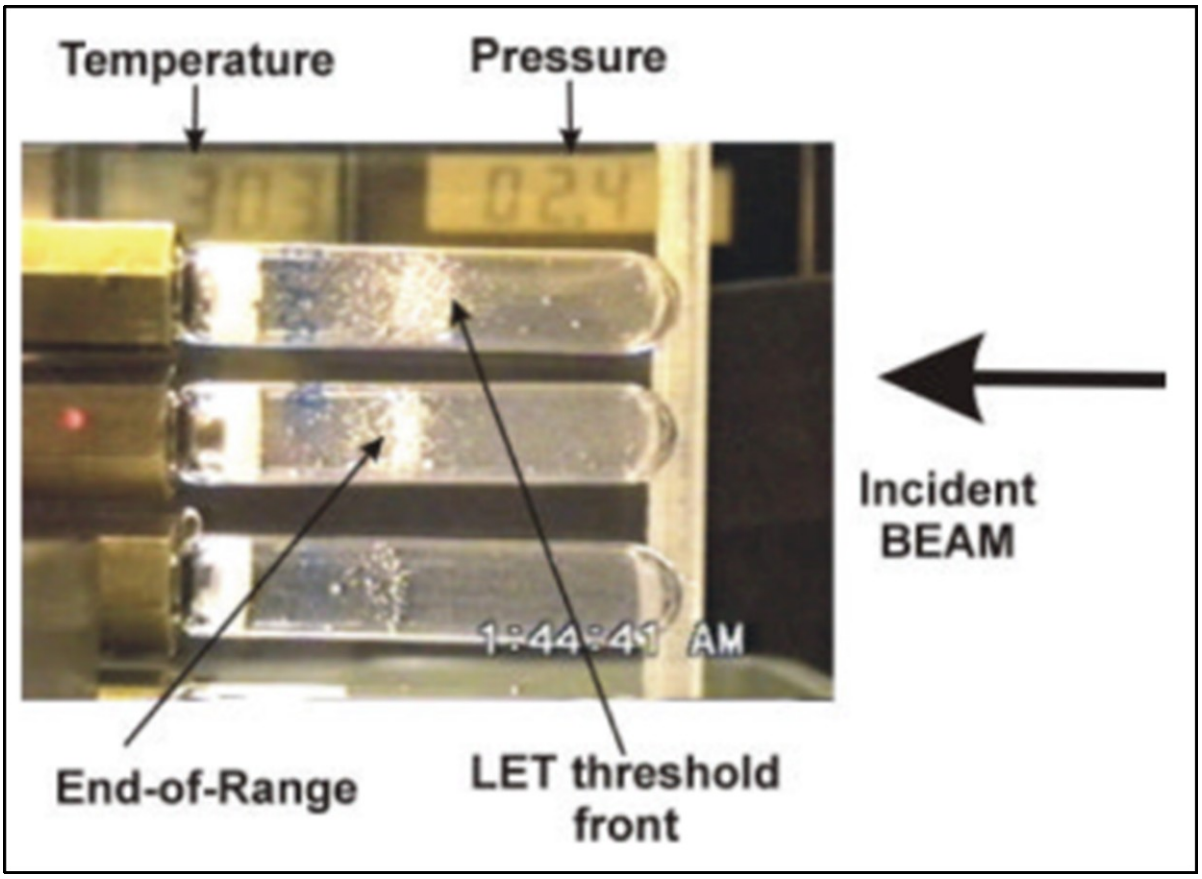

Figure 18: Image showing heavy ion irradiation of bubble detectors at HIMAC [55]

2.3 Bubble Detector Measurements aboard the International Space Station

Measurements on many manned and unmanned spacecraft missions have been performed with BTI bubble detectors including the Personal Neutron Dosimeter (PND), Bubble Detector Spectrometer (BDS), Space Bubble Detector (SBD) and the Space Bubble Detector Spectrometer (SBDS). The space type bubble detectors have a firmer polymer to slow the rate of bubble growth after formation, which allows for longer measurement periods desired in space missions (days to weeks) [14]. Although most early testing of bubble detectors has been done using PND and BDS, it is believed that space bubble detectors and SBDS should respond similarly to all kinds of radiation. Experiments were performed on the BION #9, BION #10, BION #11 and BION-m No.1 satellite missions[86]. Additional experiments were performed on MIR (1993) and on space shuttle missions STS-81, STS-84, STS-86 and STS-89 [18][86]. Despite the differences in orbital altitude and orbital parameters, all bubble detectors measured anequivalent dose rate of approximately 100 μSv/day on all of these missions. A large number of measurements with SBD and SBDS bubble detectors have been performed on the ISS and the results have been published for missions ISS-13 to ISS-40 with measured neutron ambient equivalent dose rates typically between 100 to 200 μSv/day [18][14][87][88]. Measurements have also been carried out within the same ISS missions with bubble detectors located inside the Matroshka-R tissue equivalent spherical phantoms. The bubble detectors inside the phantoms typically measured an equivalent dose rate about 25% less than the detectors located outside of the phantoms [14][87]. Variation of the neutron dose rates measured on the ISS with space bubble detectors and SBDS over time has shown no clear correlation to changes in ISS altitude, solar activity or trends displayed in other concurrent dosimeter measurements (TEPC and DB-8 silicon detectors) [87]. An attempt was made to predict the number of bubbles based on expected

neutron and heavy ion spectra and bubble detector response models on mission ISS-16. The model consistently under-predicted the number of bubbles by a factor of 2. The proton contribution to bubbles was calculated to be less than 2% and the contribution of all other heavy ions was found to be much less than 1% so protons and heavy ions have been considered negligible in all reported bubble detector measurements on the ISS [14].

Figure 19 a) shows the results of bubble detector measurements aboard the ISS between November 2009 and July 2012. The ISS altitude (apogee and perigee) is plotted in the same figure for comparison. In June 2011 there is a significant shift of the ISS altitude from ~350 km to ~400 km. It is expected that the dose rate on the ISS should increase with altitude, however, the number of bubbles in the bubble detector measurements decreased. Figure 19 b) shows measurements with TEPC and two different DB-8 detectors during the same time period. The TEPC absorbed dose rate lies between the two DB-8 detectors and all three detectors show a significant increase corresponding to the altitude increase. The DB-8 detectors increase and continue to give higher readings after the altitude shift. Interestingly, the TEPC measurements increase significantly during the altitude shift but decrease after September 2011. The DB-8 detectors are most sensitive to heavy charged particles while the TEPC detectors measure the absorbed dose from all radiation including neutrons. It may be possible that this indicates a decrease in the neutron component of the radiation field after the altitude increase. This would also be consistent with the decreased bubble detector measurements.

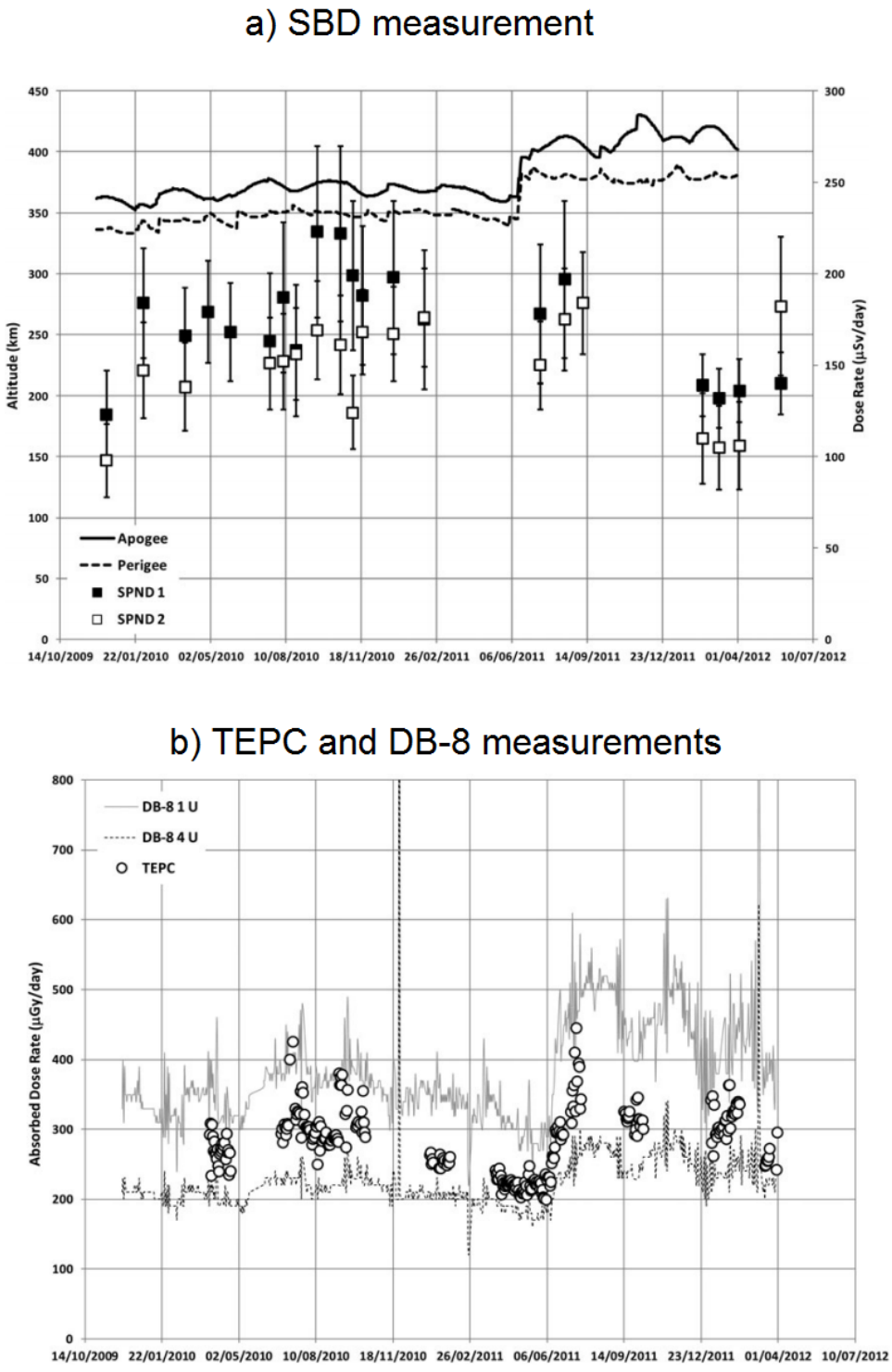

Figure 19: Comparison of space bubble detector measurements with TEPC and DB-8 detectors on ISS [87]

(Figure reproduced with permission from Oxford University Press)

CHAPTER 3: METHODOLOGY DESCRIPTION

The experimental investigations in this work were performed using BTI space type bubble detectors identical to those in use aboard the International Space Station (SBD and SBDS).In addition to experimental measurements, simulations of the experiments have been performed using the particle and heavy ion transport system (PHITS) code. Calculations of the LET, range, and energy of heavy charged particles have been done using the stopping and range of ions in matter code (SRIM) [89]. All bubble detector measurements were recorded, the number of bubbles was counted with the BDRIII bubble detector reader and images were analyzed with MATLAB image processing tools.

3.1 Experimental Investigation

The space bubble detectors have a 10 ml active volume with approximately 10^4 microscopic droplets, and a sensitivity ranging from 0.10–0.22 bubbles/μSv in an AmBe neutron field. Table 1shows all experiments performed and lists the facility, date, radiation used and the purpose of the experiment.

Table 1: Bubble Detector Irradiation Experiments

Facility	Date	Radiation	Detector	Purpose
ProCure Proton Therapy Centre Oklahoma, USA	Aug. 2013	Proton 60, 78.2, 162 and 226 MeV	SBD	- Determine the sensitivity of SBD to protons (60 to 226 MeV) - Determine SPND directional sensitivity to protons
LANSCE Ice House neutron spallation source Los Alamos, USA	Nov. 2014	Neutron 0 – 800 MeV (space equivalent spectrum)	SBD	- Determine sensitivity of SBDto space equivalent neutron spectrum - Test calibration factor (1.62)
NIRS cyclotron Chiba, Japan	Jun. 2015	Proton 33-70 MeV	SBD	- Determine sensitivity of SBDto protons (33 – 70 MeV)
HIMAC heavy ion facility Chiba, Japan	May-Jun. 2015	He 150 MeV/n Si 490 MeV/n Fe 500 MeV/n	SBD	- Determine the sensitivity of SBDto He, Si and Fe - Determine the SBDLET threshold of bubble formation for He, Si and Fe
HIMAC heavy ion facility Chiba, Japan	Mar. 2016	C 400 MeV/n O 400 MeV/n	SBD	- Determine the sensitivity of SBDto C and O ions - Determine the SBDLET threshold of bubble formation for C and O
HIMAC heavy ion facility Chiba, Japan	May 2016	He 150 MeV/n Si 490 MeV/n	SBDSBDS	- Determine the sensitivity of SBDto He and Si ions - Determine the sensitivity of SBDS to He and Si ions - Determine SBD and SBDS LET threshold of bubble formation for He and Si
HIMAC heavy ion facility Chiba, Japan	Feb. 2017	C 400 MeV/n Ne 400 MeV/n Fe 400 MeV/n	SBDSBDS	- Determine the sensitivity of SBDto C, Ne,and Fe ions - Determine the sensitivity of SBDS to C, Ne,and Fe ions - Determine SBDand SBDS LET threshold of bubble formation for C, Ne,and Fe
NIRS cyclotron Chiba, Japan	Feb. 2017	Proton ≤70 MeV	SBD	- Determine the sensitivity of SBDto protons (0 – 70 MeV) - Determine range and bubble distribution of proton irradiation in SBD
HIMAC heavy ion facility Chiba, Japan	Jun. 2017	He 150 MeV/n Si 490 MeV/n	SBD	-Additional experiments with SBDfor determination of LET threshold and sensitivity.
NIRS cyclotron HIMAC heavy ion facility Chiba, Japan	Jan. 2018	Proton≤70 MeV He 150 MeV/n C 400 MeV/n Fe 400 MeV/n	SBD	-Additional experiments with SBDfor determination of LET threshold and sensitivity

3.1.1 Neutron Experiments

Exposures of bubble detectors to high-energy neutrons in the energy range expected for neutrons encountered during space flight were carried out at the LANSCE Irradiation of Chips and Electronics (ICE House) facility. ICE House is one of the neutron beamlines from the spallation neutron source with a pulsed 800 MeV proton linear accelerator directed at a tungsten target to produce short bursts of high-energy neutrons (from 0.6 to 800 MeV). The neutrons are guided through different beamlines to the end user exposure rooms. The beamlines range in distance from 10 to 90 m from the tungsten target at angles of 15º to 90ºrelative to the proton beam direction. There are no quasi-mono-energetic neutron beams, but the neutron beam is hard at 15ºand gets softer as it approaches 90º. Each neutron beam path has been well characterized, and the neutron energy spectrum of each path has been precisely measured using a sophisticated time-of-flight spectrometer. A schematic of the facility is shown in Figure 20. The Flightpath 30L was used since the shape of the neutron spectrum is similar to that encountered during space flight. Space bubble detectors were completely insertedinside the beam and irradiated either individually or as a set of 3 detectors. The neutron spectrum of the ICE House facility is shown in Figure 21 along with the cosmic ray neutron flux for comparison. The cosmic ray spectrum is created when heavy ions interact with the earth's upper atmosphere. Although not identical to spacecraft neutron fluxes, the general trend of the flux is sufficiently similar to test the bubble detector response to neutrons in the range 1 MeV to 800 MeV. After each irradiation, the number of bubbles was counted in the automatic bubble reader and the equivalent dose measured with the uncorrected AmBe sensitivity was recorded. The equivalent dose was calculated with the ICRP74 fluence to equivalent dose conversion factors and the Ice House spectrum [90]. This experimental work has been published in [23].

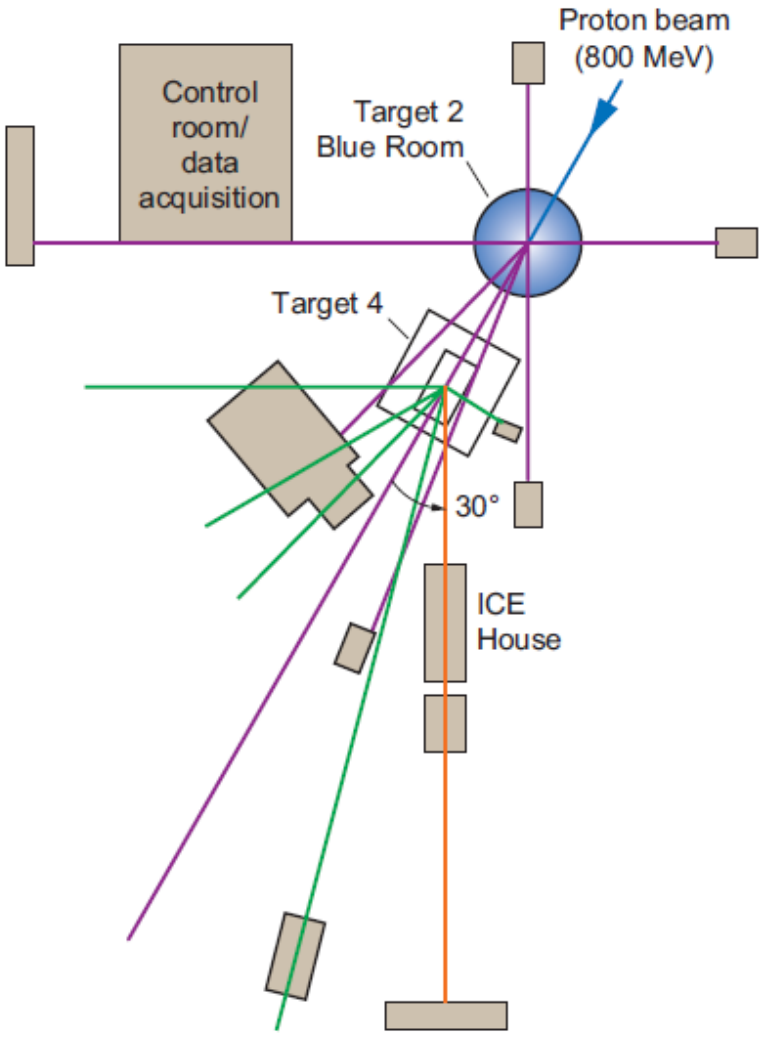

Figure 20:Beamlines at LANSCE. Neutron exposures of bubbledetectors were made along the 30° Left beam line in “ICE House” facility [91]

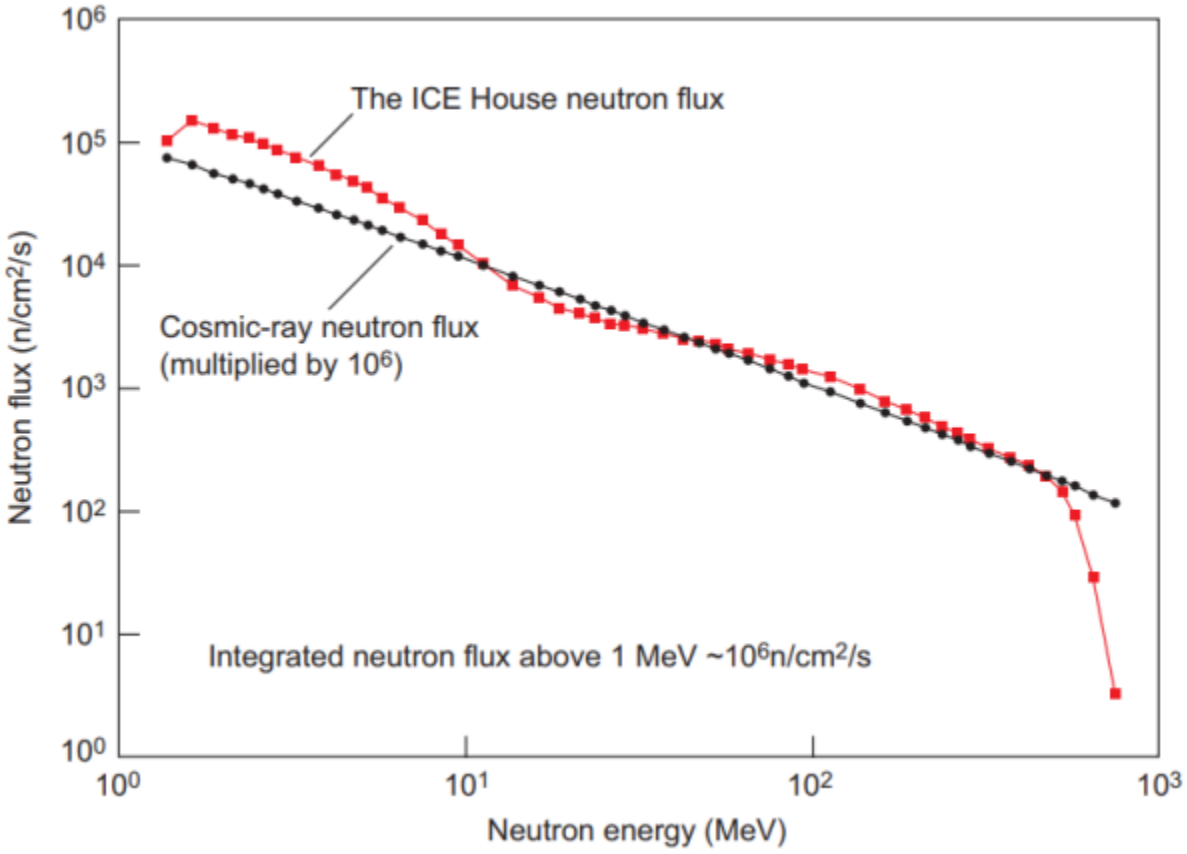

Figure 21: LANSCE ICE House facility neutron spectrum [91]

3.1.2 Proton Experiments

Proton irradiation experiments have been conducted at, the ProCure Proton therapy facility in Oklahoma USA, which consists of a cyclotron and range shifter. The detectors have been exposed to protons at different fluences such that the number of resultant bubbles ranged between 150 and 300.Some detectors were exposed outside of the proton beam to evaluate any secondary neutron contamination present. A snapshot of one of the proton beam portals used to irradiate the bubble detectors is shown in Figure 22, where one detector is inside the proton beam, and two others are at 40 cm lateral to the beam axis and at 300 cm from the beam.

(a)

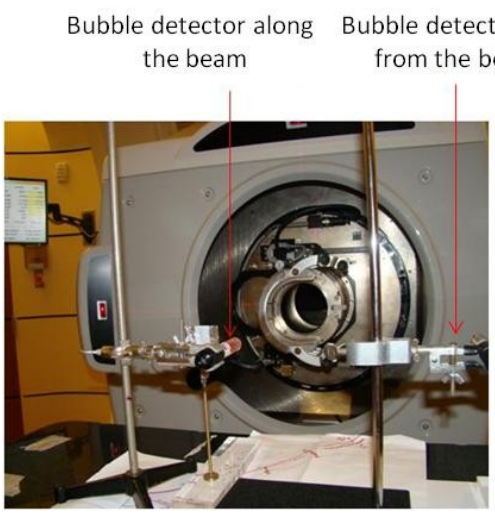

View of one of the Procure Proton Therapy facility beams and the position of two bubble detectors.

(b)

Bubble detector at 300 cm away from the beam axis.

Figure 22: Experimental setup at the Procure Proton Therapy facility

Detectors were irradiated at fluences ranging from ~2 to15×10^{7} protons/cm^{2}. Due to the firmness of the gel used in the space-type bubble detectors, the bubbles were counted at least 30 minutes after irradiation. To ensure the full decompression of the bubble detectors after the counting process, detectors were left for about 30 minutes following decompression before any re-use. The measurements were conducted with four different proton energies, Ep= 60, 78.2, 162 and 226 MeV. The detectors were irradiated in three orientations. Along the beam axis with the bubble detector axis parallel to beam axis), perpendicular to the beam axis, and finally with the bubble detector axis oriented 45º from the beam axis as shown in Figure 23.

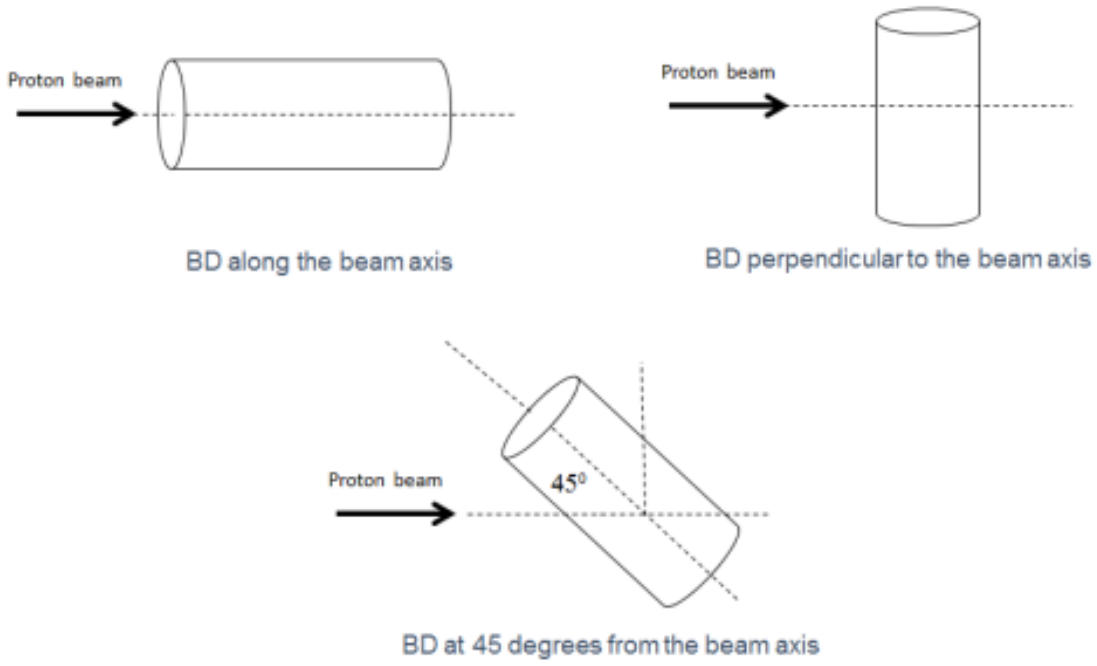

Figure 23: Bubble detector proton irradiation experiments

After each irradiation, the number of bubbles was counted and the fluence was recorded. The response of the detector in each experiment was calculated as the number of bubbles produced divided by the fluence. This was normalized to the given detector AmBe sensitivity relative to the standard AmBe sensitivity of 0.1 bubbles/μSv as shown in the following equation.

$$R_{proton}\,(E) = \frac{N_b}{\Phi \cdot \frac{S_{AmBe}}{0.1\ bubbles\ /\mu Sv}} \tag{3.1}$$

Where:

E is the proton incident energy (MeV), N_b is the number of bubbles produced

Φ is the total fluence of the irradiation (protons/cm^2)

S_{AmBe} is the detectors given sensitivity in an AmBe field (bubbles/μSv)

$R_{proton}\,(E)$ is the response of the bubble detector (bubbles/(proton/cm^2))

Normalization to the detector AmBe sensitivity is necessary because not all SBD are identical when manufactured. The calibrated sensitivity S_{AmBe} is related to the total number of microdroplet sin the detector. For example,an SBD with a calibrated sensitivity of 0.2 bubbles/μSv would be expected to produce twice as many bubbles as a detector with a calibrated sensitivity of 0.1 bubbles/μSv if exposed to the same radiation field. All SBD are calibrated with AmBe exposures and labeled with the measured sensitivity (bubbles/μSv). The normalization in equation 3.1 (*i.e.* division by the ratio of the calibrated S_{AmBe} to 0.1 bubbles/μSv) means that the measured response function $R_{proton}(E)$ is equivalent for all SBD.

In the second series of proton irradiation experiments (~30 to 70 MeV), bubble detectors were irradiated at the NIRS cyclotron facility in Chiba, Japan. The detectors were exposed to proton fluences from 0.5×10^6 to 8×10^6 protons/cm^2 along the beam axis and perpendicular to the beam axis. Different proton energies were obtained by inserting polymethyl-methacrylate (PMMA) 'Binary Filters' of different thicknesses between the beam nozzle and the bubble detectors. The Binary Filters are a collection of PMMA blocks with thicknesses from 5 mm to 1 m that can be moved into or out of the beam line. The permutation of all PMMA blocks allows for a large number of different thicknesses and can slow down the incident beam to a desired energy. A 1cm^2 plastic scintillation flux counter was used to record the particle fluence of each experiment. Similar to previous measurements, some detectors were irradiated inside as well as outside the beam. The experimental setup is shown in Figure 24. Additional similar measurements were made at the NIRS cyclotron in February 2017 that included space bubble detectors and space bubble detector spectrometers.This experimental work has been published in [23].

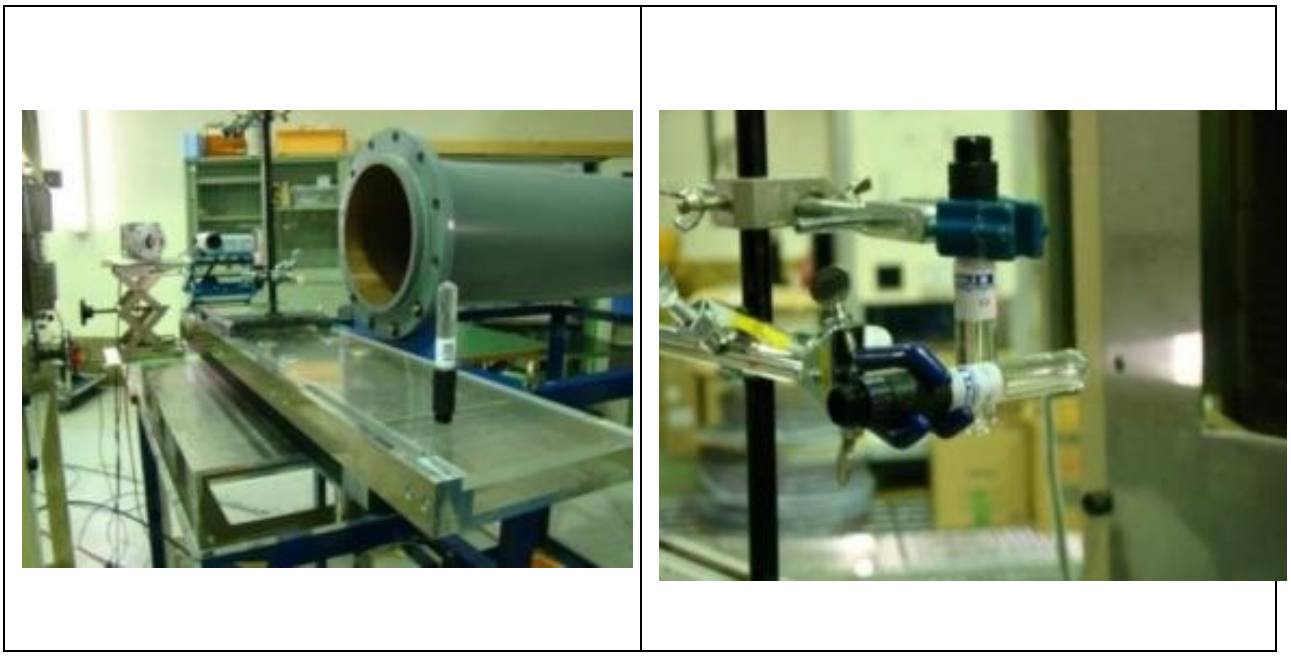

Figure 24: Experimental setup with space bubble detectors at NIRS Cyclotron

3.1.3 Heavy Ion Experiments

The Heavy Ion Medical Accelerator in Chiba, Japan (HIMAC) was used for heavy ion irradiation experiments. The facility provides different heavy ion beams at energies ranging from 100 MeV/nucleon to 800 MeV/nucleon depending on the ion. The HIMAC BIO room delivers a 10 cm diameter mono-energetic heavy ion beam. To reduce the ion energy in different experiments, polymethylmethacrylate (PMMA) 'Binary Filters' of varying thickness were placed between the beam collimator and the bubble detectors[92]. Bubble detectors were exposed to different incident heavy ion beams including 150 MeV/nucleon ^{4}He, 400 MeV/nucleon ^{12}C, 400 MeV/nucleon ^{16}O, 400 MeV/nucleon ^{20}Ne, 490 MeV/nucleon ^{28}Si, and 500 MeV/nucleon ^{56}Fe. To avoid saturating the bubble detectors with excessive particle fluences, the intensity of the beam was reduced from the normal operational intensity. A1 cm^2 plastic scintillator was

placed in the beam line, and the output of the scintillator was set to interrupt the beam when a pre-set fluence had been achieved. The experimental setup is shown in Figure 25 and Figure 26and the characteristics of the heavy ion beams are summarized in Table 2.

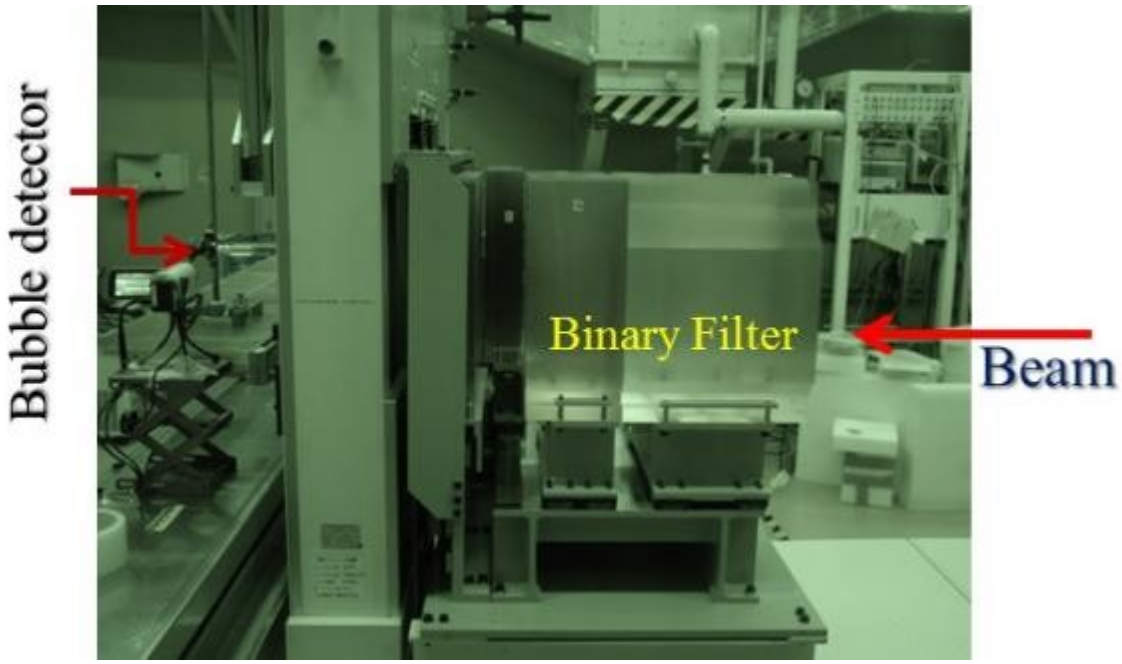

Figure 25:Experimental setup with space bubble detector at HIMAC

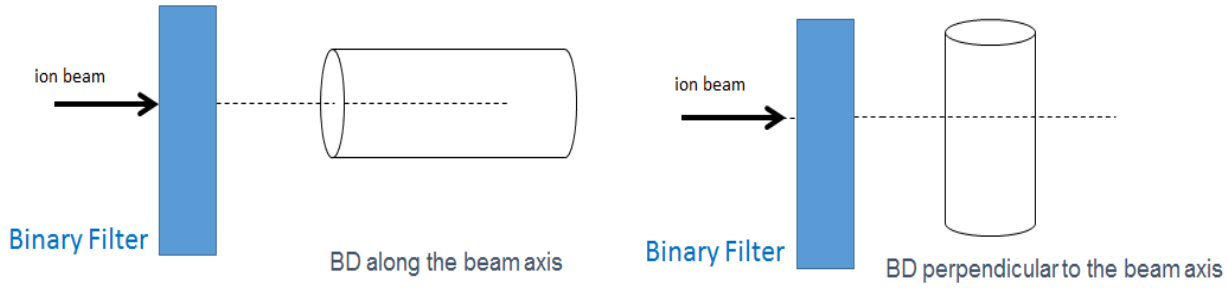

Figure 26: Heavy ion irradiation at HIMAC

Table 2: Characteristics of heavy ion beams used in characterizing bubble detector

Heavy Ion	**Energy (MeV/nucleon)**	**$LET_{\infty}H_2O$ (keV/μm)**	**Fluence (Particles/cm^2)**
^{4}He	150	2.2	$4.0 – 8.0 \times 10^{6}$
^{12}C	400	10.7	$0.8 – 9.2\times 10^{5}$
^{16}O	400	9.4	$0.7– 1.2 \times 10^{6}$
^{20}Ne	400	30.1	$1.1– 1.2 \times 10^{5}$
^{28}Si	490	54.5	$0.5– 1.0 \times 10^{4}$
^{56}Fe	500	182.5	$0.5– 3.0 \times 10^{4}$

The nominal energy listed for each particle in Table 2 is higher than the energy of the particles when they enter the HIMAC BIO room because they travel several meters through the air[92]. At the beginning of each experimental session with a specific beam, a characteristic Bragg curve is recorded with a PTW 23343 Markus Ion Chamber. This is done by measuring the absorbed dose of the beam with no Binary Filter present. A small amount of Binary Filter is inserted into the beam and the absorbed dose is recorded again. This process is repeated while gradually inserting more and more Binary Filter until the beam is fully blocked and the absorbed dose drops significantly. The result is output as a graph of absorbed dose versus depth (which is translated from PMMA to water equivalent for convenience in biological experiments). The actual incident energy of the beam entering the HIMAC BIO room can be identified by observing the range of the particles in the Bragg curve. The Bragg curve is useful for identifying the energy, range and the LET of the ions in specific experiments with different Binary

Filters[93]. See AppendixC for Bragg curve measurements, PHITS simulation results and SRIM calculations at HIMAC.

Approximately 20 bubble detector irradiations were performed for space bubble detectors with each ion beam in each session (See Table 1). For experiments with the beam oriented along the detector axis, the Binary Filter was adjusted so that the range of the ions would be less than the bubble detector length and the ions would stop inside the bubble detector. For each experiment the response of the bubble detector, $R_i(E)$ to the heavy ion, at the incident energy (after passing through any present Binary Filter) was recorded as the number of bubbles produced divided by the fluence (normalized to a standard 0.1 bubbles/μSv detector) as defined in Equation (3.1) for protons. Response functions were measured for all heavy ions with a large range of energies produced by using different Binary Filters.

3.1.4 Determination of LET Threshold for Bubble Formation

The results of each experiment have been analyzed by imaging the irradiated bubble detectors with the bubble detector reader and by observing the number and distribution of bubbles in the detectors. The position of individual bubbles inside the bubble detector images was determined in MATLAB using the Circular Hough Transform algorithm[94]. A custom MATLAB program has been constructed to determine the location of the bubbles in the bubble detector based on image processing. The BDRIII reader captures low resolution (512x480) grayscale Tagged Image File Format (TIFF) images of the bubble detector, where the 45 mm length of the bubble detector is 500 pixels long. Each pixel represents a length of approximately 90 μm. The expanded bubbles in the images are typically 5-6 pixels (450 to 540 μm) in diameter.

The largest bubbles observed in this work were 12 pixels (1080 μm) in diameter and most expanded bubbles were larger than 4 pixels (360 μm) in diameter. The Circular Hough Transform algorithm has been configured to identify bubbles with diameters from 4 to 12 pixels. This range avoids misidentifying bubbles where there are image grains and noise (typically 1 to 3-pixel diameter dark spots in the image) or refractive features of the bubble detector wall (typically larger than 20 pixels). This adequately accounts for the total number of bubbles with consideration for the size distribution [95]. An investigation of the accuracy of this MATLAB program in determining bubble positions and range of particles in SBD is presented in Appendix D.

If the Bragg peak from an individual experiment appears in the bubble detector image, there is an obvious increase in the density of bubbles at the bubble front as shown in the literature review (see Figure 18). In order to assess the bubble front in the images more directly, the location of the bubbles was translated along an elliptical curve that matches the rounded front of the bubble detector. Bubbles near the outside edge of the detector were translated the most, while bubbles directly in the middle of the detector axis were not translated at all. This translation equalizes the ion range so that ions near the outside wall of the detector would stop at the same lateral distance as ions in the centre. This compensates for the geometric effect of the rounded end of the bubble detector. Additionally, the program creates a histogram of bubble densities along the bubble detector axis. At the bubble front, the density of bubbles increases significantly. The program can detect a statistically significant increase in bubble density and designate that position as a bubble front. Conversely, the end of ion range displays a significant drop in bubble density. The program can also identify the end of range based on a statistically significant decrease in bubble density. The bubble front and the end of the range are both

affected by ion straggling so both are expected to be spread out over a finite distance. Also, secondary recoil heavy ions and neutrons produced along the beam line may act to create spurious bubbles at random locations in the bubble detectors. Nevertheless, the program is capable of determining the bubble front and end of the range, as long as the number of bubbles is statistically sufficient and the noise from spurious bubbles is not too large.

A model of the detector gel material has been input into the stopping power and ranges for ions in matter (SRIM) code in order to analyze ion energy, range and LET. The range of the bubbles in the proton experiments in the literature has been verified to match the proton range calculated by this SRIM model [79]. The SRIM data for all other heavy ions were included in the MATLAB program so that the range, energy and LET of the particles could be calculated. The program records and outputs the ion energy and LET_{∞} at the position of the bubble front. Finally, an image is generated with elliptical curves plotted over the original bubble detector image indicating the bubble front and end of the range.

3.1.5 Measurements aboard Spacecraft

All bubble detector measurements aboard spacecraft used in this work have been extracted from the published literature. A detailed account of all relevant bubble detector experiments can be found in Appendix A including dates, mission details, bubble detector locations and measurement results.

3.2 Simulations and Modeling of the Space Bubble Detector Response to Radiation on ISS

3.2.1 Monte Carlo Simulations

A Particle and Heavy Ion Transport Simulation (PHITS version 2.760) model was used to investigate the proton and heavy ion experiments. PHITS applies a Quantum Molecular Dynamics model for the transport of heavy ions through materials. PHITS is extremely versatile and a very large number of input parameters and outputs can be specified [96]. In the simulations performed for this thesis, the inputs included simplified geometry for the HIMAC BIO room and NIRS cyclotron experiments and material definitions. The heavy ion beams were input as monoenergetic 10 cm diameter cylindrical beams and divergence of the beams was modeled with the PHITS "nspread=2" command for Lych formula Coulomb diffusion (angle scattering). Energy loss straggling was modeled with the PHITS "nedisp=1" command (Landau Vavilov energy straggling). The PHITS simulations include a model of the bubble detector, a cylindrical column of air equivalent to the distance traveled by the particles in the HIMAC BIO room and NIRS cyclotron as well as an adjustable cylindrical Binary Filter made of PMMA or H_2O that could be matched to each individual experiment. For each of the beams, an absorbed dose depth curve was simulated in PHITS for comparison with the Markus Ion chamber measurements and verification of the energy of the ions in different experiments.

A PHITS simulation has also been developed to estimate the absorbed dose in a cylinder made of bubble detector polyacrylamide emulsion gel on a microscopic scale. The simulation consists of a point source of 81.5 keV/μm carbon ions incident along the central axis of a cylinder with a radius from 1 nm to 1 mm and a height of 1 μm. The output of the simulation was recorded as the absorbed dose (Gy) deposited in the cylinder per carbon ion.

3.2.2 Heavy Ion Track Structure in Bubble Detectors

Analysis of the bubble detector experiments with heavy charged particles has been performed considering heavy ion track structure models. The bubble detector model employs equations for the penumbra radius (r_{max}), and restricted LET that have been presented in Section 1.2.5 and the radial dose distribution equations from [48]. Using the Chatterjee, Katz and Keifer ion track structure models, another quantity has been defined as an average track energy density which is the total energy deposited into a cylindrical region of stopping material around an ion track divided by the volume of that cylinder with units of keV/μm^3. The cylindrical volume for an ion track has been defined to have a radius equal to the ion track penumbra (r_{max}) and a length dx where the ion traverses along the central axis of the cylinder. The volume of the cylinder is $\pi {r_{max}}^2 \cdot dx$and the average track energy density is given as follows:

$$Average\ track\ enegy\ density\ = \frac{Total\ Energy\ \ deposited\ \ in\ dx}{\pi {r_{max}}^2 \times dx} \tag{3.2}$$

The total energy deposited into the track as the ion travels a small distance *dx* is the unrestricted LET multiplied by *dx:*

$$Average\ track\ energy\ density\ = \frac{LET_\infty \times dx}{\pi {r_{max}}^2 \times dx} = \frac{LET_\infty}{\pi {r_{max}}^2} \tag{3.3}$$

More generally the average energy density may be defined for any cylinder that has a radius of size *r*. If the cylinder has a radius $r \geq r_{max,}$ then the average energy density is:

$$Average\ energy\ density\ in\ cylinder\ = \frac{LET_\infty \times dx}{\pi r^2 \times dx} = \frac{LET_\infty}{\pi r^2} \tag{3.4}$$

However, if the cylinder has a radius $r < r_{max}$ then the energy deposited into the cylinder is defined by the restricted LET_r where r is the radius of the cylinder. Using equation 1.9 for the restricted stopping power gives:

$$Average\ Energy\ density\ in\ cylinder\ = \frac{LET_r \times dx}{\pi(r)^2 \times dx} = \frac{\frac{LET\ \infty}{2}\left[1+\frac{1+2\ln(r/r_c)}{1+2\ln(r_{max}/r_c)}\right]}{\pi(r)^2} \tag{3.5}$$

Equations 3.3, 3.4 and 3.5 can be interpreted as the total absorbed dose in the respective cylinder which can be converted to units of Gy using the material density. This is different from the radial dose which is the dose at a point adjacent to an ion track at a distance *r*. The radial dose can be interpreted as the dose in a cylindrical shell with a thickness *dr*, inner radius *r,* and outer radius *r* + *dr* where the ion track passes through the central axis and secondary electrons deposit their energy in the cylindrical shell. On the other hand, the average energy density includes the energy deposited by all secondary electrons as they pass through the entire cylinder with radius *r*. In fact, the stochastic nature of ion tracks is significant on the micrometer scale. The average track density quantity may not be well defined for a single event in a bubble detector. Nevertheless, it is still useful in analyzing bubble detector experiments with heavy charged particle irradiation.

3.2.3Absorbed Dose in Space Bubble detector Micro Droplets from Heavy Ions

The average energy density of the ion track discussed in the previous section leads to the question: what is the absorbed dose in a microdroplet? The minimum LET threshold presented in the literature was calculated using the minimum deposited energy required for visible bubble

expansion and the size of the critical vapour embryos. The same values was used to determine a minimum energy density defined as the minimum energy divided by the volume of the critical vapour embryo:

$$D_{min} = \frac{E_{min}}{volume\ of\ critical\ vapor\ embryo} = \frac{E_{min}}{\frac{4}{3}\pi\ {R_c}^3} \tag{3.6}$$

Where D_{min} is the minimum energy density imparted into a vapour embryo in order to cause visible bubble expansion (in units of keV/μm^3). R_c and E_{min} are the vapour embryo critical radius and minimum energy as defined in Equations 2.1 and 2.2. Using equation 3.6 and the range of values for E_{min} and R_c quoted in the literature from [79]gives an estimated value of D_{min} between 1.06x10^4 and 9.02x10^5 keV/μm^3. Space bubble detectors have a density of 1.298 g/cm^3 so the estimated range of D_{min} is from 1.31x10^3 Gy to 1.11x10^5 Gy.

3.3 Modeling the Radiation Environment inside the ISS

The radiation environment inside the ISS contains many particle types with a wide energy range. The energy spectra of neutrons and protons vary significantly depending on conditions such as the solar cycle, solar emissions, current position of the ISS, altitude, geomagnetic cutoff rigidity, passage through the South Atlantic Anomaly, shielding and location within the ISS. To analyze the space bubble detector experiments aboard the ISS, a single time averaged neutron, proton and heavy ion spectrum was used. This was considered to be a good representation of the average net particle fluence over an extended measurement period (5-7 days) behind typical shielding consistent with the actual bubble detector measurements.

Several models of the radiation environment in LEO including GCR and trapped radiation have been developed. Software tools are available for modeling the radiation

environment inside spacecraft in LEO. Two of these tools have been used in this work; the On-Line Tool for the Assessment of Radiation in Space (OLTARIS) and the Cosmic Ray Effects on Micro-Electronics (CREME96) codes [97][98]. Both codes generate particle spectra in LEO space environments based on input parameters such as altitude, date and shielding. OLTARIS has been used to generate expected neutron, proton and heavy ion spectra inside the ISS for all bubble detector measurements between January 2008 and October 2013. CREME96 has been used for comparison with the OLTARIS results along with various measurements. CREME96 and OLTARIS have both been selected for this work because they are standard tools for assessing the radiation environment in spacecraft. Both codes produce proton and heavy ion particle spectra based on extensive radiation physics models and have been tested and validated in previous studies [99]. OLTARIS has been selected as the basis of the bubble detector measurement model because it also generates secondary neutron spectra and includes albedo neutron spectra. A full discussion of space radiation codes including CREME96 and OLTARIS can be found in [100].

3.3.1 Modeling of the GCR and trapped radiation environment in the ISS

OLTARIS uses the GCR model developed by O'Neill *et al.* which is based on balloon and satellite measured energy spectra from 1954 to 1992 and the Advanced Composite Explorer satellite from 1997 to 2002 [97]. OLTARIS is able to produce a GCR differential flux for ions from protons to nickel after passage through the solar system and into LEO. Input parameters include the start date and end date, altitude and inclination of earth orbit. Variations of the GCR spectra based on the solar cycle and solar conditions measured during the specified period are accounted for. The GCR spectrum can be transported through specified shielding using the

HZETRN2005 transport algorithms developed by Wilson *et al.* Cucinotta and Slaba *et al.*[97]. Simple shielding geometries can be specified such as aluminum or polycarbonate spheres. However, some more complicated geometries are available including various modules inside the ISS. Neutrons are not present in the GCR spectrum shielding; however, secondary neutrons produced in the transport of the GCR spectrum are included in the output. OLTARIS separately outputs the daily averaged particle differential flux energy spectra for neutrons, protons, alphas and heavy ions up to nickel.

Trapped Radiation is calculated using the AP8MIN and AP8MAX models based on Vette reduction of satellite data. Effects from the solar cycle and passage through the SAA are included in the model. The trapped radiation spectra are similarly transported through the specified shielding and the daily averaged flux is given. Albedo neutrons from the earth's atmosphere in LEO are also transported through the shielding and included in the OLTARIS output for the trapped radiation-induced neutron flux. The total daily particle flux for neutrons, protons, alphas and heavy ions is obtained by summing the GCR and trapped radiation fluxes.

Proton and Heavy ion fluxes have been generated for all ISS space bubble detector experiments using OLTARIS. Whenever possible, the OLTARIS proton and heavy ion fluxes were calculated in the same ISS location where the bubble detector measurements were made. This was possible for all measurements in the US Lab and the Russian Service Module. Unfortunately, OLTARIS does not include some of the ISS locations including the Japanese Experimental Module(JEM) and Node 2 where some bubble detector measurements were conducted. Similarly, CREME96 generates proton, alpha and heavy ion differential fluxes in LEO based on input parameters such as start date, end date, apogee, perigee and orbit inclination. It uses a semi-empirical GCR model based on Nymmik *et al.* and the AP8 models for trapped

radiation [98]. It also transports the flux through specified shielding and generates transported fluxes. However, neutrons are not transported and therefore the output does not include any neutron component. Shielding in CREME96 can be specified as simple aluminum spheres or as a shielding distribution file in which there is a distribution of aluminum thicknesses. The model is isotropic so specific geometry is not required in the input file.

For ISS Expedition 20, a comparison of the particle spectra reported in the literature with OLTARIS and CREME96 has been done. In this mission, the bubble detectors were co-located in the service module along with a tissue equivalent proportional counter (TEPC) and a set of four DB-8 silicon dosimeters. The ISS shielding has been entered in CREME96 as a shielding distribution file (.shd) based on the shield distribution reported by Benghin *et al.* for the DB-8 detectors [101] (See Appendix B, Figure B2). The shielding distribution used was for the DB-8 detector No.3 since it has an intermediate shielding which is assumed to best represent the average shielding over all experiment locations within the Service Module. The shielding distribution has a range from 2 to 450 g/cm^2 equivalent aluminum with most of the shielding between 3 and 30 g/cm^2. The shielding in the OLTARIS model was input as the ISS Service Module geometry which is included in the software. The CREME96 flux for protons and all heavy ions after transmission through the ISS shielding is shown in Figure 27(a). This produces a total proton fluence of 2.38x10^5 protons/cm^2/day and a total absorbed dose rate of 299 μGy/day in silicon according to the CREME96 DOSE calculation. This dose rate matches the average dose rate measured by the unshielded DB-8 no.3 detector in the Matroshka-R and Radi-N experiments (302 μGy/day) and is also consistent with the TEPC measurement of 277 μGy/day [101]. The proton, alpha and heavy ion spectra from OLTARIS are also shown in Figure 27(b). The trend of both are similar, but OLTARIS appears to under-represent the total proton and

heavy ion flux. The alpha flux below 100 MeV also shows an increasing trend toward lower energies in OLTARIS whereas it decreases in the CREME96 model. This is due to the fact that OLTARIS includes alphas in the trapped radiation component while CREME96 only includes protons in the trapped radiation model. The absorbed dose in silicon given by OLTARIS (117 μGy/day) is also significantly less than all of the DB-8 measurements (225 to 378 μGy/day) and the TEPC measurement (277 μGy/day). Thus, the OLTARIS proton spectrum has been scaled to match the CREME96 data and is plotted in Figure 28. With this scaling factor, the OLTARIS proton flux matches CREME96 in the region 10 to 100 MeV and is consistent with the experimental data. The proton spectrum given in the literature has also been plotted for comparison and agrees with the CREME96 and scaled OLTARIS models. This was constructed by summing the GCR and the trapped proton spectra presented in Figure 11.

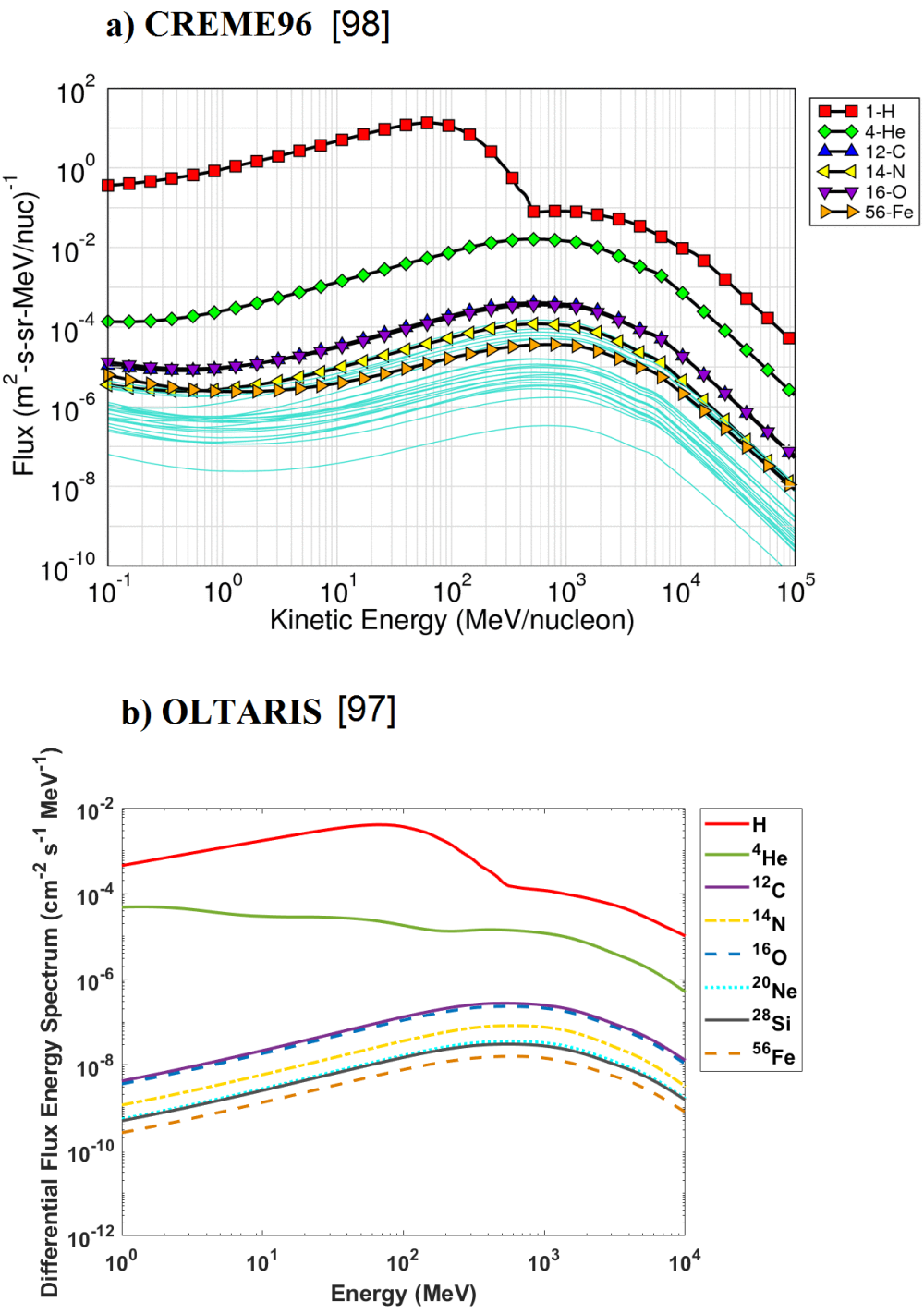

Figure 27: Proton, alpha and heavy ion flux in ISS calculated by a) CREME96 and b) OLTARIS

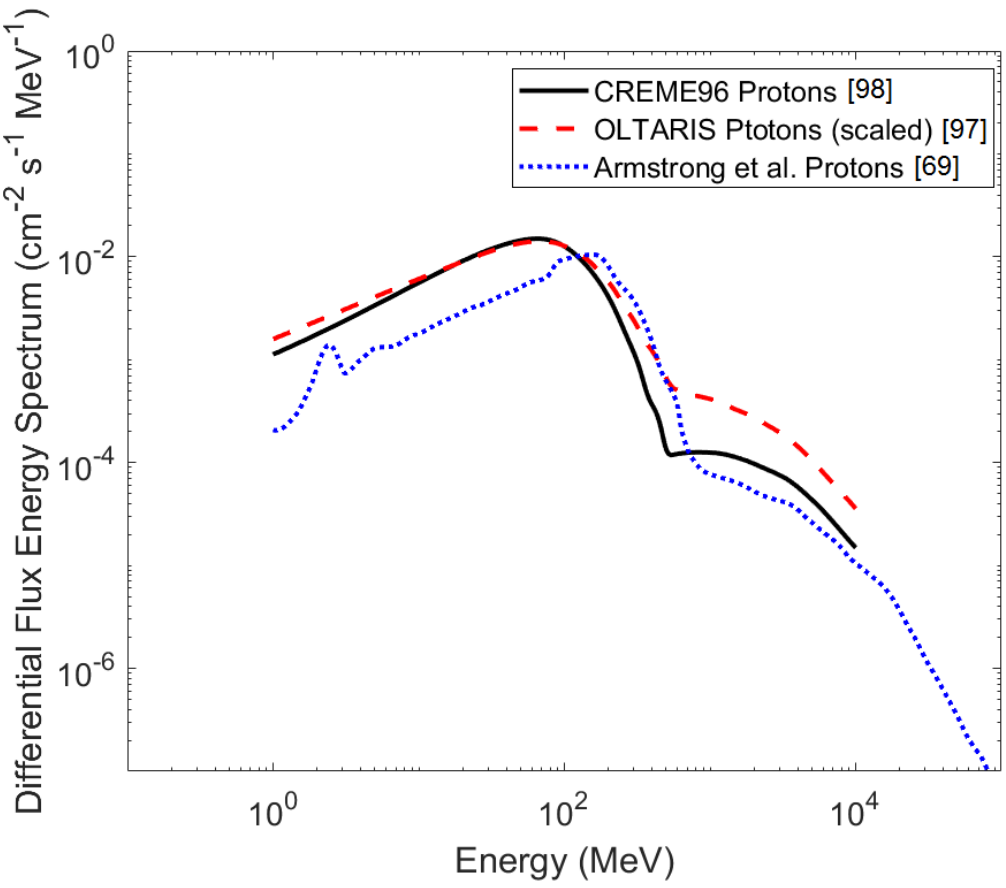

Figure 28: OLTARIS and CREME96 proton spectra on ISS Expedition 20

The neutron differential flux used in this work was constructed with OLTARIS and is based on the neutron differential flux spectrum model of Armstrong *et al.*[69]and on the measured neutron spectrum of Koshiishi*et al.*[71] (see Figure 9). The differential flux from Figure 9 has been integrated numerically from 1eV to 100 MeV in MATLAB for the BBND measurements and the Armstrong*et al.* model. The total neutron fluence was calculated to be 2.7×10^5 n/cm^2/day for the BBND measurements and 3.1×10^5 n/cm^2/day for the model spectrum. The BBND measurements were recorded in the US Lab during the period from 23rd March to 14th November 2001. The neutron and proton spectra were obtained from OLTARIS

using the input orbital inclination of 51.6° and an altitude of 396 km based on the average orbit during that period. The OLTARIS neutron spectrum has a similar shape to the BBND measurements and the Armstrong *et al.* model but is slightly underpredicted with a total fluence of only 1.6×10^5 n/cm^2/day. Thus, the spectrum has been scaled to better match the measured data where the scaled neutron spectrum has a total fluence of 2.9×10^5 n/cm^2/day between 1 eV to 100 MeV. The BBND measurements, the Armstrong *et al.* model, and the scaled OLTARIS neutron spectrum are all plotted together in Figure 29 and appear to be in good agreement. The OLTARIS proton spectrum has also been plotted along with the Armstong *et al.* proton data for comparison.

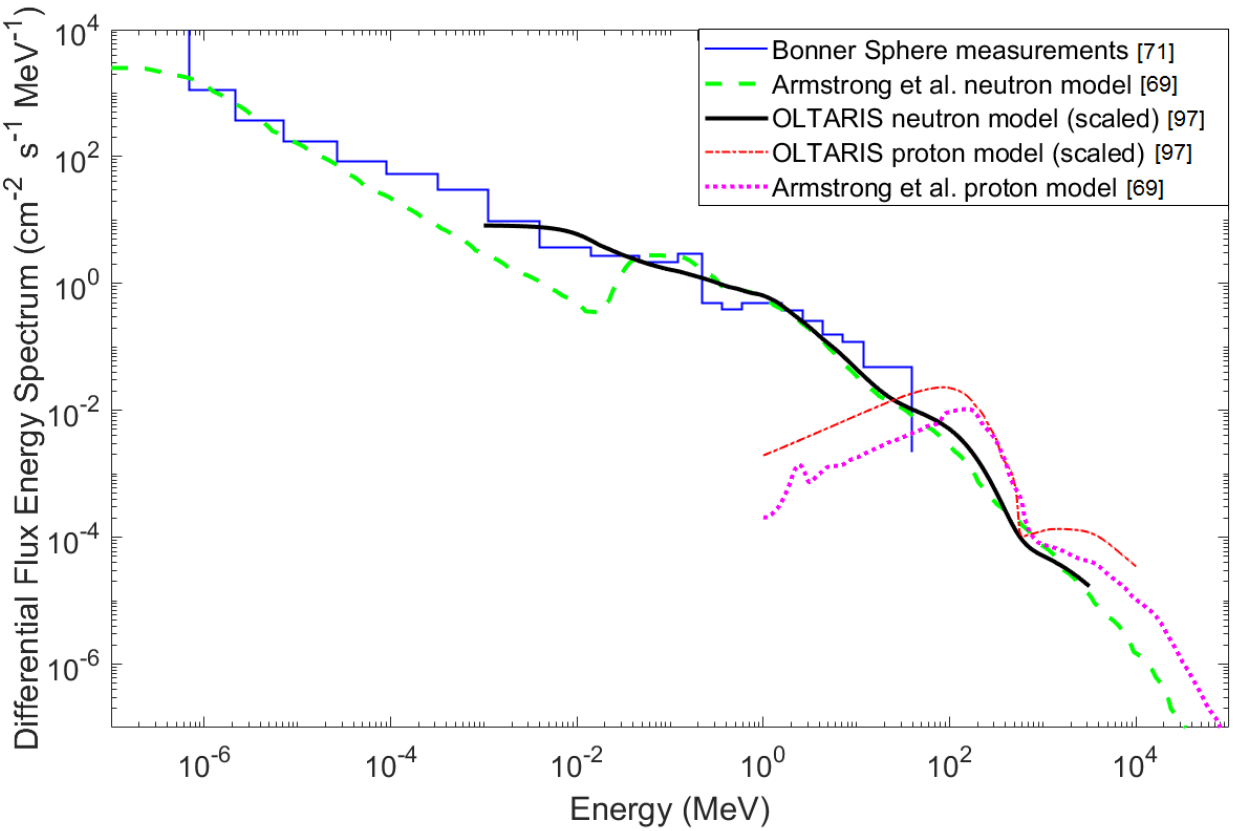

Figure 29: OLTARIS neutron and proton spectra in ISS US Lab

3.3.2 Modeling of Bubble Detector Response to Radiation inside the ISS

The number of bubbles produced in a bubble detector measurement depends on the response of the bubble detector to the particles in the radiation field, the radiation field spectra, and the total fluence during the measurement period. In principle, the number of bubbles produced in a given radiation field is given by the following equation.

$$bubbles\ produced\ in\ radiation\ field = \sum_i \int_0^\infty R_i(E) \cdot \Phi(E)\, dE \tag{3.7}$$

Where, E is radiation particle energy

$R_i(E)$ is the response function for particle type *i* in bubbles/(particle/cm^2)

$\Phi(E)$ is the total particle fluence in (particles/cm^2)

The radiation field may contain a number of different particles with different response functions so the total number of bubbles produced in a measurement would be the sum of all particle types (i) and their respective differential flux integrated over all energies for the total time of measurement. The response function $R(E)$ is a difficult parameter to calculate or model because it depends on a multitude of possible interaction effects of the radiation inside the bubble detector. The production of bubbles is also a stochastic effect due to the non-homogenous bubble detector medium with very small micro-droplets. A given particle interaction could produce a bubble inside a micro-droplet or produce no bubble if the same event occurred outside the micro-droplet. For measurements in spacecraft, the response of all present particle types is of interest. It is well known that photons and beta particles do not produce bubbles in bubble detectors. Thus, $R_{photon}(E) = 0$ and $R_{beta}(E) = 0$ for all energies and no bubbles are produced for any given fluence of these particles. The response function for neutrons $R_{neutorn}(E)$ has

been studied extensively and some experimental results have been presented (see Figure 12Figure 13 and Figure 14). In the literature, there have been relatively few experiments with protons and the response function has been reported over a limited energy range from 30 to 65 MeV (see Figure 15). The response function for alphas and heavy ions has never been reported in the literature. The neutron response for bubble detectors is believed to be essentially isotropic such that the direction of the incident particles does not affect the response function. This is because the secondary high LET radiation produced inside bubble detectors is mostly emitted isotropically and typically has a range much less than the bubble detector dimensions. For measurements in space, the neutron spectrum may have some directional variation based on location and shielding, but this is believed to have a negligible effect for bubble detector measurements on the ISS. The response to protons, alphas and heavy ions may vary significantly depending on incident energy and direction because the particle range may be greater than the bubble detector dimensions. The particle may be able to pass through the bubble detector diameter (1.6 cm), but be completely stopped if incident along the length (4.5 cm). Also, the LET and energy changes significantly after entering the detector and the population of bubbles depends on the position of the Bragg peak. Thus, the response function $R(E)$ for these particles depends on the incident particle direction. For measurements in the ISS, the proton, alpha and heavy ion spectra have directional variation based on location and shielding. The neutron, proton, and heavy ion spectra produced by OLTARIS are given as isotropic (averaged over all directions).

The response function of space bubble detectors to neutrons from energies below 1 eV to energies above 100 MeV has been measured in various ground-based experiments and modeled using Monte Carlo simulations. In order to model the number of bubbles produced by neutrons in

bubble detector measurements aboard spacecraft, a continuous response function from 10^{-6} to 10^{4} MeV has been constructed. An aggregate best-fit response curve has been constructed from experimental data using best-fit cubic splines in MATLAB referred to as $R_n(E)$. The response to neutrons above 200 MeV has not been experimentally measured so the results of PHITS simulations and the GEANT simulation from[83]have been used to extrapolate the response function from 200 to 1,000 MeV. The resulting function is shown in Figure 30 plotted along with the measured data[21]. The number of bubbles expected due neutrons for any given ISS mission can be calculated with this response function and the differential flux spectra from OLTARIS using Equation 3.7.

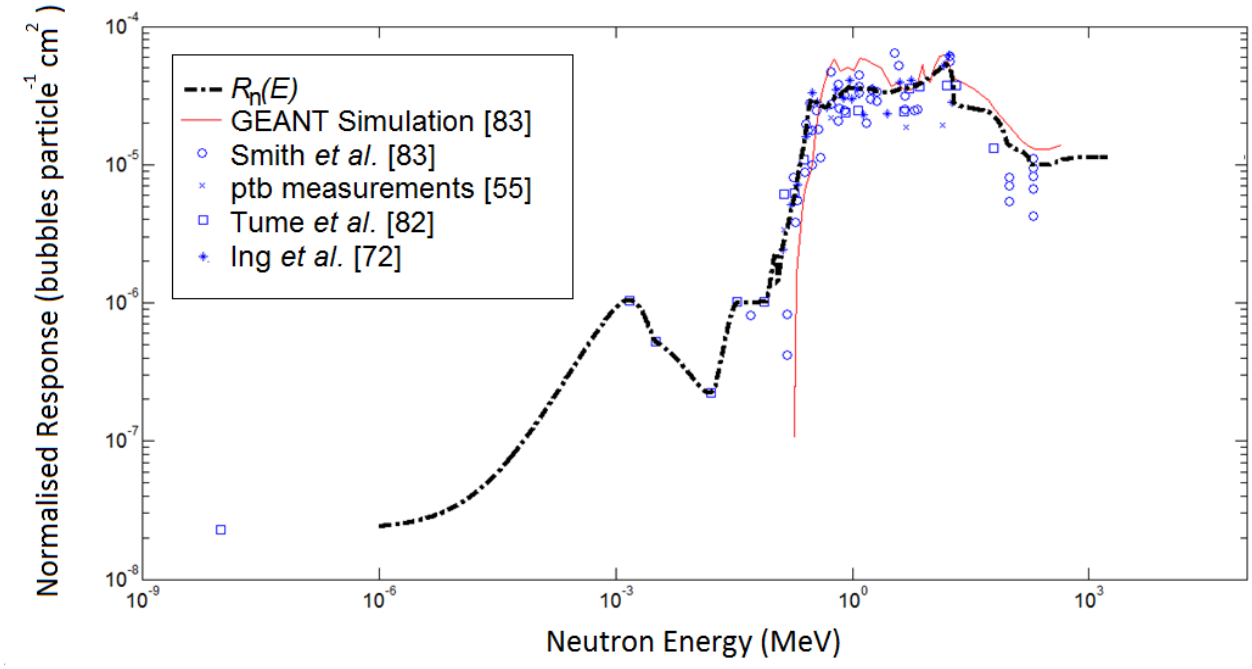

Figure 30:Space bubble detector response function to neutrons for a bubble detector normalized to an AmBe sensitivity of 0.1 bubbles/μSv

For bubble detector measurements aboard the ISS, it is impossible to differentiate between the number of bubble generated by neutrons and charged particles. Nevertheless,

bubbles have been clearly shown to occur under charged particle irradiation. In the literature, the contribution of charged particles to the reading of the bubble detector is about 2%. However, the very large flux of protons in the energy range from 50 to 500 MeV in the ISS would be responsible for generating a large number of the bubbles. In this work, estimates for the number of bubbles produced by protons in ISS measurements are based on the energy-dependent response function measured in ground-based experiments and the proton spectra generated by OLTARIS using Equation 3.7.

The radiation environment aboard the ISS also includes alpha particles and other heavy charged particles which are also capable of generating bubbles within SBD and SBDS. In fact, heavy charged particles may directly produce bubbles along the particle track. The flux of alphas aboard the ISS is a few orders of magnitudes below the flux of neutrons and protons (see Figure 29). In addition, alpha particles below 30 MeV have a range less than 1 mm in the bubble detector walls and cannot enter the sensitive volume of the detector to create bubbles. Only the high energy portion of the alpha flux (>30 MeV) would contribute to the bubbles formed. Charged particles, with $Z \geq 2$, have fluxes many orders of magnitude below neutron and protonfluxes. Therefore, they would generate a noticeable amount of bubbles only if their response functions are very large. The collective contribution of alphas and all other heavy charged particles to space bubble detector measurements during all ISS experiments has been estimated to be less than 1% [14]. The direction of the incident radiation may have the greatest effect on the response function for heavy ions where the range and LET changes significantly as the ions slow down or stop in the detector. In this work, the number of bubbles produced by heavy charged particles is estimated based on the response function when the detector is oriented along the beam axis.

CHAPTER 4: RESULTS AND ANALYSIS

The results of this work are divided into sections that summarize the main findings of each of the experimental investigations and analysis of the experimental results in the context of measuring radiation in space. The first and second sections contain results for experiments performed with space bubble detectors and SBDS. The third section focuses on the ion track structure model developed to examine the mechanism of bubble formation, while the fourth section is dedicated to the evaluation of the bubble detector measurements aboard the ISS. The neutron measurements at the LANSCE neutron facility are analyzed and a calibration factor for using AmBe calibrated detectors as neutron dosimeters in spacecraft is considered. Measurements of protons and heavy ions at ProCure Therapy Canter, the NIRS cyclotron, and HIMAC facility are presented together. The response function of space bubble detectors for each particle type is presented and compared to the neutron response function. The distribution of bubbles for each particle type is presented and the LET threshold for bubble formation is determined for space bubble detectors and SBDS. A detailed model of the LET threshold results based on ion track structure models is provided. Finally, space bubble detector measurements aboard the ISS between January 2008 and November 2013 are modeled using OLTARIS and compared to the published experimental data.

4.1Experimental Study of the Space Bubble Detector Response

4.1.1 Response to High Energy Neutrons

The bubble detectors used in all experiments were calibrated with an AmBe source at the Bubble Technology Industries facility. The sensitivity of the bubble detectors used in these experiments with high energy neutrons ranged from 0.10 to 0.22 bubbles/μSv. To investigate the response of the space bubble detectors to high energy neutrons, we used the Los Alamos Neutron Science Centre (LANSCE) spallation neutron source at the Los Alamos National Laboratory, New Mexico USA, exposing a set of bubble detectors to neutron spectra from 0.6 to 800 MeV. The LANSCE 30L beamline, used for single event effect studies of semiconductor devices, produces a neutron spectrum of similar shape to the one produced in space (10^7 times higher intensity than in space). Dosimetry control was provided by online fission foil ionization chambers. Space bubble detectors were irradiated to a number of neutron pulses from the spallation source. Following exposure and counting of bubbles in each detector, the bubble detector data (number of bubbles) was converted to equivalent dose values. Since the spectrum of the facility is well known, the equivalent dose was also calculated by the following formula:

$$H = \sum_{i=1}^{N} CF_i * \Phi i \ , \tag{4.1}$$

Where: H is the equivalent dose, CF_i is the equivalent dose to fluence conversion coefficient from ICRP74, and Φi is the neutron fluence in each energy bin. This is a discrete form of equation 1.3 and was calculated numerically in MATLAB.

The neutron spectrum for a single pulse of the 30L beam lineis shown in Figure 31. Detectors were exposed to a number of pulses that provided a total fluence of ~10^6 n.cm^{-2}.

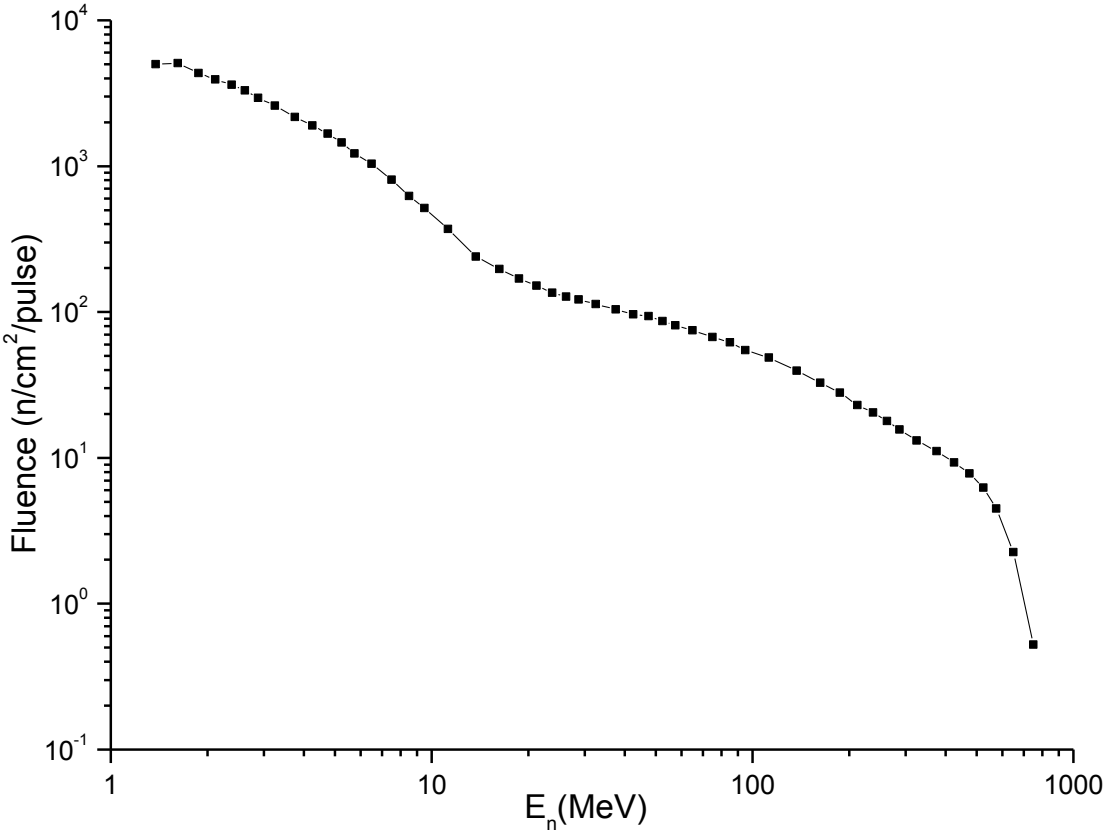

Figure 31: Beamline neutron spectrum for one pulse at ICE House facility

The spectrum along with the equivalent dose to fluence conversion factor, from ICRP 74, were used to determine the equivalent dose for each exposed bubble detector. The calculated values of the equivalent dose were compared to the measured equivalent dose values obtained from the bubble detectors, and a scaling factor was extracted for six different experiments. The data are shown in Figure 32 where both extracted equivalent dose from the neutron spectrum and the equivalent dose measured by the bubble detectors are presented for different bubble detector sensitivities (S_{AmBe}). The high energy neutron component and low response to neutrons above 20 MeV mean that the number of bubbles present will under-

represent the neutron dose (as calculated by the spectra from Figure 31convoluted with the ICRP 74 fluence to dose conversion factors) when using the AmBe calibrated sensitivity. A scaling factor of between 1.5 and 2.4 was used to correct for the difference in bubble detector readings in AmBe and the 30L high energy neutron environments. The weighted average scaling factor was found to be 1.8 ± 0.2 to compensate for the sensitivity of the bubble detector when used in space. This value is consistent with the value of 1.62 as suggested in the literature [55].

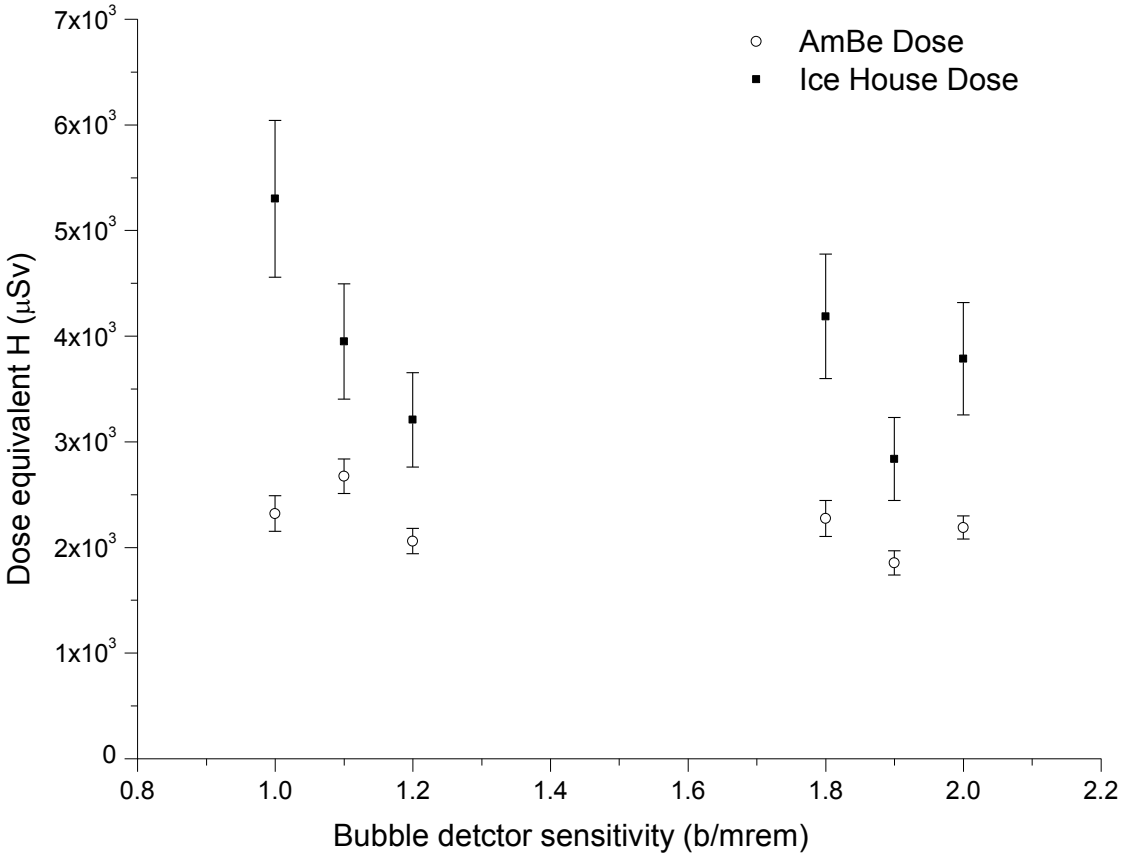

Figure 32: SPND measurements at ICE House facility

4.1.2 Response to Heavy Charged Particles

The dominance of the proton radiation in space environments implies that protons have a major contribution to the reading of the space bubble detectors compared to other charged particles. However, due to the difference in charge and mass and LET, other heavy ions could also contribute significantly depending on the sensitivity to these particles. This section discusses the results of the investigation for protons as well as for the experimentally investigated heavy charged particles He, C, O, Ne, Si, and Fe.All of the heavy charged particles studied in this work produced bubbles in space bubble detectors and SBDS. The number of bubbles produced clearly increased proportionally to the total fluence of radiation in all cases as expected. However, bubble detectors have a maximum saturation of about 300 expanded bubbles. Above this number, there is insufficient volume for further bubble expansion. In all experiments, bubble detectors were irradiated with a large enough fluence to produce a statistically significant number of bubbles (approximately 20 to 250 bubbles) without approaching the saturation limit. The response function for each particle type is expected to depend on the particle energy. Thus, a set of different binary filters was chosen from 0 mm to the thickest filter that would still allow the ions to pass through into the bubble detectors. The energy of the ions after passing through each binary filter was calculated in SRIM and recorded along with the particle fluence as read by the scintillation counter. The number of bubbles was read using the BDRIII reader and the bubble detector image was saved. The response for each energy was calculated as the number of bubbles produced divided by the fluence. This has been normalized by dividing the calibrated sensitivity in an AmBe field relative to the standard 0.1 bubbles/μSv (Equation 3.1).

Proton Response Function:

The results for all proton experiments at the ProCure facility and the NIRS cyclotron are plotted in Figure 33 along with the average results from the literature (see Figure 15). Error bars for individual measurements have been omitted for clarity. A best-fit proton response function for the data, $R_{proton}(E)$, has been estimated using the average measured value at each energy. Maximum and minimum estimates of the proton response function have also been plotted using the maximum and minimum experimental values with the addition of a 10% deviation based on the error given for the AmBe calibration factor indicated by the manufacturer. A discussion of measurement uncertainties is provided in Appendix E.

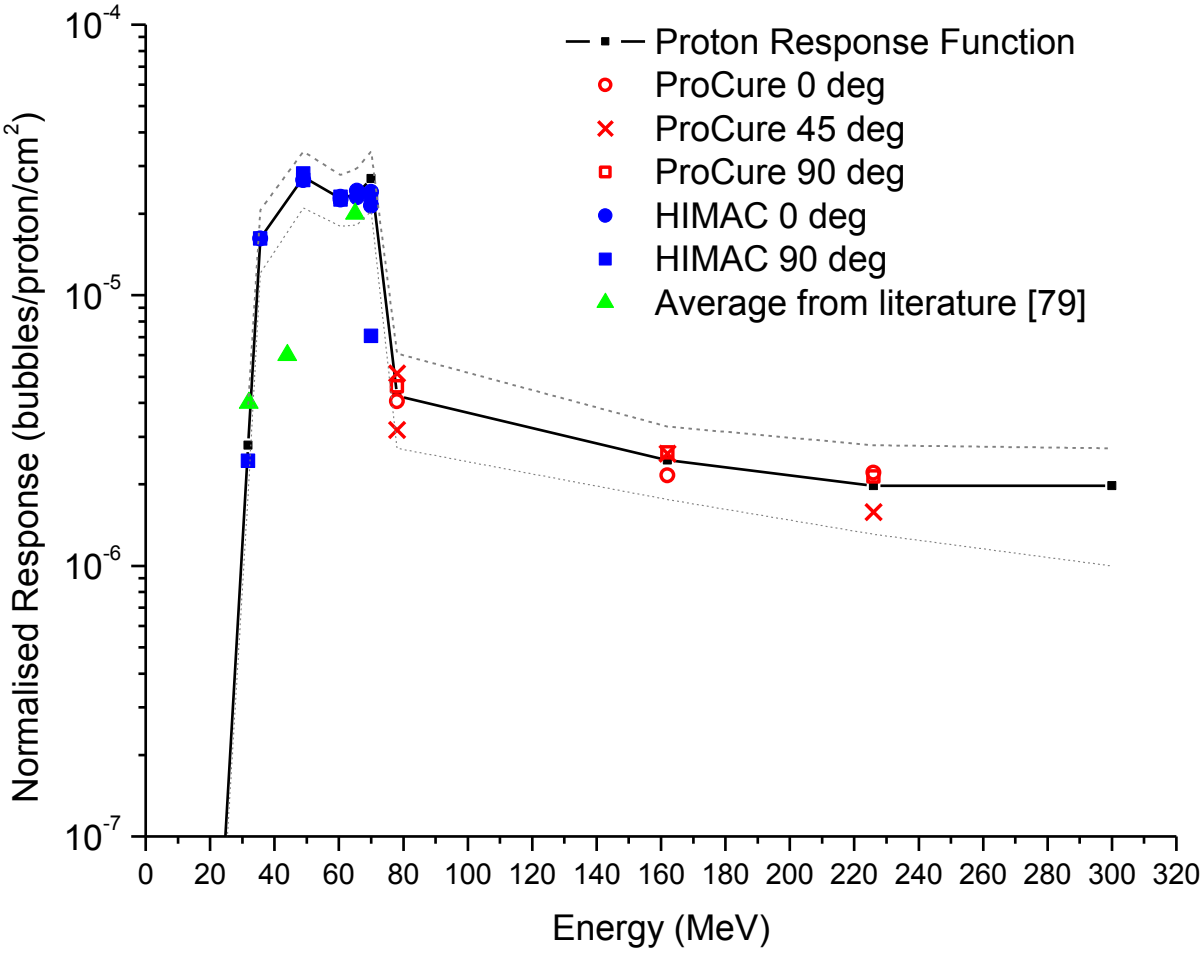

Figure 33: Space bubble detector proton response function

The results in the literature appear to be consistent with the measurements at the NIRS cyclotron for energies from 30 to 80 MeV. The ProCure measurements from 80 to 250 MeV display a sudden drop in sensitivity and a decreasing trend for higher energies. The number of bubbles produced per unit fluence is expected to drop above ~80 MeV where the range of protons becomes comparable to the length of the bubble detector (45 mm). High energy protons above 80 MeV pass through the bubble detector and produce fewer high LET events. The bubbles produced are believed to be primarily due to high LET secondary radiation from

scattering and fragmentation reactions inside the bubble detector. The total cross section for these reactions displays a gradually decreasing trend towards higher energies for the most prominent heavy nuclei in the bubble detector material which is consistent with the measured data. In all cases, the orientation appears to have no significant effect on the results except for a single data point at about 70 MeV where the detector perpendicular (90 deg) to the proton beam produced noticeably fewer bubbles than the detector parallel to the beam (0 deg). This may be explained by the fact that at this energy the range of the protons is about 33 mm which is less than the bubble detector length (45 mm) but greater than the bubble detector diameter (16 mm). So the protons easily pass through the diameter of the perpendicular detector with high energy (~70 MeV slowing down to ~30 MeV) where the total scattering and fragmentation cross sections remain low. Fewer high LET events are produced and fewer bubbles are measured. In the case of the parallel detector, the protons slow down and stop inside the detector and produce more high LET events. For energies above the maximum value of 226 MeV, the response function is extrapolated assuming the scattering and fragmentation cross sections remain relatively constant. Unfortunately, cross sections for protons above 200 MeV are not well represented in the literature. However, it is believed that there is no significant change in the region 200 MeV to 1 GeV. For this work, a constant response function for energies above 200 MeV is assumed. The maximum and minimum estimates assume a slight increase or gradual decrease based on the trend of the measured data or possible increase in total cross sections respectively. The number of bubbles produced for proton energies below ~35 MeV vanishes towards lower energies as the proton range in the bubble detector decreases. Below 10 MeV the range of the protons is less than 1 mm and they cannot pass through the plastic wall of the bubble detector into the sensitive volume. The response function has been set as 0 below this point.

Heavy Charged Particle Response Functions:

The results for all heavy charged particles are presented together inFigure 34along with the neutron response function for comparison. Figure 35 shows the same plot without the neutron or proton response functions and rescaled to increase the separation between the heavy ion data. All heavy ion data in Figure 345has been measured at HIMAC in approximately 20 individual measurements for each particle type. The data points indicate the measured values and error bars indicate the standard deviation of measurements (typically between 2 to 4 measurements at each binary filter). With the exception of the proton measurements, all data in Figure 34 has been recorded with the detector oriented along the beam axis to give a maximum expected response (see Figure 26).

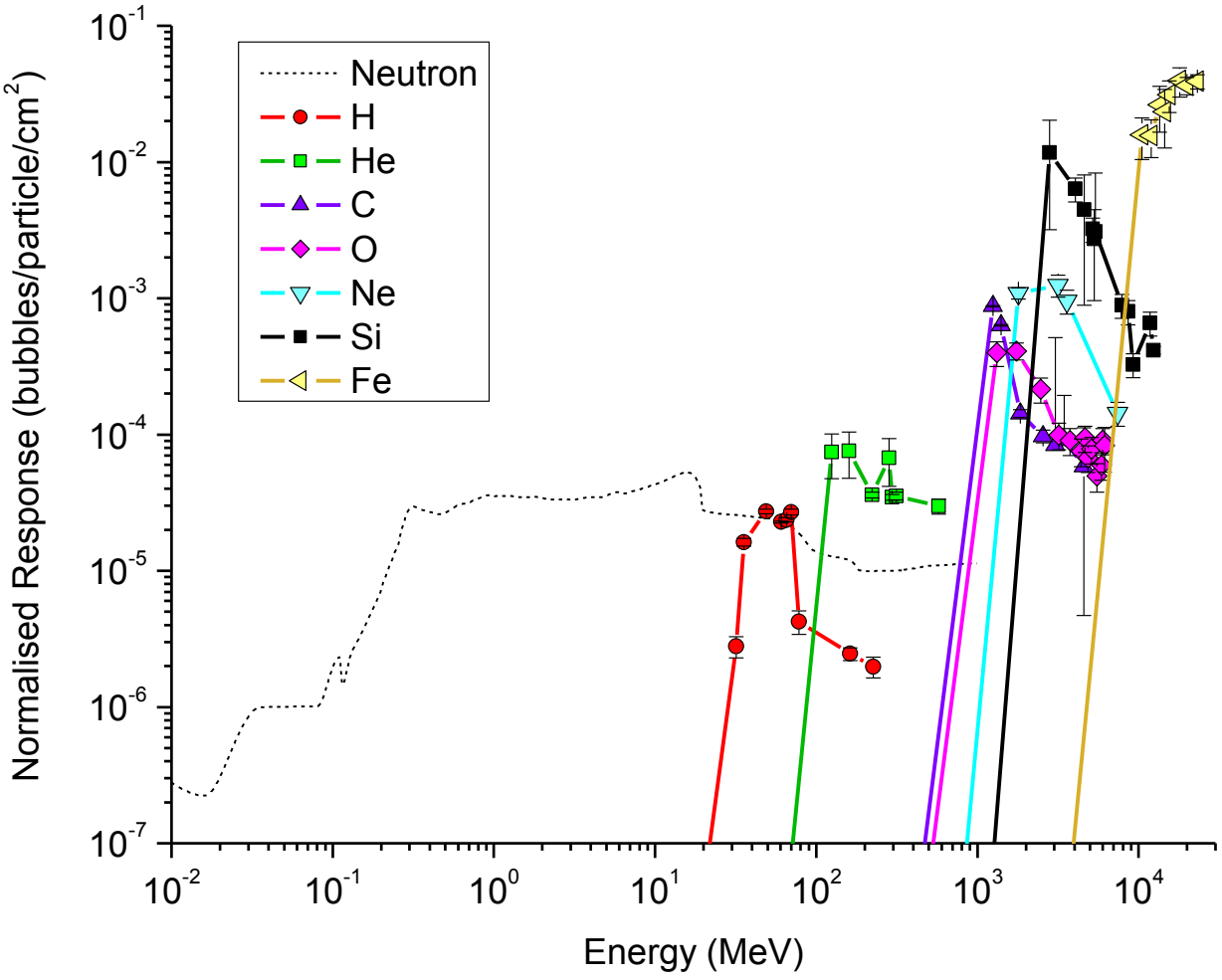

Figure 34: Neutron and charged particle response functions

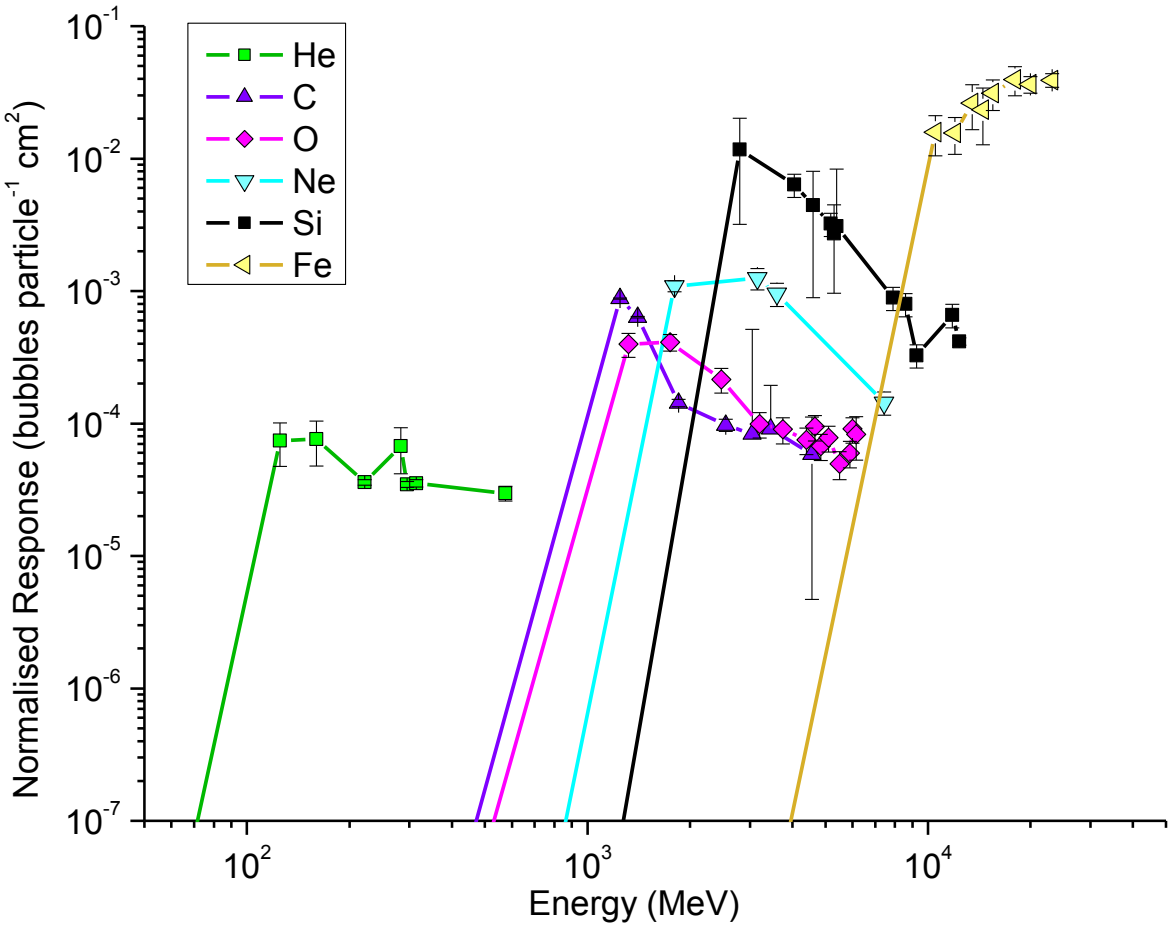

Figure 35: Charged particle response functions

A lower energy threshold for each ion-type has been estimated as the minimum energy required for the ion to pass through the 1 mm thick plastic wall into the sensitive volume of the bubble detector. This has been calculated using SRIM for each ion and the response function has been estimated as zero below this energy. For all ions, the number of bubbles produced per unit fluence increases above the threshold and displays a maximum at some energy. In general, as the energy is increased further the number of bubbles produced decreases as the range of the ion becomes larger. There is a drastic decrease when the ion range becomes larger than the bubble detector length (45 mm). In this case, the high energy ions have a much lower LET and pass

through the bubble detector producing far fewer high LET events that could produce bubbles. This is clear for carbon ions at about 1.8 GeV (range 44 mm) oxygen ions at about 3 GeV (range 47 mm), Ne ions at about 4 GeV (range 43 mm) and Si ions at about 7 GeV (range 44 mm). The He data shows a less dramatic drop from 300 to 600 MeV (range 38 mm to 1.3 m) and Fe ions are still near the maximum at the highest recorded energy around 20 GeV (range ~ 48 mm).

In Figure 34and Figure 35, the response of function increases with the charged of the incident particle. In comparison, all ions heavier than proton have response functions that lie clearly above the neutron response function. For measurements in space, this may indicate that a significant number of bubbles could be produced by heavy charged particles despite the total fluence of those particles being much less than protons and neutrons. Conversely, the high *Z* ions need a much high energy to penetrate through the 1 mm thick wall of the bubble detector.

The proton response function appears to be comparable with the neutron response function in the region of 30 to 100 MeV. This suggests that a substantial number of bubbles could be produced by protons in spacecraft measurements relative to the number of bubbles produced by neutrons considering the expected proton flux on the ISS asshown in Figure 27 and Figure 29. The lower proton response relative to the neutron response above 80 MeV is due to the lower total interaction cross section of protons relative to neutrons.

4.1.3 LET threshold for Bubble Formation in Space Bubble Detectors

The space bubble detector response functions discussed in the previous section show effects that are consistent with the bubble detector theory *i.e.* bubbles are only formed from high LET events. The neutron response function indicates that such high LET events occur mostly from neutrons above 300 keV and decrease slightly for neutrons with energies above 20 MeV.

As expected, the large number of high LET events from energetic heavy ions produces a large number of bubbles per unit fluence. However, the results in Figure 34 do not indicate exactly what high LET events are occurring inside the bubble detector and which of those events are responsible for forming bubbles. Although the HIMAC experiments were performed with monoenergetic heavy ion beams, the LET of the ions as they pass through individual microdroplets cover a broad range as the ions slow down and stop in the detector. Additionally, secondary fragments and recoil ions also deposit energy into the microdroplets with very high LET. Secondary neutrons produced along the beam line may also be responsible for creating bubbles. Therefore, the bubble detector images have been analyzed and the distribution of bubbles formed has been examined in order to determine which events may be responsible for creating bubbles. The results in this section are presented in subsections for each ion studied.

Proton Results:

A selected set of raw bubble detector images from individual experiments are shown in Figure 36. Note that each image contains two views of the bubble detector. This is done *via* a mirror inside the reader and the software uses the two separate views to account for occlusion effects in the bubble counting process. E_p indicates the incident proton energy in each experiment and in all cases, the protons are incident on the left side of the image and traverse towards the right side (except the vertical bubble image where the right-hand image is inverted). The range of the protons calculated using SRIM has been included.

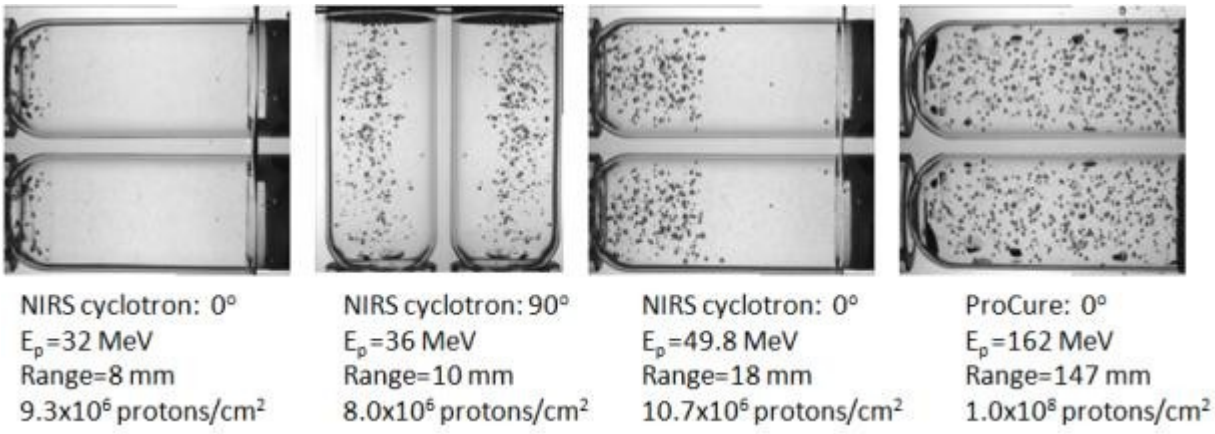

Figure 36: Bubble detector images from selected proton experiments

There appears to be a relatively constant density of bubbles in the region of the bubble detector traversed by protons. In every case, there is a lack of bubbles beyond the end of the proton range indicating that secondary neutrons produced along the beam line are not responsible for the majority of bubbles observed. Measurements with additional bubble detectors located at 40 cm and 300 cm outside the proton beam had less than 1% of the number of bubbles relative to the detectors in the beam. This is relevant because it has been suggested that secondary neutrons produced in proton beamlines may be responsible for the majority of bubbles observed in proton measurements. The density of bubbles appears to remain relatively constant and there is no apparent increase in the region of the Bragg peak. This is consistent with observations made in the literature (see Figure 17). This effect can be explained in three different possible cases as follows;

Case 1: High energy protons have sufficient LET to cause bubbles along their entire track through the bubble detector and the bubbles observed occur when the individual proton tracks traverse a microdroplet. The significant increase of LET near the Bragg peak would not affect

the number of microdroplets traversed by protons and the bubble density would remain constant until the end of the proton range.

Case 2: Protons do not have sufficient LET to directly produce bubbles, but the secondary recoil ions produced in scattering and nuclear fragmentation reactions along the proton tracks do have sufficient LET to produce bubbles. The number of secondary recoil ions along the proton tracks would probably remain relatively constant and thus the density of bubbles along the proton tracks would remain constant.

Case 3: High energy protons entering the bubble detector have a low LET that is below some minimum threshold. At some point (likely near the Bragg peak) the LET of the protons reaches this threshold and more bubbles are produced when these high LET protons traverse the microdroplets. Concurrently, secondary ions produced in scattering and nuclear fragmentation reactions have sufficient LET to produce bubbles everywhere and the net result is a constant density of bubbles along the entire proton tracks.

There is no clear way to distinguish the above three cases with the observed bubble formation data. However, it seems unlikely that protons with a very low LET are capable of producing bubbles directly (electromagnetic interaction). For example, in Figure 36 the 162 MeV protons enter the left side of the detector with an LET_{∞} of about 0.6 keV/μm and exit through the right side of the detector with an LET_{∞} of about 0.7 keV/μm. This is far less than the minimum LET threshold proposed in the literature review (23.2 to 493.7 keV/μm) and the distance traversed by protons in this experiment would need to be roughly 11 to 133 μm in order to deposit the supposed energy required for bubble formation (between 7.8 and 82.94 keV). For 20 μm diameter microdroplets, it seems unlikely that sufficient energy for bubble formation would be deposited in the entire microdroplet and certainly insufficient energy in the nm scale of

the vapour embryos produced along the proton tracks. Thus, the proposed Case 1 above seems unlikely. Case 2 and Case 3 cannot be easily distinguished since they both suggest many or all of the bubbles formed are a result of high LET secondary particles. In order to obtain a better understanding of the number of bubbles produced along the proton tracks and especially in the region of the Bragg peak, the MATLAB program described in section 3.1.4 has been used to analyze the bubble density along the proton tracks and determine if there is a notable difference near the Bragg peak. The output of the MATLAB program is shown in Figure 37 and Figure 38.

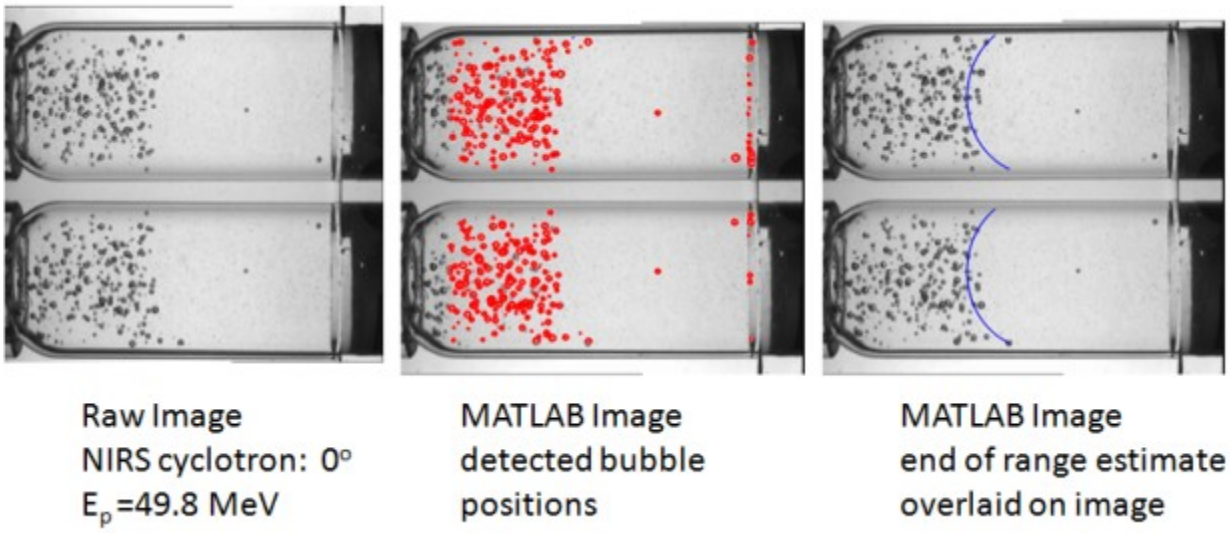

Figure 37: Output of MATLAB LET analysis program for proton experiment at NIRS cyclotron

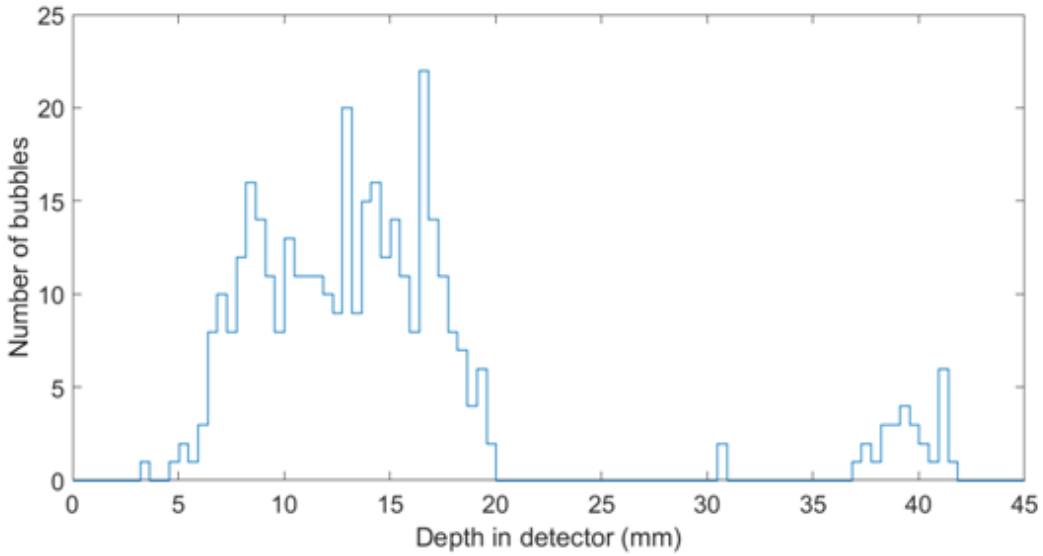

Figure 38: Bubble count using MATLAB program for proton measurement at NIRS cyclotron

The indicated bubble positions detected by the MATLAB program using the Circular Hough Transform algorithm appear to match actual bubble locations precisely with a few notable exceptions. All bubbles to the left side of the image (less than 75 pixels from the left edge of the image) are not counted. This is necessary because the visual interference of the rounded end of the bubble detector creates a large number of false bubble identifications and must be omitted. This feature is also included in the BDR III bubble image reader and counting software where regions are set by the user to omit unwanted parts of the image. Additionally, there are some false bubble identifications on the right side of the image. This is simply an aberration caused by the optical fluid depth being too low to cover the whole bubble detector in this particular image (note: this is not the typical case in bubble detector images). The software identified the beginning of the image as the bubble front (*i.e.* a high density of bubbles occurs from the beginning of the observed region of the image). The end of the range is identified by the software where a statistically significant drop in bubble density occurs at 17.8 ± 0.9 mm. The error of

0.9 mm has been estimated using the mean diameter of a single bubble in the images (10 pixels). This range is consistent with the SRIM calculated range of 18 ± 1 mm in bubble detector material for 70 MeV protons passing through a 16 mm thick PMMA binary filter (BF=18.64 mm H_20 equivalent). Figure 38 is the sum of the number of bubbles counted from both viewing perspectives where the horizontal axis is the depth in the bubble detector. The data is noisy due to the sporadic distribution of the bubbles. However, it appears to confirm that there is no discernable statistically significant increase in bubble density at the region of the Bragg peak. The MATLAB program also includes data imported from SRIM for protons traversing through bubble detector medium. The program matches the end of the range determined from the image processing to the end of the range in the SRIM data and produces a LET versus depth curve. The result is shown in Figure 39.

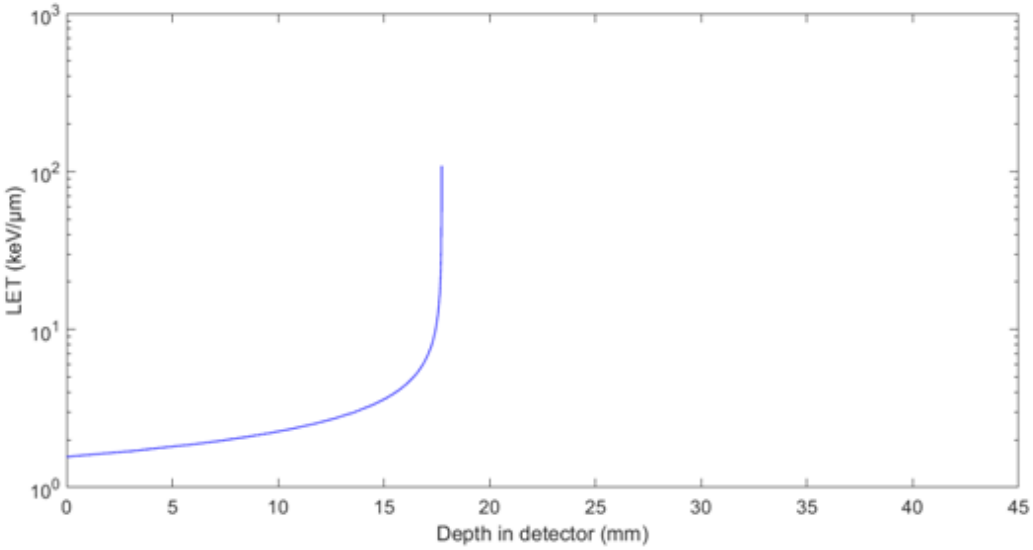

Figure 39: SRIM calculated Bragg curve for proton experiment at NIRS cyclotron

The LET of the protons increases above the minimum estimated threshold proposed in the literature (23.2 keV/µm) at about 16 mm and actually never reaches the maximum proposed

threshold (493.7 keV/µm). Since the density of bubbles appears constant from 0 to 18 mm in the bubble detector, it appears unlikely that the increased LET of the protons as they slow down and stop is directly related to the number of bubbles produced. This result is onlyfrom one individual experiment and the sporadic distribution of the bubbles makes it difficult to conclude if there is a clear increase of bubbles near the Bragg peak. All of the experiments performed with protons stopping in bubble detectors, where the bubble detectors were oriented parallel to the proton beam (0°) and the range was less than the bubble detector length (45 mm) have been analyzed with the MATLAB program. In every case, the program was able to reliably identify the end of the proton range based on bubble distributions. Eight individual experiments at the NIRS cyclotron and four experiments at the ProCure facility consistently showed a constant bubble density along the proton track and no significant increase in bubble density at the Bragg peak was observed. The output image for each experiment is shown in Figure 40.

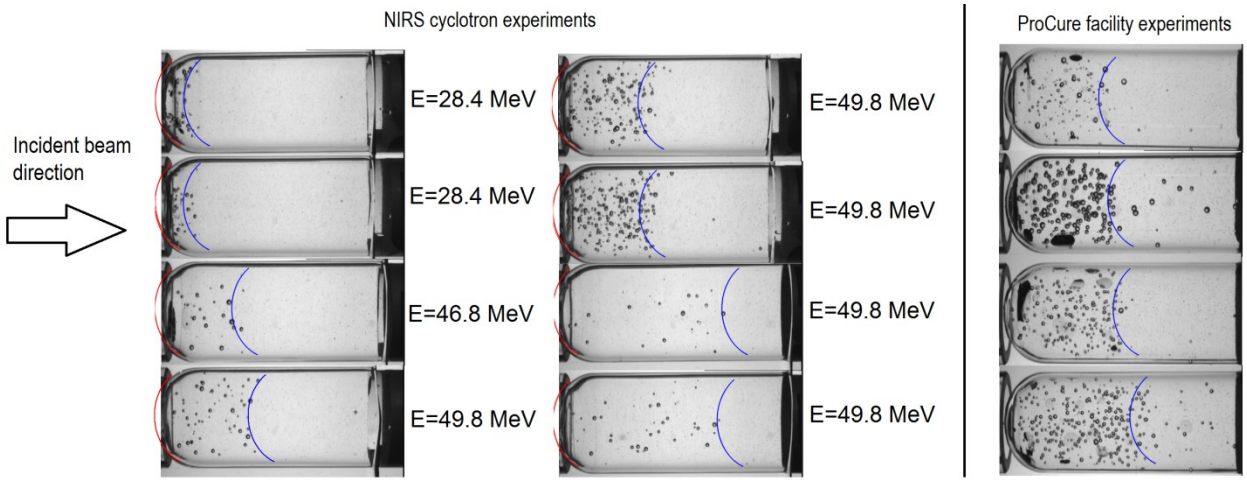

Figure 40: Range estimates for proton experiments at NIRS cyclotron and ProCure facility

The range estimates from the MATLAB program for the NIRS cyclotron experiments are listed in Table 3 along withthe SRIM calculated range for 70 MeV protons passing through the

binary filter. There is one notable difference in the ProCure experiments compared to the NIRS cyclotron experiments in Figure 40. The ProCure experiments appear to have a larger number of spurious bubbles beyond the end of the proton range. This is because the ProCure experiment had alarger initial proton energy and passing through an aluminum shield has caused more secondary neutrons. This observation has no impact on the response function presented in Figure 33 because no aluminum shielding was present in any of those experiments.

Table 3: Proton experimental range and MATLAB program estimated range

Experiment NIRS cyclotron Binary Filter (mm)	SRIM calculated energy (MeV)	SRIM calculated range (mm)	MATLAB program calculated range Determined by bubble distribution (mm)
32.64	28.4	6.5±1.4	6.8±0.9
32.64	28.4	6.5±1.4	7.7±0.9
20.96	46.8	16.1±1.4	15.0±0.9
18.64	49.8	18.1±0.8	18.2±0.9
18.64	49.8	18.1±0.8	16.8±0.9
18.64	49.8	18.1±0.8	17.8±0.9
0.56	69.5	32.9±0.8	30.9±0.9
0.56	69.5	32.9±0.8	32.0±0.9

Helium Results:

Thirty individual bubble detector measurements have been recorded at the HIMAC facility with 150 MeV/nucleon He ions. Of those experiments, eight were oriented parallel to the He ion beam line and had a range less than 45 mm. The MATLAB LET analysis program was employed to the bubble detector images. All images are oriented so that the direction of the He ion beam enters from the left side of the image and traverses toward the right side. The result of

one individual experiment is shown in Figure 41 and Figure 42. Upon initial inspection of the raw image on the left side of Figure 41, it appears there are bubbles everywhere in the bubble detector and there seems to be a high density of bubbles near the right side of the detector (about 30 to 40 mm along the detector).

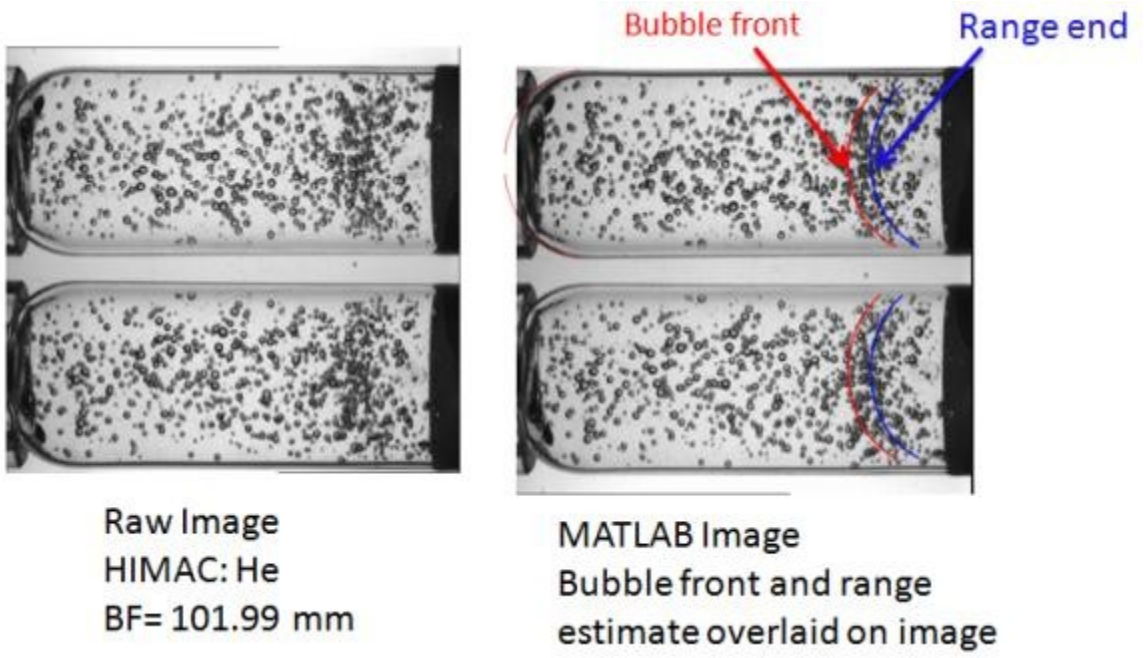

Figure 41:Raw image and output of MATLAB LET analysis program for proton experiment at NIRScyclotron

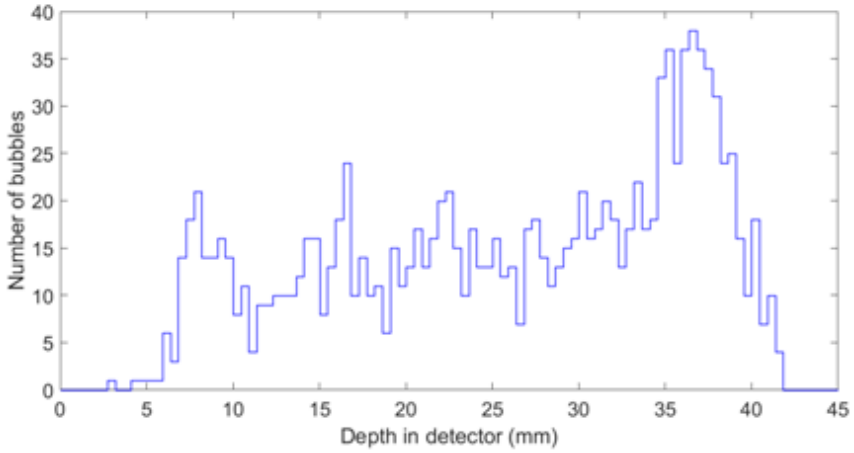

Figure 42: Bubble count using MATLAB program for He measurement at HIMAC

The formation of bubbles in the He experiment shows an obvious difference in the region of the Bragg peak unlike all of the proton measurements. Although it is somewhat difficult to resolve with visual inspection, the bubble counting data in Figure 42 display a clear and obvious increase at about 35 mm and decrease at about 38 mm. There is a 'bubble front' as observed in the literature for experiments with N and Ar ions (see Figure 18). The large number of spurious bubbles along the entire He ion tracks and beyond the He ion range suggests that there are many bubbles being produced by secondary particles. However, the sudden and drastic increase in the region of the Bragg peak suggests that the increasing LET of the He ions as they slow down and stop is playing a role in the number of bubbles formed. The LET versus depth profile for the program matched to the estimated range of 36.8±0.9 mm is shown in Figure 43. The position of the bubble front is indicated with a red dashed line where the LET is 15.7 keV/µm. This is less than the LET minimum threshold proposed in the literature (23.2 keV/µm) but of the same order of magnitude and it is conceivable that the He ions are directly (electromagnetic interaction) causing bubbles in this region. The LET of the He ions at the bubble front position is between

12 keV/µm and 33 keV/µm considering the error in both the position of the bubble front and the end of the range(See Appendix E for a discussion).

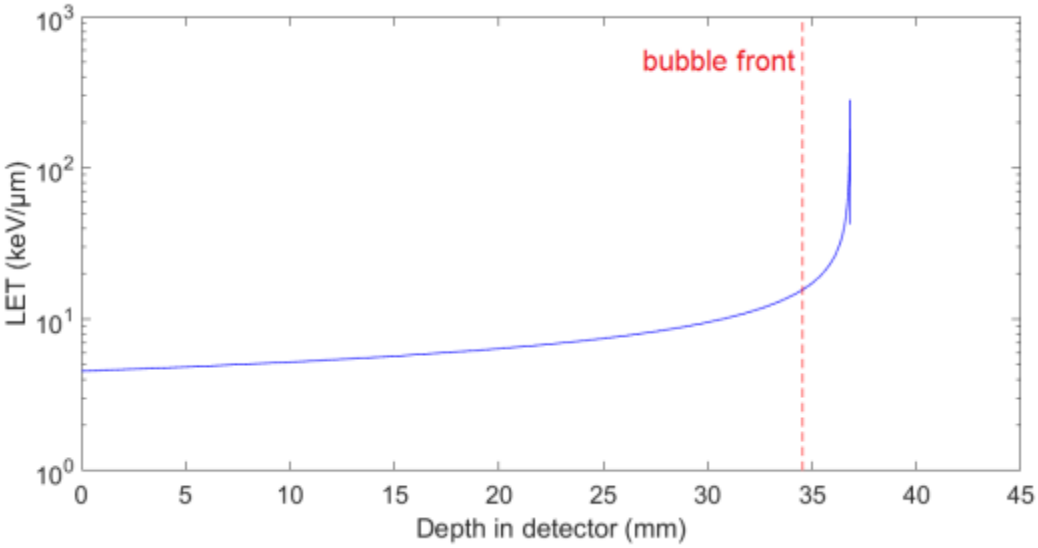

Figure 43: SRIM calculated Bragg curve for He experiment at HIMAC

The visual output of the MATLAB program for eight separate He experiments are shown together in Figure 44. Only one viewing perspective is shown for each experiment. In all cases, the program was able to identify a bubble front and end of the range which appears to correspond well to the bubbles in the images. The results are summarised in Table 4 along with the LET of the He ions identified at the bubble front position. The uncertainty in the LET was estimated using the LET obtained for the closest distance from the bubble front (maximum estimate) to the SRIM range. These uncertainties are very large compared to the calculated value for each experiment due to the quickly increasing LET at the Bragg peak which jumps from 20 keV/µm to over 250 keV/µm in only 1 mm.

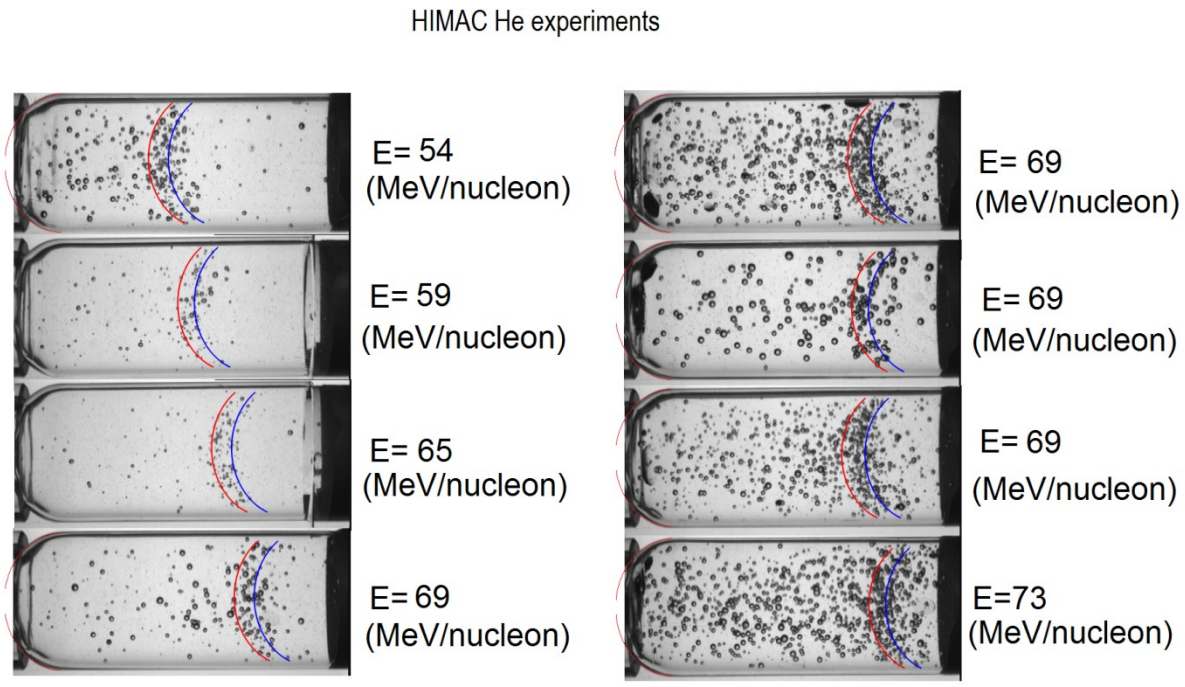

Figure 44: Bubble front and end of the range for 150 MeV/nucleon He experiments at HIMAC. Bubble front is indicated by red curve and end of the range is indicated by blue curve overlaid on each image

Table 4: LET threshold data for 150 MeV/nucleon He ion experiments at HIMAC

Experiment HIMAC Binary Filter (mm H_2O)	SRIM calculated incident energy (MeV/nucleon)	Bubble front position (mm)	End of range position (mm)	SRIM calculated end of Range	LET_∞ at bubble front position (keV/µm)
120.18	54	19.5±0.9	22.3±0.9	20.6±0.8	14±20
115.43	59	23.6±0.9	25.9±0.9	24.9±1.0	16±20
110.2	65	27.7±0.9	30.9±0.9	29.2±1.2	14±20
105.44	69	31.8±0.9	35.0±0.9	32.8±1.4	14±20
105.44	69	30.8±0.9	34.5±0.9	32.8±1.4	16±20
105.44	69	30.9±0.9	34.1±0.9	32.8±1.4	14±20
105.44	69	31.4±0.9	34.1±0.9	32.8±1.4	14±20
101.99	73	34.5±0.9	36.8±0.9	35.6±1.5	16±20

The images in Figure 44 show that the end of range appears to shift towards the back of the detector as the binary filter thickness is decreased. This is expected since higher energy ions have a longer range. There is consistently an even distribution of bubbles along the He ion range, an increase in bubbles at the Bragg peak, then another region of fewer bubbles evenly distributed after the end of the He ion range in all experiments. The bubble front appears to shift proportionally such that the bubble front consistently begins roughly 2.5 mm before the end of the range. The LET_{∞} of the He ions at the position of the bubble front is estimated as 15 ± 7 keV/μm averaged over all experiments. This is apparently the threshold LET required for bubble formation by He ions which is consistent (within error) to the minimum calculated LET threshold for space bubble detectors in the literature. However, it is less than the LET threshold reported in the literature for N ions and Ar ions in space bubble detectors (116 ± 40 keV/μm and 231 ± 15 keV/μm, espectively). This suggests that there is a difference in minimum LET threshold for different ions.

Carbon Results:

Thirty individual bubble detector measurements have been recorded at the HIMAC facility with the 400 MeV/nucleon C ion beam. Ten experiments had the bubble detector oriented along the beam with the ions stopping inside the bubble detector. The MATLAB LET analysis was employed for all of the experiments and a bubble front and end of the range similar to the literature and the He ion experiments were observed. The resulting images are shown in Figure 45 with the bubble front and end of the range overlaid on each image. These results appear very similar to the He ion results with a few subtle differences. The carbon experiments seem to have a relatively even distribution of bubbles before and after the Bragg peak suggesting that secondary particles are responsible for many of the bubbles outside of the Bragg peak.

Neutrons formed along the beam line and even in the bubble detector itself could penetrate far beyond the carbon ion range and be responsible for the relatively even distribution of bubbles in the detector. Other high LET secondary radiation may also be creating bubbles. However, it seems likely that in the region of the Bragg peak, the carbon ions themselves are responsible for the large number of bubbles as the particles slow down and stop with a very high LET.

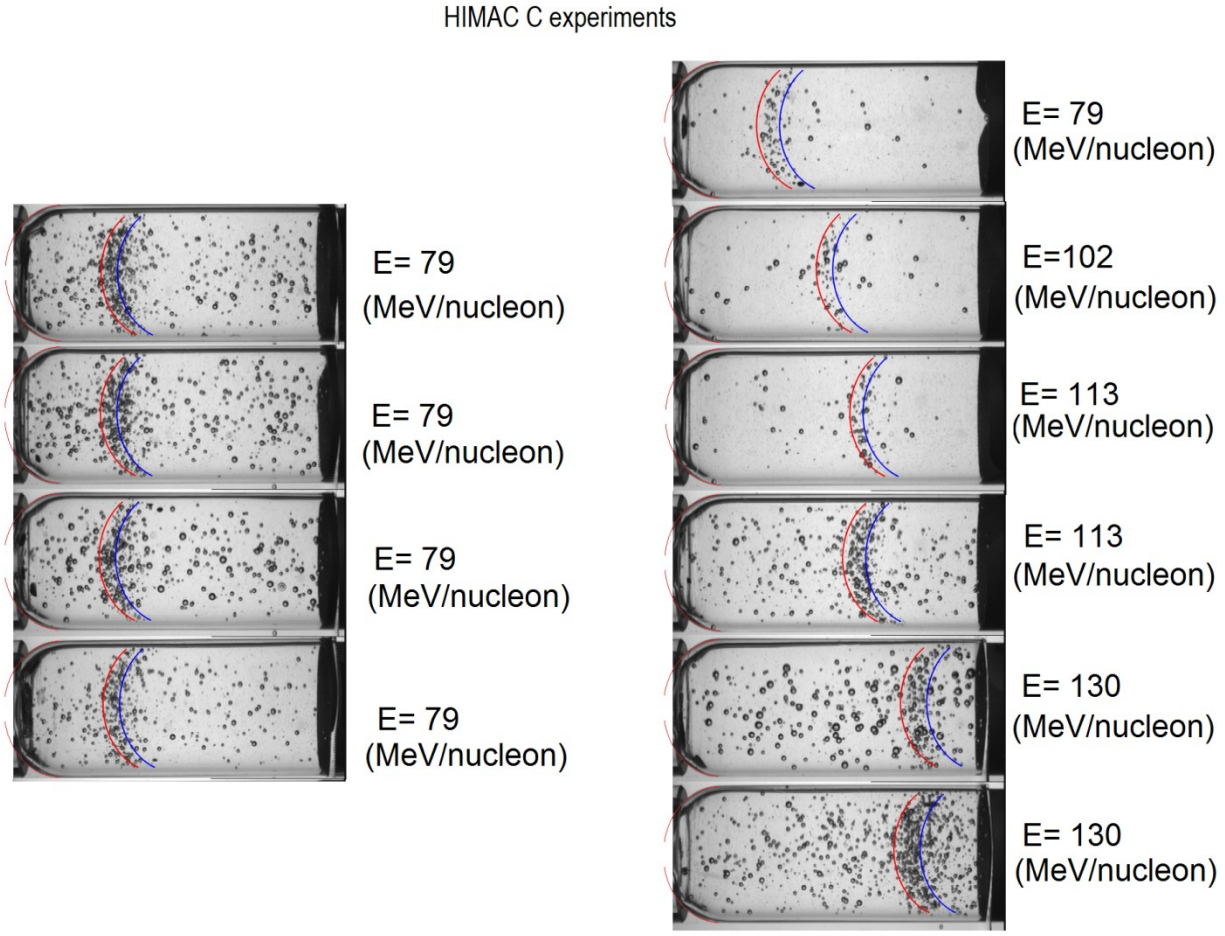

Figure 45: Bubble front and end of the range for 400 MeV/nucleon C experiments at HIMAC. Bubble front is indicated by red curve and end of the range is indicated by blue curve overlaid on each image

The bubble count distribution and LET curve for one individual experiment (BF=230.33 mm) are plotted in Figure 46 and Figure 47. The LET of the carbon ion Bragg peak is higher than the He ions and the LET at the bubble front position is 85 keV/µm.

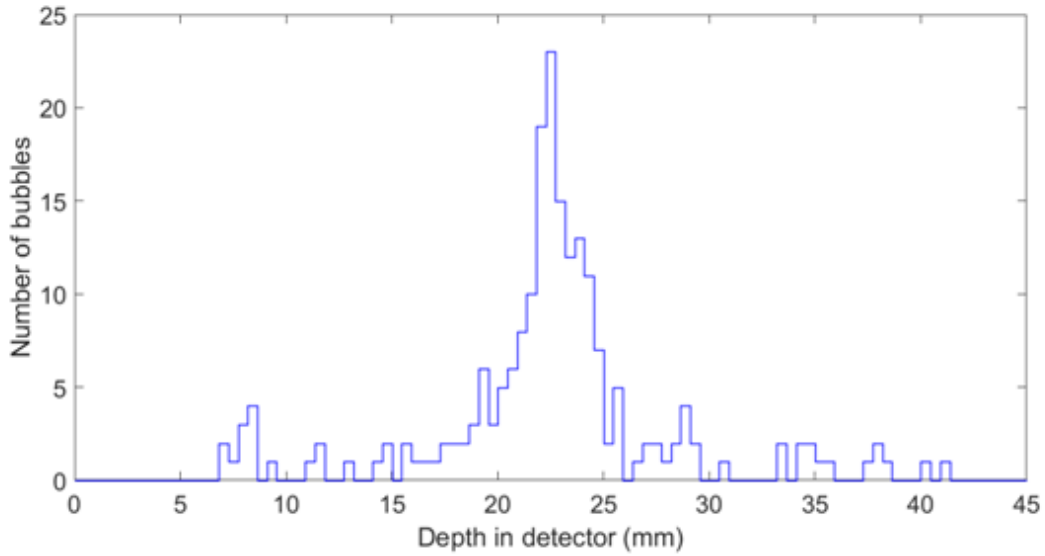

Figure 46: Bubble count using MATLAB program for C measurement at HIMAC

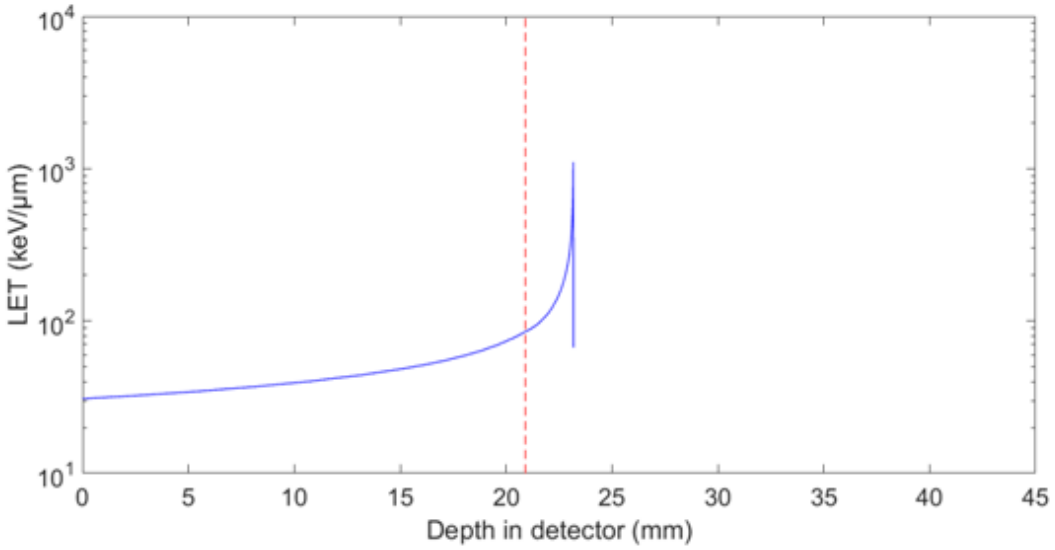

Figure 47: SRIM calculated Bragg curve for C experiment at HIMAC

The bubble counting results from Figure 46 show that the number of bubbles increases significantly at the Bragg peak with a clear and obvious bubble front. The relative fraction of bubbles inside the Bragg peak compared to bubbles outside the Bragg peak is larger for C ions

than it was for He ion experiments (see Figure 42 for comparison). The LET of the C ions at the bubble front position has been estimated for all experiments and is listed in Table 5. The error in the LET estimate is larger than the He experiments due to the much larger increase of LET at the Bragg peak for C ions.

Table 5: LET threshold data for 400 MeV/nucleon C ion experiments at HIMAC

Experiment HIMAC Binary Filter (mm H_2O)	SRIM calculated incident energy (MeV/nucleon)	Bubble front position (mm)	End of range position (mm)	SRIM calculated end of Range	LET_∞ at bubble front position (keVμm)
240.23	79	13.2±0.9	15.5±0.9	15.2±0.6	85±70
240.23	79	13.2±0.9	15.5±0.9	15.2±0.6	85±70
240.23	79	13.2±0.9	15.5±0.9	15.2±0.6	85±70
240.23	79	13.6±0.9	15.9±0.9	15.2±0.6	85±70
240.00	79	12.7±0.9	15.9±0.9	15.1±0.7	74±70
230.33	102	20.9±0.9	23.2±0.9	23.6±1.0	85±70
225.03	113	24.5±0.9	27.3±0.9	28.6±1.1	93±70
225.03	113	24.5±0.9	27.3±0.9	28.6±1.1	74±70
215.61	130	32.7±0.9	36.4±0.9	36.1±1.4	69±70
215.61	130	31.8±0.9	35.5±0.9	36.1±1.4	69±70

The experimental averaged LET_∞ of the carbon ions at the bubble front is 80 ± 20 keV/μm. This value lies between 15 keV/μm measured in the He experiments and 116 keV/μm quoted in the literature for N ion experiments. There appears to be a trend where the LET threshold for bubble formation increases with the charge Z.

Oxygen Results:

A total of eighteen experiments were conducted with 400 MeV/nucleon oxygen ions at the HIMAC facility. Only four experiments were performed with the bubble detectors oriented along the beam axis with the Bragg peak located inside the bubble detector. The distribution of bubbles outside the Bragg peak and the increased high density of bubbles inside the Bragg peak are very similar to the C ion results. The output of the MATLAB LET analysis program with the bubble front and the end of the range estimates overlaid on the images is shown in Figure 48, while the bubble counting output from one individual experiment with a binary filter of 170.42 mm is shown in Figure 49. The LET curve for the same experiment is shown in Figure 50 with the bubble front indicated by a dashed line where the LET is 134.5 keV/μm. Table 6 summarizes the results for all four experiments.

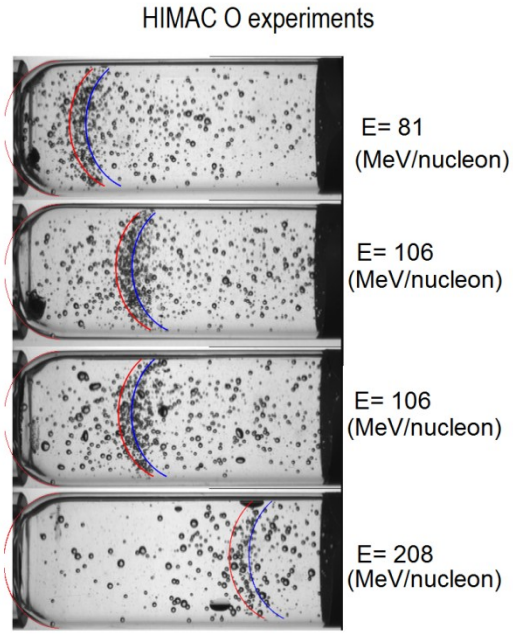

Figure 48: Bubble front and end of the range for 400 MeV/nucleon O experiments at HIMAC. Bubble front is indicated by red curve and end of the range is indicated by blue curve overlaid on each image

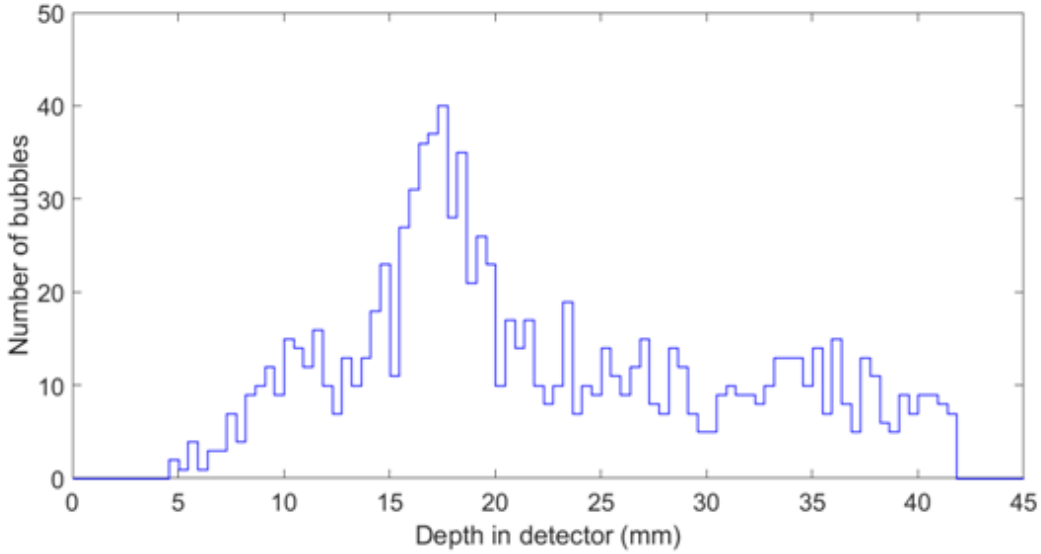

Figure 49: Bubble count using MATLAB program for O measurement at HIMAC

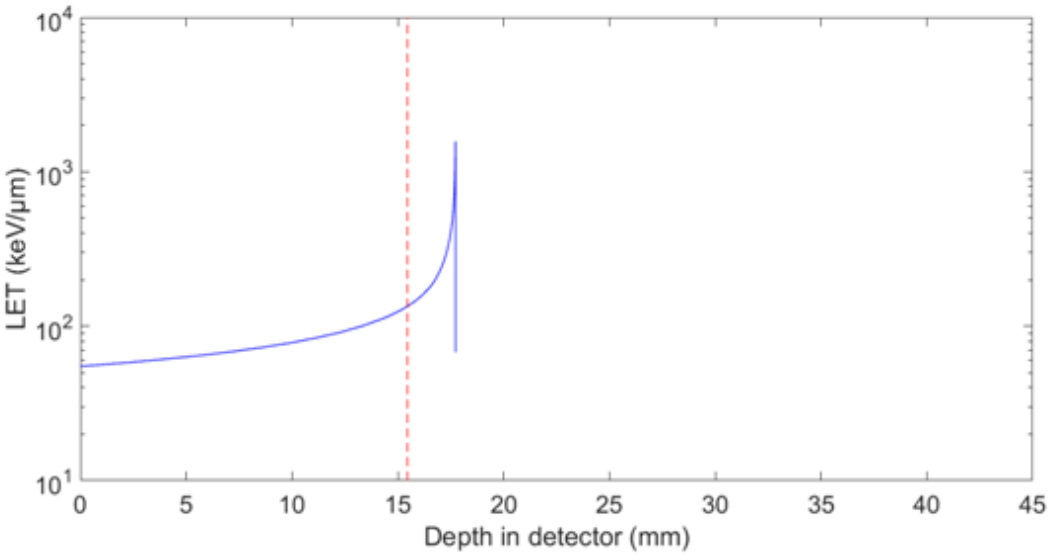

Figure 50: SRIM calculated Bragg curve for O experiment at HIMAC

Table 6: LET threshold data for 400 MeV/nucleon O ion experiments at HIMAC

Experiment HIMAC Binary Filter (mm H_2O)	SRIM calculated incident energy (MeV/nucleon)	Bubble front position (mm)	End of range position (mm)	SRIM calculated end of Range	LET_∞ at bubble front position (keVμm)
179.69	81	9.1±0.9	11.4±0.9	10.2±0.4	140±50
170.42	106	15.5±0.9	17.7±0.9	17.8±0.8	140±50
170.42	106	15.9±0.9	17.7±0.9	17.8±0.8	150±50
150.45	208	31.4±0.9	34.1±0.9	34.6±1.4	120±50

The bubble distribution inFigure 49shows a large jump in bubble density at the position of the Bragg peak. Unlike the C ion experiments, there is a more gentle increase in bubble density from the beginning of the detector until the bubble front. After the end of the O ion range, there is a relatively constant bubble density until the end of the detector. The steady rise in bubble density along the bubble detector, before the bubble front, is apparent when observing the experiment performed with a binary filter of 150.15 mm in Figure 48. This trend may indicate that more high LET secondary radiation is produced along the O ion tracks. The large number of bubbles in the region of the Bragg peak is caused by the O ions. The LET of the ions at the bubble front is estimated as 140 ± 20 keV/μm. The minimum threshold for bubble formation for O ions is comparable to the value quoted in the literature for *N* ions and appears consistent with the trend of increasing LET threshold with the ion charge *Z*.

Neon Results:

Seven experiments were performed with the 400 MeV/nucleon ions at HIMAC with SBD and SBDS. Of those experiments, six data sets have been collected with space bubble detectors oriented parallel to the Ne ion beam with the Bragg peak inside the bubble detector. The results

of the MATLAB LET analysis program are shown in Figure 51 with the bubble count and LET curve for an individual experiment shown in Figure 52 and Figure 53. The resulting data for all experiments are listed in Table 7.

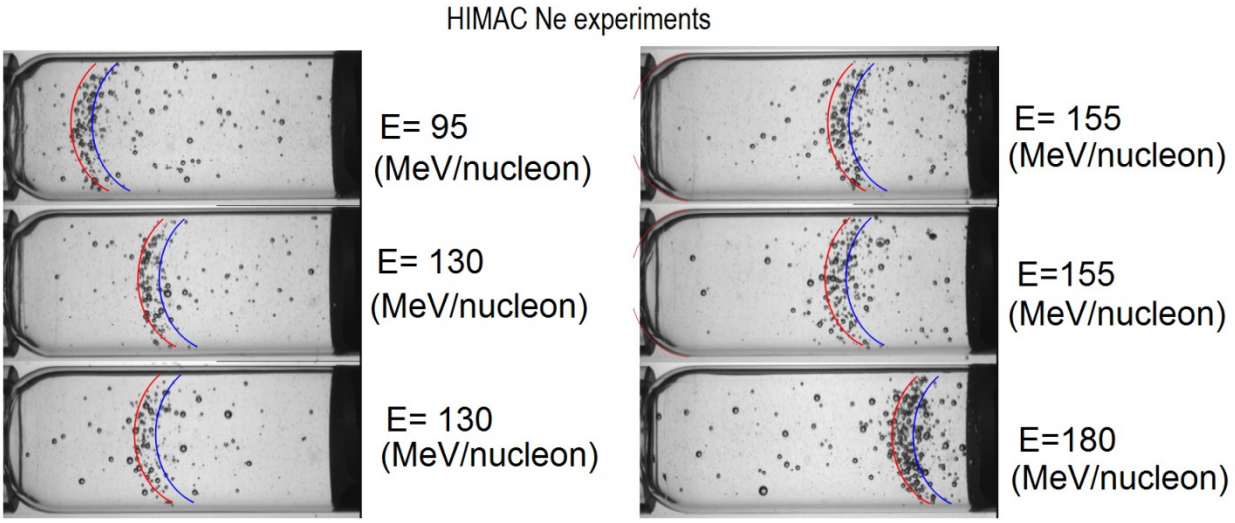

Figure 51: Bubble front and end of the range for 400 MeV/nucleon Ne experiments at HIMAC. Bubble front is indicated by red curve and end of the range is indicated by blue curve overlaid on each image

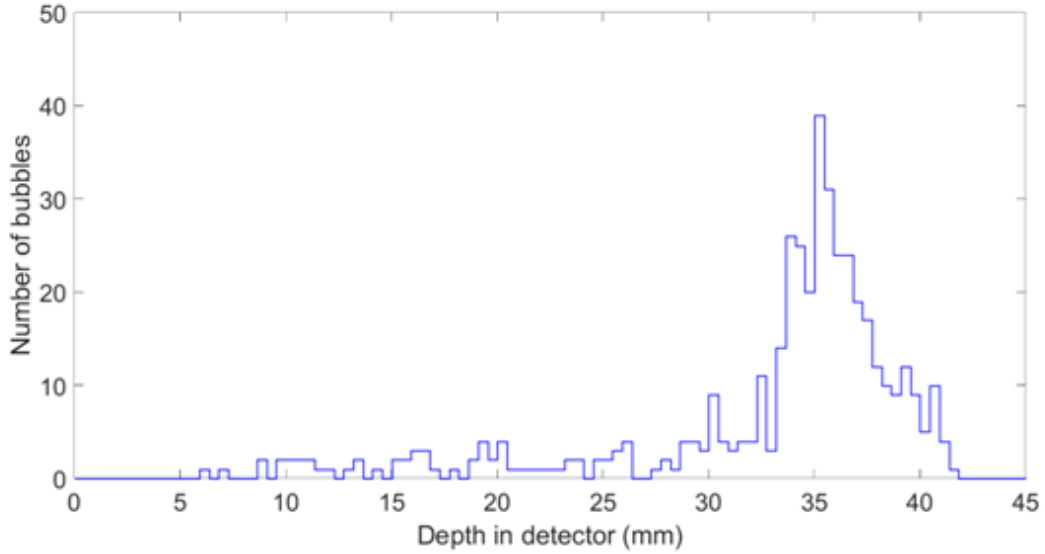

Figure 52: Bubble count using MATLAB program for Ne measurement at HIMAC

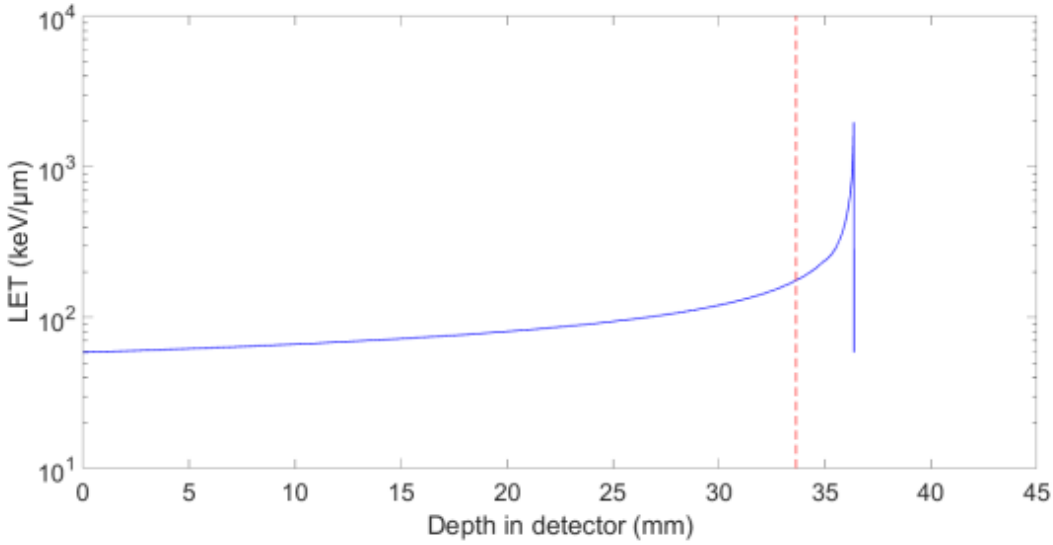

Figure 53: SRIM calculated Bragg curve for Ne experiment at HIMAC

Table 7: LET threshold data for 400 MeV/nucleonNe ion experiments at HIMAC

Experiment HIMAC Binary Filter (mm H_2O)	SRIM calculated incident energy (MeV/nucleon)	Bubble front position (mm)	End of range position (mm)	SRIM calculated end of Range	LET_∞ at bubble front position (keVμm)
130.44	95	10.0±0.9	12.7±0.9	11.6±0.4	177±50
120.18	130	16.8±0.9	19.5±0.9	20.0±0.8	177±50
120.18	130	17.3±0.9	20.0±0.9	20.0±0.8	177±50
110.20	155	25.0±0.9	27.7±0.9	28.1±1.1	177±50
110.20	155	25.5±0.9	28.2±0.9	28.1±1.1	177±50
100.42	180	33.6±0.9	36.4±0.9	36.2±1.4	177±50

The Ne ions appear to have fewer bubbles before the Bragg peak compared to the oxygen experiments and the bubble front is slightly easier to resolve. The average LET of the Ne ions at the bubble front position from all experiments is 180 ± 20 keV/μm.

Silicon Results:

Twenty-nine experiments were performed with space bubble detectors at HIMAC with 440 MeV/nucleon Silicon beam. Ten representative experiments where the detectors were oriented parallel to the ion beam with the Bragg peak inside the detector are shown in Figure 54 along with the bubble front and end of the range identified by the MATLAB LET analysis program.

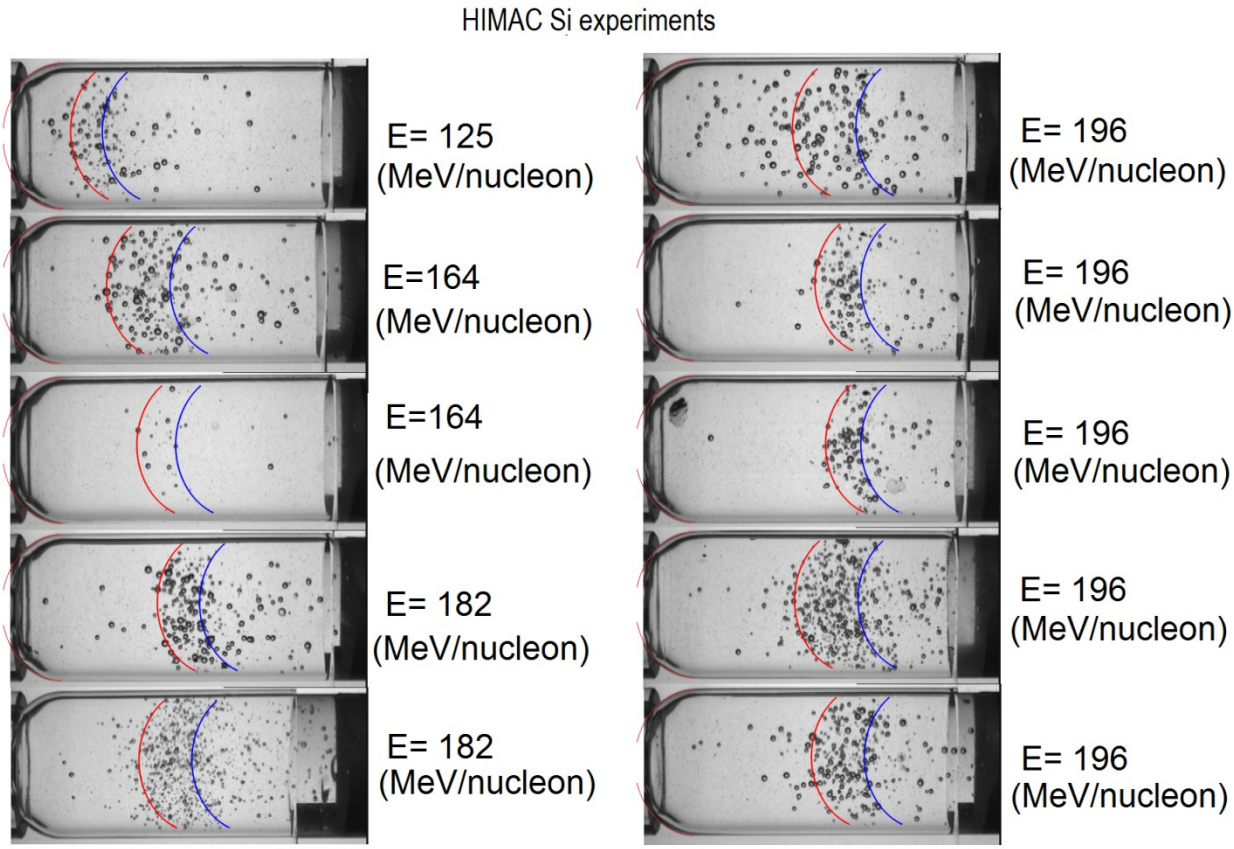

Figure 54: Bubble front and end of the range for 440 MeV/nucleon Si experiments at HIMAC. Bubble front is indicated by red curve and end of the range is indicated by blue curve overlaid on each image

The distribution of bubbles in Figure 54 shows few bubbles outside the Bragg peak and a significant increase at the bubble front position similar to all other ions studied. However, the results with Si display some notable differences. First, there are very few bubbles along the Si ion tracks before the bubble front in all cases. In many cases, there is a complete lack of bubbles or fewer than 10 bubbles along the Si ion tracks for more than 1 cm despite the fact that the Si ions enter the detector with an LET_{∞} around 100 keV/μm. This suggests that very few bubbles are produced by secondary particles. The distance from the bubble front to the end of the particle range is also visibly larger than all experiments with other ions. The large number of bubbles in the region of the Bragg peak is produced directly by the Si ions (electromagnetic interaction).

However, the region of the bubble detector beyond the Si ion range shows a relatively constant density of bubbles that is much higher than the region before the bubble front and is from secondary particles such as scattered neutrons. The bubble count data for a single experiment with a binary filter of 100.42 mm is shown in Figure 55 and the LET curve with the bubble front indicated by a dashed line is shown in Figure 56. A summary of all experiments is shown in Table 8.

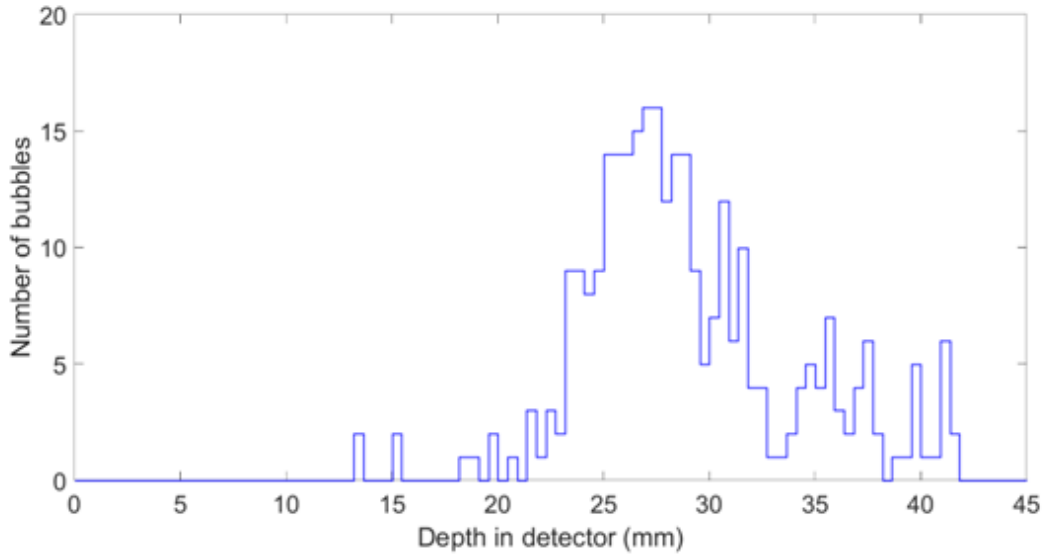

Figure 55: Bubble count using MATLAB program for Si measurement at HIMAC

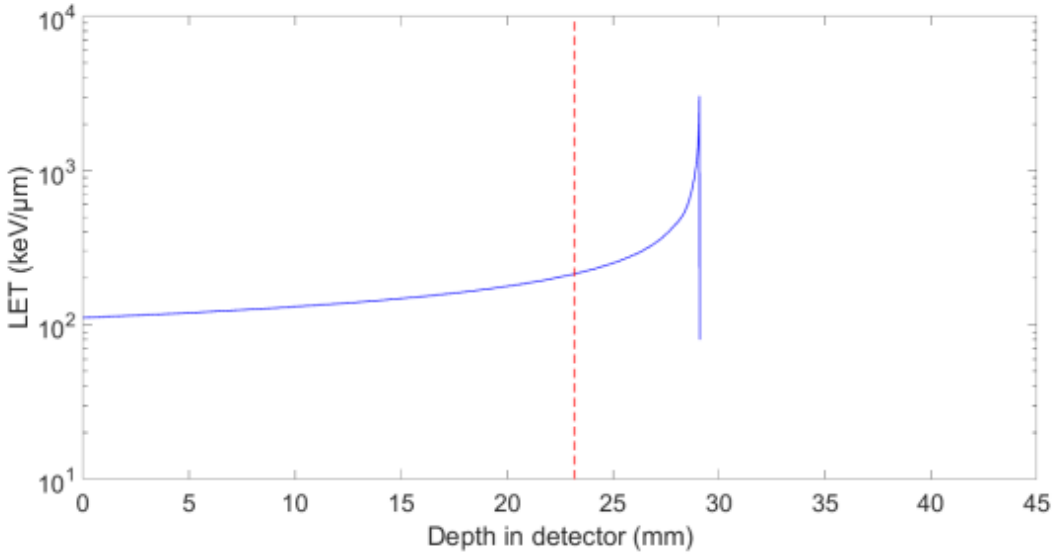

Figure 56: SRIM calculated Bragg curve for Si experiment at HIMAC

Table 8: LET threshold data for 440 MeV/nucleon Si ion experiments at HIMAC

Experiment HIMAC Binary Filter (mm H_2O)	SRIM calculated incident energy (MeV/nucleon)	Bubble front position (mm)	End of range position (mm)	SRIM calculated end of Range	LET_∞ at bubble front position (keVµm)
120.18	125	8.6±0.9	12.7±0.9	13.5±0.5	251±80
110.20	164	17.2±0.9	22.3±0.9	21.7±0.8	230±80
110.20	164	13.6±0.9	21.8±0.9	21.7±0.8	186±80
105.44	182	20.0±0.9	25.5±0.9	25.6±1.0	221±80
105.44	182	17.7±0.9	24.5±0.9	25.6±1.0	201±80
100.42	196	20.5±0.9	28.6±0.9	29.8±1.2	185±80
100.42	196	23.2±0.9	29.1±0.9	29.8±1.2	214±80
100.42	196	24.5±0.9	29.1±0.9	29.8±1.2	240±80
100.42	196	20.5±0.9	28.6±0.9	29.8±1.2	185±80
100.42	196	22.7±0.9	29.5±0.9	29.8±1.2	201±80

The average LET of the ions at the bubble front position for Si ions is 210 ± 30 keV/μm. Experiments with Si ions showed slightly more variation in the appearance and width of the bubbles in the Bragg peak region. For example, all five experiments on the right-hand side of Figure 54 were conducted with a binary filter of 100.42 mm. The end of the range is found to be almost the same for all five experiments, but the bubble front position varies from 20.5 mm to 24.5 mm. However, the mean of the data shows that the LET threshold for bubble formation is fairly consistent and that the Si ion beam only begins to produce a large number of bubbles beyond the bubble front position.

Iron Results:

Twenty-nine individual measurements with space bubble detectors have been carried out at HIMAC with the 490 MeV/nucleon Fe beam. Unlike measurements with all other heavy ions, there was no bubble front visible for any of the experiments with the bubble detector oriented parallel to the beam, whether or not the Bragg peak resided inside the detector. This can be seen in Figure 57 for a selected sample of six measurements with various binary filters. The MATLAB LET analysis program was unable to find a bubble front in any experiment but was able to identify an end of the range for experiments where the end of the range lies inside the bubble detector.

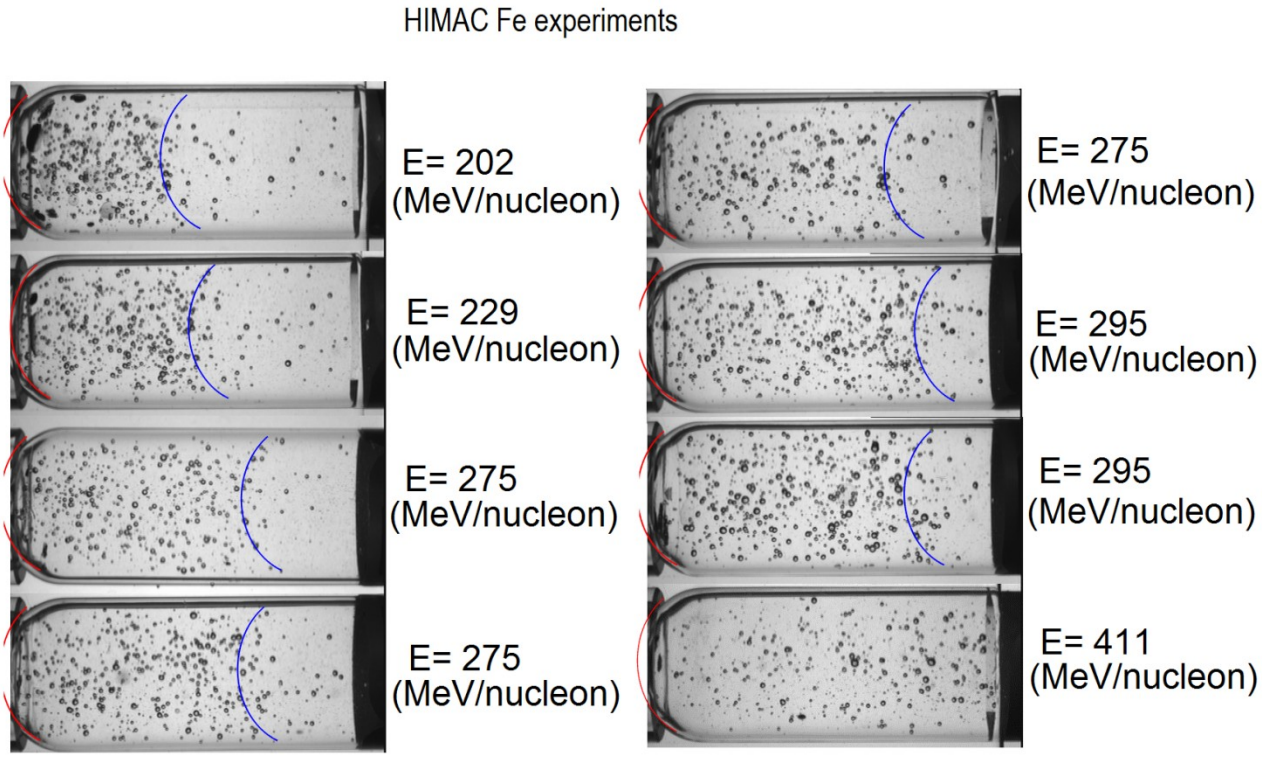

Figure 57: Fe experiments at HIMAC. Bubble front not present and end of range is indicated by blue curve overlaid on each image

The Fe ion experiments all display a relatively constant density of bubbles along the entirety of the ion track, followed by a large drop in bubble density at the end of the ion range. There are an appreciable number of bubbles beyond the end of range that appear to have a relatively constant density suggesting that secondary radiation is responsible for these bubbles. The bubble count data and LET curve for one individual experiment with a binary filter of 50.44 mm is shown in Figure 58 and Figure 59.

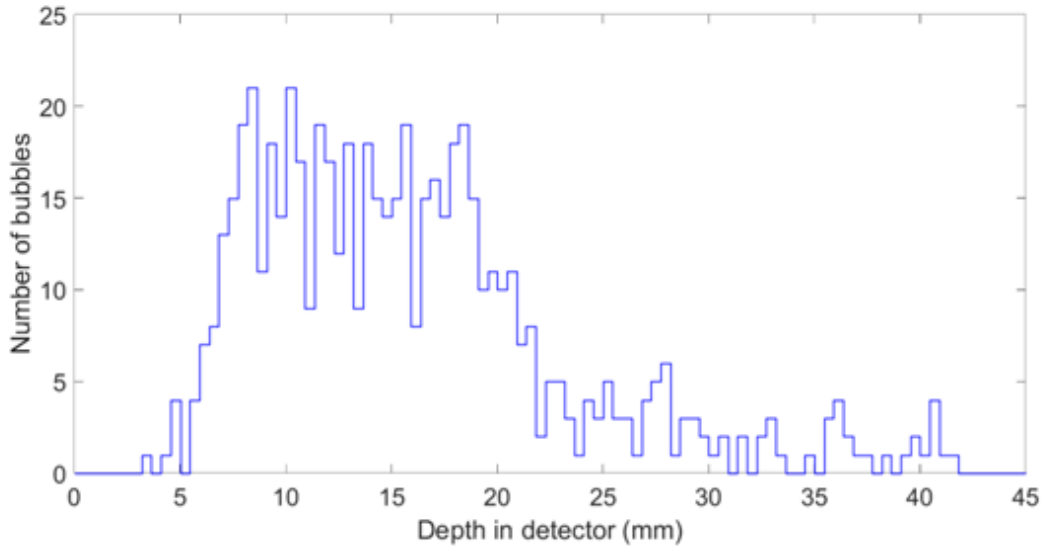

Figure 58 Bubble count using MATLAB program for Si measurement at HIMAC

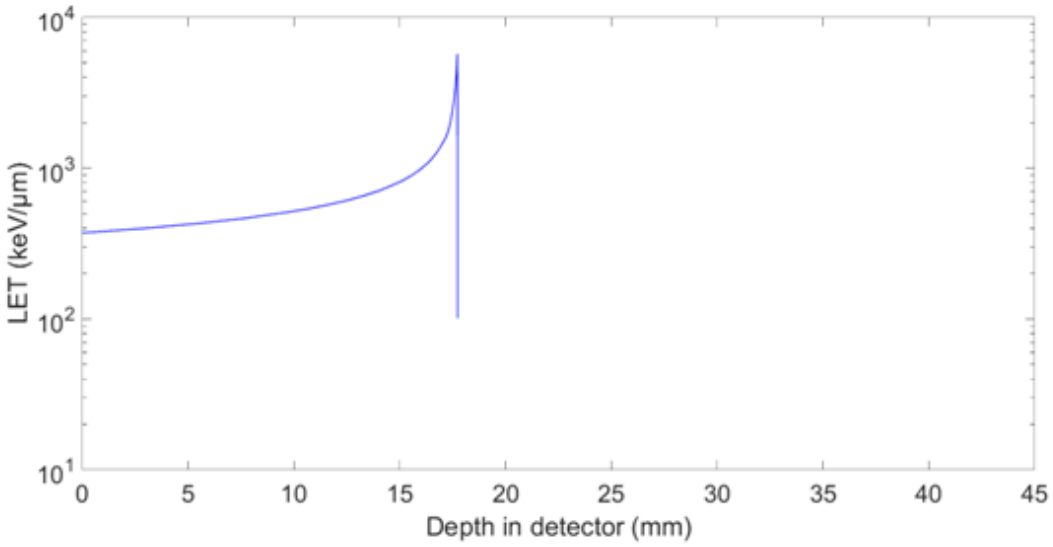

Figure 59: SRIM calculated Bragg curve for Fe experiment at HIMAC

The constant bubble density along the Fe ion tracks may be explained by the same three cases proposed for the proton experiments.

For Fe ions, case 2 (ions do not have sufficient LET to form bubbles) is not correct since they have a much higher LET than the other heavy ions measured at HIMAC which all clearly were able to directly produce bubbles. Case 3 is possible (bubble density increases after LET threshold) although there is no clear evidence in any of the bubble count data to clearly support any increase in bubbles at a bubble front. Case 1 (ion always sufficient LET to cause bubbles) appears to be the correct explanation for Fe and it is reinforced by the LET curve shown in Figure 59 where the LET of the Fe ions entering the bubble detector is over 300 keV/μm and increases to over 5,000 keV/μm. A summary of the experiments from Figure 57 is presented in Table 9.

Table 9: LET threshold data for 500 MeV/nucleon Fe ion experiments at HIMAC

Experiment HIMAC Binary Filter (mm H_2O)	SRIM calculated incident energy (MeV/nucleon)	End of range position (mm)	SRIM calculated end of Range	LET_∞ entering bubble detector (keVμm)
50.44	202	20.5±0.9	18.6±0.8	353±10
45.3	229	22.7±0.9	22.8±0.9	339±10
35.44	275	30.5±0.9	31.1±1.1	307±10
35.44	275	30.5±0.9	31.1±1.1	306±10
35.44	275	30.1±0.9	31.1±1.1	304±10
30.68	295	34.1±0.9	34.9±1.3	294±10
30.68	295	33.6±0.9	34.9±1.3	296±10
0.0	411	NA	59.8±2.3	242±10

For all experiments with no binary filter present (BF= 0.0 mm), there were bubbles present from the beginning of the Fe ion tracks. The lack of a bubble front makes it impossible to calculate an exact minimum LET threshold for bubble formation by Fe ions. The lowest LET was 240± 10 keV/μm so it is reasonable to suppose the LET threshold for Fe ions is ~ 240 keV/μm. According to the trend observed from all other ions, the minimum LET threshold increases with increasing charge so it is likely the LET threshold for Fe ions is above 210 ± 30 keV/μm measured for Si ions and 231 keV/μm reported in the literature for Ar ions. Observations with SBDS in the following section indicate that there is a minimum LET threshold for bubble formation in space bubble detectors for Fe ions at 240 ± 60 keV/μm. This would mean that a bubble front would only be apparent for Fe ions above this LET which was not measured in any HIMAC experiments. Also, the range of Fe ions with LET above the minimum threshold would be almost 60 mm (much larger than the bubble detector length of 45 mm). This would explain the relatively constant density of bubbles seen in all experiments and suggest the Fe ions are indeed similar to all other heavy ion experiments except the distance from the bubble front to the end of the range is larger than the length of the bubble detector. This explanation shall be clarified in the following section with the results of the SBDS experiments.

4.2 Experimental Study of the Space Bubble Detector Spectrometer Response

Experiments have been carried out with SBDS sets at HIMAC with 150 MeV/nucleon He, 400 MeV/nucleon C, 400 MeV/nucleon Ne, 440 MeV/nucleon Si and 500 MeV/nucleon Fe heavy ion beams. In all experiments, all six detectors in the set were irradiated simultaneously with the detectors oriented parallel to the beam. The detector set was placedat the centre of the beam so that all detectors would receive the same fluence. PMMA binary filters were used to

slow down the beams as with the SBD measurements. In all cases where the Bragg peak was inside the bubble detector, there was an observable bubble front and an increase in bubble density at the Bragg peak in some of the detectors of the set. The MATLAB LET analysis program was used to identify the LET of the ions at the position of the bubble front and identify any differences in the LET required for bubble formation between the six detectors.

4.2.1 He Results with SBDS

Six experiments were performed with SBDS sets with 150 MeV/nucleon He ion beam at HIMAC. Of those experiments, two individual experiments are shown in Figure 60 with the identified bubble front and end of range overlaid on the image. The images collected by the BDR III reader for each detector in the SBDS set are identical to the space bubble detector images so the MATLAB LET analysis program could be employed without modification. Additionally, the He ions in each experiment should have the same range in all six detectors (they are physically similar in terms of construction material and density). Thus, the range could be determined using all six detectors simultaneously giving better statistical accuracy.

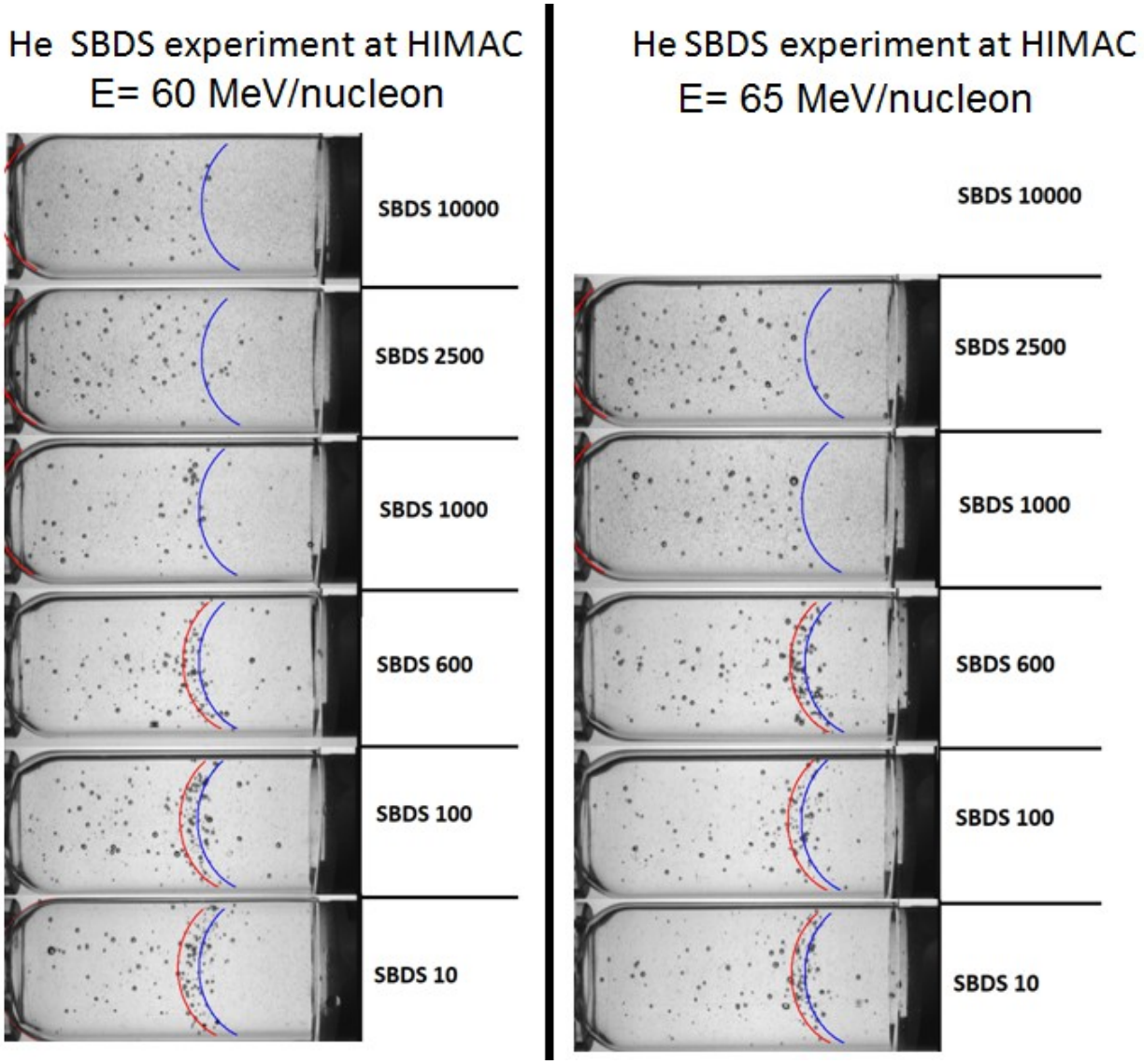

Figure 60: Bubble front and end of the range for 150 MeV/nucleon He experiments at HIMAC with SBDS. Bubble front is indicated by red curve and end of the range is indicated by blue curve overlaid on each image

There is no image available for the SBDS 10000 detector in the experiment with a binary filter of 110.2 mm because this detector was malfunctioning (a large number of bubbles was present and could not be eliminated *via* compression). The results appear similar to the space bubble detector measurements for SBDS 10, SBDS 100 and SBDS 600 where an obvious bubble front is present and an increase in bubble density near the Bragg peak. SBDS 1000, SBDS 2500

and SBDS 10000 show no increase in bubble density near the Bragg peak, although all detectors exhibit a drastic decrease in bubble density after the end of the He ion range.

Table 10 LET threshold for bubble formation with He ions in SBDS

Binary Filter	LET at bubble front SBDS 10 (keV/μm)	LET at bubble front SBDS 100(keV/μm)	LET at bubble front SBDS 600(keV/μm)	LET at bubble front SBDS 1000 (keV/μm)	LET at bubble front SBDS 2500 (keV/μm)	LET at bubble front SBDS 10000 (keV/μm)
BF=115.42	14±19	15±19	16±19	NA	NA	NA
BF=110.2	14±19	16±19	19±19	NA	NA	NA
Mean:	15±13	16.0±13	18±13	NA	NA	NA

The data suggest that He ions are incapable of directly causing bubbles in the SBDS 1000, SBDS 2500 and SBDS 10000 detectors where the bubbles observed are likely from high LET secondary radiation. There appears to be a slight increase in the LET at the bubble front position from SBDS 10, SBDS 100 to SBDS 600 but it is difficult to conclude such a trend within the large errors.

4.2.2 C Results with SBDS

Four experiments were performed with SBDS sets with 400 MeV/nucleon C ion beam at HIMAC. Of those experiments, two individual experiments are shown in Figure 61. Unlike the He ion experiments, a clear bubble front and end of the rangewere identified for all six bubble detectors in both experiments. The bubble distributions in all six detectors look somewhat similar except there are far fewer bubbles outside of the Bragg peak for the SBDS 10000 measurements. Also, the distance from the bubble front to the end of range seems to increase as the SBDS

neutron threshold (*i.e.* 10000, 2500, 1000, 600, 100, 10) decreases. The results are summarized in Table 11.

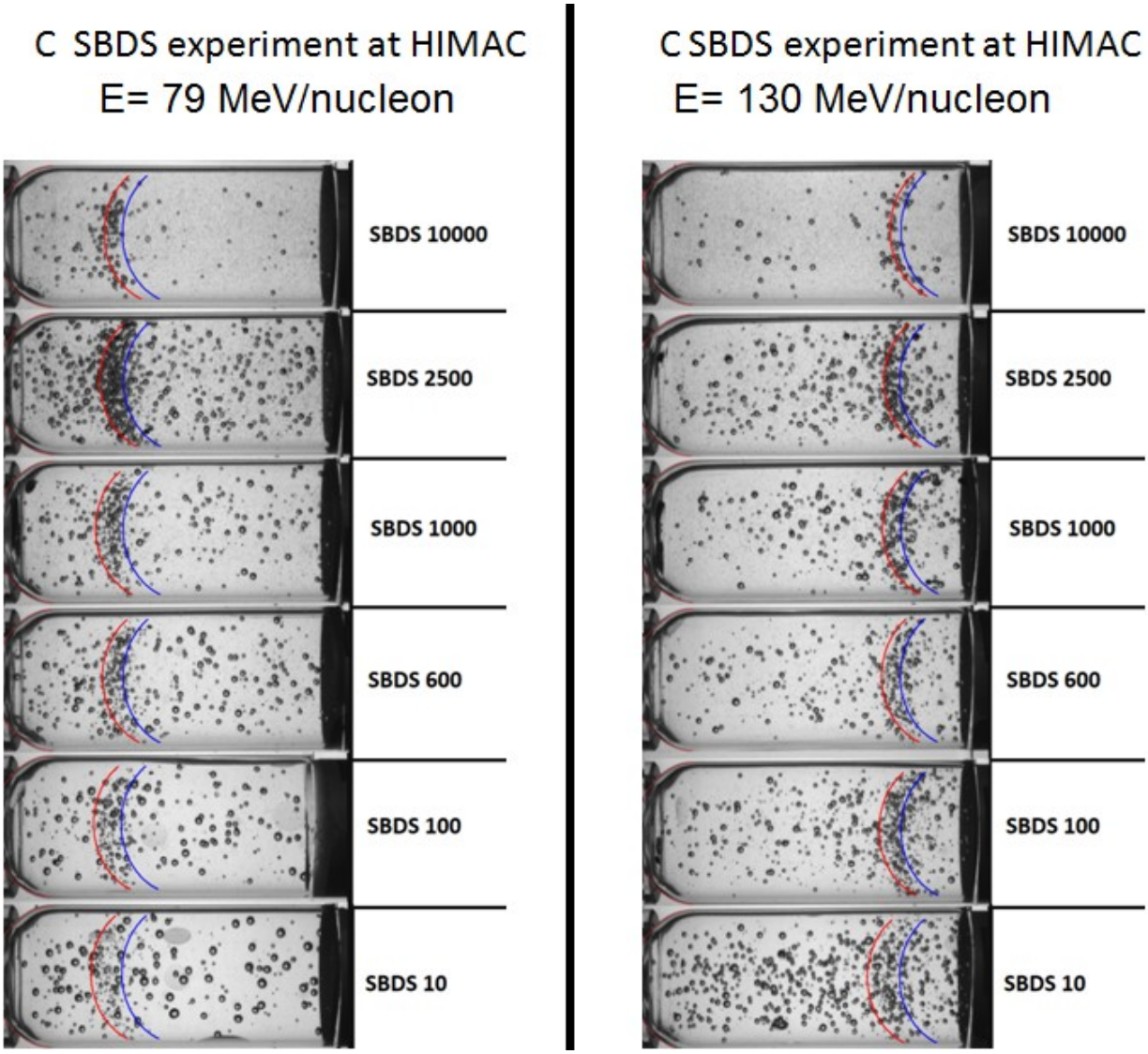

Figure 61: Bubble front and end of the range for 400 MeV/nucleon C experiments at HIMAC with SBDS. Bubble front is indicated by red curve and end of the range is indicated by blue curve overlaid on each image

Table 11: Threshold for bubble formation with C ions in SBDS

Binary Filter	LET at bubble front SBDS 10 (keV/µm)	LET at bubble front SBDS 100 (keV/µm)	LET at bubble front SBDS 600 (keV/µm)	LET at bubble front SBDS 1000 (keV/µm)	LET at bubble front SBDS 2500 (keV/µm)	LET at bubble front SBDS 10000 (keV/µm)
BF=240.23	65±39	69±36	80±100	80±110	73±31	80±100
BF=215.61	64±28	76±51	82±46	82±46	88±17	100 ±30
Mean:	65±24	73±31	80±56	77±59	81±18	90±53

The LET threshold for bubble formation by C ions is larger for detectors with a larger neutron energy threshold as observed in the He ion data. There is a larger increase from BDS 10 to BDS 10000, but the large uncertainty makes it difficult to see a steady increase across the SBDS set.

4.2.3 Ne Results with SBDS

Five experiments were performed with SBDS set with 400 MeV/nucleon Ne ion beam at HIMAC. Two individual experiments are shown in Figure 62. A clear bubble front and end of the rangewas identified for all five bubble detectors in both experiments. SBDS 10 data is missing due to a detector malfunction. The results of the MALTAB LET analysis program for all detectors are summarized in Table 12.

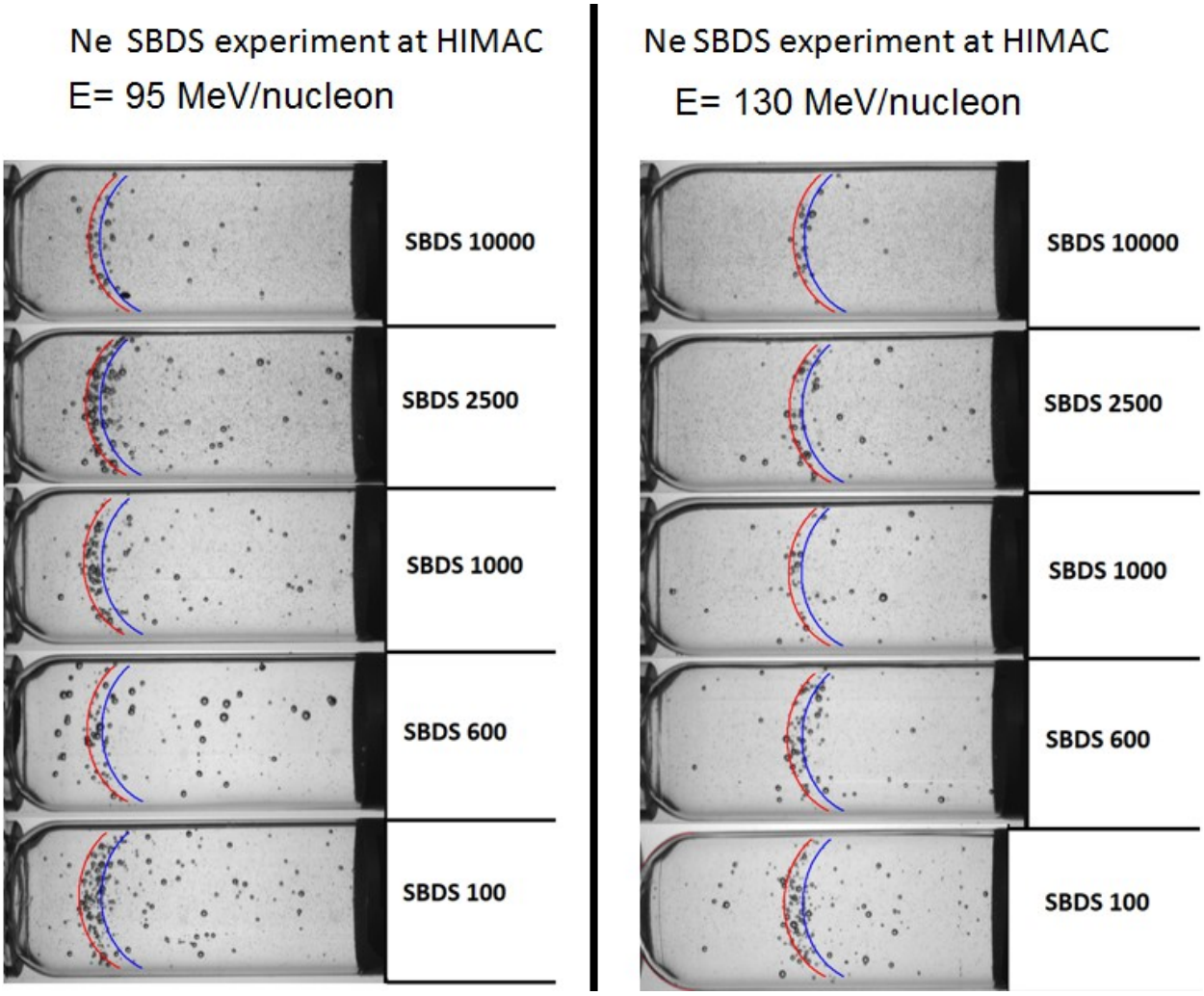

Figure 62: Bubble front and end of the range for 400 MeV/nucleon Ne experiments at HIMAC with SBDS. Bubble front is indicated by red curve and end of the range is indicated by blue curve overlaid on each image

Table 12: threshold for bubble formation with Ne ions in SBDS

Binary Filter	LET at bubble front SBDS 10 (keV/µm)	LET at bubble front SBDS 100 (keV/µm)	LET at bubble front SBDS 600 (keV/µm)	LET at bubble front SBDS 1000 (keV/µm)	LET at bubble front SBDS 2500 (keV/µm)	LET at bubble front SBDS 10000 (keV/µm)
BF=130.44	NA	210±70	190±60	210±200	210±190	240±160
BF=120.18	NA	190±60	210±70	230±200	239±50	240±160
Mean:	NA	200±40	200±40	220±100	220±100	240±110

4.2.4 Si Results with SBDS

Nine experiments were performed with SBDS sets with 440 MeV/nucleon Si ion beam at HIMAC. ,Three individual experiments are shown in Figure 63. A clear bubble front and end of the rangewere identified for all bubble detectors in all experiments except the SBDS 10000 detectors in several experiments where there was an insufficient number of bubbles to establish a statistically significant bubble front and end of the range position. The results of the MALTAB LET analysis program for all detectors are summarized in Table 13.

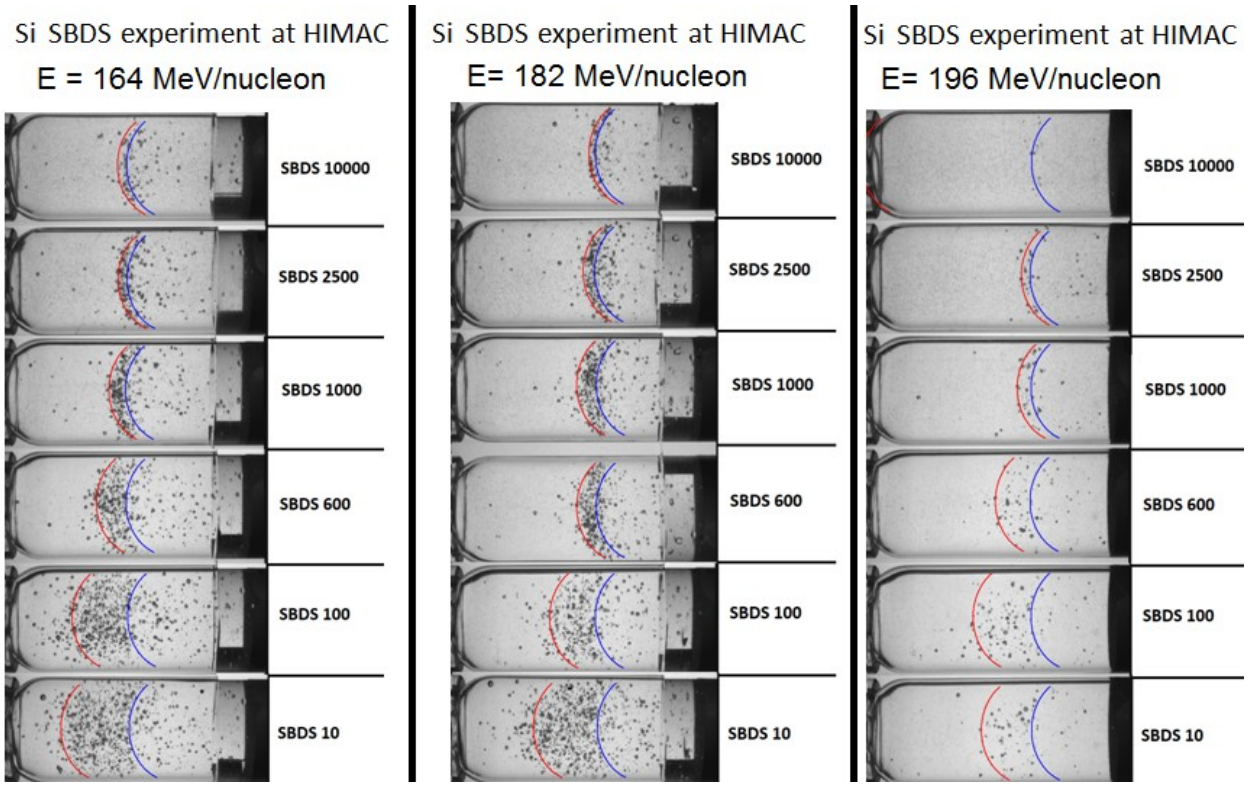

Figure 63: Bubble front and end of the range for 440 MeV/nucleon Si experiments at HIMAC with SBDS. Bubble front is indicated by red curve and end of the range is indicated by blue curve overlaid on each image

Table 13: threshold for bubble formation with Si ions in SBDS

Binary Filter	LET at bubble front SBDS 10 (keV/µm)	LET at bubble front SBDS 100 (keV/µm)	LET at bubble front SBDS 600 (keV/µm)	LET at bubble front SBDS 1000 (keV/µm)	LET at bubble front SBDS 2500 (keV/µm)	LET at bubble front SBDS 10000 (keV/µm)
BF=110.2	160±10	170±30	230±40	290±40	390±60	490±70
BF=105.44	170±20	190±10	220±50	270±40	345±110	460±100
BF=100.42	180±30	170±30	210±50	320±80	395±180	NA
Mean:	170±10	180±20	220±30	290±30	380±70	470±60

The Si experiments show an obvious difference in the bubble distribution between the SBDS 10, SBDS 100, SBDS 600, SBDS 1000 and SBDS 10000 as seen in Figure 63 where the bubble front is clearly different for each detector in the set. Table 13 indicates that the LET of the silicon ions at the bubble front increases with increasing energy threshold for the six bubble detectors (10, 100, 600, 1000, 2500, 10000). The trend is evident where the SBDS 10 detectors have the lowest LET and the SBDS 10000 detectors have the largest LET. There is clearly a connection between the neutron energy threshold and the minimum LET threshold required for bubble formation. This indicates the same trend noted in the He, C and Ne ion experiments where the larger uncertainty and noisier data made it difficult to conclude such an increasing trend.

4.2.5 Fe Results with SBDS

Five experiments were performed with SBDS sets with 500 MeV/nucleon Fe ion beam at HIMAC. Three individual experiments are shown in Figure 64. The distribution of bubbles in the

Fe SBDS experiments appears similar to the Si experiments with a distinct difference in the six detectors in the set. The results of the MALTAB LET analysis program for all detectors are summarized in Table 14.

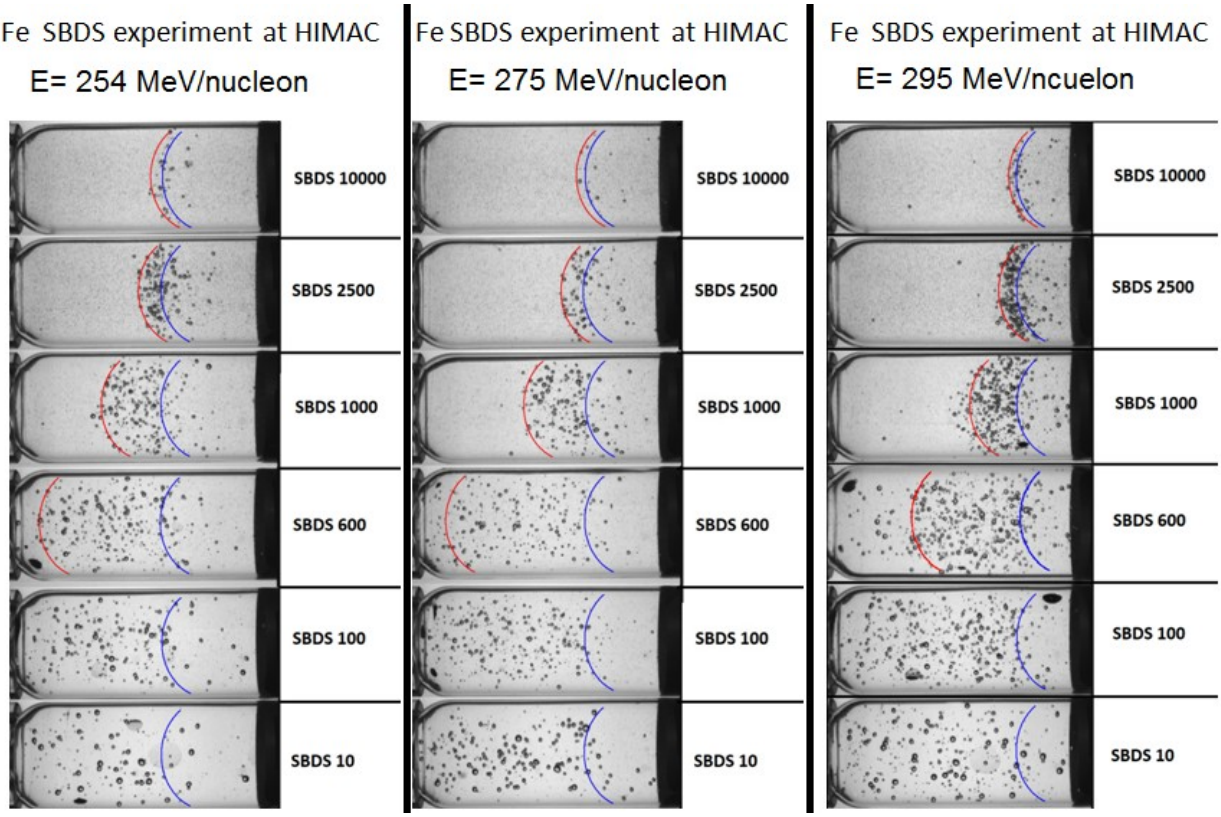

Figure 64: Bubble front and end of the range for 500 MeV/nucleon Fe experiments at HIMAC with SBDS. Bubble front is indicated by red curve and end of the range is indicated by blue curve overlaid on each image

Table 14: Threshold for bubble formation with Fe ions in SBDS

Binary Filter (mm)	LET at bubble front SBDS 10 (keV/μm)	LET at bubble front SBDS 100 (keV/μm)	LET at bubble front SBDS 600 (keV/μm)	LET at bubble front SBDS 1000 (keV/μm)	LET at bubble front SBDS 2500 (keV/μm)	LET at bubble front SBDS 10000 (keV/μm)
BF=40.03	NA	NA	370±40	480±40	750±110	1160±260
BF=35.44	NA	NA	340±40	460±40	700±90	930±280
BF=30.68	NA	NA	320±30	460±50	700±90	1050±250
Mean:	NA	NA	340±20	470±30	720±60	1020±150

There is a clear end of the range and bubble front in all SBDS 10000, SBDS 2500 and SBDS 1000 measurements. SBDS 600 measurements show a clear end of the range and a bubble front has been identified in each image, although it is not clearly visible because many bubbles appear before the bubble front. Experiments with binary filters 40.03 mm and 35.33 mm show very subtle bubble fronts for SBDS 600's. The measurement with binary filter 30.68 mm displays a much more distinct bubble front in the SBDS 600 detector, yet there are still many bubbles before the bubble front unlike the SBDS 10000, SBDS 25000 and SBDS 1000 results. The bubble distribution for the SBDS 100 and SBDS 10 appear very similar to the space bubble detector results with a constant density along the Fe ion tracks and a sudden drop in density beyond the Fe ion range. According to the manufacturer, the SBDS 100 is very similar to the space bubble detector and this is consistent with previous experiments. Observing Figure 64 and inspecting the bubble detectors in the set from top to bottom, the bubble front appears to shift to the left with increasing neutron energy threshold. This verifies that the constant density of bubbles formed in the space bubble detector measurements are indeed from Fe ion tracks where the LET of the ions is sufficient to cause bubbles as the beam enters the detector. Evidently, the

range of Fe ions with LET above the minimum threshold to create bubbles is large compared to the entire bubble detector length. Although the bubble front is not present in the SBDS 100 and SBDS 10 detector images, one could imagine that the bubble front would be present for a longer detector where the energy of the incident Fe ions to the left was much larger (and consequently the LET smaller). Analysis using an ion track structure model in the following section suggests that the minimum LET threshold for bubble formation in SBDS 10 and SBDS 100 is about 190 keV/μm and 240 keV/μm respectively for Fe ions. The ranges of these Fe ions at the minimum threshold LET are about 60 mm and 140 mm respectively which is consistent with the results where the bubble front and end of the range never appear in the 45 mm bubble detector at the same time.

4.3 Ion Track Structure Model of Visible Bubble Formation

The results in the previous sections show that there is some minimum threshold LET for bubble detectors and only ions above that minimum threshold can produce bubbles. This property is indicated by a bubble front in the heavy ion irradiation experiments where the LET increases above the minimum LET threshold as the ions slow down. The data suggest that this is true for the space bubble detector and all six detectors in the SBDS set where the minimum LET threshold is different for each of the SBDS detectors.

4.3.1 Z-Dependence of LET Threshold

The average LET of all heavy ions at the position of the bubble front for all HIMAC experiments is summarized in Table 15 for space bubble detector and SBDS. The experimental

data indicate that the minimum LET threshold for bubble formation is different for different ions, which is consistent with the literature.

Table 15: LET threshold for bubble formation from all HIMAC experiments with SBD and SBDS

Detector type	He LET threshold (keV/µm)	C LET threshold (keV/µm)	O LET threshold (keV/µm)	Ne LET threshold (keV/µm)	Si LET threshold (keV/µm)	Fe LET threshold (keV/µm)
SBD	15± 6	80 ± 30	140 ± 20	180 ± 20	210 ± 30	240 ± 60
SBDS 10	20±10	70±20		NA	170±10	NA
SBDS 100	20±10	70±30		200±40	180±20	NA
SBDS 600	20±10	80±60		200±40	220±30	340±20
SBDS 1000	NA	80±60		220±100	290±30	470±30
SBDS 2500	NA	80±20		220±100	380±70	720±60
SBDS 10000	NA	90±50		240±110	470±60	1000±200

The LET threshold seems to increase proportionally to the ion charge, Z, for space bubble detectors and all SBDS detectors. The LET of the ions at the bubble front is expected to represent the minimum threshold for bubble formation with each ion. However, the data suggests that there is a Z dependence for the minimum LET threshold in the SBDS detectors and the space bubble detectors. This may be explained by the differences in ion track structure. The LET threshold results for space bubble detectors from Table 15 are plotted inFigure 65. Data for N and Ar ion experiments with space bubble detectors have been included from the literature and these values are consistent with the trend of the current results[55]. Results published by Andrews *et al.* with different bubble detectors have also been included for comparison[62]. In these experiments, the reduced superheat of the bubble detectors was altered and the LET of the ions at the bubble front position was calculated using SRIM. The two data points included in

Figure 65 have been interpolated from the published results for a reduced superheat of 0.33 which is the published value calculated for space bubble detectors. The LET thresholds for these bubble detectors also appear to increase with Z and are consistent with the trend of the current results.

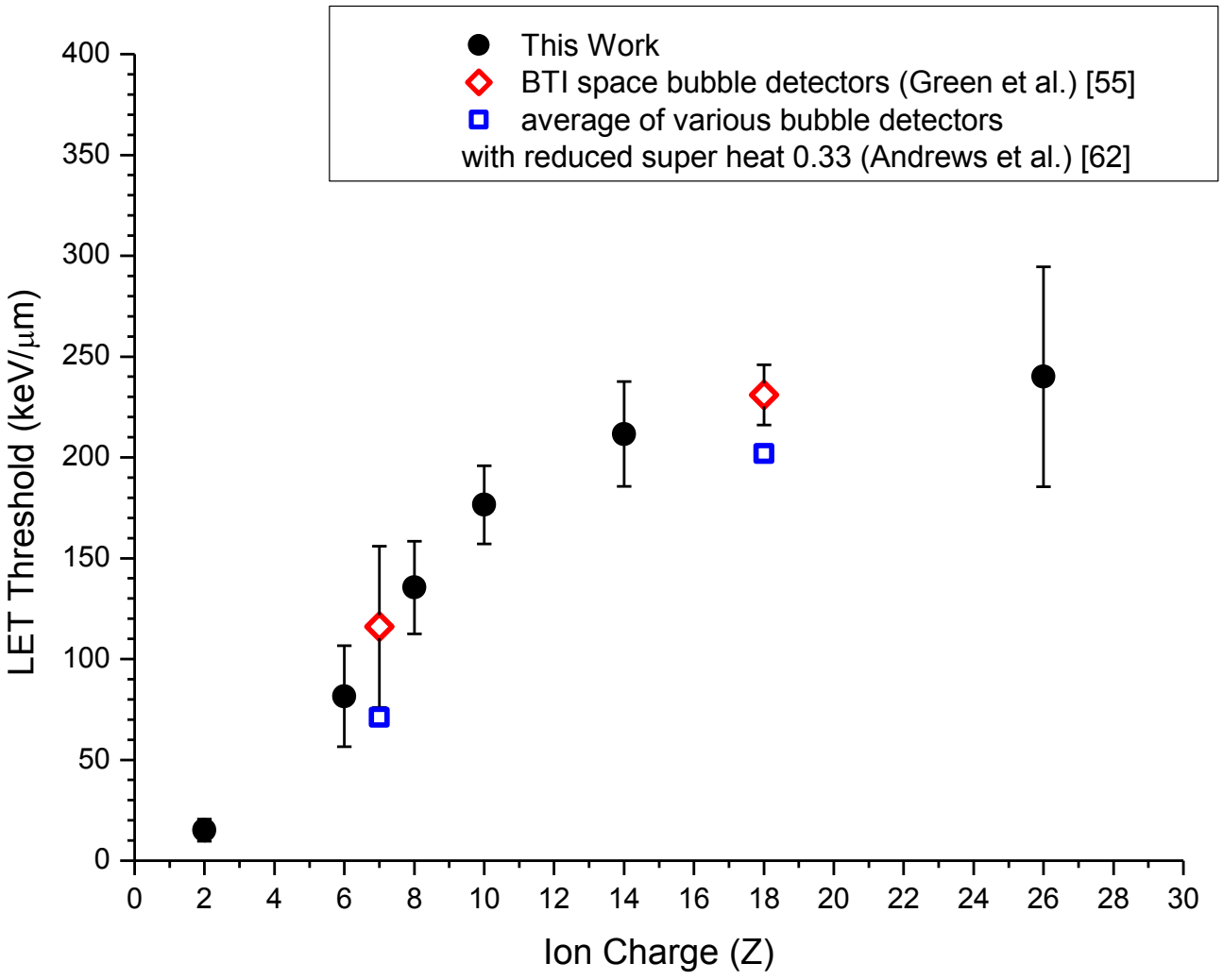

Figure 65: Z-dependence of LET threshold for visible bubble expansion in space bubble detectors

4.3.2 Ion Track Structure Model for Space Bubble Detector

Considering the size of the microdroplets (~20 μm diameter) and the predicted size of the critical radius of vapour embryos along the ion tracks (28 – 56 nm), $LET_{\infty}$is not the best parameter to fully describe visible bubble formation in bubble detectors. Observing the restricted stopping power and determining the energy deposited into the microdroplets could provide a better model to explain whether or not a particular event can produce an expanded bubble. The thermal spike theory of bubble formation is reasonable since the expansion of the microdroplets into visible bubbles is essentially driven by an increase in thermal energy and evaporation. Unfortunately, the physical shape and spatial distribution of energy over time in a thermal spike event are extremely complicated. It may not be easily modeled in a complex heterogeneous structure like a superheatedmicrodroplet inside an elastic polymer. Alternatively, a much simpler approach may explain the expansion of microdroplets into visible bubbles and be consistent with the LET threshold results observed in the HIMAC experiments. Accordingly, track structure effects have been examined to explain the apparent correlation of the LET threshold required for bubble formation in bubble detectors and the charge of the incident particles. The condition for bubble formation is expected to be related to energy density ($keV/\mu m^3$) and not simply described by LET_{∞} alone. For different ions with the same LET_{∞}, the energy density along the ion track is very different. Thus, it reasonable that the LET threshold for bubble formation could varies from ion to ion. The Katz, Chatterjee and Keifer track structure models have been investigated assuming visible bubble formation in bubble detectors occurs along the ion tracks when the ions intercept a microdroplet [17].

The heavy ions in all HIMAC experiments have an effective track radius which has been defined by the ion track "penumbra" (r_{max}) in the Chatterjee, Katz and Keifer models (see equations 1.7, 1.8 and 1.9 in Section 1.2.5 Heavy Ion Track Structure. The LET of the ions at the bubble front position was recorded with the MATLAB LET analysis program along with the kinetic energy E. The velocity has been calculated using relativistic kinetic equations and β has been used to calculate the effective ion track radii. The radii ranged from 3μm to130μm at the bubble front from He to Fe for all HIMAC experiments. Figure 66 shows the track size (r_{max}) for the ions of each experiment at the point of bubble formation due to ionization (using the Chatterjee model equation 1.7).Assuming a microdroplet size of approximately 20μm diameter, it appears that tracks from He are smaller than the microdroplets while Fe has tracks that are much larger than the microdroplets. Other ions are between with some having tracks that are comparable to the microdroplet radius. N and Ar ions have also been calculated based on the LET threshold reported by Green *et al.*[55].

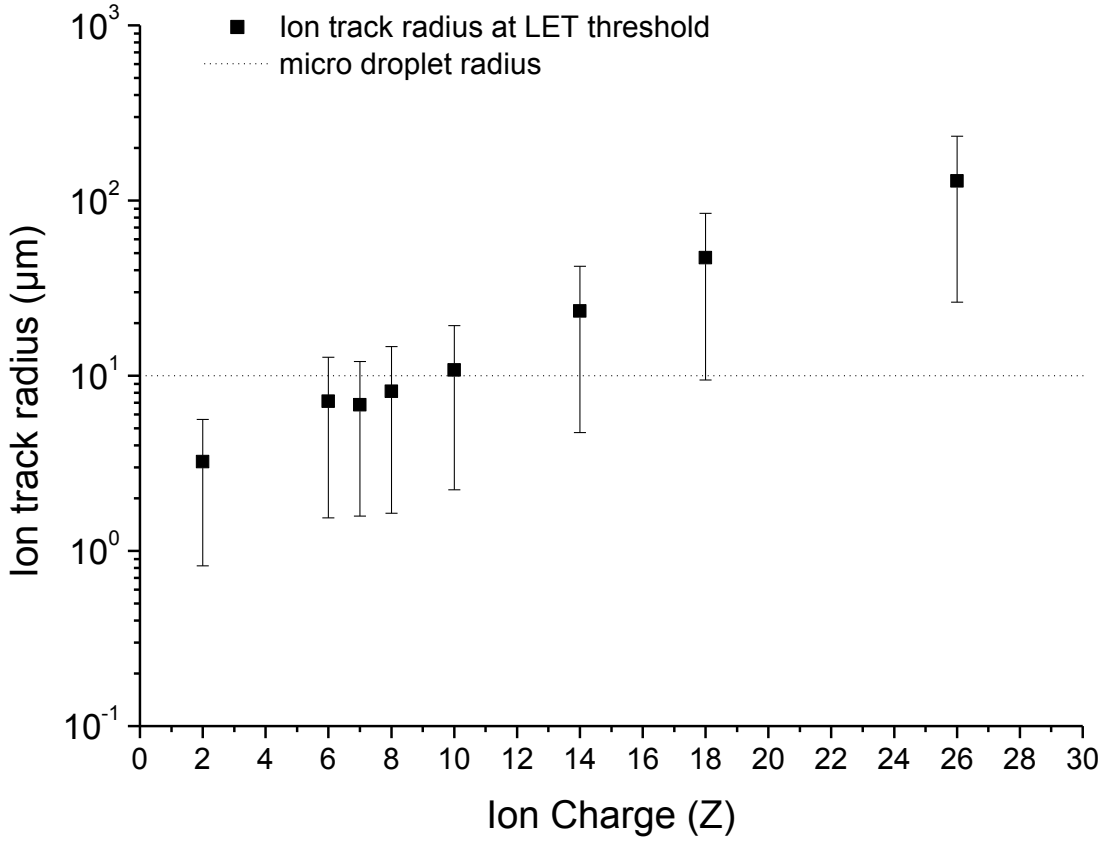

Figure 66: Chatterjee model of ion track radius at bubble front for HIMAC heavy ion experiments

The microdroplets are approximately 20 μm in diameter. Thus, when a low Z track collides directly with a microdroplet, all of the energy in the ion track is deposited directly into that droplet since r_{max}< droplet radius. For the large Z ions, when an ion track hits a microdroplet directly, the energy of the whole ion track is deposited in a region that is much greater than the size of the entire microdroplet. Only some of the energy contributes to the expansion of the bubble and the rest is dissipated into the gel surrounding the microdroplet.

The threshold for bubble formation is determined by the energy density (keV/μm^3) of the ion track in the microdroplet. Actually, the distribution of energy in the whole ion track is not uniform and is usually described by a radial dose distribution (as seen in Figure 4). The energy density is higher at the ion core and falls off significantly toward the edge of the ion track radius (vanishing beyond r_{max}). The average energy density of the ion track is considered for simplicity and it is believed that this simplification is sufficiently accurate to explain the HIMAC experimental results without contradicting the actual physics. Bubbles expand from thermal energy, so it is appropriate to consider that within the time of bubble formation the energy deposited along the ion track by ionization (secondary electrons) may dissipate to a more even distribution as thermal energy. Certainly, the thermal energy will spread and dissipate completely over time as the material returns to thermal equilibrium. Therefore the average track energy density could be sufficient to describe bubble formation from heavy ions. The average track energy density has been defined in section 3.2.2 (see Equation 3.3).

If the ion track radius is larger than a microdroplet ($r_{max} \geq 10$ μm) in a bubble detector, then some portion of the energy is deposited outside of the microdroplet. In this case, the energy density inside the microdroplet is restricted to a cylinder of 10 μm. The total energy deposited within the 10 μm radius cylinder is the LET restricted to 10 μm multiplied by the distance dx.

$$Energy\ density\ in\ micro\ droplet\ = \frac{LET_{10\mu m}\ \times dx}{\pi(10\mu m)^2 \times dx} = \frac{LET_{10\mu m}}{\pi(10\mu m)^2} \tag{4.2}$$

Thus, for instances where the ion track radius is larger than the bubble detector microdroplets the energy density is calculated with the restricted LET (Equation 1.9),

$$Energy\ density\ in\ micro\ droplet\ = \frac{LET_{10\mu m}}{\pi(10\mu m)^2} = \frac{\frac{LET_\infty}{2}\left[1+\frac{1+2\ln(10\mu m/r_c)}{1+2\ln(r_{max}/r_c)}\right]}{\pi(10\mu m)^2} \quad (4.3)$$

This method has been used to examine the energy density along the ion tracks and in the microdroplets for all ions used in the HIMAC experiments. The energy density of the ions has been calculated at the position of the bubble front in the space bubble detectors for He, C, O, Ne, Si, and Fe. The energy density for N and Ar ions has also been calculated based on the LET at the bubble front given in the literature[55]. For ions with a track larger than 10 μm, the energy density in the microdroplet has been calculated and converted to dose (density=1.298 g/cm^3 for bubble detectors). Figure 67 shows the calculated energy density of the ion tracks inside the microdroplets at the position of the bubble front for all HIMAC experiments.

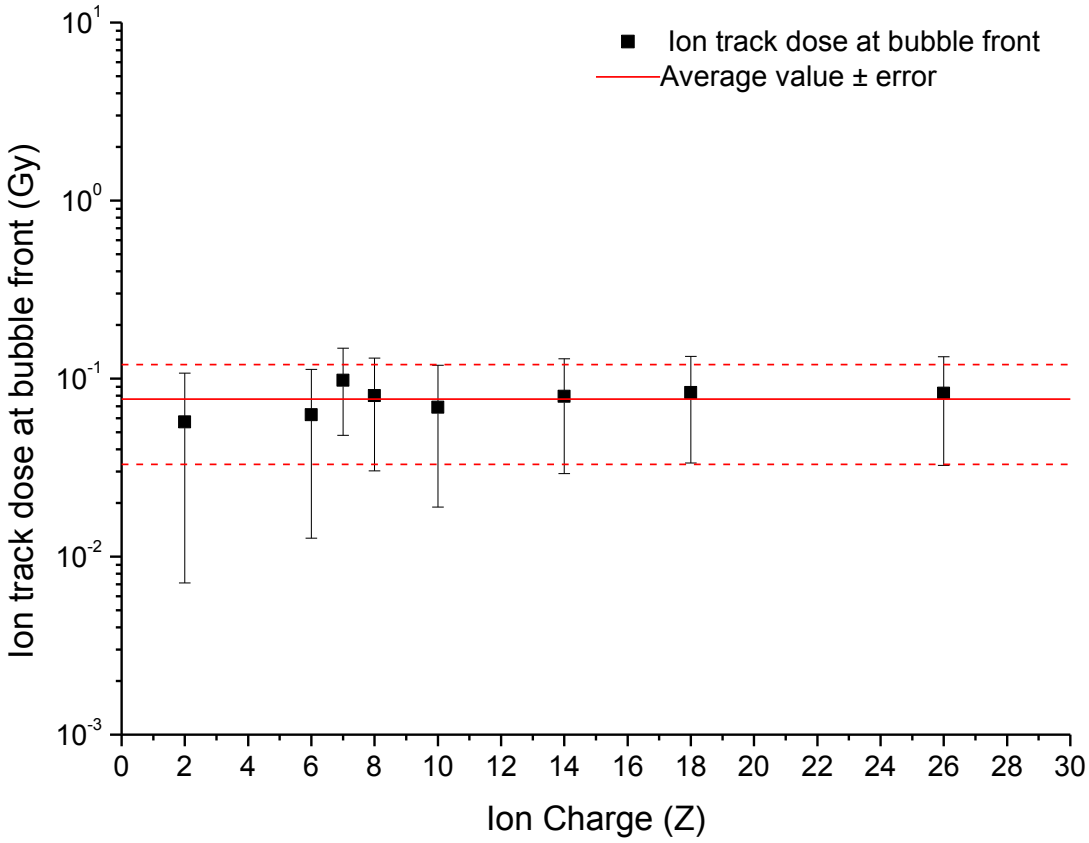

Figure 67: Ion track dose at bubble front for all HIMAC experiments

The data in Figure 67 suggest that the average track energy density in the microdroplets is the same for all ions at the bubble front despite the fact that the LET is significantly different. The mean value of 0.08±0.04 Gy could be considered a minimum threshold for bubble expansion and shall be referred to as $D_{threshold}$. Figure 68 shows a full average track energy density curve for each of the ions measured at HIMAC. A MATLAB program was made to calculate the average track energy density using data imported from SRIM and Equations 3.3 – 3.5. The calculated average track energy density (converted to dose in Gy) is plotted as a function of LET for each ion starting with the low LET of the ions at maximum energy upon entering the bubble detector. As the ions slow down the energy decreases, the LET increases, the penumbra radius (r_{max})

decreases and the average track energy density increases. The LET reaches a maximum at the Bragg peak in all curves near the top of the figure. The ions continue to slow down with a decreasing LET as they begin to pick up electrons from the surrounding material. The average track energy density continues to increase as the penumbra decreases, vanishing at the end of the range (see Figure 3 for a visualization of this process). The average track energy density at the bubble front position in the HIMAC experiments is also plotted as a point on each of the curves using the LET from Figure 65. For regions that have a track radius larger than 10 µm, the curves have also been calculated using Equation 4.2. This MATLAB program has also been adapted to include a model for variability in the size of microdroplets. In reality, not every microdroplet is expected to have a radius of exactly 10 µm so 10 ± 3 µm has been input assuming a Poisson distribution and the mean curve has been compiled from the result with the microdroplet size distribution.

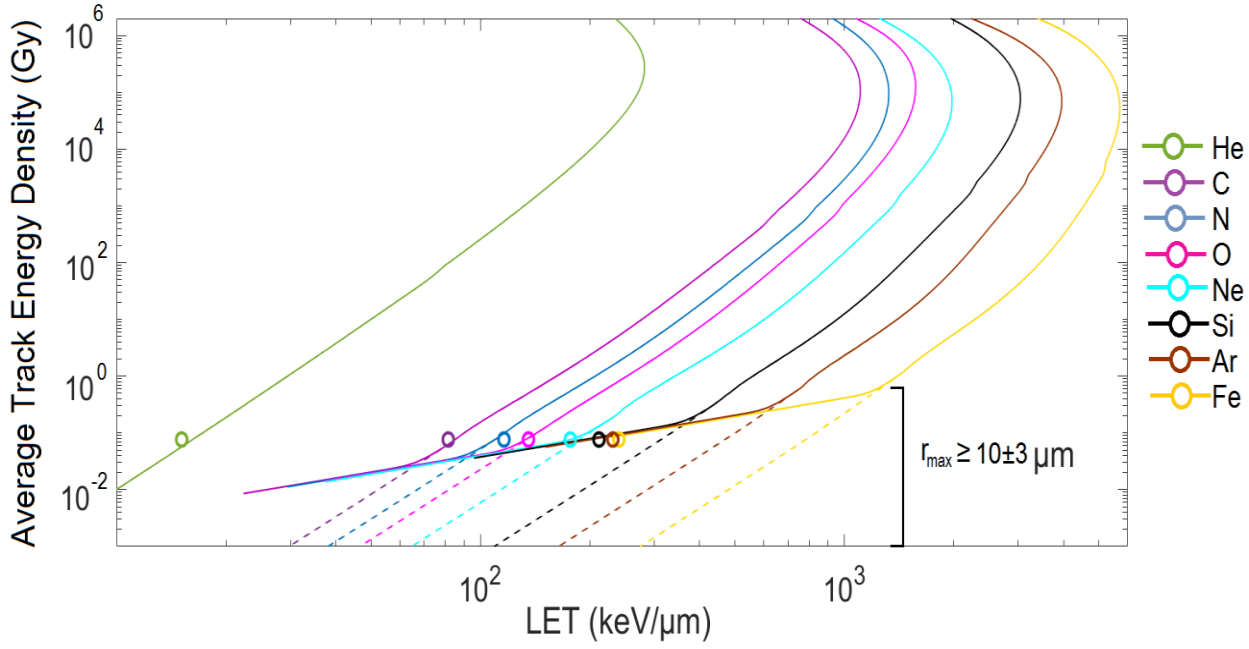

Figure 68: Average track energy density for heavy ions in bubble detectors as a function of LET

The experimental data points in Figure 68 lie very close to the curves for each ion. The dashed lines show the result without considering the microdroplet dimensions and only using r_{max} with LET_{∞}. Data for all ions with a charge from Z=1 to Z=30 in bubble detector material has been calculated in SRIM and imported into the same MATLAB program. In each case, the LET at the point of average track energy density = 0.0766 Gy has been recorded (or average energy density restricted to 10 ± 3μm whenever r_{max}> 10 ± 3 μm). The result is a set of LET thresholds that correspond to each ion charge and this is plotted in Figure 69. This result is interpreted as a minimum LET threshold ($\frac{dE}{dx}_{min}$) as a function of ion charge Z. All values are consistent with the range of $\frac{dE}{dx}_{min}$ values calculated in the literature for space bubble detectors. However, it appears to be a function that depends on the ion charge which was not discussed in the literature.

The entire calculation process described above has been repeated using the Keifer and Katz ion track structure models (See Appendix F, Figure F1 for Katz and Kiefer results). All three models showed a trend similar to the results seen in Figure 65, although the results using the Chatterjee model most closely matched the experimental data points. The best fit Chatterjee model was plotted along with the experimental data and a maximum and minimum estimate based on the largest and smallest LET results using all three ion track structure models with a range of $D_{threshold}$ determined by the statistical error of the calculated value of $D_{threshold}$. A discussion of the model uncertainties is provided in Appendix E.

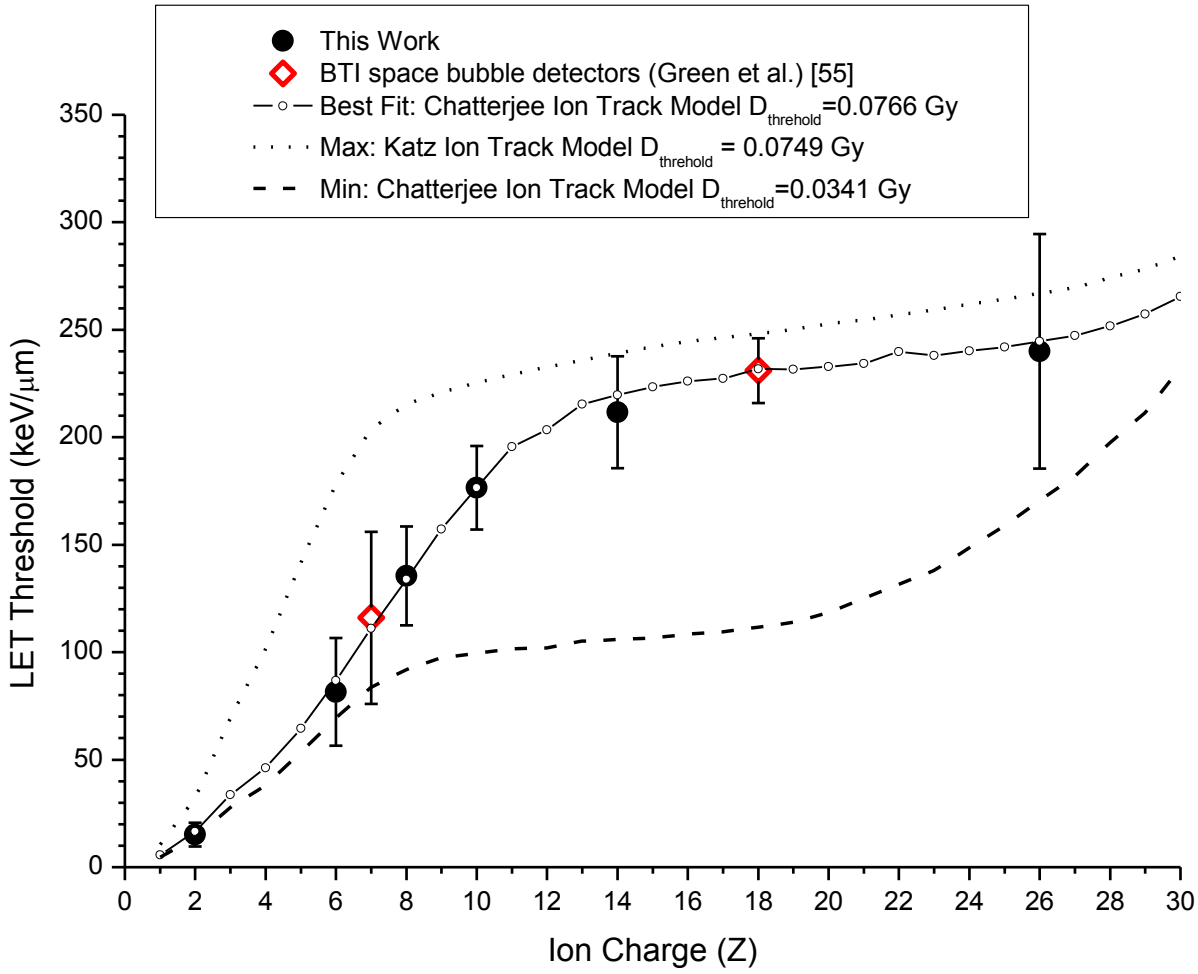

Figure 69: LET threshold for bubble formation in space bubble detectors calculated with ion track structure models

There is an excellent agreement between the experimental data and the ion track structure models. However, the values of $D_{threshold}$ are a few orders of magnitude smaller than the value D_{min} calculated for bubble detectors in Section 3.2.3. This is not unexpected since D_{min} was calculated on the scale of the vapour embryos (R_c = 28 to 56 nm) while $D_{threshold}$ has been calculated on the scale of the ion track radii or the entire microdroplet (3 to 10 µm). A plot has been constructed in order to reconcile the difference in energy density at these very different

scales. Figure 69 shows the radial dose distribution calculated using the Chatterjee, Katz and Kiefer ion track structure models for carbon ions in a bubble detector with an energy of 371.5 MeV and LET_{∞} of 81.51 keV/μm (as calculated at the bubble front position with SRIM). The average track energy density (calculated using Equations 3.4 and 3.5) is also plotted as a function of radial distance along with a PHITS simulation. Vapour embryos are expected to form primarily closest to the ion track core where the energy density is highest. The critical radius of the vapour embryos (28 to 56 nm) has been indicated on the figure with dashed lines along with the calculated minimum dose in the vapour embryos D_{min} ($1.3x10^3$ to $1.1x10^5$ Gy). The region of the figure where D_{min} intersects with R_c is believed to indicate the threshold for vapour embryos to cause evaporation of the microdroplets and expansion into visible bubbles. Average track energy density curves have also been calculated for 1820 MeV and 35.13 MeV carbon ions corresponding to the LET threshold range presented in the literature (23.21 to 493.7 keV/μm).

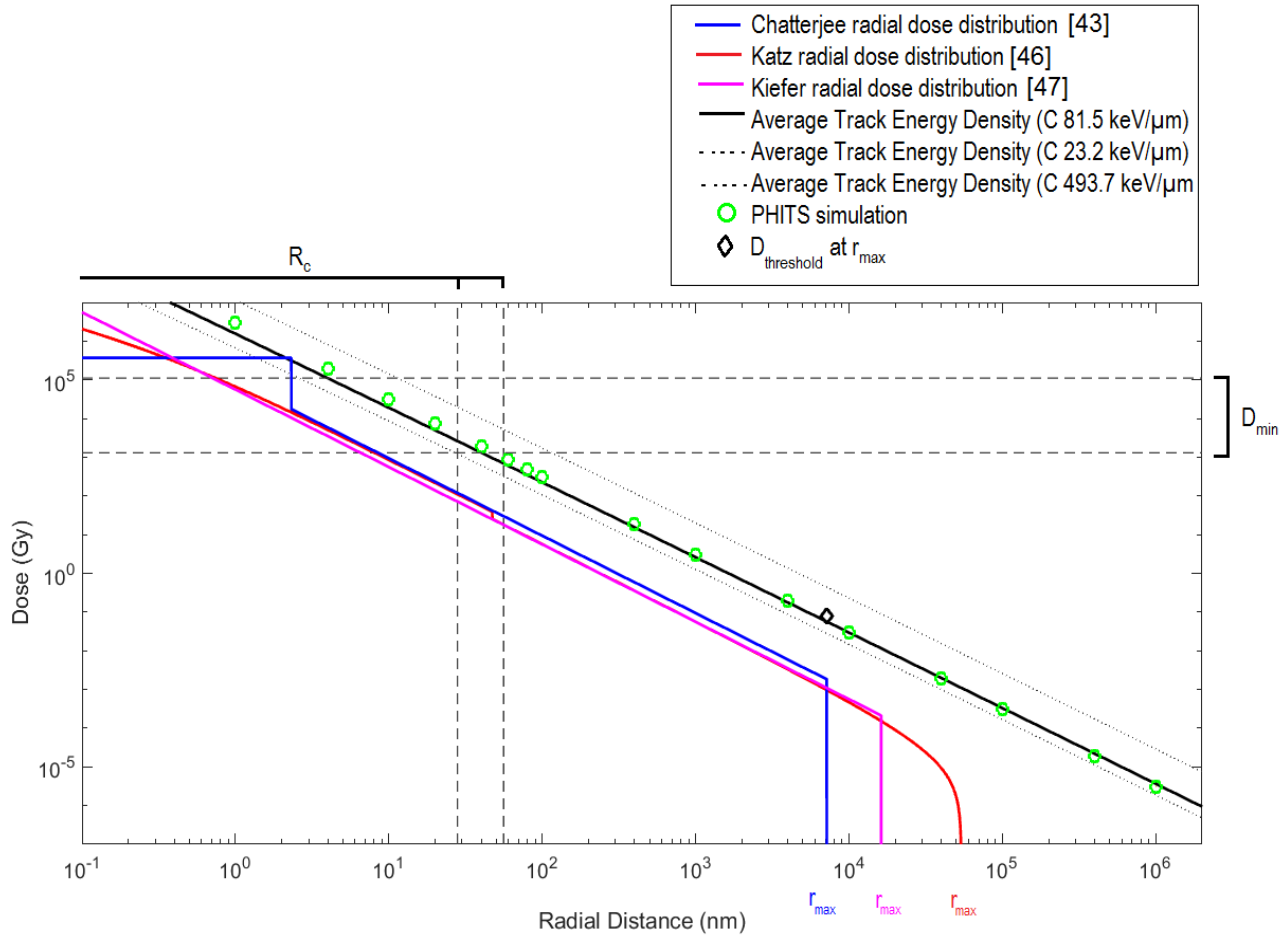

Figure70: Radial dose distribution and average track energy density of C ion at bubble front

The PHITS simulation matches the calculated average ion track density above ~100 nm. Below ~100 nm the PHITS simulation gives a slightly larger dose where the restricted LET becomes much less than the unrestricted LET. This is not accounted for in the PHITS continuous slowdown approximation model. Nevertheless, Figure 69 shows that the dose in the region of the critical radius of the vapour embryos (R_c) is indeed within the expected range of the minimum dose threshold in the ion track D_{min}. The average ion track energy density for the maximum and

minimum LET thresholds from the literature are both consistent with D_{min} and R_c. Identical plots for He, C, N, O, Ne, Si, Ar and Fe all show similar results and are included in Appendix F, Figure F2. All results are consistent with D_{min} and R_c where only the He result does not intersect the region of expected expansion of visible bubbles but lies only slightly outside this region.

4.3.3 Ion Track Structure Model for Space Bubble Detector Spectrometer

The success of the ion track structure models for space bubble detectors implies that a similar approach may be useful for the SBDS detectors. The Chatterjee ion structure model has been selected to calculate r_{max} and $D_{threshold}$ for all experiments because this model was the most successful with the space bubble detector results. The best-fit curves for each of the six detectors in the SBDS set are plotted in Figure 71 along with the experimentally measured LET thresholds for He, C, Si and Fe from Table 15. Results with other ion track structure models and experimental error bars have been omitted for clarity. Please see Appendix C, Figure C 2 for full results with error bars.

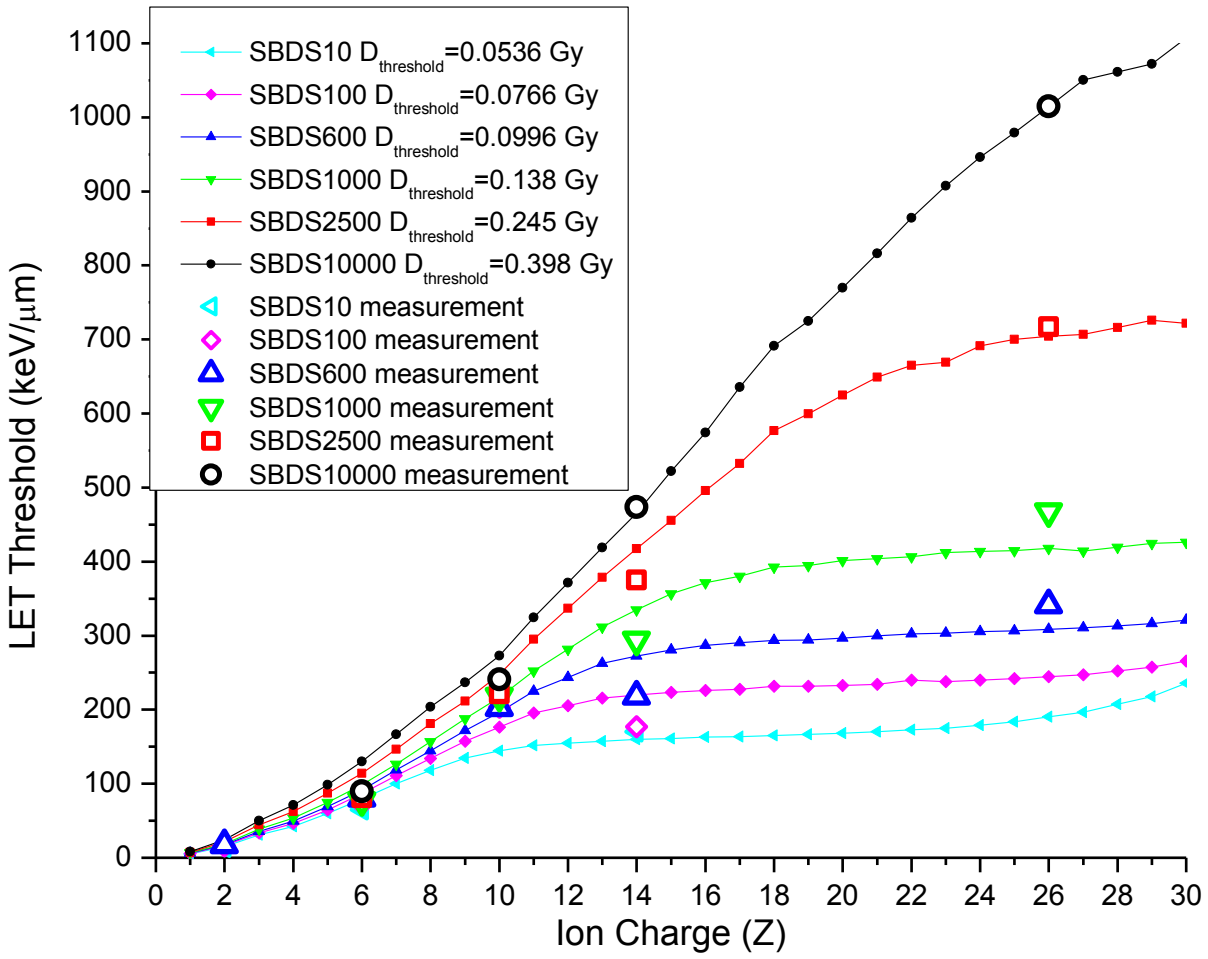

Figure 71: LET threshold for bubble formation in SBDS calculated with ion track structure models

The calculated curves in Figure 71 fit the trend of the experimental data very well. The six detectors in the set appear to have an increasing $D_{threshold}$ with increasing neutron energy threshold (10, 100, 600, 1000, 2500 and 10000 keV). This is reasonable because the neutron energy thresholds are a result of the external pressure exerted on the micro droplets. As the pressure is increased, the amount of energy required to evaporate a microdroplet and expand it

into a visible bubble increases and so $D_{threshold}$ also likely increases. As the energy density required increases, the LET threshold also increases.

4.4 Evaluation of Bubble Detector Measurements aboard the ISS

The published bubble detector measurement results from the ISS between 2008 and 2014 raise some questions on what is being measured and how the measurements should be interpreted. Currently, the results are interpreted as equivalent dose measurements for neutron radiation only, assuming protons and heavy ions produce a negligible number of bubbles during the approximately seven day measurement periods. The equivalent dose is taken by dividing the number of bubbles produced by the AmBe calibrated sensitivity (bubbles/μSv) and scaling by a correction factor of 1.62. However, the results of the experiments performed in this work suggest that the response functions for protons and heavy ions are not negligible compared to the neutron response function and consideration for the number of bubbles produced directly by heavy charged particles should be considered. Furthermore, the bubble detector measurements should be consistent with other detectors on the ISS and any changes or trends in the bubble detector measurements over time should be explained by changes in the radiation environment.

4.4.1 OLTARIS Model Results and Comparison with Experimental Measurements

An OLTARIS model of the radiation environment aboard the ISS has been built for every bubble detector measurement performed between January 2008 and October 2014 (forty-five individual measurement periods, details listed in Appendix A). The ISS altitude has been input into the model using published altitude data (see Appendix B, Figure B3). Measurements

performed in the Service Module, the Mini-Research Module 1 (MRM-1) and the US Lab were modeled as described in Section 3.3. Three measurements were recorded inside the JEM and one in the Japanese Pressurized Module (JPM). OLTARIS does not include a shielding model for JEM or JPM so the radiation environment for these locations was modeled with the US Lab because it is in the same approximate location and may have a similar shielding distribution. The differential energy spectra from OLTARIS were convoluted with the corresponding response function from Figure 34 for all particles using Equation 3.7. The result is a predicted number of bubbles produced per day from each particle type hence called the "OLTARIS bubble count model". See Appendix D for a discussion of the verification and validation of the MATLAB bubble count model.

The differential energy spectra for one individual measurement period during ISS Expedition 16 are plotted in Figure 72. During this measurement session, four space bubble detectors were placed in the Service Module at various locations. The detectors were exposed for 4.9 days from February 22nd to 27th 2008. The ISS had a perigee of 333 km and an apogee of 354 km at that time.

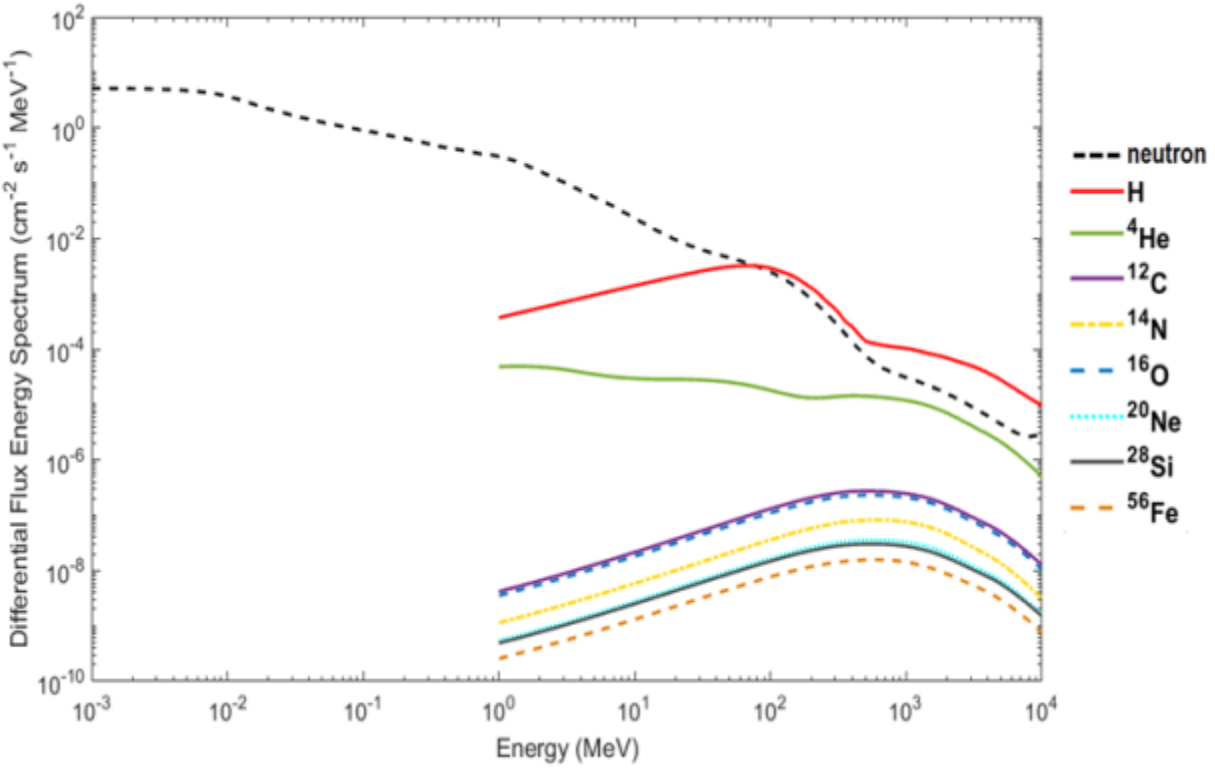

Figure 72:Differential flux energy spectra for ISS Service Module (Feb. 22-27 2008). (Spectra generated with OLTARIS) [97]

Equation 3.7 has been used along with the spectra in Figure 71 and the response functions from Figure 34 (using the trapezoid rule and appropriate integration limits) for each particle. The results are summarized in Table 16where the number of bubbles recorded per day of exposure has been normalized to a standard 0.1 bubble/μSv detector by dividing the total number of bubbles by the time of exposure and then dividing by the ratio of the detector AmBe calibration compared to 0.1 bubbles/μSv.

Table 16: Space bubble detector measurements and OLTARIS bubble count model for measurements in ISS Service Module

Detector name and location	S_{AmBe} (bubbles/μSv)	Number of bubbles	Bubbles per day (normalized to 0.1 bubbles/μSv)
B04 - Service Module, Starboard Cabin	0.18	100	11.3
B06 – Service Module Astronaut working desk	0.16	86	10.9
B07 – Service Module Astronaut working desk	0.15	64	8.7
B08 – Service Module On the ceiling	0.14	57	8.3
Experimental average	0.1	48±8	10±2
OLTARIS bubble count model	0.1	50±20	10±3

The total numbers of bubbles predicted by the OLTARIS bubble count model match the experimental average. The OLTARIS bubble count model is summed from the response to all particles, so these may be separated out to give some insight into how many bubbles are created by neutrons, protons and heavy ions. The results for this model are presented in Table 17.See Appendix E, Table E4 and Table E5 for all values and calculated uncertainties.

Table 17: Relative contribution of particles to bubbles counted in OLTARIS model

Particle:	neutron	proton	He	C	O	Ne	Si	Fe
Bubbles per day	8.04	1.38	0.051	0.0017	0.0015	6.5×10^{-4}	0.0022	0.035
Total bubbles	39.5	6.8	0.2	0.008	0.007	0.003	0.01	0.2
Contribution to the total number of bubbles in the OLTARIS bubble count model (%)	85% ± 2%	15% ± 8 %	< 1% ± 2%	< 1% ± 0.4%	< 1% ± 0.4%	< 1 % ± 0.3%	< 1 % ± 0.5%	< 1% ± 2%

The results in Table 17 indicate that neutrons contribute to the majority of bubbles in the OLTARIS bubble count model. However, protons produce a considerable number of bubbles as well. All of the heavy charged particles are calculated to produce less than 1 bubble over the entire measurement period (*i.e.* the probability of a bubble being produced from a heavy ion is low). The majority of the heavy ion contribution is from He, which is included in the trapped radiation model in OLTARIS. The contribution of all other heavy ions is expected to depend on the response function and relative abundance. For example, Ne was calculated to have a very low contribution and C a much higher contribution despite the much larger response function for Ne. Also, Fe has the lowest flux in Figure 72 but a larger contribution due to the much larger response function compared to the other ions. The total contribution from the six listed heavy ions in this model is very low (only 0.4 bubbles during the entire measurement period). Considering the large relative uncertainty, it is impossible to conclude exact contributions of each heavy ion with $Z \geq 2$. However, the contributions are expected to be very low and the probability of bubbles being produced directly from heavy ions passing through the bubble detector is very small(See Appendix E for a discussion on particle contribution uncertainties). A rough estimate of the contribution of heavy ions from $Z = 3$ to $Z = 13$ not included in the experimental part of this work has been made using the average contribution from C, O, Ne and Si. For $Z = 15$ to $Z = 25$ the contribution has been estimated with the Si result divided by 10 corresponding to the relative abundance from Figure 7. Ions with $Z > 26$ have such a low relative abundance that the contribution is likely negligible. Altogether the sum of all heavy ions ($Z \geq 2$) gives a maximum estimate of about 0.5 bubbles during the entire measurement period (~ 1% of the total) in this OLTARIS bubble detector model. This is close to the estimate of the heavy ion

contribution to bubble detector measurements in the ISS reported in the literature which was calculated to be< 0.6% for all heavy ions with $Z \geq 2$ [14].

Equation 3.7 has also been used with the average ISS neutron and proton spectra given in the literature (see Figure 29). The experimental neutron spectrum from the BBND measurements in the literature and the CREME96 proton spectra modeled for ISS Expedition 16 have also been included for comparison. The results are summarized in Table 18. All heavy ions with $Z \geq 2$ are not expected to produce a significant number of bubbles and have been omitted.

Table 18: Comparison of space bubble detector measurements with OLTARIS model, CREME96, and literature

Measurement	Neutron and Proton Spectra	Location	Bubbles per day from neutrons	Bubbles per day from protons	Total bubbles per day
Space bubble detector measurement	NA	Service Module Feb.22-27 2008	NA	NA	9.8 ± 1.5
bubble count model using OLTARIS	OLTARIS [97]	Service Module Feb.22-27, 2008	8.0 ± 2.8	1.4 ± 1.4	9.5 ± 3.1
bubble count model using published ISS spectra	Predicted neutron and proton spectra from literature [69]	ISS (average)	7.8 ± 2.8	1.1 ± 1.0	9.0 ± 3.0
bubble count model using BBND neutron measurements	BBND measured neutron spectrum [71]	US Lab Mar.23-Nov.14, 2001	8.0 ± 2.8	NA	NA
bubble count model using CREME96	CREME96 proton spectrum [98]	Service Module Feb.22-27 2008	NA	1.3 ± 1.1	NA

The results in Table 18 are consistent between the models and the total number of bubbles in the measurements. This indicates that the OLTARIS bubble count model has merit and that protons are likely contributing an appreciable amount to the total number of bubbles measured.

The results of all bubble count models using OLTARIS between January 2008 and October 2014 are plotted in Figure 73 along with the published experimental data (bubbles per day normalized to a detector with a 0.1 bubbles/μSv AmBe calibration). The mean value of each experimental measurement is plotted as a point with error bars representing the standard deviation for measurements. Some measurements were made with only one bubble detector and in these cases, error bars were estimated using the square root of the number of bubbles (assuming a Poisson distribution). Connecting lines have been added to help distinguish the model from the measured data, but do not imply any interpolation between measurement periods. A dashed line has also been added to indicate the large altitude increase of the ISS in June 2011. Error bars for the OLTARIS bubble count models have been excluded from this figure for clarity. However, Figure G1 has been added to Appendix G with all space bubble detector measurements plotted individually with the OLTARIS bubble count model results including error bars.

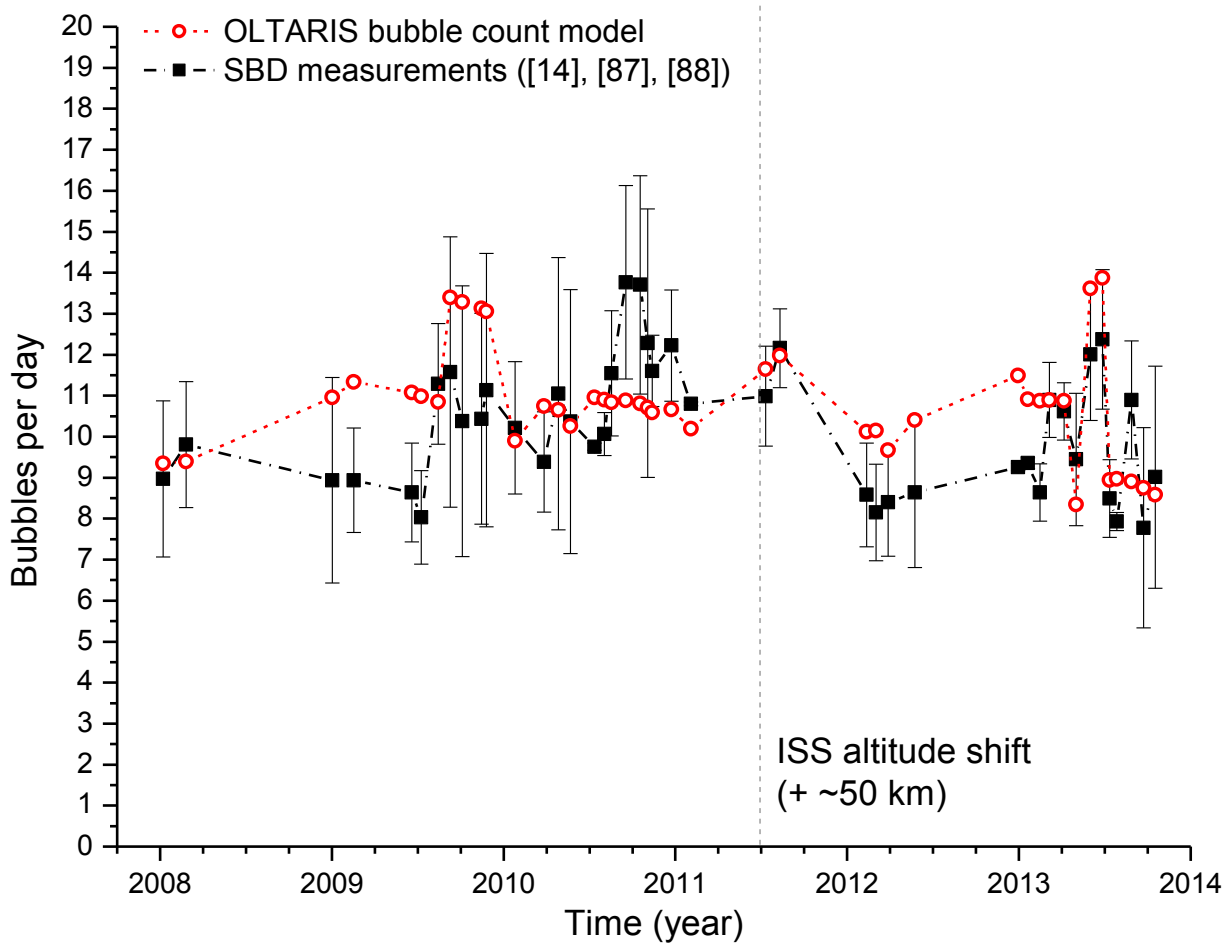

Figure 73: OLTARIS bubble count model results and experimental data for space bubble detector measurements aboard the ISS

The experimental data in Figure 73 indicate that the bubble detector measurements are varying with time, but they are also noisy where the variations are small compared to the size of the error bars. This level of noise is expected since space bubble detectors are essentially single hit detectors that count individual high LET events where bubble expansion is infrequent (approximately 10 bubbles per day). This is many orders of magnitude less than the total number of particles passing into the detector per day. Neutrons, protons and heavy charged particles in the ISS radiation environment are capable of producing bubbles but rarely do so. It is reasonable to assume that there is a random probability that a particular particle entering the bubble detector

will enter into a microdroplet and a random probability that enough energy will be imparted in that microdroplet to cause the expansion into a visible bubble. These kinds of random chance events with a low probability of success are well described by a Poisson distribution. For a mean frequency of about 10 bubbles per day as seen in Figure 73one can expect a variation typically from 7 to 13 bubbles per day which is consistent with the measured data. A frequency histogram of the number of bubbles counted per day in all space bubble detector measurements is included in Appendix G, Figure G2 and is indeed similar to the calculated Poisson distribution. However, there are some variations in the data over time that are consistent in both the experimental data and the OLTARIS bubble count model results and these may help explain how the number of bubbles produced in a measurement is affected by changes in the radiation environment aboard the ISS. For example, the decrease in the measurements after the ISS altitude shift (originally presented in Figure 19) are present in the OLTARIS bubble count model results. The period from January 2008 to January 2011 is plotted in Figure 74 with labels A, B and C indicating the trends in the data over different measurement periods.

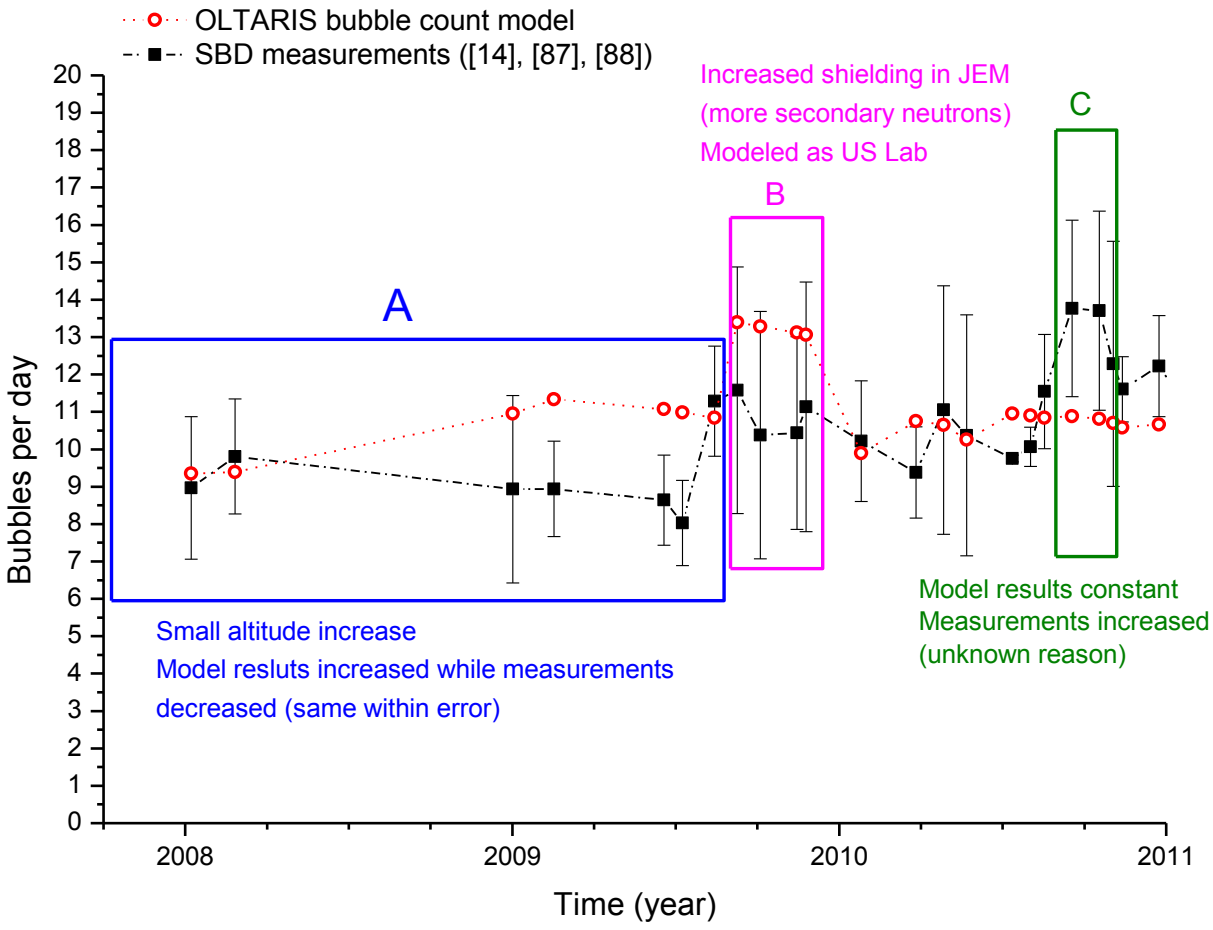

Figure 74: OLTARIS bubble count model results and experimental data 2008 to 2011

Region A in Figure 74 represents measurements in ISS Expeditions 16 to 20 in the Service Module. The OLTARIS results show a slight increase due to a slight increase in altitude. The average data show a slight decrease, but there is essentially no change in the level of the error bars. The final data point in region A shows a close agreement between the measured data and the OLTARIS bubble count model results. Region B has a large increase in the OLTARIS bubble count model results because this region was modeled using the US Lab during ISS Expedition 20. The US Lab has more shielding and as a result, more secondary neutrons are produced, causing more bubbles to be created. The experimental data were measured in the JEM

and it may have less shielding than the US Lab. Consequently, the OLTARIS model may be overestimating the number of bubbles produced by secondary neutrons based on the US Lab spectra. The region between B and C was measured in the Service Module and shows good agreement between the model and measured data. Region C was also recorded in the Service Module and there appears to be a sudden increase in the measured data. This is unexpected and unexplained because there were no significant changes in altitude or shielding. The OLTARIS bubble count model remains relatively constant in this region as expected. The experimental data decreases and are consistent with the OLTARIS bubble count model for the final three data points. The period from January 2011 to January 2014 is plotted in Figure 74 with labels D, E, and F indicating the trend in the data over different measurement periods.

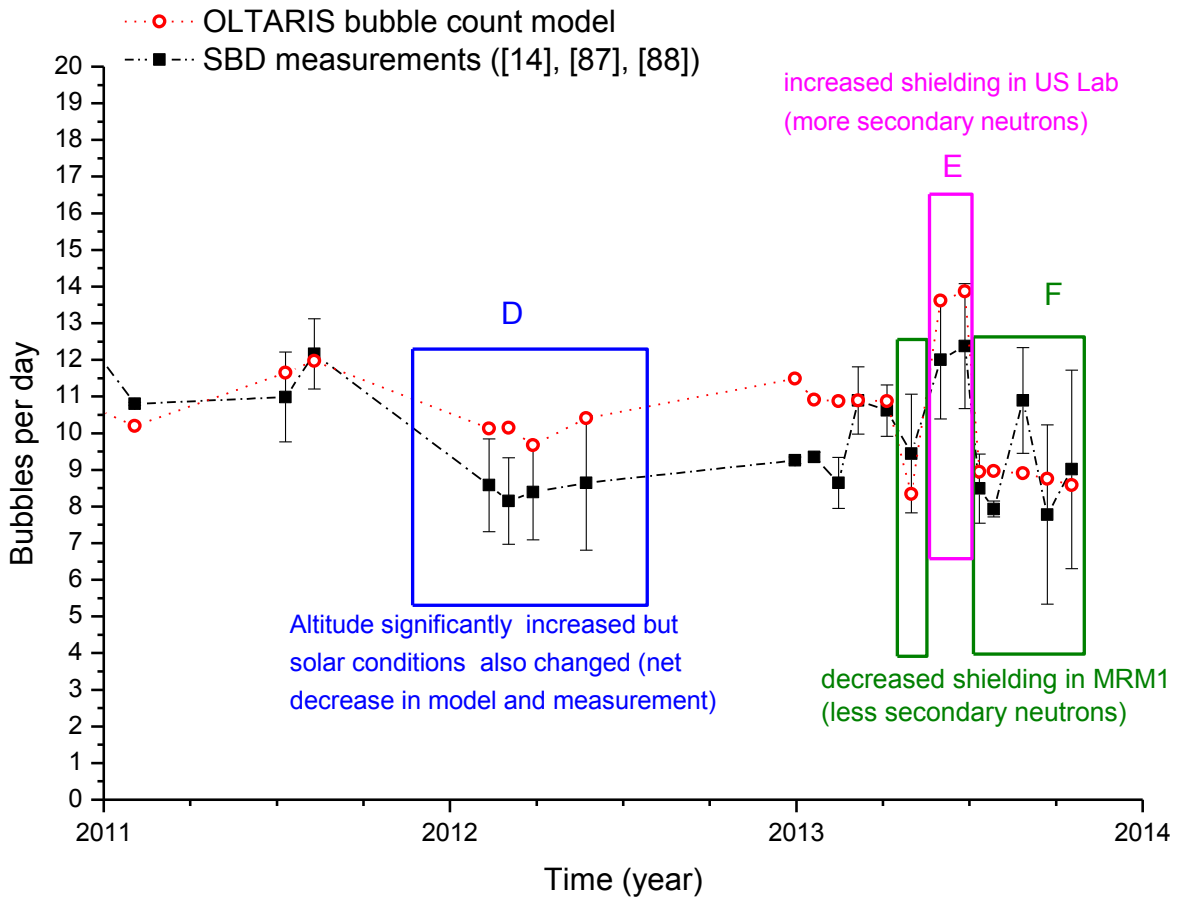

Figure 75: OLTARIS bubble count model results and experimental data 2011 to 2014

The first three data points in Figure 75 between January 2011 and August 2011 show good agreement between the OLTARIS bubble count model and the measured data. The data in region D was measured in the Service Module and shows a decrease from the previous measurements despite the fact that the ISS altitude has increased significantly. Between region D and region F, measurements were performed in the Service Module and show no significant change in either the OLTARIS model or the experimental data. The two points inside region E were recorded inside the US Lab with four different bubble detectors. The measurements show a significant increase in the number of bubbles compared to the other experiments made at the

same time in MRM-1. This is also represented in the OLTARIS bubble count model results which agree with the measured data within the error bars. This is a result of the larger number of secondary neutrons produced because of thicker shielding. Conversely, all measurements recorded in MRM-1 have a relatively lower number of bubbles due to less shielding and less production of secondary neutrons.

The total average for all experimental measurements in Figure 73 is 10 ± 2 bubbles per day while the total average of the OLTARIS model is 11 ± 1 bubbles per day. There is only a 6 % difference between the average of the model and the experimental data, suggesting a good overall correspondence.

4.4.2 Effects of Shielding on Space Bubble Detector Measurements

The shielding of galactic cosmic rays, trapped radiation, and albedo neutrons creates a secondary particle radiation environment inside the ISS. In general, more shielding blocks and slows down protons and heavy charged particles such that as the shield thickness increases, the flux of particles decreases. However, generated secondary particle fluxes increase as the shielding thickness increases. The shielding material is also important in determining the secondary radiation. For example, high Z elements tend to undergo spallation reactions and produce a significant number of neutrons, while low Z materials (especially hydrogenous materials) tend to thermalize and scatter neutrons. In order to examine this effect with bubble detector measurements, the OLTARIS model has been used to generate particle spectra for different shielding conditions. The spectra from Figure 72 has been used to represent measurements inside the Service Module. Spectra have also been generated during the same

period for simple aluminum spheres with density thickness from 0 to 150 g/cm^2. Additional spectra were also created using the US Lab and MRM-1 shielding. The expected number of bubbles from protons and neutrons was calculated using equation 3.7 for all different shielding. The results are plotted in Figure 76.

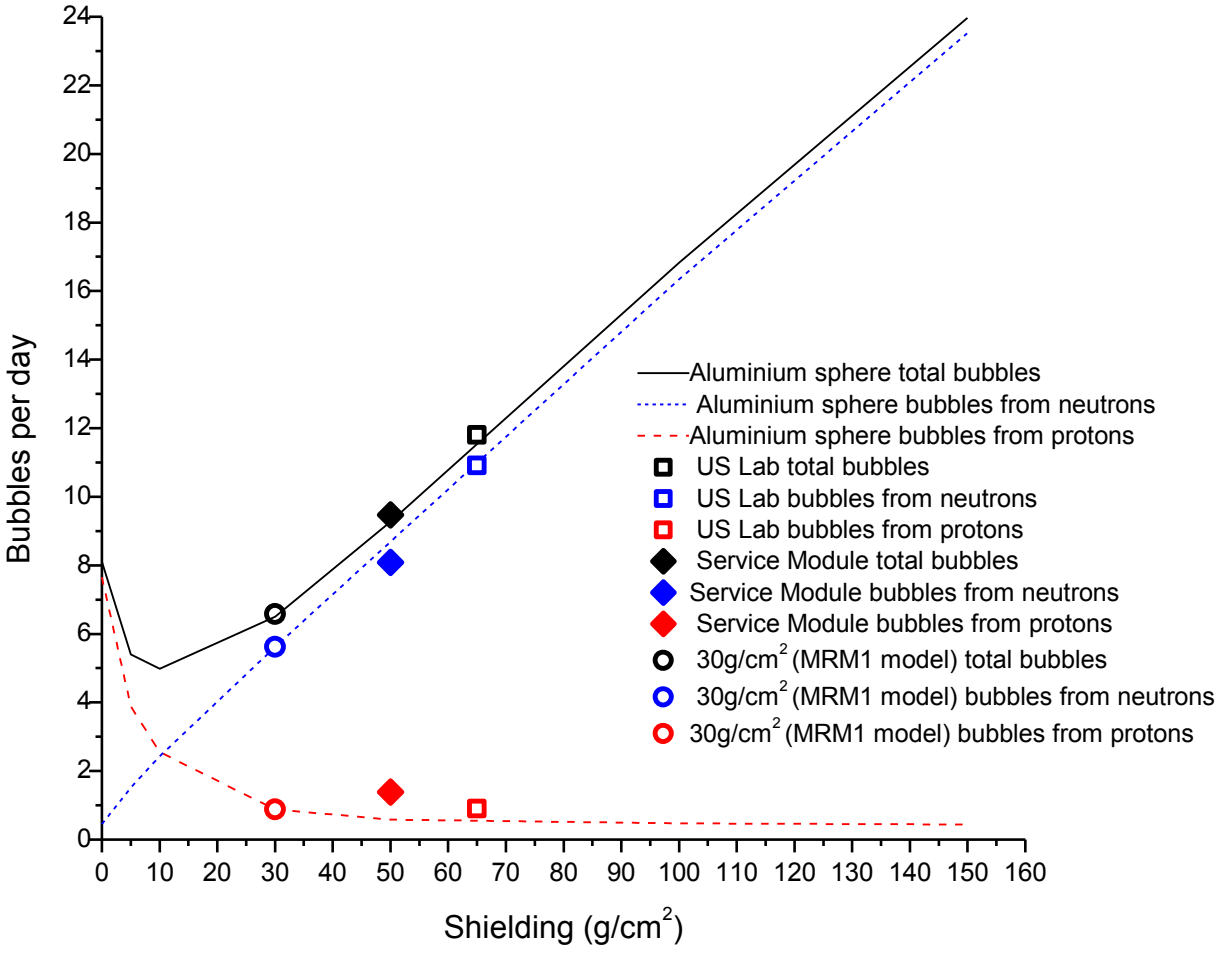

Figure 76: Model of bubbles produced in space bubble detectors behind different shielding

It is apparent in Figure 76 that with no shielding present, there are very few neutrons and all the bubbles measured are from protons. As the shielding is increased, more secondary neutrons are produced and protons are blocked. This figure illustrates why measurements in the

US Lab consistently produced more bubbles than measurements in the other locations. The relative contribution of protons may depend on location and shielding in the ISS. The results in Figure 76 indicate that more high Z shielding produces more bubbles in space bubble detector measurements.

4.4.3 Effects of ISS Altitude on Space Bubble Detector Measurements

The overall decrease in space bubble detector measurements after the ISS altitude increase in June 2011 are reflected in the OLTARIS bubble count model. It is expected that radiation increases with altitude, so a figure has been constructed to explain this result. First, a total time-averaged spectra were generated for the ISS inside the Service Module over the entire period of January 2008 to January 2014 with a static orbital altitude. This was done for eighteen altitudes between 300 and 470 km. The number of bubbles that would be produced per day with the particle spectra generated in OLTARIS has been calculated with equation 3.7 and is plotted as a function of ISS altitude in Figure 77. The experimental data and the OLTARIS bubble count model results for all space bubble detector measurements inside the Service module form Figure 73 have also been plotted.

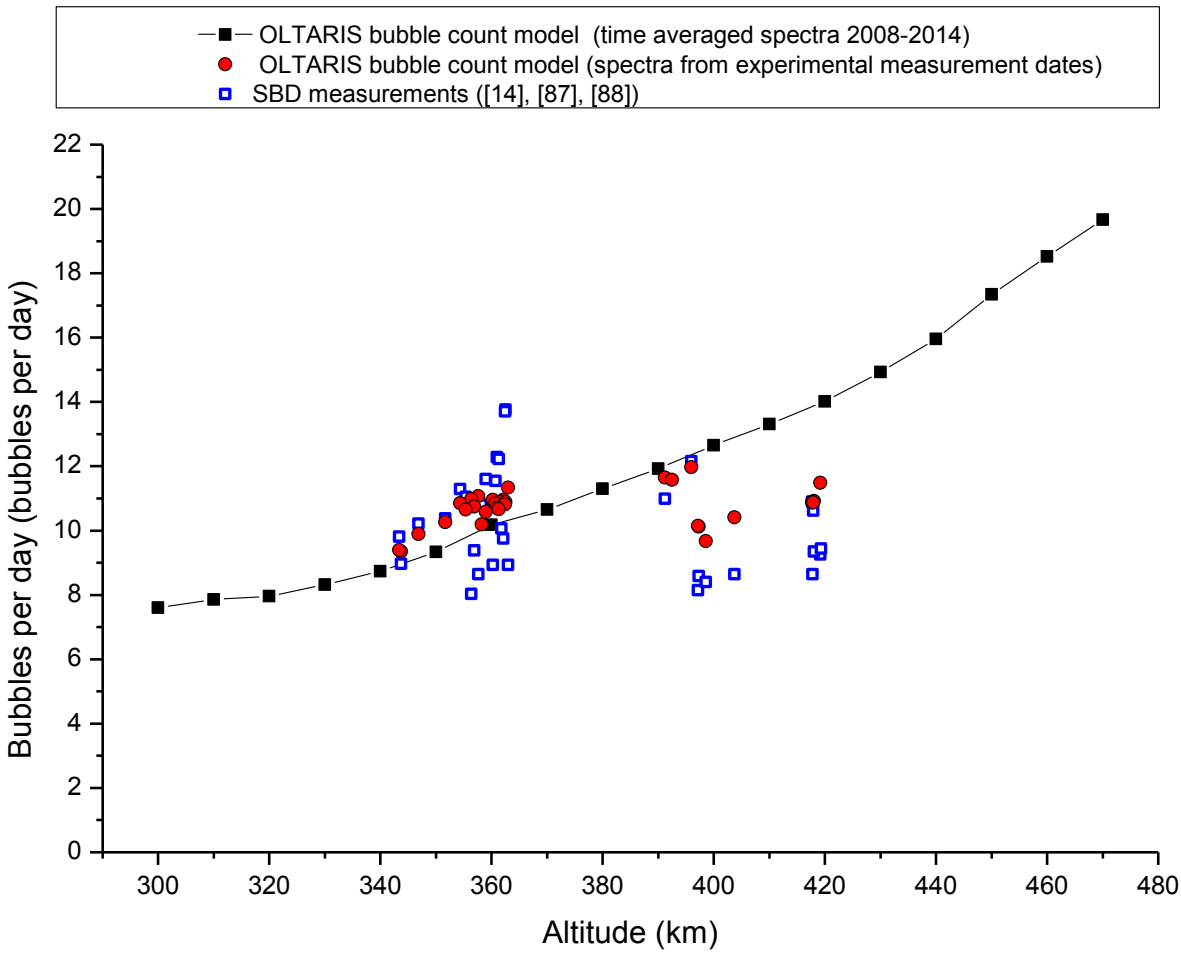

Figure 77: Space bubble detector measurements on ISS as a function of orbital altitude

The time-averaged OLTARIS bubble count model results show a clear increase in the number of bubbles produced as a function of altitude as expected. Conversely, the OLTARIS bubble count model results using the actual space bubble detector measurement dates show some increase with altitude from 340 km to 360 km and a decrease after the ISS altitude increase in June 2011. The experimental data also shows the same trend. Obviously, there is another factor affecting the particle spectra that depends on the date of measurement that appears to be accurately represented in the OLTARIS bubble count model. A final figure has been constructed to examine the changes in the OLTARIS bubble count model results over time without changes

in altitude. Particle spectra were generated inside the Service module for a static ISS altitude of 420 km for eleven of the space bubble detector measurement dates and four additional interpolated dates. The number of bubbles was calculated with equation 3.7 and the result is plotted in Figure 78.

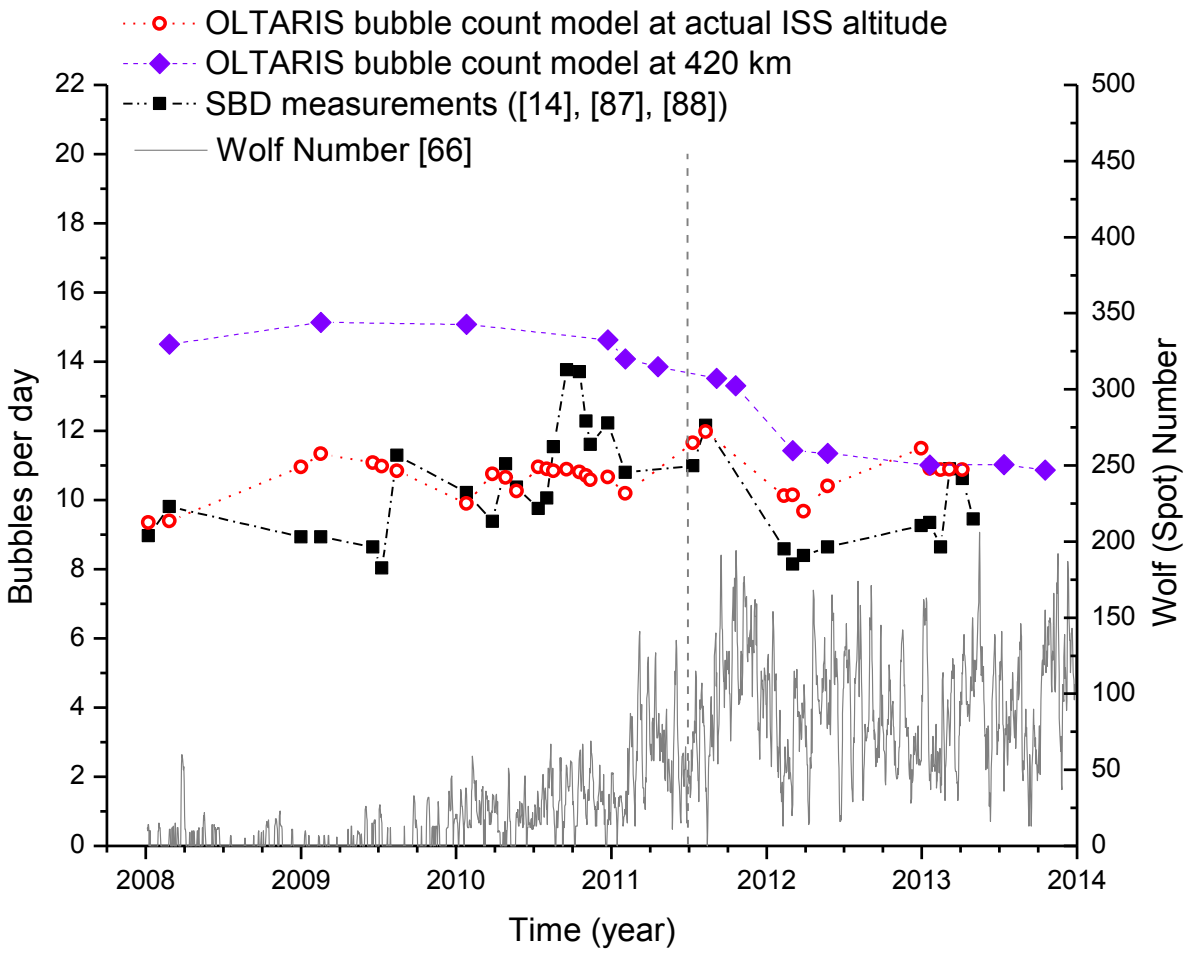

Figure 78: Space bubble detector measurements modeled at ISS altitude of 420 km

Beginning in 2008, the OLTARIS model suggests that the number of bubbles measured would be much larger if the ISS was at an altitude of 420 km at that time. After March 2011 the OLTARIS bubble count model results at 420 km decrease significantly. In January 2013, the OLTARIS bubble count model at 420 km matches the experimental data and the OLTARIS model of the space bubble detector measurements from Figure 73 where the actual altitude of the ISS was 418 km. The decrease corresponds to the increase in solar activity which acts to decrease the particle fluence on the ISS due to changes in the earth's magnetic field [9]. This is plotted in Figure 78 with the Wolf Spot number which represents the level of solar activity based on number and frequency of sunspots[66].The model shows that the aggregate of the increase in bubble count from the increase in altitude and the decrease in bubble count due to the increasing solar activity resulted in a net decrease in bubble count (as observed in the measurements). This result is also in good agreement with the DOSIS radiation monitoring program where the daily measured absorbed dose rate from GCR was shown to decrease by roughly 12.5 % from 2008 to 2014 [102].

4.4.4 Contribution of Protons to Space Bubble Detector Measurements

One of the primary concerns for using space bubble detectors as neutron dosimeters is the effect of protons and heavy charged particles in the measurements. If many bubbles are created from protons or heavy charged particles, then determining the neutron equivalent dose becomes very difficult. The varying particle spectra depending on shielding and location in the ISS make dose measurements even more difficult, especially if the detectors are worn on an astronaut's body and moved all around the ISS. The results in Table 17 indicates that the total number of bubbles created by heavy charged particles with $Z \geq 2$ is negligible. However, protons may be

contributing more than 15% of the total number of bubbles measured. Many of the protons present in the ISS radiation environment come from the trapped radiation environment and especially form passage through the SAA. This means that ISS altitude should affect the relative contribution of protons because higher altitude orbits experience a greater intensity of trapped radiation. The ISS completes approximately 16 orbits per day and may pass through the SAA from 50 to over 100 times during a bubble detector measurement period. The contribution of protons to the number of bubbles measured lies around 15% according to the OLTARIS model and varies with altitude and shielding. However, the deviation of the number of bubbles produced per day on the ISS governed by Poisson statistics means that it is impossible to state the relative contribution of protons and neutrons with certainty. On average the total number of bubbles produced from protons over the entire exposure period is expected to be around 15 ± 10 % and could vary significantly depending on conditions such as shielding and altitude.

CONCLUSION

As a part of the space bubble detector ground testing program space bubble detectors similar to those currently in use aboard the International Space Station have been irradiated in different high LET particle fields. Experiments with space bubble detectors in high energy neutron fields from 0.6 MeV to 800 MeV were performed. Several experiments were conducted with high-energy protons from 30 to 230 MeVand high-energy heavy charged particles including He, C, O, Ne, Siand Fe. The study has led to the following conclusions:

1. Bubble Detectors are high-LET threshold detectors and the passage of charged particles with LET above the threshold through the sensitive volume of the detector produces visible bubbles while charged particles of LET below the threshold do not directly produce bubbles:
   - Heavy charged particles with LET greater than the LET threshold will produce bubbles through direct ionization (*i.e.* electromagnetic rather than nuclear processes).
   - High-energy (relativistic) protons, α-particles and light ions of LET below the LET threshold can only produce bubbles *via* nuclear reactions that yield secondary charged particles of LET above the threshold within the sensitive volume of the detector.
2. The minimum threshold LET is not constant, but it depends on the charge of the ion (Z) and the reduced superheat of the detector. An ion track structure model has been developed wherein the LET threshold for bubble formation is determined by the average energy density along an ion track. The model is consistent with experimentally measured LET thresholds for different ions with the space bubble detector and SBDS set.
3. The number of bubbles withina unit volume of the detector will scale with incident particle fluence up to a certain saturation threshold. This is dictated by the number of superheated droplets suspended in the bubble detector gel (total number is 10^4 droplets per 10 ml) and the

total volume available for visible bubble expansion. For high-LET charged particles delivered in accelerator experiments, this threshold may be rather low, *i.e.* the passage of only a few hundred high LET charged particles through the sensitive volume of the detector may be sufficient to saturate the detector by activating a significant fraction of the superheated droplets within that volume. This is less of an issue for neutrons, energetic protons and light ions due to the fact they must first undergo a nuclear interaction, the probability of which is dependent on the nuclear cross section.

4. High LET radiation fields are present in spacecraft and the formation of visible bubbles is possible from neutrons, protons and heavy charged particles. A large total fluence of these particles is incident on bubble detectors during typical measurements. However, only a few bubbles are produced per day on typical ISS measurements. The probability that a bubble is created from a heavy ion with $Z \geq 2$ is small due to the relatively low particle fluence and high LET threshold. The majority of bubbles observed are most likely to be produced from neutron interactions, but there are also a sizeable number of bubbles that are created directly from protons (~15±10% of all bubbles). The relative contribution of neutrons, protons,and heavy ions may change depending on ISS altitude, solar cycle conditions, shielding and location in the ISS.

5. The determination of absorbed dose or equivalent dose based on thenumber of bubbles for bubble detectors exposed in highly complex and mixed radiation fields like those found in space is difficult and requires additional information, either from measurements made by other instruments or from model calculations.

6. The bubble detector provides a single, integrated scalar quantity: number of expanded visible bubbles. This number is proportional to the fluence of charged particles with LET above the

bubble formation threshold. Absorbed dose and equivalent dose are related to both fluence and LET.

FUTURE WORK

Future work will include analysis of additional bubble detector measurements aboard the ISS and in other orbital spacecraft such as the Bion satellite and possible future interplanetary missions using the models developed in this work. A more robust model may be possible using Monte Carlo simulations to better assess the effects of specific shielding geometry, materials, and secondary high LET particles. Additional experiments with SBDS may be used to measure the response functions of the SBDS set to protons, neutrons and heavy charged particles. A bubble count model will be developed for the SBDS set and similarly compared to experimental measurements aboard the ISS and other spacecraft. Experiments will be performed to better understand the relative contribution of different particles in mixed radiation fields with neutrons, protons and heavy ions. This can be achieved by measuring successive experiments in different beams or facilities where the total number of bubbles produced will be the result of the sum of the contribution from each particle.

REFERENCES

[1] M. Grande and T. M. Knight, "The Future of Spacecraft Radiation Design: A Workshop at Aberystwyth University, UK, 28-30 November 2012: MEETING REPORT," *Space Weather*, vol. 11, no. 10, pp. 543–544, Oct. 2013.

[2] F. M. Sulzman and A. E. Nicogossian, Eds., *Space biology and medicine:: joint U.S./Russian publication in five volumes. Vol. 2: Life support and habitability*. Washington, DC, 1994.

[3] C. Arena, V. De Micco, E. Macaeva, and R. Quintens, "Space radiation effects on plant and mammalian cells," *Acta Astronaut.*, vol. 104, no. 1, pp. 419–431, 2014.

[4] National Research Council (U.S.), Ed., *A strategy for research in space biology and medicine into the next century*. Washington, DC, 1998.

[5] S. El-Jaby, L. Tomi, L. Sihver, T. Sato, R. B. Richardson, and B. J. Lewis, "Method for the prediction of the effective dose equivalent to the crew of the International Space Station," *Adv. Space Res.*, vol. 53, no. 5, pp. 810–817, 2014.

[6] W. Schimmerling, "Genesis of the NASA Space Radiation Laboratory," *Life Sci. Space Res.*, vol. 9, pp. 2–11, Jun. 2016.

[7] G. F. Knoll, *Radiation detection and measurement*, 3rd ed. New York: Wiley, 2000.

[8] J. N. Pelton and F. A. Allahdadi, *Handbook of cosmic hazards and planetary defense*. 2016.

[9] V. M. Petrov, "Radiation risk during long-term spaceflight," *Adv. Space Res.*, vol. 30, no. 4, pp. 989–994, Jan. 2002.

[10] T. Liu, D. Xu, H. Li, H. Pei, M. Zhu, J. Wang, and G. Zhou, "Risk assessment of space radiation during manned space flights," *Rendiconti Lincei*, vol. 25, no. S1, pp. 17–21, Mar. 2014.

[11] M. Shahmohammadi Beni, T. C. Hau, D. Krstic, D. Nikezic, and K. N. Yu, "Monte Carlo studies on neutron interactions in radiobiological experiments," *PLOS ONE*, vol. 12, no. 7, p. e0181281, Jul. 2017.

[12] C. Arena, V. De Micco, E. Macaeva, and R. Quintens, "Space radiation effects on plant and mammalian cells," *Acta Astronaut.*, vol. 104, no. 1, pp. 419–431, Nov. 2014.

[13] C. S. L. Huntoon, V. V. Antipov, and A. I. Grigoriev, Eds., *Space Biology and Medicine - Volume III Books 1 & 2 - Humans in Spaceflight*. Reston, V.A: American Institute of Aeronautics and Astronautics, Inc., 1996.

[14] M. B. Smith, Y. Akatov, H. R. Andrews, V. Arkhangelsky, I. V. Chernykh, H. Ing, N. Khoshooniy, B. J. Lewis, R. Machrafi, I. Nikolaev, R. Y. Romanenko, V. Shurshakov, R. B. Thirsk, and L. Tomi, "Measurements of the neutron dose and energy spectrum on the International Space Station during expeditions ISS-16 to ISS-21," *Radiat. Prot. Dosimetry*, vol. 153, no. 4, pp. 509–533, Mar. 2013.

[15] R. Machrafi, K. Garrow, H. Ing, M. B. Smith, H. R. Andrews, Y. Akatov, V. Arkhangelsky, I. Chernykh, V. Mitrikas, V. Petrov, V. Shurshakov, L. Tomi, I. Kartsev, and V. Lyagushin, "Neutron dose study with bubble detectors aboard the International Space Station as part of the Matroshka-R experiment," *Radiat. Prot. Dosimetry*, vol. 133, no. 4, pp. 200–207, Feb. 2009.

[16] F. d'Errico, W. G. Alberts, and M. Matzke, "Advances in Superheated Drop (Bubble) Detector Techniques," *Radiat. Prot. Dosimetry*, vol. 70, no. 1, pp. 103–108, Apr. 1997.

[17] S. Agosteo, M. Silari, and L. Ulrici, “Improved Response of Bubble Detectors to High Energy Neutrons,” *Radiat. Prot. Dosimetry*, vol. 88, no. 2, pp. 149–156, Mar. 2000.
[18] B. J. Lewis, M. B. Smith, H. Ing, H. R. Andrews, R. Machrafi, L. Tomi, T. J. Matthews, L. Veloce, V. Shurshakov, I. Tchernykh, and N. Khoshooniy, “Review of bubble detector response characteristics and results from space,” *Radiat. Prot. Dosimetry*, vol. 150, no. 1, pp. 1–21, Jun. 2012.
[19] A. R. Green, L. G. I. Bennett, B. J. Lewis, P. Tume, H. R. Andrews, R. A. Noulty, and H. Ing, “Characterisation of bubble detectors for aircrew and space radiation exposure,” *Radiat. Prot. Dosimetry*, vol. 120, no. 1–4, pp. 485–490, Sep. 2006.
[20] M. A. Buckner, R. A. Noulty, and T. Cousins, “The Effect of Temperature on the Neutron Energy Thresholds of Bubble Technology Industries’ Bubble Detector Spectrometer,” *Radiat. Prot. Dosimetry*, vol. 55, no. 1, pp. 23–30, Aug. 1994.
[21] A. R. Green, H. R. Andrews, L. G. I. Bennett, E. T. H. Clifford, H. Ing, G. Jonkmans, B. J. Lewis, R. A. Noulty, and E. A. Ough, “Bubble detector characterization for space radiation,” *Acta Astronaut.*, vol. 56, no. 9–12, pp. 949–960, 2005.
[22] S.-L. Guo, “Bubble detector investigations in China,” *Radiat. Prot. Dosimetry*, vol. 120, no. 1–4, pp. 491–494, Sep. 2006.
[23] A. Miller, R. Machrafi, E. Benton, H. Kitamura, and S. Kodaira, “Comparison of the space bubble detector response to space-like neutron spectra and high energy protons,” *Acta Astronaut.*, vol. 151, pp. 1–6, Oct. 2018.
[24] K. Alikaniotis, M. Severgnini, G. Giannini, and V. Milan, “Measurements of The Parasitic Neutron Dose at Organs From Medical LINACS at Different Energies By Using Bubble Detectors,” *Radiat. Prot. Dosimetry*, vol. 180, no. 1–4, pp. 267–272, Aug. 2018.
[25] B. Mukherjee, R. Hentschel, J. Lambert, and J. Farr, “32 Measurement of Parasitic Neutron Field in The Treatment Environment of a Varian CLINAC 2100 Medical LINAC Using Superheated Bubble Detectors,” *Radiother. Oncol.*, vol. 102, p. S9, Mar. 2012.
[26] L. Bourgois, D. Delacroix, and A. Ostrowsky, “Use of Bubble Detectors to Measure Neutron Contamination of a Medical Accelerator Photon Beam,” *Radiat. Prot. Dosimetry*, vol. 74, no. 4, pp. 239–246, Dec. 1997.
[27] C. G. Orton, *Radiation dosimetry: physical and biological aspects*. 1986.
[28] J. Y. Choi, C. H. Lyoo, J. S. Kim, K. M. Kim, M. Lee, and Y. H. Ryu, “Biodistribution and Radiation Dosimetry of [18F]Mefway in Humans,” *Mol. Imaging Biol.*, vol. 18, no. 6, pp. 803–806, Dec. 2016.
[29] A. D. Martin, A. D. Martin, S. A. Harbison, K. Beach, and P. Cole, *An introduction to radiation protection*, Sixth edition. London: Hodder Arnold, 2012.
[30] L. Lindborg and A. Waker, *Microdosimetry: experimental methods and applications*. Boca Raton: CRC Press, Taylor & Francis Group, 2017.
[31] H. H. Rossi and M. Zaider, *Microdosimetry and its applications*. Berlin: Springer-Verlag Berlin, 2012.
[32] F. H. Attix, *Introduction to radiological physics and radiation dosimetry*. New York: Wiley, 1986.
[33] A. Endo on behalf of ICRU Report Committee 26 on Operational Radiation Protection Quantities for External Radiation, “Operational quantities and new approach by ICRU,” *Ann. ICRP*, vol. 45, no. 1_suppl, pp. 178–187, Jun. 2016.

[34] R. M. Ribeiro and D. Souza-Santos, “Comparison of the neutron ambient dose equivalent and ambient absorbed dose calculations with different GEANT4 physics lists,” *Radiat. Phys. Chem.*, vol. 139, pp. 179–183, Oct. 2017.
[35] J. Leake, “The effect of ICRP (74) on the response of neutron monitors,” *Nucl. Instrum. Methods Phys. Res. Sect. Accel. Spectrometers Detect. Assoc. Equip.*, vol. 421, no. 1–2, pp. 365–367, Jan. 1999.
[36] S. E. Andreevsky, V. D. Kuznetsov, and V. M. Sinelnikov, “Registration of the Atmospheric Gamma Radiation on Board the Russian Segment of the International Space Station,” *Pure Appl. Geophys.*, vol. 174, no. 3, pp. 1091–1099, Mar. 2017.
[37] C. Leroy and P.-G. Rancoita, *Principles of radiation interaction in matter and detection*. Hackensack, NJ: World Scientific, 2004.
[38] K. Wang and B. Shi, “Calculation of mean projected range and range straggling of heavy ions in polyatomic targets,” *J. Phys. Appl. Phys.*, vol. 23, no. 10, pp. 1282–1289, Oct. 1990.
[39] E. Fermi, S. Esposito, and O. Pisanti, *Neutron physics for nuclear reactors: unpublished writings*. Singapore ; London: World Scientific, 2010.
[40] R. Machrafi, A. L. Miller, and N. Khan, “New approach to neutron spectrometry with multi-element scintillator,” *Radiat. Meas.*, vol. 80, pp. 10–16, Sep. 2015.
[41] H. T. Nguyen-Truong, “Modified Bethe formula for low-energy electron stopping power without fitting parameters,” *Ultramicroscopy*, vol. 149, pp. 26–33, Feb. 2015.
[42] G. Laczko, V. Dangendorf, M. Krämer, D. Schardt, and K. Tittelmeier, “High-resolution heavy ion track structure imaging,” *Nucl. Instrum. Methods Phys. Res. Sect. Accel. Spectrometers Detect. Assoc. Equip.*, vol. 535, no. 1–2, pp. 216–220, Dec. 2004.
[43] A. Chatterjee and H. J. Schaefer, “Microdosimetric structure of heavy ion tracks in tissue,” *Radiat. Environ. Biophys.*, vol. 13, no. 3, pp. 215–227, Oct. 1976.
[44] D. Harder, R. Blohm, and M. Kessler, “Restricted LET Remains a Good Parameter of Radiation Quality,” *Radiat. Prot. Dosimetry*, vol. 23, no. 1–4, pp. 79–82, Jun. 1988.
[45] F. A. Cucinotta, R. Katz, J. W. Wilson, and R. Dubey, “Heavy Ion Track Structure Calculations of Radial Dose in Arbitrary Materials.,” 1995.
[46] R. Katz, F. A. Cucinotta, and C. X. Zhang, “The calculation of radial dose from heavy ions: predictions of biological action cross sections,” *Nucl. Instrum. Methods Phys. Res. Sect. B Beam Interact. Mater. At.*, vol. 107, no. 1–4, pp. 287–291, 1996.
[47] J. Kiefer and H. Straaten, “A model of ion track structure based on classical collision dynamics,” *Phys. Med. Biol.*, vol. 31, no. 11, pp. 1201–1209, 1986.
[48] E. Benton, “Comparison between Experimental Measurements of Radial Dose Distributions and Predictions from three Track Structure Models,” *OSU Phys. Dept*, vol. PHYS6010-353, no. Course notes, 2009.
[49] W. Gieszczyk, P. Bilski, P. Olko, and B. Obryk, “Radial distribution of dose within heavy charged particle tracks – Models and experimental verification using LiF:Mg,Cu,P TL detectors,” *Radiat. Meas.*, vol. 71, pp. 242–246, Dec. 2014.
[50] M. N. Varma, “Review of radial dose measurement technique and data,” *Int. J. Radiat. Appl. Instrum. Part Nucl. Tracks Radiat. Meas.*, vol. 16, no. 2–3, pp. 135–139, Jan. 1989.
[51] S. Tsuda, T. Sato, and T. Ogawa, “Measurement of The Stochastic Radial Dose Distribution For A 30-MeV Proton Beam Using a Wall-Less Tissue-Equivalent Proportional Counter,” *Radiat. Prot. Dosimetry*, p. ncv285, May 2015.

[52] J. Chen, A. Keller, and H. Rossi, “Radially restricted linear energy transfer for high-energy protons: a new analytical approach,” *Radiat Env. Biophys*, vol. 33, no. 3, pp. 181–187, Sep. 1994.
[53] S. C. Roy, R. E. Apfel, and Y.-C. Lo, “Superheated drop detector: A potential tool in neutron research,” *Nucl. Instrum. Methods Phys. Res. Sect. Accel. Spectrometers Detect. Assoc. Equip.*, vol. 255, no. 1–2, pp. 199–206, Mar. 1987.
[54] R. Sarkar, P. K. Mondal, M. Datta, and B. K. Chatterjee, “Note: A new optical method for the detection of bubble nucleation in superheated droplet detector,” *Rev. Sci. Instrum.*, vol. 88, no. 6, p. 066106, Jun. 2017.
[55] A. Green, B. Ough, B. Lewis, L. Bennett, H. Andrews, H. Clifford, H. Ing, R. Noulty, and G. Jonkmans, “Bubble Detector Characterization for Space Radiation – Ground-Based Study,” Canadian Space Agency (CSA), Ottawa, ON, 00-SCI-1180, Mar. 2003.
[56] F. d’Errico, W. G. Alberts, E. Dietz, G. Gualdrini, J. Kurkdjian, P. Noccioni, and B. R. L. Siebert, “Neutron Ambient Dosimetry with Superheated Drop (Bubble) Detectors,” *Radiat. Prot. Dosimetry*, vol. 65, no. 1, pp. 397–400, Jun. 1996.
[57] “Bubble detector reader BDR-III manual.” Bubble Technology Industries, Jan-2010.
[58] M. Das and N. Biswas, “Detection of bubble nucleation event in superheated drop detector by the pressure sensor,” *Pramana*, vol. 88, no. 1, Jan. 2017.
[59] F. Vanhavere, M. Loos, and H. Thierens, “The Life Span of the BD-PND Bubble Detector,” *Radiat. Prot. Dosimetry*, vol. 85, no. 1, pp. 27–30, Sep. 1999.
[60] W. Rosenstock, J. Schulze, T. Köble, G. Kruzinski, P. Thesing, G. Jaunich, and H. L. Kronholz, “Estimation of Neutron Energy Spectra with Bubble Detectors: Potential and Limitations,” *Radiat. Prot. Dosimetry*, vol. 61, no. 1–3, pp. 133–136, Aug. 1995.
[61] V. P. Bramblevski, F. Spurn, and V. E. Dudkin, “Neutron Spectrometry with Bubble Damage Neutron Detectors,” *Radiat. Prot. Dosimetry*, vol. 64, no. 4, pp. 309–311, May 1996.
[62] H. R. Andrews, “LET dependence of bubble detector response to heavy ions,” *Radiat. Prot. Dosimetry*, vol. 120, no. 1–4, pp. 480–484, Apr. 2006.
[63] F. Vanhavere, H. Thierens, and M. Loos, “Testing the Temperature Compensated BD-PND Bubble Detector,” *Radiat. Prot. Dosimetry*, vol. 65, no. 1, pp. 425–428, Jun. 1996.
[64] D. Shahbazi-Gahrouei, S. Setayandeh, and M. Gholami, “A review on natural background radiation,” *Adv. Biomed. Res.*, vol. 2, no. 1, p. 65, 2013.
[65] D. Thomas, R. Bedogni, R. Méndez, A. Thompson, and A. Zimbal, “Revision Of ISO 8529—Reference Neutron Radiations,” *Radiat. Prot. Dosimetry*, pp. 1–4, Sep. 2017.
[66] D. H. Hathaway, “The Solar Cycle,” *Living Rev. Sol. Phys.*, vol. 12, no. 1, Dec. 2015.
[67] J. Heirtzler, “The future of the South Atlantic Anomaly and implications for radiation damage in space,” *J. Atmospheric Sol.-Terr. Phys.*, vol. 64, no. 16, pp. 1701–1708, Nov. 2002.
[68] P. Jiggens, A. Varotsou, P. Truscott, D. Heynderickx, F. Lei, H. Evans, and E. Daly, “The Solar Accumulated and Peak Proton and Heavy Ion Radiation Environment (SAPPHIRE) Model,” *IEEE Trans. Nucl. Sci.*, vol. 65, no. 2, pp. 698–711, Feb. 2018.
[69] T. Armstrong and B. Colborn, “Predictions of secondary neutrons and their importance to radiation effects inside the international space station,” *Radiat. Meas.*, vol. 33, no. 3, pp. 229–234, 2001.

[70] L. H. Heilbronn, T. B. Borak, L. W. Townsend, P.-E. Tsai, C. A. Burnham, and R. A. McBeth, "Neutron yields and effective doses produced by Galactic Cosmic Ray interactions in shielded environments in space," *Life Sci. Space Res.*, vol. 7, pp. 90–99, Nov. 2015.
[71] H. Koshiishi, H. Matsumoto, A. Chishiki, T. Goka, and T. Omodaka, "Evaluation of the neutron radiation environment inside the International Space Station based on the Bonner Ball Neutron Detector experiment," *Radiat. Meas.*, vol. 42, no. 9, pp. 1510–1520, 2007.
[72] H. Ing, R. Noulty, and T. McLean, "Bubble detectors—A maturing technology," *Radiat. Meas.*, vol. 27, no. 1, pp. 1–11, Feb. 1997.
[73] H. Ing, T. McLean, R. Noulty, and A. Mortimer, "Bubble Detectors and the Assessment of Biological Risk from Space Radiations," *Radiat. Prot. Dosimetry*, vol. 65, no. 1, pp. 421–424, Jun. 1996.
[74] F. d'Errico and M. Matzke, "Neutron spectrometry in mixed fields: superheated drop (bubble) detectors," *Radiat. Prot. Dosimetry*, vol. 107, no. 1–3, pp. 111–124, Nov. 2003.
[75] T. Němec, "Homogeneous bubble nucleation in binary systems of liquid solvent and dissolved gas," *Chem. Phys.*, vol. 467, pp. 26–37, Mar. 2016.
[76] H. J. Maris, "Introduction to the physics of nucleation," *Comptes Rendus Phys.*, vol. 7, no. 9–10, pp. 946–958, Nov. 2006.
[77] H. Firouzjahi, S. Jazayeri, A. Karami, and T. Rostami, "Bubble nucleation and inflationary perturbations," *J. Cosmol. Astropart. Phys.*, vol. 2017, no. 12, pp. 029–029, Dec. 2017.
[78] S.-L. Guo, T. Doke, D.-H. Zhang, B.-L. Chen, L. Li, N. Hasebe, J. Kikuchi, N. Yasuda, and T. Murakami, "Parameters of 500 MeV/u 56Fe tracks in bubble detector (BD) T-15 – A new technique to estimate the number and diameter of superheated droplets in bubble detectors," *Radiat. Meas.*, vol. 83, pp. 5–11, Dec. 2015.
[79] M. Takada, "Measured proton sensitivities of bubble detectors," *Radiat. Prot. Dosimetry*, vol. 111, no. 2, pp. 181–189, Jul. 2004.
[80] S.-L. Guo, T. Doke, L. Li, B.-L. Chen, D.-H. Zhang, J. Kikuchi, K. Terasawa, M. Komiyama, K. Hara, T. Fuse, N. Yasuda, and T. Murakami, "Comparison between theoretical model and experimental calibrations and its inference for track formation in bubble detectors," *Radiat. Meas.*, vol. 40, no. 2–6, pp. 229–233, 2005.
[81] S.-L. Guo, L. Li, T. Doke, J. Kikuchi, A. Kyan, E. Yoshihira, T. Kato, and T. Murakami, "Characteristics of heavy ion tracks in bubble detectors," *Radiat. Meas.*, vol. 34, no. 1–6, pp. 269–272, 2001.
[82] P. Tume, B. Lewis, L. G. Bennett, and T. Cousins, "Characterisation of neutron-sensitive bubble detectors for application in the measurement of jet aircrew exposure to natural background radiation," *Nucl. Instrum. Methods Phys. Res. Sect. Accel. Spectrometers Detect. Assoc. Equip.*, vol. 406, no. 1, pp. 153–168, Mar. 1998.
[83] M. B. Smith, H. R. Andrews, H. Ing, and M. R. Koslowsky, "Response of the bubble detector to neutrons of various energies," *Radiat. Prot. Dosimetry*, vol. 164, no. 3, pp. 203–209, Apr. 2015.
[84] S.-L. Guo, T. Doke, D.-H. Zhang, L. Li, B.-L. Chen, J. Kikuchi, N. Hasebe, K. Terasawa, K. Hara, T. Fuse, N. Yasuda, and T. Murakami, "Experimental investigation of bubble occurrence and locality distribution of bubble detectors bombarded with high-energy helium ions," *Radiat. Meas.*, vol. 50, pp. 31–37, Mar. 2013.
[85] S.-L. Guo, L. Li, H.-Y. Guo, C.-Q. Tu, Y.-L. Wang, T. Doke, T. Kato, K. Ozaki, A. Kyan, Y. Piao, and T. Murakami, "High energy heavy ion tracks in bubble detectors," *Radiat. Meas.*, vol. 31, no. 1–6, pp. 167–172, Jun. 1999.

[86] H. Ing, “Neutron measurements using bubble detectors — terrestrial and space,” *Radiat. Meas.*, vol. 33, no. 3, pp. 275–286, 2001.
[87] M. B. Smith, S. Khulapko, H. R. Andrews, V. Arkhangelsky, H. Ing, B. J. Lewis, R. Machrafi, I. Nikolaev, and V. Shurshakov, “Bubble-detector measurements in the Russian segment of the International Space Station during 2009-12,” *Radiat. Prot. Dosimetry*, vol. 163, no. 1, pp. 1–13, Jan. 2015.
[88] M. B. Smith, S. Khulapko, H. R. Andrews, V. Arkhangelsky, H. Ing, M. R. Koslowksy, B. J. Lewis, R. Machrafi, I. Nikolaev, and V. Shurshakov, “Bubble-Detector Measurements of Neutron Radiation In The International Space Station: ISS-34 To ISS-37,” *Radiat. Prot. Dosimetry*, p. ncv181, Apr. 2015.
[89] J. F. Ziegler, M. D. Ziegler, and J. P. Biersack, “SRIM – The stopping and range of ions in matter (2010),” *Nucl. Instrum. Methods Phys. Res. Sect. B Beam Interact. Mater. At.*, vol. 268, no. 11–12, pp. 1818–1823, Jun. 2010.
[90] ICRP, “ICRP Publication 74,” *Ann. ICRP*, vol. 26, no. 3–4, pp. 1–3, 1996.
[91] B. Takala, “The ICE House.” Los Alamos Science, 30-Nov-2006.
[92] O. Ploc, T. Dachev, Y. Uchihori, H. Kitamura, and L. Sihver, “Fragmentation from heavy ion beams in HIMAC BIO room calculated with PHITS and measured with Liulin,” 2017, pp. 1–10.
[93] A. Miller, R. Machrafi, and A. Fariad, “Investigation of the LaBr 3 scintillator response to heavy ions,” *Radiat. Meas.*, vol. 115, pp. 43–48, Aug. 2018.
[94] R. M. Haralick and L. G. Shapiro, *Computer and robot vision*. Reading, Mass: Addison-Wesley Pub. Co, 1992.
[95] J. Ilonen, R. Juránek, T. Eerola, L. Lensu, M. Dubská, P. Zemčík, and H. Kälviäinen, “Comparison of bubble detectors and size distribution estimators,” *Pattern Recognit. Lett.*, vol. 101, pp. 60–66, Jan. 2018.
[96] T. Sato, K. Niita, N. Matsuda, S. Hashimoto, Y. Iwamoto, S. Noda, T. Ogawa, H. Iwase, H. Nakashima, T. Fukahori, K. Okumura, T. Kai, S. Chiba, T. Furuta, and L. Sihver, “Particle and Heavy Ion Transport code System, PHITS, version 2.52,” *J. Nucl. Sci. Technol.*, vol. 50, no. 9, pp. 913–923, Sep. 2013.
[97] R. C. Singleterry, S. R. Blattnig, M. S. Clowdsley, G. D. Qualls, C. A. Sandridge, L. C. Simonsen, T. C. Slaba, S. A. Walker, F. F. Badavi, J. L. Spangler, A. R. Aumann, E. Neal Zapp, R. D. Rutledge, K. T. Lee, R. B. Norman, and J. W. Norbury, “OLTARIS: an On-line tool for the assessment of radiation in space,” *Acta Astronaut.*, vol. 68, no. 7–8, pp. 1086–1097, Apr. 2011.
[98] A. J. Tylka, J. H. Adams, P. R. Boberg, B. Brownstein, W. F. Dietrich, E. O. Flueckiger, E. L. Petersen, M. A. Shea, D. F. Smart, and E. C. Smith, “CREME96: a revision of the C_osmic R_ay E_ffects on M_icro-E_lectronics code,” *IEEE Trans. Nucl. Sci.*, vol. 44, no. 6, pp. 2150–2160, Dec. 1997.
[99] A. I. Mrigakshi, D. Matthiä, T. Berger, G. Reitz, and R. F. Wimmer-Schweingruber, “Assessment of galactic cosmic ray models: Assessment of Galactic Cosmic Ray Models,” *J. Geophys. Res. Space Phys.*, vol. 117, no. A8, Aug. 2012.
[100] L. Lund, “High-Performing Simulations of the Space Radiation Environment for the International Space Station and Apollo Missions,” University of Utah, Utah, USA, 2016.
[101] V. Benghin, V. Petrov, M. Panasyuk, and A. Volkov, “Nine Years of The Radiation Monitoring System Operating InService Module of ISS,” 2010.

[102] T. Berger, S. Burmeister, D. Matthiä, B. Przybyla, G. Reitz, P. Bilski, M. Hajek, L. Sihver, J. Szabo, I. Ambrozova, F. Vanhavere, R. Gaza, E. Semones, E. G. Yukihara, E. R. Benton, Y. Uchihori, S. Kodaira, H. Kitamura, and M. Boehme, "DOSIS & DOSIS 3D: radiation measurements with the DOSTEL instruments onboard the Columbus Laboratory of the ISS in the years 2009–2016," *J. Space Weather Space Clim.*, vol. 7, p. A8, 2017.

APPENDICES

Appendix A: Space Bubble Detector Measurements aboard ISS

Table A1:SPND Measurements [14]

Locations and orientations of bubble detectors used during the ISS-16, ISS-18 and ISS-19 expeditions.

Detector label	ISS-16, session 8 ISS-18, session 2 ISS-19, session 1	ISS-16, session 9 ISS-18, session 1 ISS-19, session 2
A01/B01	Pirs module, inside phantom, facing phantom surface	Pirs module, inside phantom, facing phantom centre
A02/B02	Pirs module, inside phantom, facing phantom surface	Pirs module, inside phantom, facing phantom centre
A03/B03	Pirs module, inside phantom, facing phantom surface	Pirs module, inside phantom, facing phantom centre
A04/B04	Service module, starboard cabin	Service module, starboard cabin
A05/B05	Service module, starboard cabin	Service module, starboard cabin
A06/B06	Service module, close to the astronaut working desk	Service module, close to the astronaut working desk
A07/B07	Service module, close to the astronaut working desk	Service module, close to the astronaut working desk
A08/B08	Service module, on the ceiling	Service module, on the ceiling

Table A2: SPND Measurements [14]

Locations of detectors used during the ISS-20 and ISS-21 expeditions.

Session	A09	A10	SBDS
Matroshka	Service module P327	Service module P327	Service module P327
Session 1	Worn by Robert Thirsk	JEM sleeping quarters	Columbus 1A3
Session 2	Worn by Robert Thirsk	JEM sleeping quarters	US laboratory 1S4
Session 3	Worn by Robert Thirsk	JEM sleeping quarters	JPM 1F2 (water shield)
Thirsk	JPM 1F2 forward	JPM 1F2 inboard	JPM 1F2 forward

Table A3: SPND Measurements [87]

Dates, detector configurations and detectors used for measurements during the ISS-22 to ISS-33 missions.

Session	Initialisation date	Retrieval date	Detector configuration	SPND	SBDS
A	9 December 2009	14 December 2009	1	A09, A10	A11–A16
B	26 January 2010	1 February 2010	2	A09, A10	A11–A16
C	22 March 2010	29 March 2010	2	A09, A10	A11–A16
D	21 April 2010	28 April 2010	2	A09	Not used
E	21 May 2010	28 May 2010	3	A09	Not used
F	12 July 2010	19 July 2010	4	A27, A28	A21–A26
G	30 July 2010	6 August 2010	5	A27, A28	A21–A26
H	16 August 2010	23 August 2010	4	A27, A28	A21–A26
I	13 September 2010	20 September 2010	5	A27, A28	A21–A26
J	15 October 2010	21 October 2010	5	A27, A28	A21–A26
K	28 October 2010	6 November 2010	6	A27, A28	A21–A26
L	8 November 2010	19 November 2010	6	A27, A28	Not used
M	22 December 2010	30 December 2010	6	A27, A28	Not used
N	1 February 2011	9 February 2011	6	A27, A28	Not used
O	5 July 2011	13 July 2011	6	A27, A28	Not used
P	8 August 2011	15 August 2011	6	A27, A28	Not used
Q	1 September 2011	8 September 2011	6	A28	Not used
R	8 February 2012	14 February 2012	6	A47, A48	A41–A46
S	29 February 2012	7 March 2012	6	A47, A48	Not used
T	28 March 2012	3 April 2012	6	A47, A48	Not used
U	21 May 2012	28 May 2012	6	A47, A48	Not used

Table A4: Space Bubble Detector Locations ISS-22 to ISS-33 missions [87]

Detector configuration	Detector locations		
	SBDS	SPND 1	SPND 2
1	Pirs module, panel 1, near phantom	Pirs module, inside phantom	Pirs module, inside phantom
2	Service module, panel 443, below the illuminator	Service module, panel 443, left of the SBDS	Service module, panel 443, right of the SBDS
3	Service module, panel 240	Service module, left of the SBDS	Not used
4	Service module, on the top of the radiation shield	Service module, panel 442, left of the SBDS (unshielded)	Service module, on the top of the radiation shield, right of the SBDS
5	Service module, on the radiation shield (cabin side)	Service module, panel 443, left of the SBDS (unshielded)	Service module, right of the SBDS, on the radiation shield (cabin side)
6	Service module, on the radiation shield (between shield and illuminator)	Service module, panel 443, left of the SBDS (unshielded)	Service module, right of the SBDS, on the radiation shield (between shield and illuminator)

Table A5: Space Bubble Detector Locations ISS-34 to ISS-40 missions [88]

Session	Initialisation date	Retrieval date	Location, SBDS 1	Location, SBDS 2
A	27 December 2012	3 January 2013	Columbus	Service module
B	18 January 2013	25 January 2013	JEM	Service module
C	11 February 2013	18 February 2013	US laboratory	Service module
D	5 March 2013	12 March 2013	Node 2	Service module
E	3 April 2013	10 April 2013	Service module	Service module
F	1 May 2013	8 May 2013	MRM1	MRM1
G	30 May 2013	6 June 2013	US laboratory	MRM1
H	27 June 2013	5 July 2013	US laboratory	MRM1
I	12 July 2013	19 July 2013	MRM1	MRM1
J	25 July 2013	2 August 2013	JEM	MRM1
K	23 August 2013	30 August 2013	JEM	MRM1
L	16 September 2013	23 September 2013	MRM1	MRM1
M	15 October 2013	22 October 2013	MRM1	MRM1

Appendix B: International Space Station Information

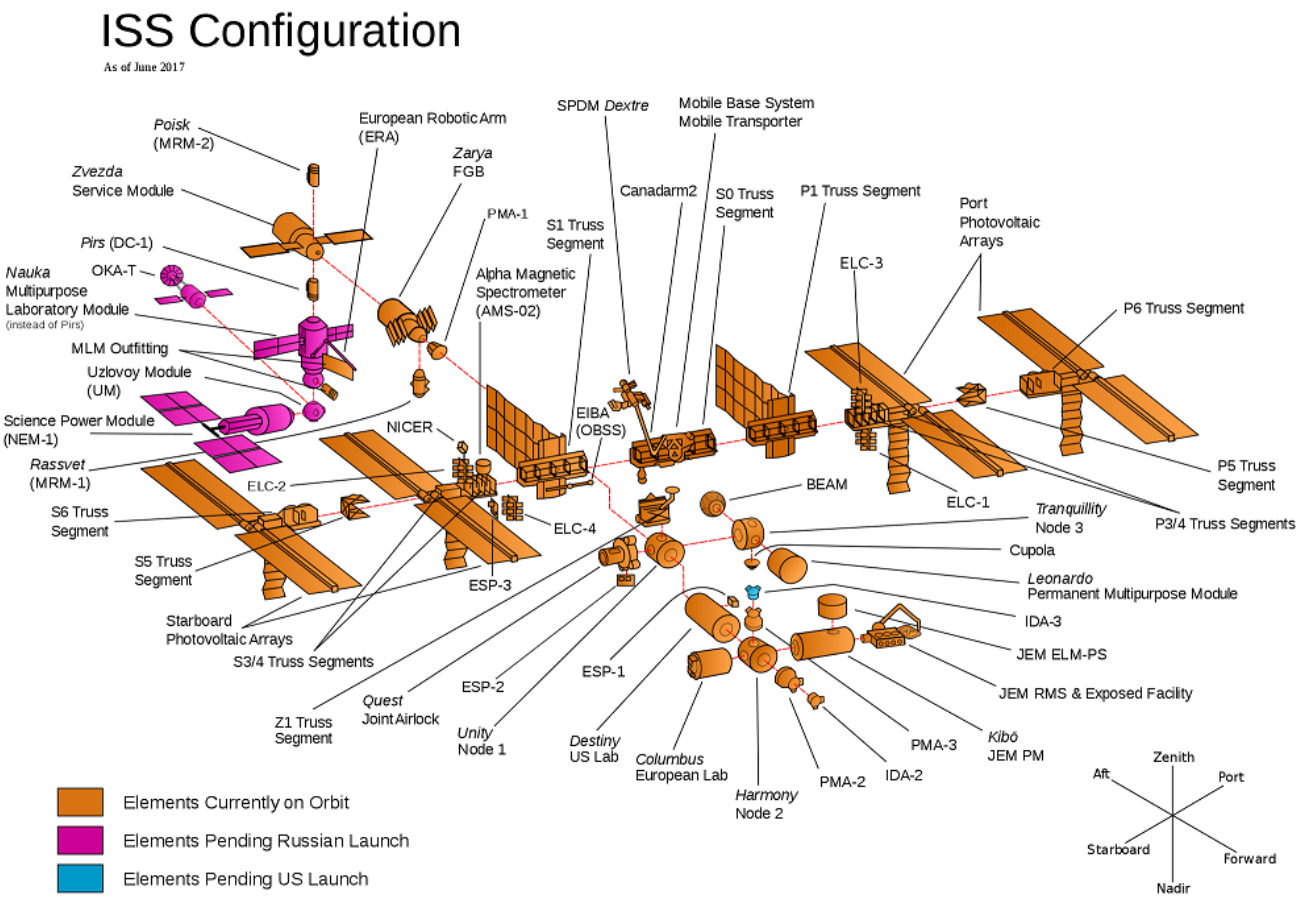

Figure B1: Diagram of International Space Station (exploded view, public domain image)

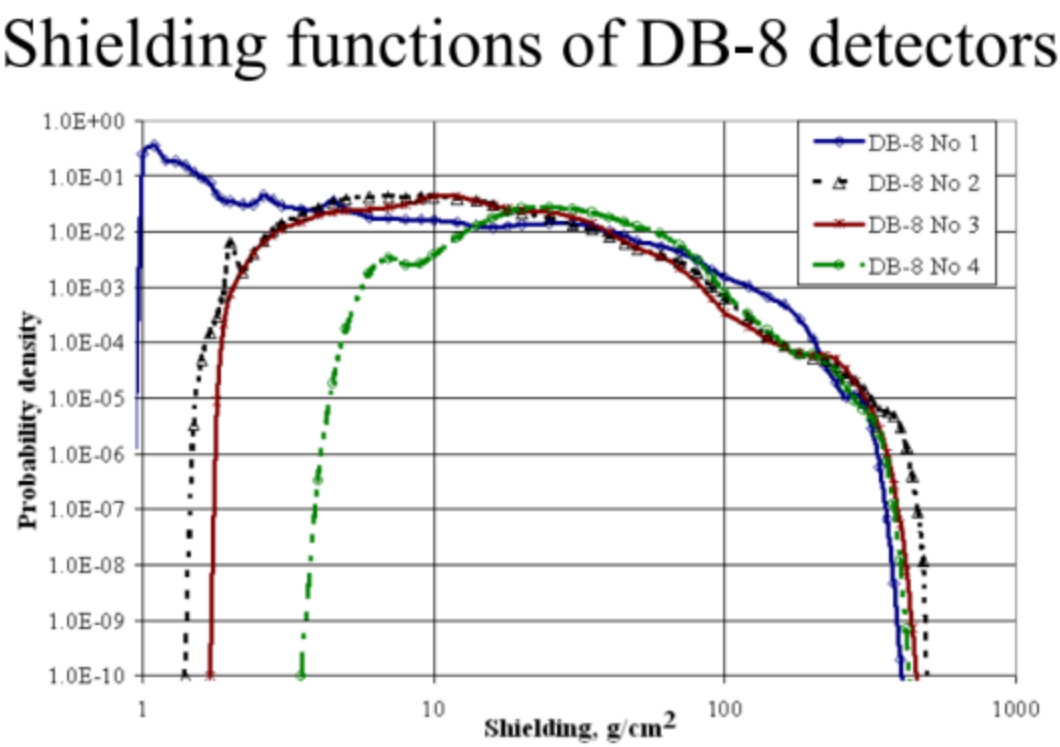

Figure B2: Shielding distribution of DB-8 detectors in ISS Service Module [101]

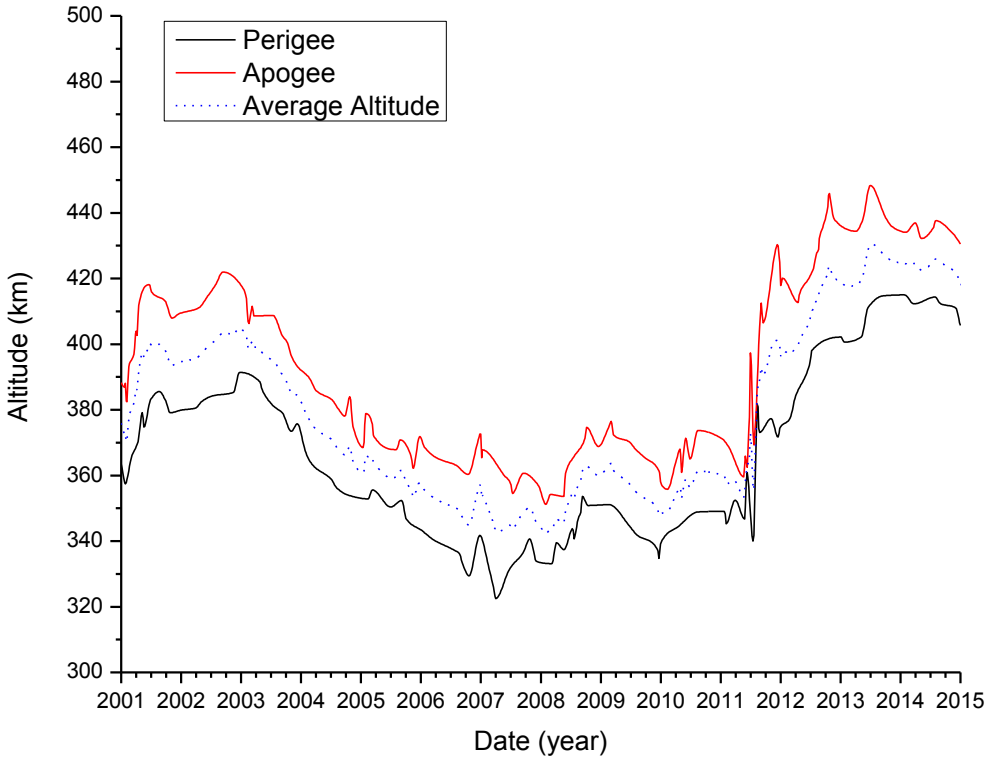

Figure B3: ISS Altitude from 2001 to 2015

Appendix C:HIMAC Bragg Curve Measurements

Table C1: Heavy Charged Particle Experimental Range in PMMA with Calculated Energy and Range in H_2O

Ion	Range in PMMA	Range in H_2O: SRIM calculation	Calculated Energy
H	34.0 mm	40.16 mm	70 (MeV/nucleon)
He	125.5 mm	144.37 mm	143 (MeV/nucleon)
C	222.0 mm	256.9 mm	385 (MeV/nucleon)
O	165.0 mm	190.86 mm	385 (MeV/nucleon)
Ne	124.5 mm	143.84 mm	371 (MeV/nucleon)
Si	118.0 mm	136.48 mm	441 (MeV/nucleon)
Fe	63.0 mm	37.04 mm	411 (MeV/nucleon)

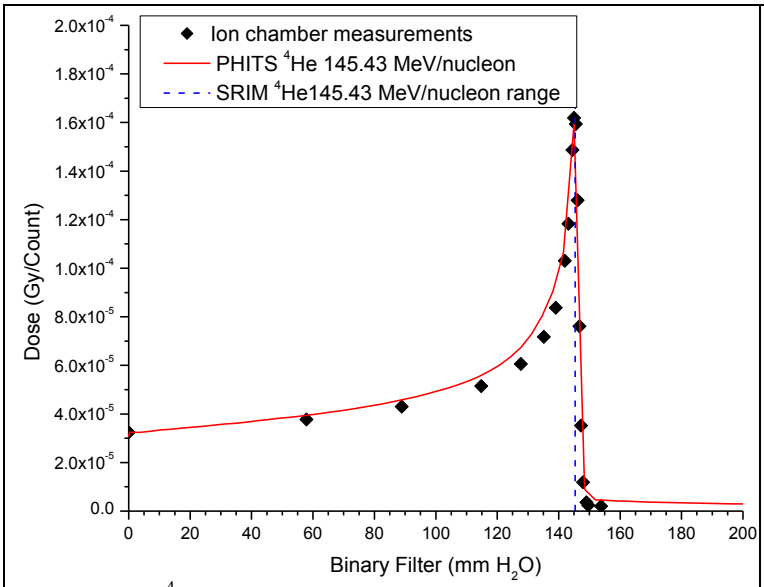

Figure C1: ^{4}He Bragg Curve measurement at HIMAC with PHITS simulation

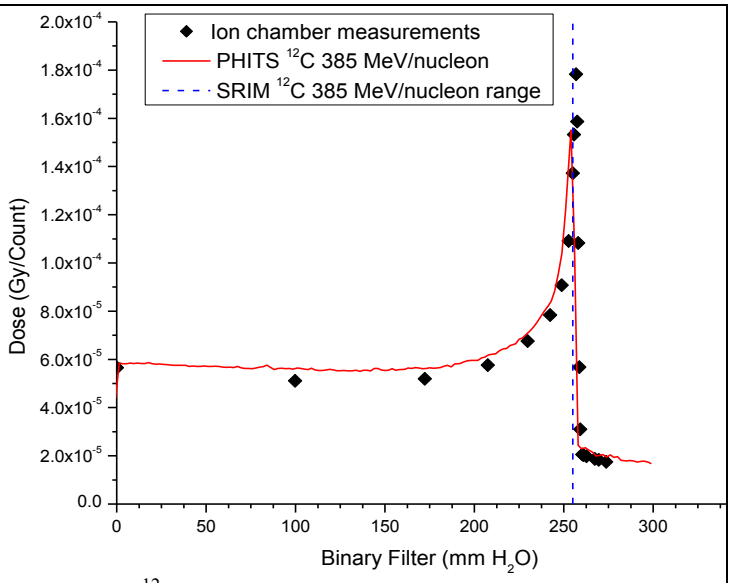

Figure C2: ^{12}C Bragg Curve measurement at HIMAC with PHITS simulation

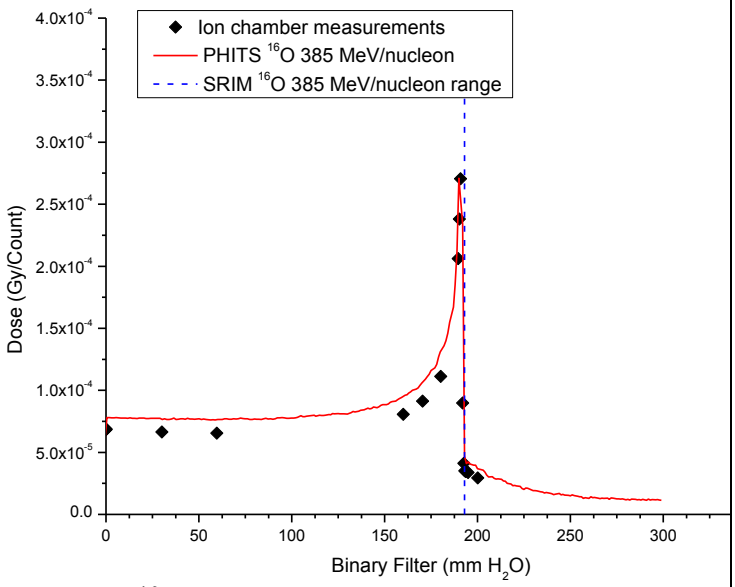

Figure C3: ^{16}O Bragg Curve measurement at HIMAC with PHITS simulation

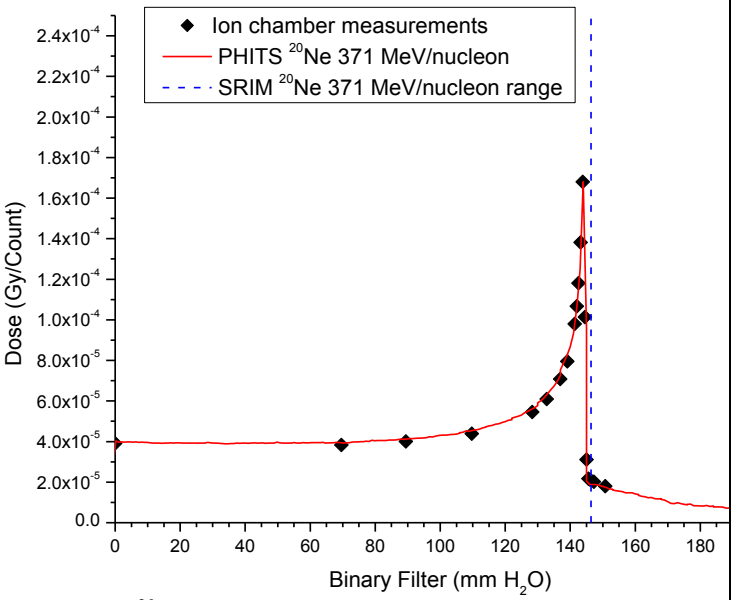

Figure C4: ^{20}Ne Bragg Curve measurement at HIMAC with PHITS simulation

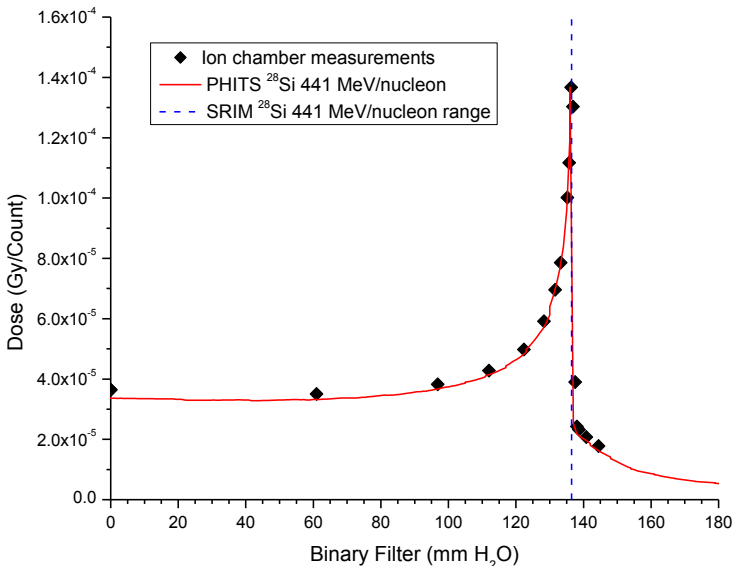

Figure C5:^{28}Si Bragg Curve measurement at HIMAC with PHITS simulation

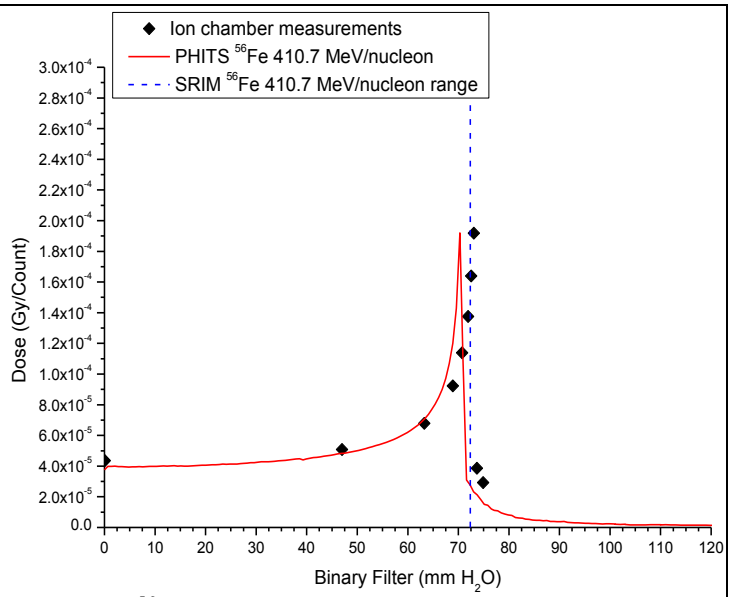

Figure C6:^{56}Fe Bragg Curve measurement at HIMAC with PHITS simulation

Appendix D: MATLAB Program Validation

Verification of the MATLAB LET analysis program

A test case has been constructed to verify the bubble counting and range determination of the MATLAB program designed in this thesis. A bubble reader image was recorded for a detector with no bubbles present. Twelve bubbles were added to the image, 230 pixels from the cap of the detector corresponding to a depth of 20.7 mm in the detector (moving from left to right in the image). The input image is shown in Figure D1 along with the identified bubbles highlighted with overlaid circles. The MATLAB program correctly counted twelve bubbles. The histogram of the number of bubbles located along the horizontal are plotted in Figure D2. The end of the range was identified by the program as 20.9 ± 0.9 mm which is in good agreement with the bubble positions. The estimated end of range position is also shown in Figure D1 as a curve overlaid on the image and it intersects with all twelve bubbles.

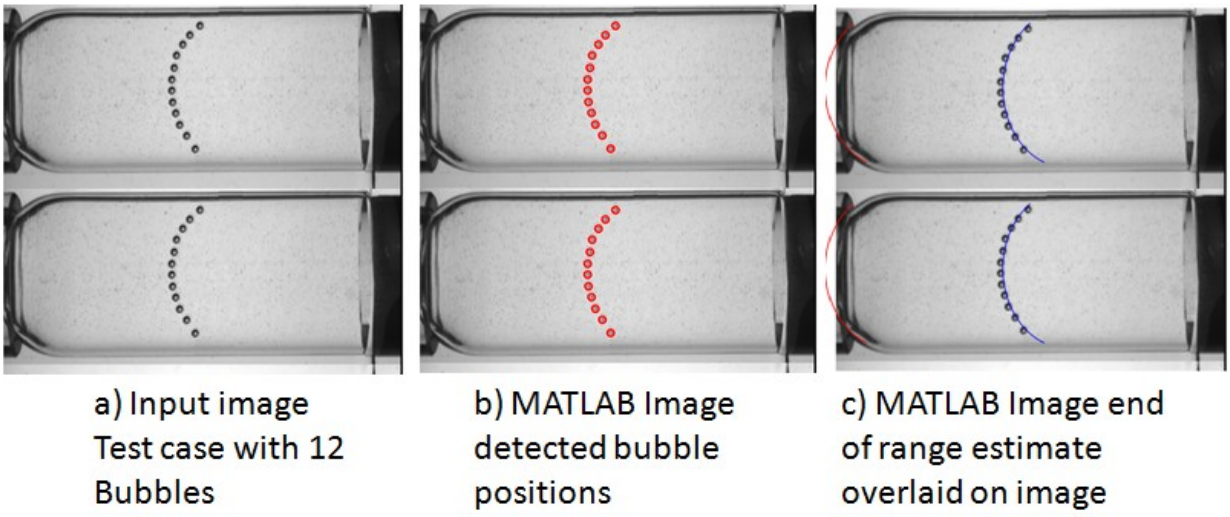

Figure D1: Bubble detector image and MATLAB program estimation of bubble position and end of the range

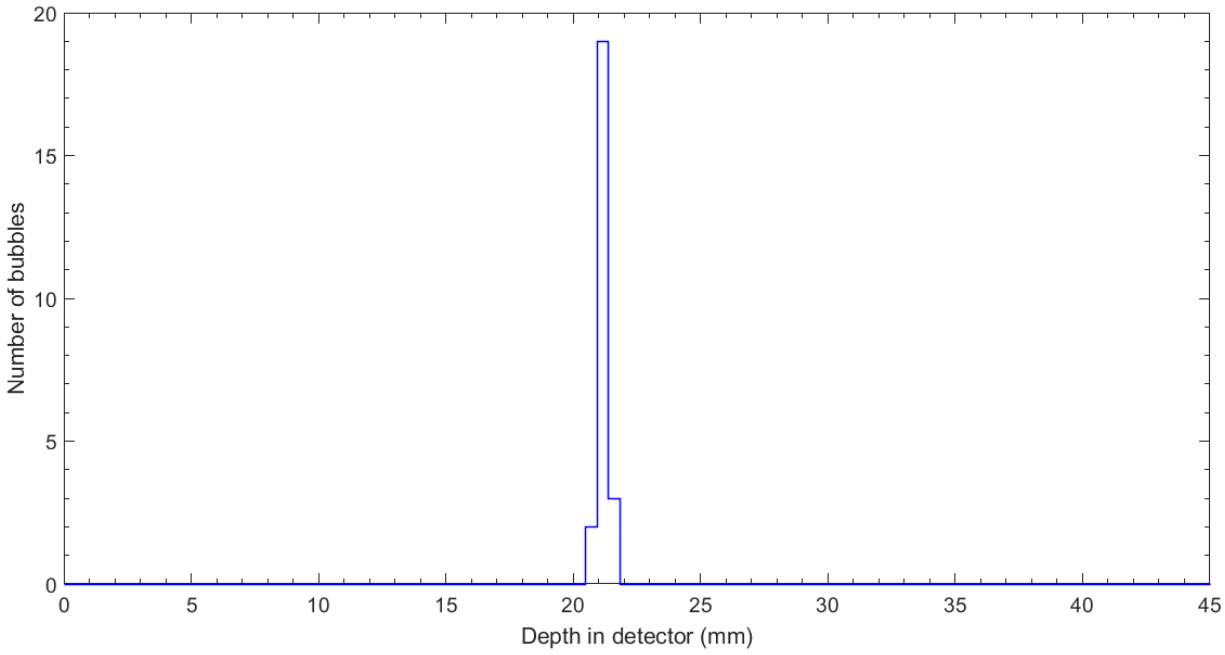

Figure D2: MATLAB program counting of bubbles along the horizontal axis for test case image

The accuracy of the MATLAB program in detecting bubble positions and identifying the end of the range positions in all bubble detector experiments has been further verified using two methods. The first is a comparison of the total number of bubbles identified in each experiment with the value given by the BDRIII reader (instrument). The second method is to compare the end of the range position identified by the MATLAB program to the particle range calculated by SRIM for each experiment. Figure D3 shows the number of bubbles counted with the MATLAB program plotted against the number of bubbles counted with the BDRIII reader for all experiments in this work. There is a good overall one-to-one correspondence where almost all of the MATLAB readings are within 20 % of the BDRIII readings. The average relative difference in the number of bubbles counted is less than 10 %. In approximately 1/2 of the experiments, the

relative difference between the number of bubbles counted in the MATLAB and the number of bubbles counted in the BDRIII reader was less than 5 %. This indicates an acceptable level of accuracy for identifying bubbles using the MATLAB program.

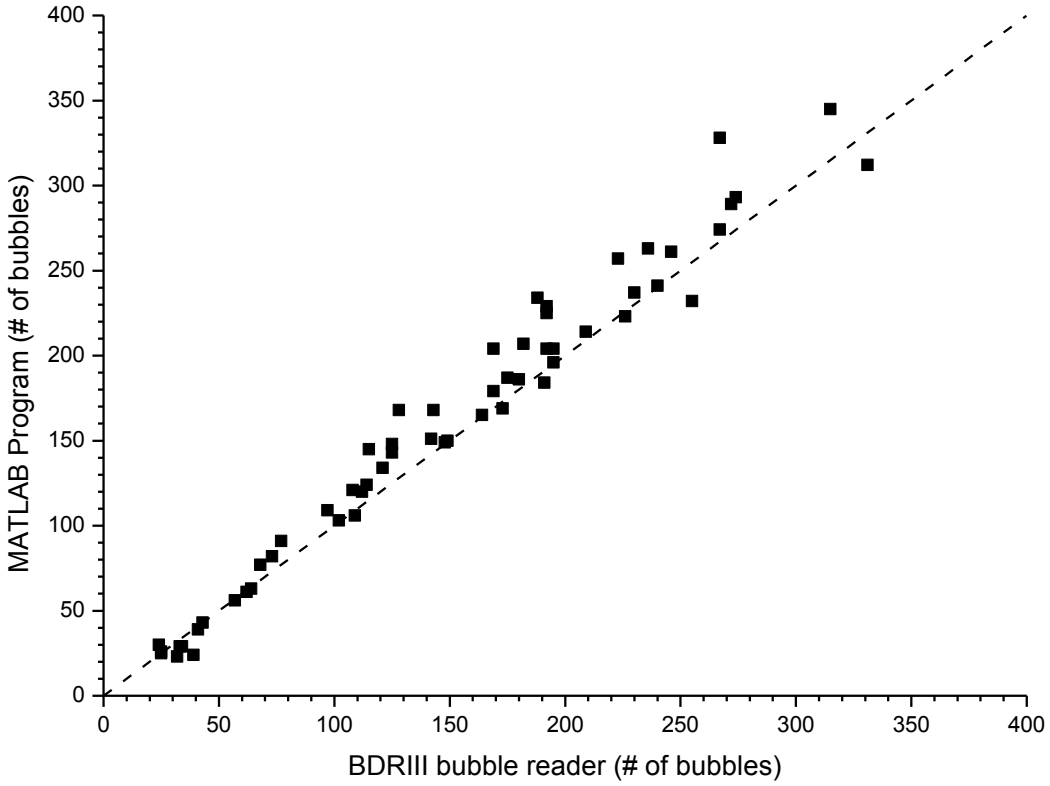

Figure D3: MATLAB program bubble count compared to BDRIII reader

The end of the range estimate using the MATLAB program is plotted in Figure D4 for all experiments as a function of the end of the range calculated by SRIM. This plot also shows a good one-to-one correspondence. The average relative difference between the SRIM calculated range and the MATLAB program identified end of the range is 3.7 %. All experiments have a difference less than 16 % and ¾ of the experiments have a relative difference less than 5 %. The

average absolute difference between the SRIM calculated end of the range and the MATLAB program estimated end of the range is less than 0.9 mm.

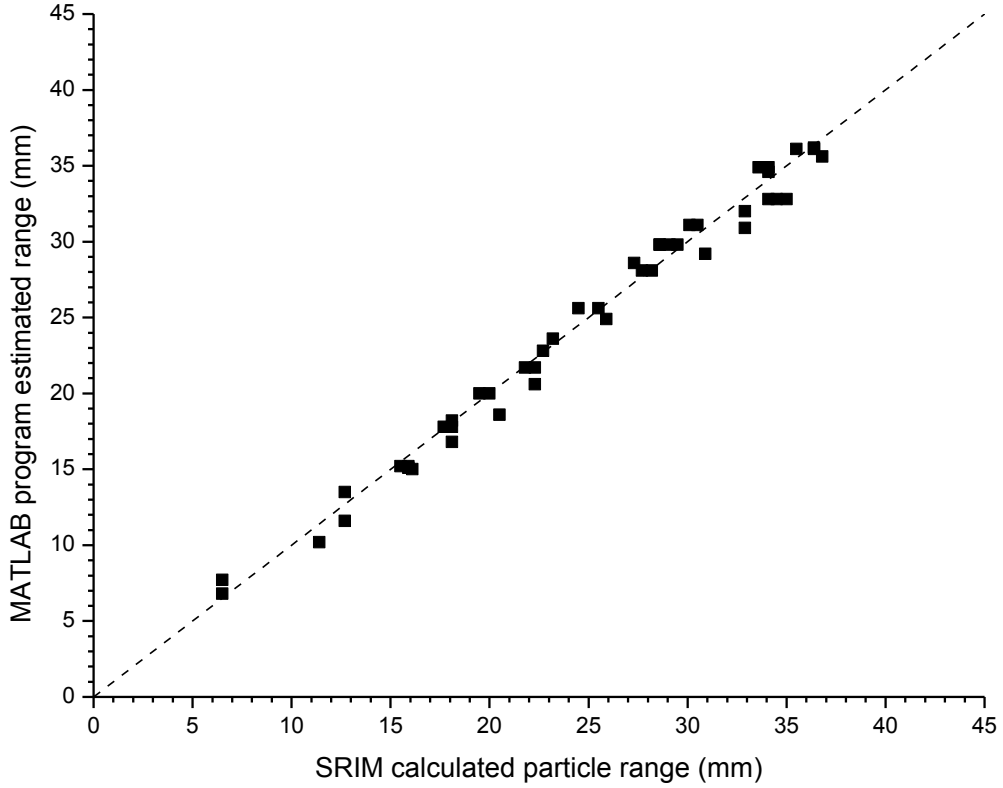

Figure D4: MATLAB program compared to SRIM calculated range for all experiments

Verification of the MALTAB SBD bubble count model

The bubble count model described in Section 4.4 has been tested and validated for SBD measurements using the known response to AmBe neutrons. The MATLAB SBD bubble count model uses the neutron response function $R_n(E)$ from Figure 30 with equation 3.7 and the particle fluence $\Phi(E)$. A test case has been constructed using the ISO 8529.2 recommended AmBe neutron spectrum (see Figure 6) with a SBD exposure that would produce a total equivalent dose of 1,000 μSv. For a SBD with a standard sensitivity of 0.1 bubbles/μSv, this exposure would produce 100 bubbles. The MATLAB SBD bubble count model has been performed for the total fluence of AmBe neutrons required for an equivalent dose of 1,000 μSv. This has been calculated using the NCRP38 dose conversion factors and the ICRP74 ambient dose equivalent conversion factors. The model was also performed using the NCRP 38 weighted average conversion factor for the AmBe spectrum weighted average energy (4.15 MeV) with an equivalent dose conversion factor of $3.7 \times 10^{-5} \mathrm{mRem} \cdot \mathrm{cm}^2$. This is the method used for SBD calibration. The recommended weighted average equivalent dose conversion factor from ICRU66 for AmBe neutrons (4.11×10^{-4} Sv $\cdot \mathrm{cm}^2$) was also used for comparison. The results are shown in Table D1.

Table D1: MATLAB bubble count model for SBD exposed to AmBe source

Dose Equivalent Conversion Factor	Total AmBe neutron fluence to give 1,000 μSv equivalent dose (neutrons/cm^2)	Number of bubbles produced in MATLAB bubble count model for SBD with S_{AmBe} = 0.1 bubbles/μSv
NCRP38 weighted average conversion factor for AmBe source (4.15 MeV neutrons)	2.70×10^6	93.6 ± 9.7
NCRP38	2.68×10^6	92.9 ± 9.6
ICRP74, $H^*(10)$	2.48×10^6	86.0 ± 9.3
ICRU66 AmBe conversion factor	2.43×10^6	84.2 ± 9.2
Expected value from SBD calibration	2.68×10^6	100 ± 10

The results in Table D1 are all within 20 % of the expected 100 bubbles. The MATLAB bubble count model prediction was found to be 90 ± 10 bubbles for the NCRP38 weighted average conversion factor calculation with a 6.4 % difference (under prediction) from the expected number of bubbles. In fact, the SBD bubble BDRIII reader has a stated uncertainty of ± 10% for bubble counting experiments so the number of bubbles predicted in the MATLAB program is consistent with the number of bubbles expected for a SBD measurement within the level of uncertainty using all four dose calculation models. The OLTARIS bubble count model has been shown to be consistent with SBD measurements aboard the ISS with an overall difference of about 6 % (over prediction). Using an estimated Poisson distribution, the uncertainty of individual SBD measurements is approximately ± 30 % in most of the OLTARIS bubble count models (10 ± 3 bubbles/day) which is slightly larger than, but comparable to the differences in Table D1.

Appendix E: Discussion of Uncertainties

Uncertainty in LET threshold for bubble formation

The LET threshold for bubble formation has been determined in this work using energy, range and LET calculations in SRIM based on the distribution of bubbles in individual experiments. The typical error between SRIM calculations and experiments for energy, range and LET of heavy ions stopping in matter is less than 5% [89]. However, for the bubble detector measurements in this work, the measured LET threshold has a much larger uncertainty. This is because the LET of bubble formation is based on determining the location of the bubble front which may be spread out due to ion straggling and difficult to discern among spurious bubbles formed before and after the Bragg peak due to high LET secondary particles. The bubble positions can only be determined to within ± 0.9 mm. Table E1 shows an example of how this position uncertainty leads to the total uncertainty of the LET threshold for an individual experiment with carbon ions in SBD (see Table 5).

Table E1: Uncertainty in LET threshold measurement for carbon ion

Bubble front (mm from edge of detector)	End of range (mm from edge of detector)	Range at LET threshold (mm)	LET for mean range (keV/μm)	LET for maximum range (keV/μm)	LET for minimum range (keV/μm)	σ_{LET} (keV/μm)
25.5 ± 0.9	27.3 ± 0.9	1.8±1.6	93	167	75	± 74

The measured value of the LET threshold in this experiment is therefore 90 ± 70. The uncertainty of a single measurement is large. Repeated independent experiments with the same uncertainty were carried out. The uncertainty in the average value measured in N experiments with error σ is given by the following equation;

$$\sigma_{\bar{x}} = \frac{\sigma}{\sqrt{N}} \qquad \text{(Equation E1)}$$

There were ten experiments so the average was found to be 80 keV and $\sigma_{\bar{x}}$ = 20 keV. Therefore the LET threshold for carbon ions in SBD was found to be 80 ± 20 keV/µm.

The uncertainty in the average track energy density model from Secion 4.3 was determined by the uncertainty in the LET thresholds. The average track energy density was calculated for the mean, minimum and maximum LET threshold using the Chatterjee, Katz and Keifer track structure models. The mean value and the standard deviation of the average track energy density was calculated for all three models. This is summarized in Table E2.

Table E2: Uncertainty in $D_{threshold}$

Track structure model	$D_{threshold}$ (Gy)	$\sigma D_{threshold}$ (Gy)
Chatterjee	0.08	± 0.04
Katz	0.06	± 0.02
Keifer	0.06	± 0.02

The LET threshold model for SBD was calculated using SRIM with these ion track energy densities and equations 3.3 to 3.5. The best fit, maximum and minimum models were determined and the results are presented in Figure 68 and in Appendix F, Figure F2.

Uncertainty in SBD response functions

The uncertainty in all measured bubble detector response experiments was determined by the statistical variation observed in successive identical measurements.

Table E3: Uncertainty in response function R_{He}

Plastic Scintillator fluence (He/cm^2)	Detector Sensitivity S_{AmBe} (bubbles/μSv)	Number of bubbles	Normalized Sensitivity $\left(\frac{bubbles}{He/cm^2}\right)$
5.25×10^{6}	0.018	497	5.26×10^{-5}
1.11×10^{6}	0.018	192	9.60×10^{-5}
5.29×10^{6}	0.018	435	4.57×10^{-5}
1.79×10^{6}	0.012	195	9.07×10^{-5}

The sensitivity of SBD to ions at this energy is calculated as the mean value with an uncertainty given by the standard deviation of the measured values. Therefore the sensitivity of SBD to He ions at this energy is $(7.1\pm 2.6)\times10^{-5}\ \frac{bubbles}{He/cm^2}$.

Uncertainty in OLTARIS bubble count model

The error in the OLTARIS bubble count model is determined by the uncertainty in all bubble response measurements and the uncertainty in the particle spectra. However, the uncertainty in the particle spectra is largely unknown because the difference between the OLTARIS spectra and the actual particle spectra present aboard the ISS could be very large for individual simulations. Therefore, Poisson statistics have been used to estimate the level of uncertainty involved with individual measurements. The Poisson distribution applies counting events where the number of events is large and the probability of success is low. For bubble detector measurements aboard the ISS, the number of events is the number of particles that pass through the bubble detector and the number of "successful" events is the number of bubbles that

are expanded into visible bubbles and counted. The Poission distribution has been show to fit the experimental measurements fairly well. The model results are calculated as the number of bubbles produced in a one day measurement and the total number of bubbles produced. The relative uncertainty of individual particle contributions may be large, especially for the heavy ions which were all calculated to produce < 1 % of the total number of bubbles. The results from Table 17 are shown in Table E4 with the original calculated values and the uncertainty calculated for each particle by propagation of errors.

Table E4: Relative particle contributions to OLTARIS bubble count model

Particle:	neutron	proton	He	C	O	Ne	Si	Fe
Bubbles per day	8.04	1.38	0.051	0.0017	0.0015	6.5×10^{-4}	0.0022	0.035
$\sigma_{bubbles}$ (per day)	± 2.8	± 1.2	± 0.2	± 0.04	± 0.04	± 0.03	± 0.05	± 0.2
Contribution to the total number of bubbles in the OLTARIS bubble count model (%)	84.5%	14.5%	0.5%	0.02%	0.02%	0.007%	0.02%	0.4%
$\sigma_{\%}$	± 2.4 %	± 7.7 %	± 2%	± 0.4%	± 0.4%	± 0.3%	± 0.5%	± 2%

The calculation of the proton contribution uncertainty is provided as an example. The OLTARIS bubble count model indicates the number of bubbles produced due to protons in one day is, N_p = 1.38 bubbles with an uncertainty of, σ_{Np} = ± 1.2 bubbles as given by the Poisson distribution (i.e. $\sigma_x \approx \sqrt{x}$). The contribution of protons to the total number of bubbles is $\frac{1.38}{9.51} = 14.5\ \%$. The uncertainty of dividing the number of bubbles from protons (N_p) by the total number of bubbles (N_{total}) is given by the following equation:

$$\sigma_{\%} = \frac{N_p}{N_{total}} \sqrt{\left(\frac{\sigma_{Np}}{Np}\right)^2 + \left(\frac{\sigma_{Ntotal}}{Ntotal}\right)^2 - 2\left(\frac{\sigma_{Np\cdot Ntotal}}{N_p \cdot N_{total}}\right)} \qquad \text{(Equation E2)}$$

All variables from equation E2 are presented in Table E5 with the definition and the calculated value.

Table E5: Variables for calculation of uncertainty in relative proton contribution

Symbol	definition	value
N_p	Number of bubbles produced by protons	1.38
N_{total}	Total number of bubbles produced by all particles	9.51
$\frac{N_p}{N_{total}}$	Relative contribution of protons to the total number of bubbles	0.145
σ_{Np}	Uncertainty of bubbles produced by protons	1.17
σ_{Ntotal}	Uncertainty of total bubbles produced	3.08
$\sigma_{Np\cdot Ntotal}$	Covariance of number total number of bubbles produced and number of bubbles produced by protons	3.62
$\rho_{p\cdot total}$	Correlation between total number of bubbles and the number of bubbles from protons	1
$\sigma_{\%}$	Uncertainty in the relative contribution of protons	0.077

The covariance has been calculated as, $\sigma_{Np\cdot Ntotal} = \rho_{p\cdot total} \times \sigma_{Np} \times \sigma_{Ntotal}$ where the correlation ($\rho_{p\cdot total}$) is 1 because the total number of bubbles is the sum of the contribution from all bubbles including protons. Using the values from Table E5 the relative contribution from protons to the total number of bubbles is found to be 15 ± 8 %.

Appendix F: Ion Track Structure Model Results

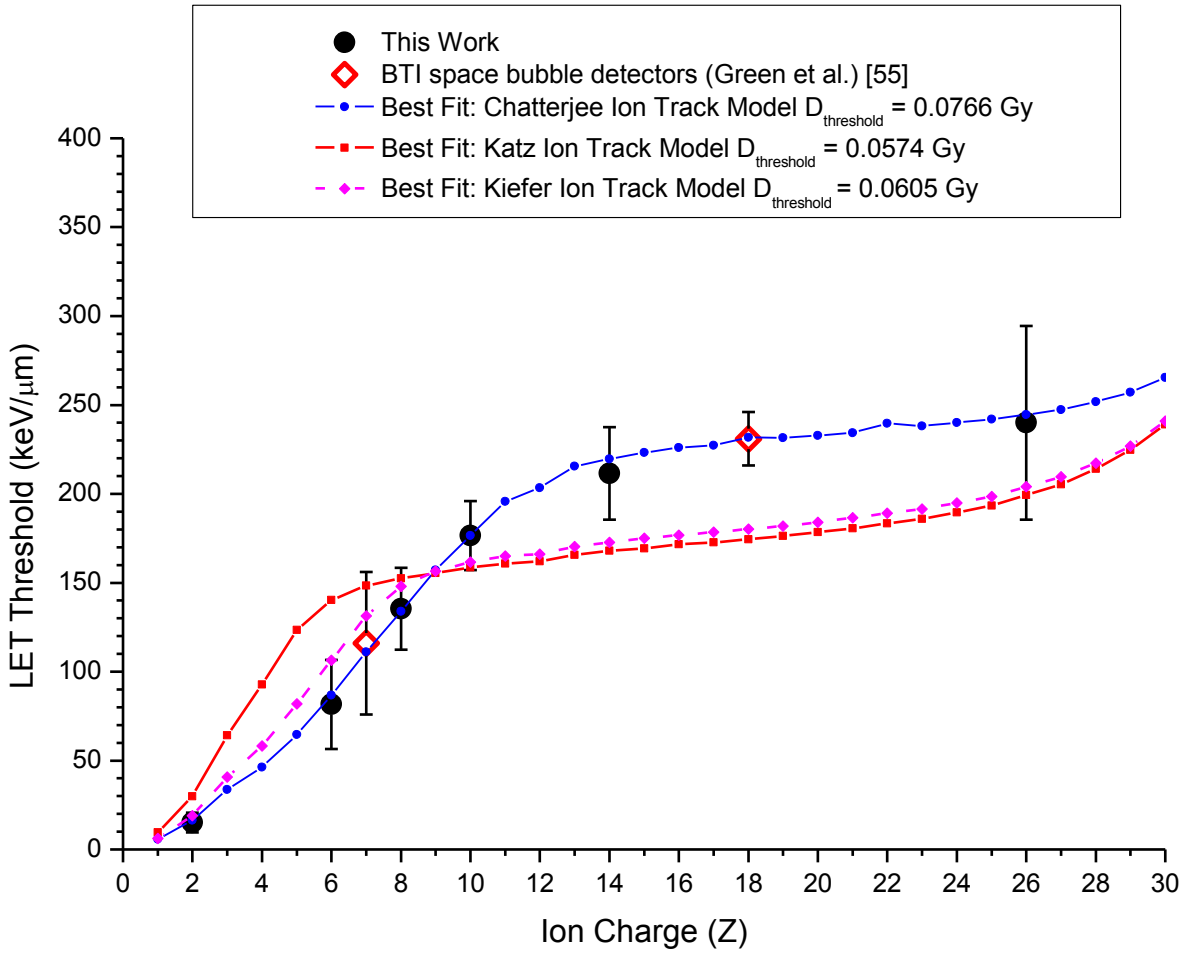

Figure F1: LET threshold ion track structure results

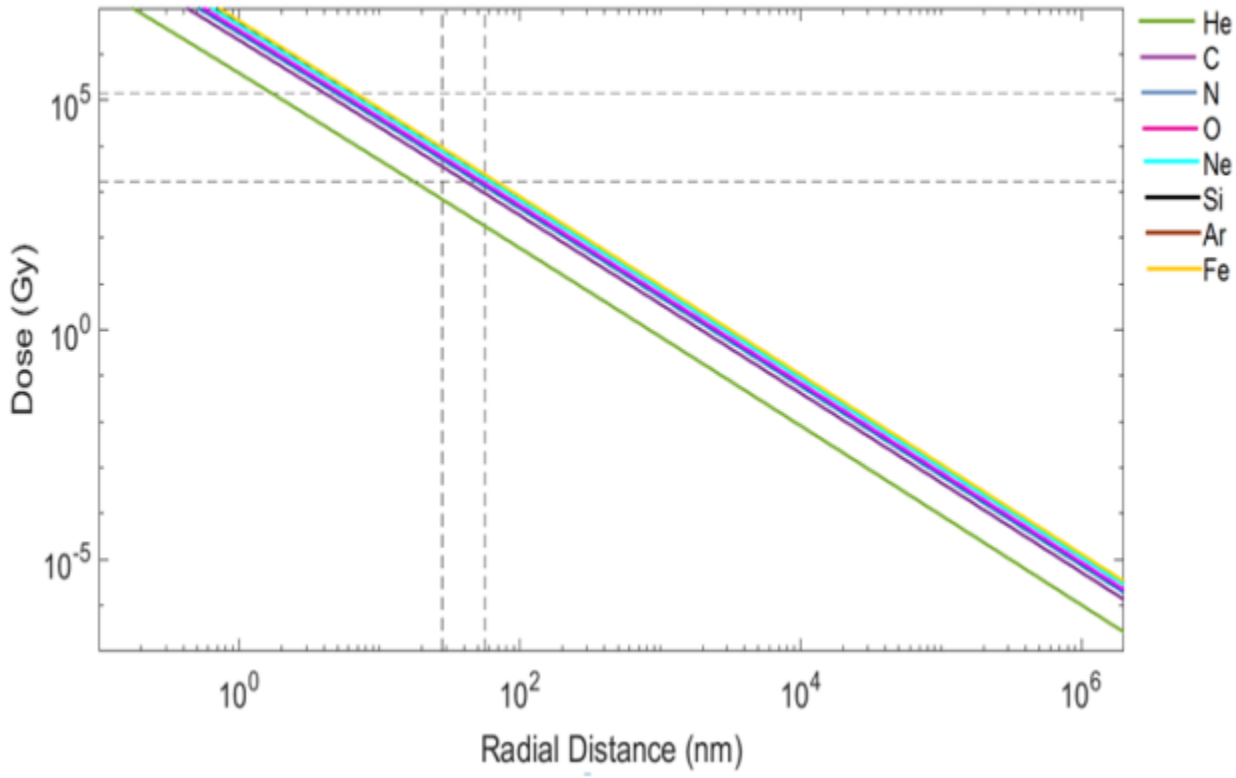

Figure F2: Average ion track energy density at LET threshold in space bubble detectors

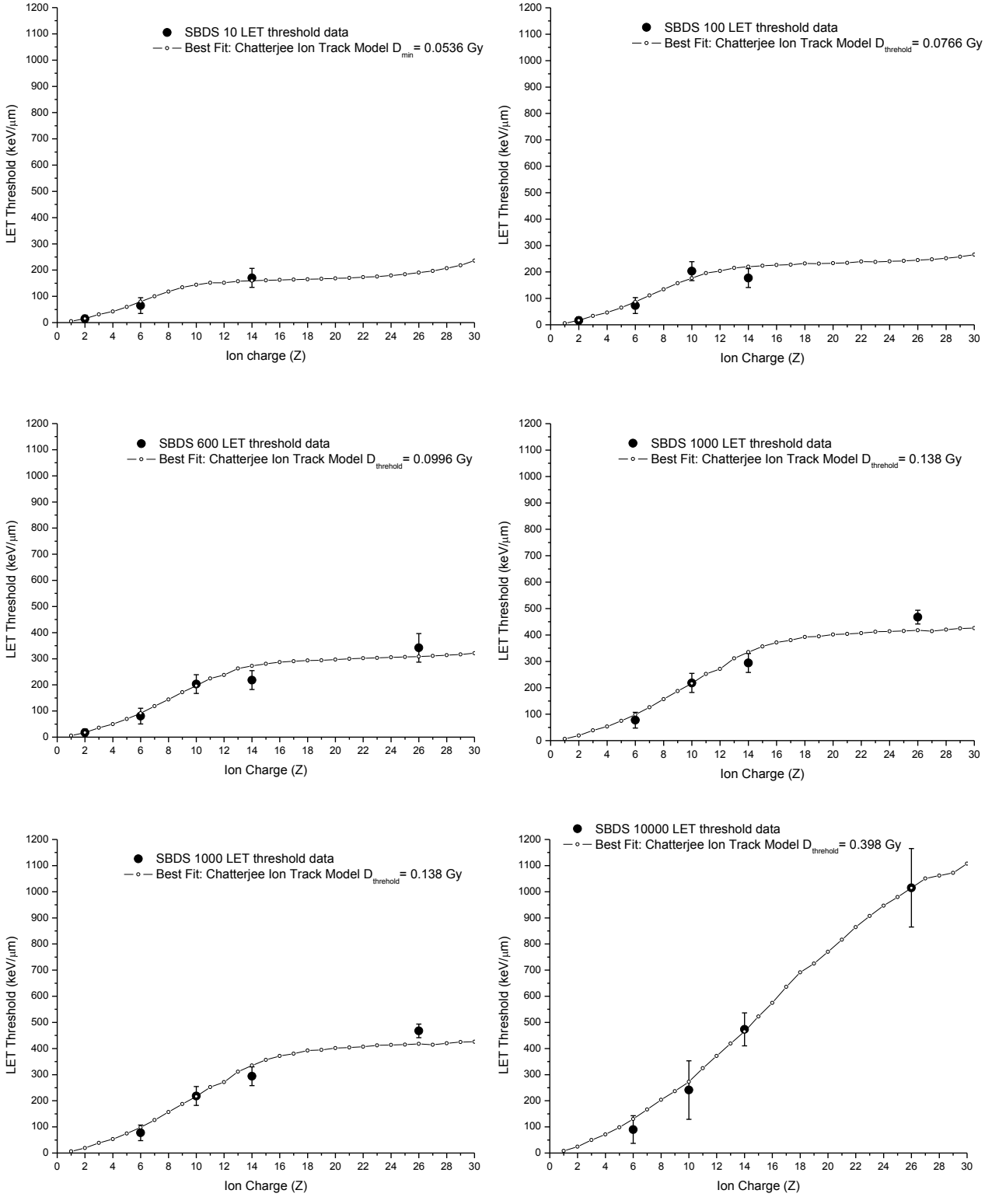

Figure F3: LET threshold for SBDS set with best fit ion track structure model

Appendix G: OLTARIS Bubble Count Model Results

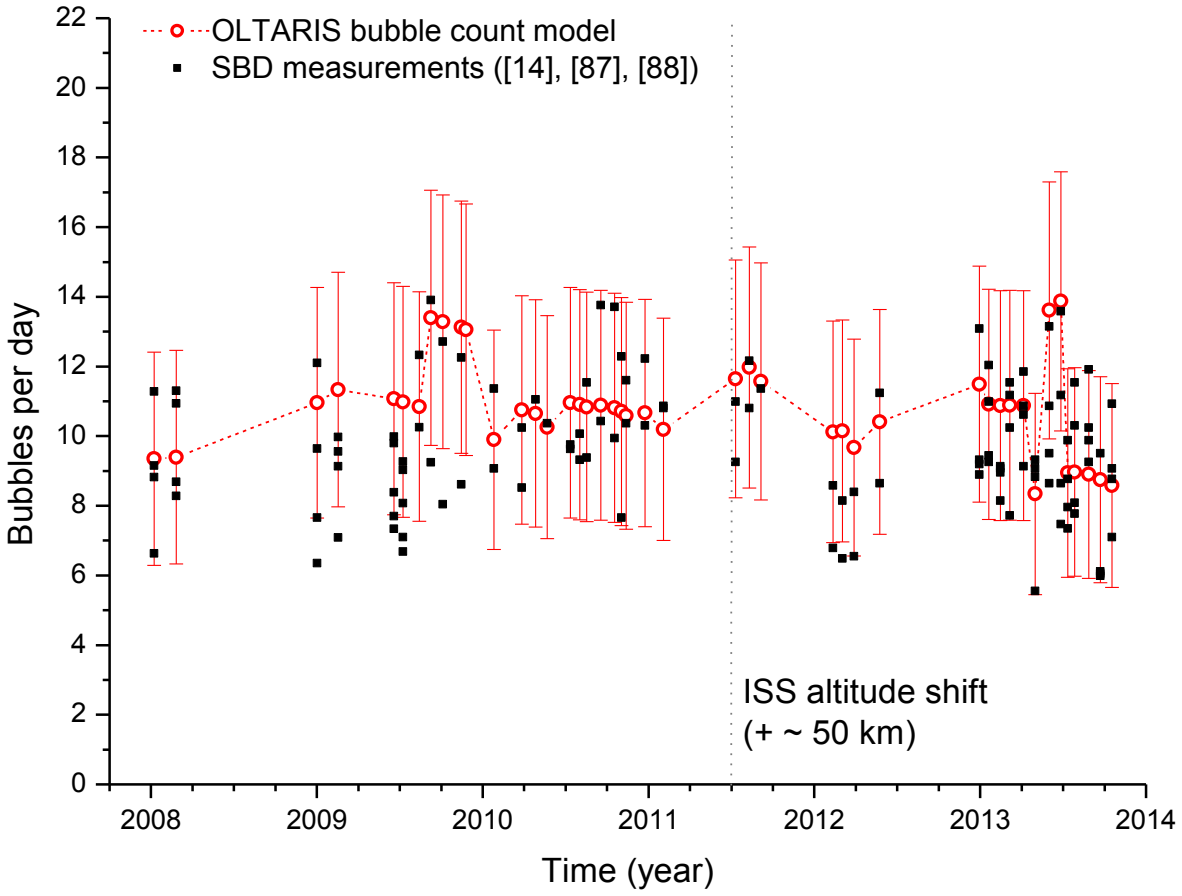

Figure G1: All Space bubble detector measurements between 2008 to 2014 and OLTARIS bubble count model

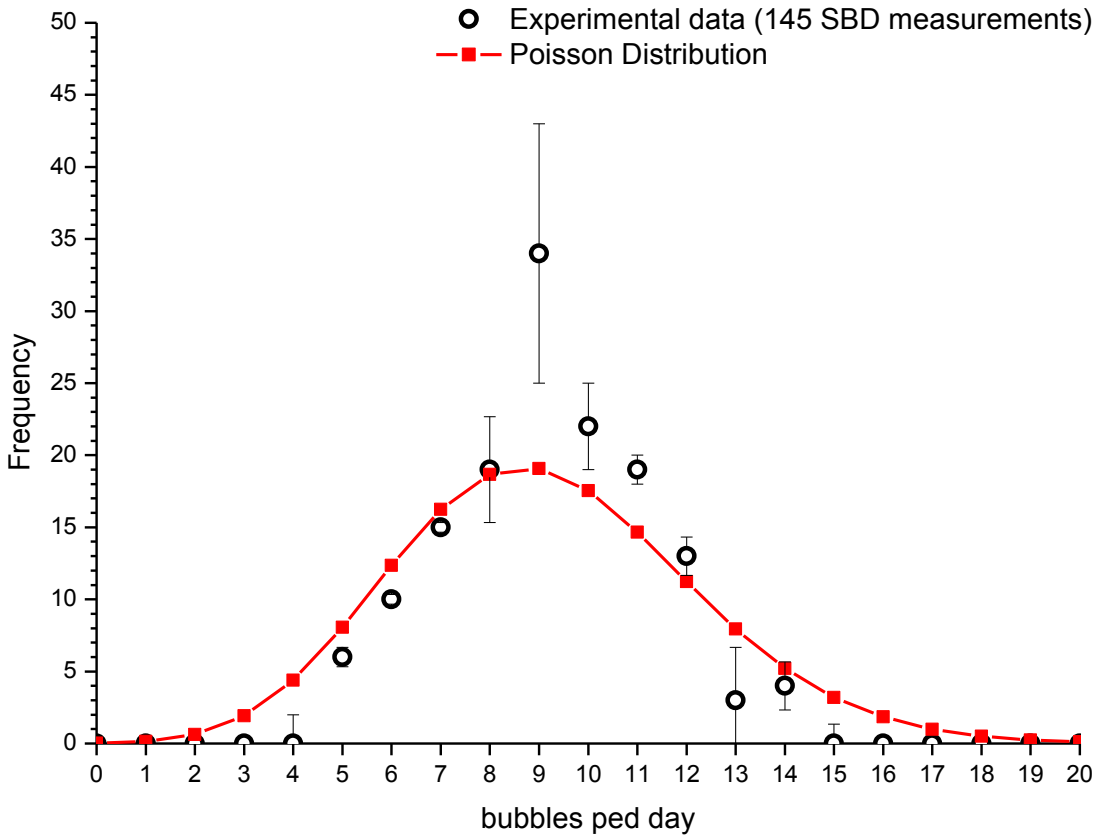

Figure G2: Frequency histogram of bubbles measured per day with space bubble detectors in ISS measurements ([14], [87], [88])

Table G1: Space Bubble Detector Experimental Results and OLTARIS Model

Date of measurement (year)	Measured number of bubbles per day	Measurement ID	Location	OLTARIS model total bubbles	OLTARIS model bubbles from neutrons	OLTARIS model bubbles from protons
2008.018	9.0	ISS16s8	S Module	9.3759	7.9963	1.3796
2008.152	9.8	ISS16s9	S Module	9.4668	8.0849	1.3819
2009.002	8.9	ISS18s1	S Module	11.0011	9.2307	1.7704
2009.128	8.9	ISS18s2	S Module	11.3815	9.4596	1.9219
2009.464	8.6	ISS19s1	S Module	11.119	9.316	1.803
2009.521	8.0	ISS19s2	S Module	11.0249	9.2516	1.7733
2009.619	11.3	ISS20mat	S Module	10.8886	9.1477	1.7409
2009.689	11.6	ISS20s1	JEM	13.32	12.1574	1.1626
2009.759	10.4	ISS20s2	JEM	13.359	12.2162	1.1428
2009.871	10.4	ISS20s3	JEM	13.1423	12.0173	1.125
2009.899	11.1	ISS20 Thirsk	JPM	13.0763	11.9512	1.1251
2010.067	10.2	ISS22-33 B	S Module	9.9266	8.4274	1.4992
2010.235	9.4	ISS22-33 C	S Module	10.7063	8.9779	1.7284
2010.319	11.0	ISS22-33 D	S Module	10.395	8.6818	1.7132
2010.389	10.4	ISS22-33 E	S Module	10.338	8.73	1.608
2010.53	9.8	ISS22-33 F	S Module	10.9984	9.1588	1.8396
2010.586	10.1	ISS22-33 G	S Module	10.9449	9.1187	1.8262
2010.628	11.5	ISS22-33 H	S Module	10.8803	9.067	1.8133
2010.712	13.8	ISS22-33 I	S Module	10.9308	9.08	1.8508
2010.796	13.7	ISS22-33 J	S Module	10.8536	9.0135	1.8401
2010.838	12.3	ISS22-33 K	S Module	10.7458	8.9421	1.8037
2010.866	11.6	ISS22-33 L	S Module	10.6239	8.8564	1.7675
2010.978	12.2	ISS22-33 M	S Module	10.7045	8.8993	1.8052
2011.09	10.8	ISS22-33 N	S Module	10.2289	8.6202	1.6087
2011.525	11.0	ISS22-33 O	S Module	11.7075	9.3797	2.3278
2011.609	12.2	ISS22-33	S Module	12.0409	9.5583	2.4826
2011.679	NA	ISS22-33 Q	S Module	11.5279	9.292	2.2359
2012.113	8.6	ISS22-33 R	S Module	10.1677	8.3322	1.8355
2012.169	8.1	ISS22-33 S	S Module	10.1929	8.3437	1.8492
2012.239	8.4	ISS22-33 T	S Module	9.7217	7.8531	1.8686
2012.393	8.6	ISS22-33 U	S Module	10.4571	8.4829	1.9742
2012.996	9.3	ISS34-40 A	S Module	11.5583	9.1952	2.3631
2013.052	9.4	ISS34-40 B	S Module	10.9746	8.8522	2.1224
2013.122	8.6	ISS34-40 C	S Module	10.948	8.8343	2.1137
2013.178	10.9	ISS34-40 D	S Module	10.8447	8.8364	2.0083
2013.262	10.6	ISS34-40 E	S Module	10.8761	8.864	2.0121
2013.332	9.4	ISS34-40 F	MRM1	8.394	6.7615	1.6325
2013.416	12.0	ISS34-40 G	US Lab	13.6446	12.1301	1.5145
2013.486	12.4	ISS34-40 H	US Lab	13.9062	12.3317	1.5745
2013.529	8.5	ISS34-40 I	MRM1	9.0027	7.2015	1.8012
2013.571	7.9	ISS34-40 J	MRM1	9.0296	7.2219	1.8077
2013.655	10.9	ISS34-40 K	MRM1	8.9646	7.17	1.7946
2013.725	7.8	ISS34-40 L	MRM1	8.8105	7.057	1.7535
2013.795	9.0	ISS34-40 M	MRM1	8.6375	6.9222	1.7153

Appendix H: List of Publications

Journal Publications

1. Alex Miller, Rachid Machrafi, Abuzar Fariad. (2018). Investigation of the $LaBr_3$ Response to Heavy Ions. Radiation Measurements. 115: 43-48 (Peer-reviewed)

2. Alex Miller, Rachid Machrafi, Eric Benton, Hisashi Kitamura, Satoshi Kodaira. (2018). Comparison of the Space Bubble Detector Response to Space-like Neutron Spectra and High Energy Protons. ActaAstronautica. 151: 1-6 (Peer-reviewed)

3. Leslie Kicka, Rachid Machrafi, Alex Miller. (2017). Study of Neutron Fields around an Intense Neutron Generator. Applied Radiation and Isotopes. 130: 276-79 (Peer-reviewed)

4. Rachid Machrafi, Alex Miller, Nafisah Khan. (2015). New Approach to Neutron Spectrometry with Multi Element Scintillator. Radiation Measurements. 80: 10-16. (Peer-reviewed)

5. Alex Miller, Rachid Machrafi, Atef Mohany. (2015). Development of a Semi-autonomous Directional and Spectroscopic Radiation Detection Mobile Platform. Radiation Measurements. 72: 53-59. (Peer-reviewed)

6. Rachid Machrafi, Nafisah Khan, Alex Miller. (2014). Response Functions of Cs2LiYCl6:Ce Scintillator to Neutron and Gamma Radiation. Radiation Measurements. 70: 5-10. (Peer-reviewed)

Conference Publications

1. Alex Miller, Rachid Machrafi, Eric Benton, Hisashi Kitamura, Satoshi Kodaira. (2017).Characterization of Bubble Detectors Used in Space Radiation Dosimetry: Charged Particle. 68th International Astronautical Congress, 2017-09-27. (Paper and oral presentation, peer reviewed)

2. Alex Miller, Rachid Machrafi. (2015). Neutron Spectrometry Using a 7-Li Enriched CLYC Scintillation Detector. Workshops on Radiation Monitoring for the International Space Station, 2015-09-08. (Abstract and oral presentation)

3. Rachid Machrafi, Alexander Miller, Eric Benton, Leena Tomi, Brad Gersey, Richard Wilkins. (2015). Ground Testing of Bubble Detectors used in Space Radiation Dosimetry: Response to High Energy Neutrons. Workshops on Radiation Monitoring for the International Space Station, 2015-09-08. (Abstract and oral presentation)

4. Patrick Dolloso, Rachid Machrafi, Alexander Miller, Sergey Khulapko. (2015). Preliminary attempt of implementing a full-scale geometrical input file of the International Space Station (ISS) and BION-M #1 Biosatellite in MCNPX using AutoCAD solid modeling. Workshops on Radiation Monitoring for the International Space Station, 2015-09-08. (Abstract and oral presentation)

5. Alex Miller, Rachid Machrafi. (2015). Development of a Low Cost Gamma-Ray Imaging System Using Handheld Scintillation Detectors for Visual Surveying of Radiation Fields with Robots. IEEE Xplore Computer and Robot Vision (CRV), 2015 12th Conference on. Computer and Robot Vision (CRV), 2015-06-03 (1 -7). (IEEE Xplore publication and oral presentation, peer-reviewed)

6. Alex Miller, Rachid Machrafi. (2015). Development of a Simple Gamma Ray Camera Using Handheld Scintillation Detectors. 39th Annual CNS/CNA Student Conference, 2015-05-31. (Conference publication and poster, peer-reviewed)

7. Patrick Dolloso, Alexander Miller, Rachid Machrafi, Vyacheslav Shurshakov, Sergey Khulapko and OlgaIvanova. (2015). Neutron Dose Measurement aboard Biosatellite BION-M #1 (AutoCAD implementation into MCNPX) 39th Annual CNS/CNA Student Conference, 2015-05-31. (Conference publication and poster, peer-reviewed)

8. Alex Miller, Rachid Machrafi, Atef Mohany. (2014). Development Of A Simple Gamma Ray Point Source Seeking Mobile Platform. 19th Pacific Basin Nuclear Conference, 2014-08-24. (Conference publication and poster, peer-reviewed)